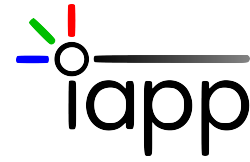**Technische Universität Dresden**

iapp

Fakultät für Mathematik und Naturwissenschaften
Institut für Angewandte Photophysik

Exciton Dynamics in White Organic Light-Emitting Diodes comprising Triplet Harvesting

DISSERTATION

zur Erlangung des akademischen Grades

DOCTOR RERUM NATURALIUM

(Dr. rer. nat.)

vorgelegt von

Simone Hofmann

geboren am 10.06.1985 in Bautzen

Dezember 2012

Eingereicht am: 18.12.2012

Verteidigt am: 01.07.2013

1. Gutachter: Prof. Dr. Karl Leo

2. Gutachter: Prof. Dr. Klaus Meerholz

Abstract

This work comprises different approaches for the efficiency enhancement of white organic light-emitting diodes (OLEDs). In particular, diffusion and transfer processes of excited singlet and triplet states are investigated.

Generation of white light is realized by using the so-called triplet harvesting method where the otherwise nonradiatively decaying triplets of a blue fluorescent emitter are transferred to a highly efficient phosphorescent emitter and result in additional emission at lower energies. Triplet harvesting significantly increases the internal quantum efficiency in OLEDs.

First, the well-known blue emitter 4P-NPD is investigated as model case. Using time-resolved spectroscopy, triplet harvesting by a yellow and red phosphorescent emitter, respectively is directly proven. However, triplet harvesting by a green emitter is not possible due to the low triplet energy of 4P-NPD. Using quantum chemical calculations, two new emitter molecules, 8M-4P-NPD and 8M-4P-FPD, are synthesized with the aim to rise the triplet energy. Their properties and their ability to facilitate triplet harvesting by a green emitter are studied. For the first time, a white triplet harvesting OLED is demonstrated where triplet harvesting occurs directly from a blue emitter to a green and a red emitter.

Furthermore, an additional singlet transfer is observed in the triplet harvesting OLEDs under investigation. Using the phosphorescent emitter as singlet sensor, this effect allows the determination of the singlet diffusion length in 4P-NPD. By varying the distance between singlet generation zone and singlet sensor, a singlet diffusion length of 4.6 nm is found.

One further approach to increase the efficiency is the optimization of a tandem OLED which comprises two single OLED units stacked on top of each other. At a luminance of 1,000 cd/m², the white tandem OLED shows an external quantum efficiency of 25%, a luminous efficacy of 33 lm/W, a color rendering index (CRI) of 62, and Commission Internationale de l'Eclairage (CIE) color coordinates of (0.53/0.43). These efficiencies are comparable to state-of-the-art efficiencies of white OLEDs.

Finally, the highly efficient white tandem structure is applied on an alternative electrode consisting of flattened silver nanowires. In comparison to the conventional OLED with indium-tin oxide (ITO) electrode, this OLED shows similarly high efficiencies as well as a superior color stability in terms of viewing angles. The color stability can be assigned to the light scattering properties of the nanowires. The OLED with silver nanowire electrode shows efficiencies of 24% and 30 lm/W at 1,000 cd/m² with a CRI of 69 and CIE coordinates of (0.49/0.47).

Kurzfassung

In dieser Arbeit werden verschiedene Ansätze zur Effizienzsteigerung in weißen organischen lichtemittierenden Dioden (OLEDs) erforscht. Hierfür werden im Besonderen Diffusions- und Transferprozesse von angeregten Singulett- und Triplettzuständen untersucht.

Zur Erzeugung von weißem Licht wird die sogenannte "triplet harvesting" Methode verwendet, bei der die sonst nicht zur Emission beitragenden Triplettzustände eines fluoreszenten blauen Emitters auf einen hocheffizienten phosphoreszenten Emitter übertragen werden. Dieser liefert dann zusätzliche Emission im niederenergetischen Spektralbereich. Durch triplet harvesting kann die interne Quantenausbeute in OLEDs beträchtlich gesteigert werden.

Zunächst wird der bekannte blaue Emitter 4P-NPD als Modellbeispiel untersucht. Mittels zeitlich aufgelöster Spektroskopie kann triplet harvesting auf einen gelben bzw. roten Emitter direkt nachgewiesen werden. Allerdings ist auf Grund der niedrigen Triplettenergie triplet harvesting auf einen grünen Emitter nicht möglich. In Anbetracht dieser Tatsache werden unter Zuhilfenahme quantenchemischer Betrachtungen zwei neue Emittermoleküle, 8M-4P-NPD und 8M-4P-FPD, synthetisiert und auf ihre Eigenschaften und ihre Eignung für triplet harvesting untersucht. Dabei wird zum ersten Mal eine weiße OLED realisiert, in der triplet harvesting von einem blauen Emitter direkt auf einen grünen und einen roten Emitter erfolgt.

Des Weiteren wird bei den untersuchten triplet harvesting OLEDs ein zusätzlicher Singulettübertrag auf den phosphoreszenten Emitter beobachtet. Dieser Effekt wird zur Bestimmung der Singulettdiffusionslänge in 4P-NPD genutzt. Der phosphoreszente Emitter dient dabei als Singulettsensor. Über eine Variation des Abstands zwischen Singulettgenerationszone und Sensor wird eine Singulettdiffusionslänge von 4,6 nm bestimmt.

Ein weiterer Ansatz zur Effizienzsteigerung besteht in der Optimierung einer aus zwei OLEDs zusammengesetzten Tandem OLED. Bei einer Leuchtdichte von 1000 cd/m² erzielt diese weiße Tandem OLED eine externe Quanteneffizienz von 25% und eine Leistungseffizienz von 33 lm/W mit einem Farbwiedergabeindex (CRI) von 62 und Commission Internationale de l'Eclairage (CIE) Farbkoordinaten von (0,53/0,43). Diese Effizienzen sind vergleichbar mit dem aktuellen Forschungsstand weißer OLEDs.

Schließlich wird diese hocheffiziente weiße Tandemstruktur auf eine alternative Elektrode bestehend aus flachgedrückten Silbernanodrähten aufgebracht. Im Vergleich zur konventionellen OLED mit Indiumzinnoxid (ITO) Elektrode erreicht diese ähnlich hohe Effizienzen sowie eine verbesserte Farbstabilität bezüglich des Betrachtungswinkels, was auf die Streueigenschaften der Nanodrähte zurückgeführt werden kann. Bei einer Leuchtdichte von 1000 cd/m² zeigt die OLED mit Silbernanodrahtelektrode Effizienzen von 24% und 30 lm/W bei einem CRI von 69 und CIE Koordinaten von (0,49/0,47).

Contents

List of Publications

Articles

[A1] M. Furno, R. Meerheim, M. Thomschke, S. Hofmann, B. Lüssem, and K. Leo, "Outcoupling efficiency in small-molecule OLEDs: from theory to experiment", *Proceedings of SPIE* **7617**, 761716 (2010).

[A2] R. Meerheim, M. Furno, S. Hofmann, B. Lüssem, and K. Leo, "Quantification of energy loss mechanisms in organic light-emitting diodes", *Applied Physics Letters* **97**, 253305 (2010).

[A3] S. Hofmann, M. Thomschke, P. Freitag, M. Furno, B. Lüssem, and K. Leo, "Top-emitting organic light-emitting diodes: Influence of cavity design", *Applied Physics Letters* **97**, 253308 (2010).

[A4] S. Hofmann, M. Thomschke, P. Freitag, M. Furno, B. Lüssem, and K. Leo, "Red Top-Emitting Organic Light-Emitting Diodes with 29 % External Quantum Efficiency Using Doped Charge Transport Layers and Optical Simulation", *Solid-State and Organic Lighting* **SOThA1** (2010).

[A5] J. Lee, S. Hofmann, M. Furno, M. Thomschke, Y. H. Kim, B. Lüssem, and K. Leo, "Influence of Organic Capping Layers on the Performance of Transparent Organic Light Emitting Diodes", *Optics Letters* **36**, 1443 (2011).

[A6] M. Thomschke, S. Hofmann, S. Olthof, M. Anderson, H. Kleemann, M. Schober, B. Lüssem, and K. Leo, "Improvement of voltage and charge balance in inverted top-emitting organic electroluminescent diodes comprising doped transport layers by thermal annealing", *Applied Physics Letters* **98**, 083304 (2011).

[A7] S. Mladenovski, S. Hofmann, S. Reineke, L. Penninck, T. Verschueren, and K. Neyts, "Integrated optical model for organic light-emitting devices", *Journal of Applied Physics* **109**, 083114 (2011).

[A8] P. Freitag, S. Hofmann, M. Furno, T. C. Rosenow, S. Reineke, B. Lüssem, S. Mogck, T. Wański, C. May, and K. Leo, "Novel Approaches for OLED Lighting", *SID Symposium Digest of Technical Papers* **42**, 1067 (2011).

[A9] J. Lee, S. Hofmann, M. Furno, M. Thomschke, Y. H. Kim, B. Lüssem, and K. Leo, "Systematic investigation of transparent organic light- emitting diodes depending on top metal electrode thickness", *Organic Electronics* **12**, 1383 (2011).

[A10] J. Lee, S. Hofmann, M. Thomschke, M. Furno, Y. H. Kim, B. Lüssem, and K. Leo, "Increased and balanced light emission of transparent organic light-emitting diodes by enhanced microcavity effects", *Optics Letters* **36**, 2931 (2011).

[A11] J. Lee, S. Hofmann, M. Thomschke, M. Furno, Y. H. Kim, B. Lüssem, and K. Leo, "Highly efficient bi-directional organic light- emitting diodes by strong micro-cavity effects", *Applied Physics Letters* **99**, 073303 (2011).

[A12] S. Hofmann, M. Thomschke, B. Lüssem, and K. Leo, "Top-emitting Organic Light-Emitting Diodes", *Optics Express* **19**, A1250 (2011).

[A13] T. Schwab, M. Thomschke, S. Hofmann, M. Furno, K. Leo, and B. Lüssem, "Efficiency enhancement of top-emitting organic light-emitting diodes using conversion dyes, *Journal of Applied Physics* **110**, 083118 (2011).

[A14] V. Gohri, S. Hofmann, S. Reineke, T. Rosenow, M. Thomschke, M. Levichkova, B. Lüssem, and K. Leo, "White top-emitting organic light-emitting diodes employing a heterostructure of down-conversion layers", *Organic Electronics* **12**, 2126 (2011).

[A15] T. Schwab, S. Hofmann, M. Thomschke, K. Leo, and B. Lüssem, "Efficiency Improvement in Top-Emitting Organic Light Emitting Diodes Using Color Conversion Layer". *OSA Technical Digest* **JWD4** (2011).

[A16] M. Thomschke, P. Freitag, S. Hofmann, M. Furno, S. Reineke, B. Lüssem, and K. Leo, "Top-Emitting OLEDs for Lighting Applications", *Proceedings of OptoElectronics and Communications Conference* (OECC) **16th**, 504 (2011).

[A17] L. Penninck, S. Mladenovski, T. Verschueren, K. Neyts, S. Hofmann, and S. Reineke, "The efficiency of radiative decay inside organic light emitting diodes", *Display Research,* **31st** *International conference, Papers* (2011).

[A18] L. Müller-Meskamp, Y. H. Kim, T. Roch, S. Hofmann, R. Scholz, S. Eckard, K. Leo, and A. F. Lasagni, "Efficiency Enhancement of Organic Solar Cells by Fabricating Periodic Surface Textures using Direct Laser Interference Patterning", *Advanced Materials* **24**, 906 (2012).

[A19] M. Furno, R. Meerheim, S. Hofmann, B. Lüssem, and K. Leo, "Excitonic and optical processes in organic electroluminescent devices", *Physical Review B* **85**, 115205 (2012).

[A20] J. Lee, S. Hofmann, M. Furno, Y. H. Kim, J.-I. Lee, H. Y. Chu, B. Lüssem, and K. Leo, "Combined effects of micro-cavity and dielectric capping layer on bi-directional organic light emitting diodes", *Optics Letters* **37**, 2007 (2012).

[A21] S. Hofmann, T. C. Rosenow, Malte C. Gather, B. Lüssem, and K. Leo, "Singlet Diffusion Length in Organic Light-Emitting Diodes", *Physical Review B* **85**, 245209 (2012).

[A22] B. Lüssem, R. Meerheim, S. Hofmann, M. Furno, S. Reineke, M. Thomschke, and K. Leo, "Top-Emitting OLEDs for Solid State Lighting: High Efficiency by Optical Modeling", *SID Symposium Digest of Technical Papers* **43**, 691 (2012).

[A23] H.-W. Chang, Y. H. Kim, J. Lee, S. Hofmann, B. Lüssem, L. Müller-Meskamp, K. Leo, and C.-C. Wu, "Efficiency Enhancement in ITO-free Green Organic Light Emitting Diodes Utilizing Nano-Composite Scattering Films", *SID Symposium Digest of Technical Papers* **43**, 1496 (2012).

[A24] C. Fuchs, T. Schwab, R. Scholz, T. Roch, A.-F. Lasagni, S. Hofmann, B. Lüssem, L. Müller-Meskamp, K. Leo, and M. C. Gather, "Quantitative description of the scattering angles in electrically-driven OLEDs fabricated on periodically corrugated substrates", *OSA Technical Digest* **LT2B** (2012).

[A25] W. Gaynor, S.Hofmann, M. G. Christoforo, C. Sachse, A. Salleo, M. D. McGehee, M. C. Gather, B. Lüssem, L. Müller-Meskamp, P. Peumans, and K. Leo, "Color in the Corners: ITO-Free White OLEDs with Angular Color Stability", in preparation.

[A26] C. Fuchs, T. Schwab, R. Scholz, T. Roch, S. Eckardt, A. Lasagni, S. Hofmann, B. Lüssem, L. Müller-Meskamp, K. Leo, and M. C. Gather "Quantitative allocation of Bragg-scattering effects in high efficient OLEDs fabricated on periodically corrugated substrates", submitted to Nano Letters.

[A27] Y. H. Kim, J. Lee, W. M. Kim, S. Hofmann, L. Müller-Meskamp, and K. Leo, "A simple way to gain hidden light: extreme enhancement of an out-coupling efficiency in white organic light emitting diodes", in preparation.

[A28] Y. H. Kim, J. Lee, S. Hofmann, M. C. Gather, L. Müller-Meskamp, and K. Leo, "Achieving high efficiency and long-term stability of ITO-free transparent organic light-emitting diodes with conductive polymer electrodes", in preparation.

[A29] H.-W. Chang, J. Lee, S. Hofmann, Y. H. Kim, B. Lüssem, C.-C. Wu, K. Leo, and M. C. Gather, "Nano-particle based scattering layers provide efficient and universal light-extraction for optical efficiency enhancement of organic light-emitting diodes and organic solar cells", in preparation.

[A30] S. Hofmann, M. Furno, M. C. Gather, B. Lüssem, and K. Leo, "Investigation of Triplet Harvesting and Outcoupling Efficiency in Highly Efficient Two-Color Hybrid White Organic Light-Emitting Diodes", in preparation.

Conference Contributions

[C1] S. Hofmann, M. Thomschke, P. Freitag, M. Furno, B. Lüssem, and K. Leo, "Red Top-Emitting Organic Light-Emitting Diodes with 29 % External Quantum Efficiency Using Doped Charge Transport Layers and Optical Simulation", *Solid State and Organic Lighting*, Karlsruhe (2010), talk.

[C2] S. Hofmann, T. C. Rosenow, S. Reineke, B. Lüssem, and K. Leo, "White Organic Light-Emitting Diode by Triplet-Harvesting", *Plastic Electronics*, Dresden (2010), poster.

[C3] S. Hofmann, M. Thomschke, P. Freitag, M. Furno, B. Lüssem, and K. Leo, "Investigation of Cavity Design of Highly Efficient Red Top- emitting Organic Light-emitting Diodes for Display Application", *Electronic Displays*, Nürnberg (2011), poster.

[C4] S. Hofmann, W. Gaynor, G. Christoforo, P. Peumans, C. Sachse, M. Thomschke, L. Müller-Meskamp, B. Lüssem, and K. Leo, "White Organic Light Emitting Diodes with improved Angular Emission Characteristics employing Silver Nanowire Electrodes", *SPIE Optics and Photonics*, San Diego (2011), talk.

[C5] S. Hofmann, T. C. Rosenow, R. Luschtinetz, M. Hummert, B. Lüssem, and K. Leo, "Fluorescent Blue Emitter for Triplet- Harvesting in OLEDs", *Plastic Electronics*, Dresden (2011), poster.

[C6] S. Hofmann, M. C. Gather, B. Lüssem, and K. Leo, "Singlet Diffusion Length in Organic Light-Emitting Diodes", *International Conference on Electroluminescence & Organic Optoelectronics, ICEL*, Fukuoka (2012), talk.

Patents

[P1] A. F. Lasagni, T. Roch, L. Müller-Meskamp, S. Hofmann, R. Scholz, and Y. H. Kim, "Laserstrukturierte Polymeroberfläche zur Verbesserung der Lichtein- und -auskopplung und der Effizienzsteigerung durch Vergrößerung der effektiven Oberfläche von organischen Solarzellen oder Leuchtdioden", DE 10 2011 101 585.3

[P2] Y. H. Kim, J. Lee, W. M. Kim, S. Hofmann, L. Müller-Meskamp, and K. Leo, "Organic light-emitting diode using metal oxide nano-structure and method of fabricating the same", in preparation.

List of Important Abbreviations

CE	current efficiency
CIE	Commission Internationale d'Eclairage
CRI	colour rendering index
DEML	double emission layer
EBL	electron blocking layer
EL	electroluminescence
EML	emission layer
EQE	external quantum efficiency; determined by angular dependent emission
EQE^L	external quantum efficiency;
	determined by the assumption of a Lambertian emission characteristic
EQE^S	external quantum efficiency; determined by an integrating sphere
ETL	electron transport layer
HBL	hole blocking layer
HOMO	highest occupied molecular orbital
HTL	hole transport layer
ISC	intersystem crossing
ITO	indium tin oxide
LCAO	linear combination of atomic orbitals
LE	luminous efficacy; determined by angular dependent emission
LE^L	luminous efficacy;
	determined by the assumption of a Lambertian emission characteristic
LE^S	luminous efficacy; determined by an integrating sphere
LED	light-emitting diode
LUMO	lowest unoccupied molecular orbital
NW	nanowire
OLED	organic light-emitting diode
pin-OLED	organic light-emitting diode with p-doped, intrinsic, and n-doped layers
PH	phosphorescence
PL	photoluminescence
SEML	single emission layer
SPP	surface plasmon polariton
TADF	thermally activated delayed fluorescence
TH	triplet harvesting
TPA	triplet-polaron annihilation
TTA	triplet-triplet annihilation
UPS	ultraviolet photoelectron spectroscopy
UV	ultraviolet

1 Introduction

Since June 2012, Tokyo airport features a 9.6 x 1.9 m sized, concave-shaped organic light-emitting diode (OLED) display (Fig. 1.1) fabricated by Mitsubishi Electric.[1] It is the first 160° panorama display made of OLEDs worldwide. Basically, OLEDs consist of thin layers (~100 nm) of organic (carbon based) semiconducting materials sandwiched between two electrodes. With the size of a soccer goal, the panorama display demonstrates the huge potential of OLEDs for future applications. This is even more impressive when taking into account that the demonstration of the first lab-made OLED was only 25 years ago.[2]

Figure 1.1: Photograph of the world's first 160° OLED panorama display (9.6 x1.9 m) at Tokyo airport fabricated by Mitsubishi Electric and installed in June 2012.

Nowadays, TVs (Sony, LG) and smart-phones with OLED displays (Samsung, Motorola, Nokia, HTC) are already commercially available.[3]

Furthermore, OLEDs are promising candidates for lighting applications. In comparison to common light sources, such as incandescent bulbs, fluorescent tubes, or inorganic LEDs, OLEDs have several advantages: they are flat area emitters offering a pleasant diffuse light perception, wide viewing angles, vivid colors, and new design alternatives. OLEDs as well as other organic electronic devices such as organic solar cells (OSC), transistors, etc. offer the possibility to be made transparent or to be processed on flexible substrates by a low cost roll-to-roll production. Some examples of white OLEDs are shown in Fig. 1.2. First white OLED tiles and lamps (Osram, Philips, Benwirth, and others) are commercially available, too.
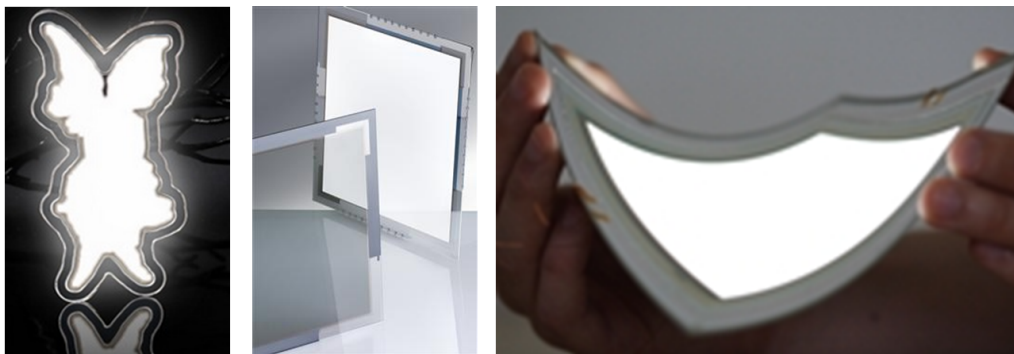
Figure 1.2: Photographs of white OLEDs from Philips, Osram, and Holst centre (left to right), demonstrating the freedom of the technology in terms of shape, transparency, and flexibility.[4–6]

However, the efficient generation of white light in OLEDs remains challenging, since this requires an adequate understanding of **electric**, **excitonic,** and **optical** processes: Electrical improvements regarding charge injection from the contacts and charge carrier transport can be achieved by adding blocking layers and (molecularly) doped transport layers. This topic has been intensively studied in the past years.[7–11]

Excitons are excited states that are responsible for light emission. They are generated by the recombination of holes and electrons, either forming a singlet or a triplet. Due to spin statistics, about 25% singlets and 75% triplets are generated inside the OLED. Their distribution on the different emitter molecules is crucial for the design of efficient white OLEDs.

In most cases, white light is obtained by the combination of several (blue, green, and red) emitter molecules. Two forms of emitter systems are known: First, there are fluorescent emitters, where light emission occurs from the radiative decay of the singlet state. Here, the triplet state decays non-radiatively and therefore does not contribute to light emission. Second, there are phosphorescent emitters which have a high singlet to triplet transfer rate and a radiative triplet state.

The internal quantum yield, i.e. the conversion efficiency of charge carriers into photons, in OLEDs comprising only phosphorescent emitters (PH OLEDs) can be very high, in the range of 70 to 100%.[12, 13] White PH OLEDs reaching fluorescent tube efficiencies have already been demonstrated.[14] However, finding blue phosphorescent emitters with saturated blue emission color and long lifetimes has turned out to be challenging.[15]

A method to overcome these problems is known as triplet harvesting (TH).[16–18] TH is based on triplet diffusion and allows the use of a blue fluorescent emitter while providing similarly high internal quantum yields as PH OLEDs.[19, 20] The usually lost triplets diffuse towards an appropriately inserted phosphorescent emitter, where they are harvested, and subsequently lead to additional light emission. The challenge is to assure that singlet transfer and direct recombination of charge carriers on the phosphorescent emitter are avoided at the same time. This requires a sophisticated device design which is furthermore impeded by the fact that the triplet energy of most blue emitters is not sufficient to facilitate TH by a green phosphorescent emitter.[21]

Due to internal losses (total internal reflection, absorption, surface plasmon polaritons), about 70 to 80% of the generated photons are trapped inside the OLED thin film structure and the substrate.[13] Hence, optical properties and light outcoupling enhancement methods have to be considered to achieve highly efficient white OLEDs. These days, much effort is spent on the development of light outcoupling enhancement techniques for OLEDs.[22] In particular, this includes research on the emitter dipole orientation, scattering techniques, and alternative electrodes to replace the commonly used indium-tin oxide (ITO).[23, 24]

This work focuses on the device design and efficiency enhancement of white TH OLEDs. Especially excitonic processes, like diffusion and transfer of singlets and triplets, but also the development of new blue fluorescent emitters, are of interest. Furthermore, light outcoupling is addressed by using an electrode with light scattering properties.

This introduction is followed by a quantitative description of light perception, the definition of white light, and a comparison of conventional light sources to OLEDs (Chapter 2). The physical fundamentals of organic semiconductors and OLEDs are described in Chapters 3 and 4, respectively. Materials, sample preparation, characterization of OLEDs, and used methods are given in Chapter 5.

Chapter 6 describes the investigation of TH OLEDs using the commercially available blue fluorescent emitter molecule 4P-NPD. Based on quantum chemical calculations, two new emitters "8M-4P-NPD" and "8M-4P-FPD" are synthesized with the aim to facilitate TH by a green phosphorescent emitter. Their performance and ability for efficient white TH will be described in the second part of Chapter 6.

Chapter 7 addresses the determination of the singlet diffusion length in 4P-NPD using spatial emission quenching and two excitation mechanisms: On the one side, singlets are generated by electrical excitation inside the OLED structure and on the other side, singlets are generated in a pure layer via optical excitation.

Based on the work of Rosenow *et al.*[19], the development of an efficient white tandem OLED, where a green/yellow PH OLED is stacked on a blue/red TH OLED is continued. In Chapter 8, the achieved improvements of the single OLED units as well as of the tandem OLED are presented.

Finally, Chapter 9 describes the use of silver nanowire (NW) electrodes as replacement for ITO. The influence of the scattering properties of these NWs is studied. Using the tandem OLED structure developed in Chapter 8, highly efficient white OLEDs on NW electrodes will be demonstrated.

2 White Light and Color

Colors and their perception by humans is one of natures most remarkable phenomena, since the human eye can distinguish between millions of different colors. In this chapter, an introduction into radiometry and photometry is presented, which gives the background for the quantification of colors in a two dimensional color space. As this work is concerned with the generation of white light, important quality criteria for light sources like color coordinates, color correlated temperature, and color rendering index are described.

2.1 Radiometry and Photometry

Radiometry

In optics, radiometry is the mathematical description of electromagnetic waves and radiation including effects like refraction, reflection, absorption, and transmission. In contrast, all quantities connected to the perception of the human eye are described by photometry. In 1931, the International Commission on Illumination (**Commission Internationale de l'Éclairage, CIE**) defined the radiometric and photometric quantities as following.

Electromagnetic radiation is the propagation of, in phase and perpendicular to each other, oscillating electrical and magnetic field components. Both components are perpendicular to the propagation direction.[25] Radiation, in particular light, is emitted in form of quantified energy packages, each with an energy E:

$$E = h\nu = \frac{hc}{\lambda}, \tag{2.1}$$

where $h = 6.626 \cdot 10^{-34}$ Js is the Planck constant, ν the frequency, $c = 299,792$ km/s the speed of light, and λ the wavelength. As shown in Fig. 2.1, the wavelength of electromagnetic radiation found in nature covers several orders of magnitudes, from femtometer cosmic rays to several meters for radio waves. The human eye is able to identify only a very small wavelength range from 380 to 780 nm (1.59 to 3.26 eV), the visible wavelength regime. Adjacent to the visible wavelength regime is the ultraviolet radiation (UV, 10 to 380 nm, 3.26 to 124 eV) and the infrared radiation (IR, 0.78 to 300 μm, 0.004 to 1.59 eV).

The **radiant flux** Φ_e (also called radiant power) is the radiant energy per unit time. The unit is watt [W]. Radiometric quantities are denoted with the index "e" (for energetic). The **radiant intensity** I_e is defined as radiant flux per solid angle Ω:
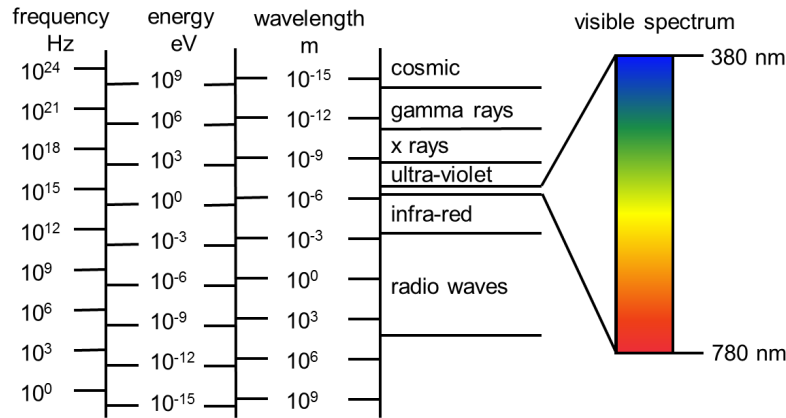
$$I_e = \frac{d\Phi_e}{d\Omega}. \tag{2.2}$$

The unit is watt per steradian [W/sr]. In Fig. 2.2 (a), the geometry of the solid angle is shown, which determines the emission direction and the radiation cone. The solid angle is given by:

$$\Omega = \frac{A}{r^2}\Omega_0, \tag{2.3}$$

with A as the area of the segment of a sphere, r as sphere radius, and Ω_0 the unit solid angle. The unit is steradian [sr] and the full solid angle is $4\pi\,\mathrm{sr}$.

Figure 2.1: The electromagnetic radiation spectrum ranges from femtometer waves to radio waves of several meters. The human eye can perceive only the visible spectrum, a very small part from 380 to 780 nm.
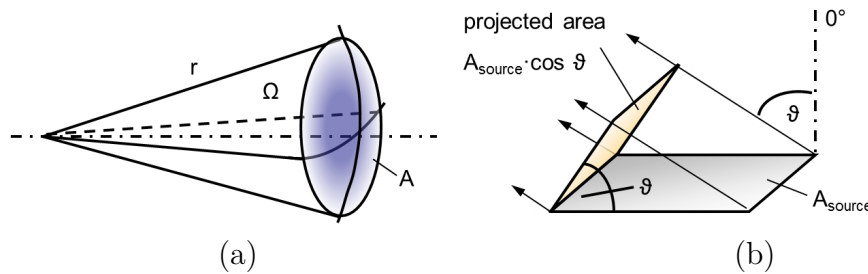
Figure 2.2: Geometry of the solid angle Ω (a) determined by radius r and area A as a segment of a sphere and the projected area of a source (b). For different viewing angles ϑ, the projected area is given by the area of the source A_{source} corrected with the cosine of the viewing angle.

A light source which holds the Lambert cosine law $I_\mathrm{e} = I_\mathrm{e}^0 \cdot \cos\vartheta$ is called a **Lambertian surface** or **Lambertian emitter** [26]. It states that the radiant intensity observed from a Lambertian surface is directly proportional to the cosine of the angle ϑ between the emission direction and the surface normal. As shown in Fig. 2.2 (b), $\vartheta = 0°$ will be referred to as emission perpendicular to the surface or emission in forward direction. Typical examples for non-Lambertian light sources

are the incandescent bulb ($I_e(\vartheta) = const.$) or the LED, which emits preferentially in the forward direction. Since OLEDs are area emitters they are generally considered to be Lambertian emitters. However, due to the complicated thin film structure of the OLED (see Chapter 4) this statement does not have to be true in every case. The **radiance** L_e is the radiant flux per unit solid angle per unit projected area (cf. Fig. 2.2 (b)) of the radiator A_{source}:

$$L_e = \frac{d^2\Phi_e}{dA_{\text{source}} \cdot d\Omega \cdot \cos\vartheta} = \frac{I_e}{A_{\text{source}} \cdot \cos\vartheta}, \tag{2.4}$$

with the unit [W/m²sr]. The projected area (Fig. 2.2) is the area of the emitting surface multiplied by the cosine of the viewing angle ϑ. In case of a Lambertian emitter the radiance is given by:

$$L_e^{\text{Lamb.}} = \frac{I_e^0 \cdot \cos\vartheta}{A_{\text{source}} \cdot \cos\vartheta} = const. \tag{2.5}$$

The radiant intensity and the radiance are defined as properties of a radiating source. The energy received by a detector is given as irradiance E_e and depends on the area of the optical receiver A_{receiver}:

$$E_e = \frac{d\Phi_e}{dA_{\text{receiver}}} = \frac{I_e d\Omega}{dA_{\text{receiver}}} = \frac{L_e\, A_{\text{radiator}} \cos\vartheta\, d\Omega}{dA_{\text{receiver}}}. \tag{2.6}$$

If the distance r between source and receiver is larger than ten times the diagonal of sender or receiver, the area A (Fig. 2.2(a)) can be assumed to be planar (Ten Times Law) and Eq. (2.3) reads:

$$\Omega = \frac{A_{\text{receiver}}}{r^2}\Omega_0. \tag{2.7}$$

Using Eq. (2.6), the relation between irradiance E_e and the radiant intensity I_e is thus given by the Inverse Square Law [27]:

$$E_e = \frac{\Omega_0}{r^2}I_e. \tag{2.8}$$

Radiometric quantities can be expressed either spectrally resolved or integrated over a certain wavelength range:

$$X_e = \int_{\lambda_1}^{\lambda_2} X_e(\lambda)\, d\lambda, \tag{2.9}$$

where X can be either radiant flux Φ_e, radiant intensity I_e, radiance L_e, or irradiance E_e.

Human eye

It is important to mention that the light perceived by humans is not the same as the light emitted from a source. The reason is the anatomy of the human eye (Fig. 2.3) and the processing of the information inside the brain. Light penetrates into the vitreous humor through the cornea, iris, and the lens reaching finally the retina. Inside the retina there are two major types of irregularly distributed light-sensitive photoreceptor cells, namely rods (approx. $1.3 \cdot 10^8$) and cones (approx. $7 \cdot 10^6$). Rods are sensitive to low light intensity and cannot distinguish colors (scotopic vision). On the other hand, the three types of cones (long-wavelength, medium-wavelength, and short-wavelength) are responsible for color perception at high light intensity (photopic vision).
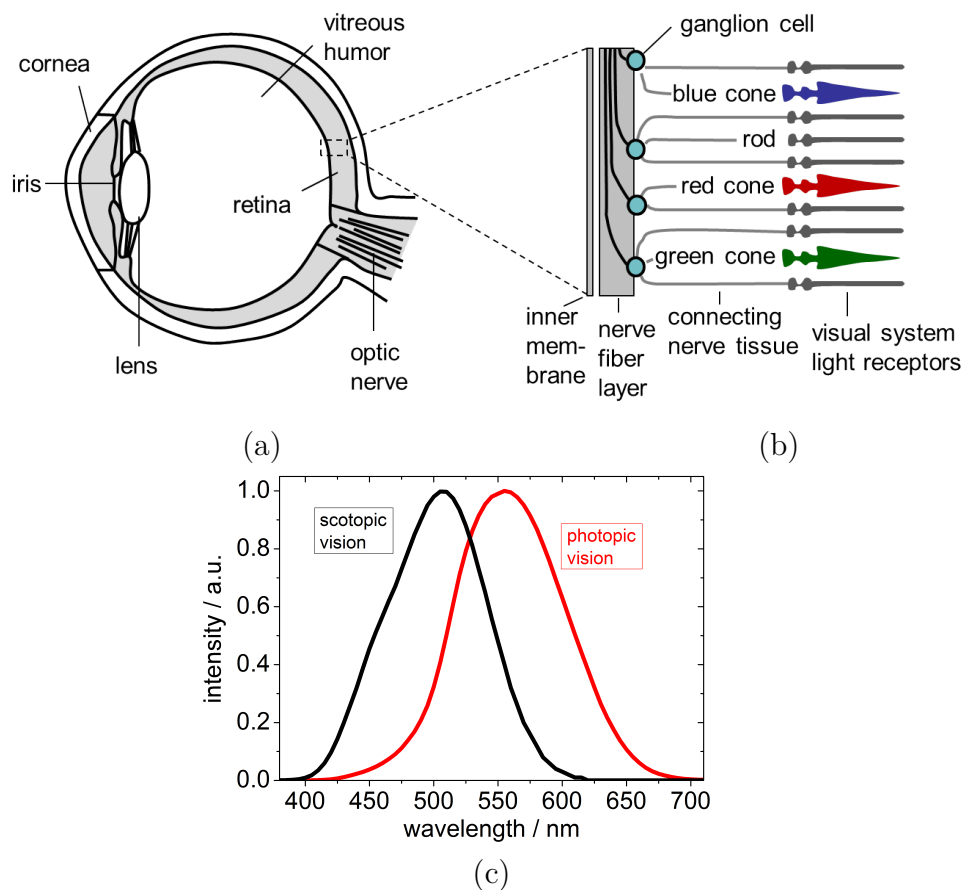
Figure 2.3: The anatomy of the human eye (a) and the detailed structure of the retina (b). Light propagates through the cornea, iris, and the lens to the retina. The light sensitive photoreceptor cells (rods for scotopic vision and cones for photopic vision) are responsible for vision. These two photoreceptor cells lead to two luminosity function curves (c) describing the sensitivity of the eye to light of different wavelengths.

The perception of brightness and colors arises in the brain by impulses of the optic nerve, which are a result of the absorbed radiant flux in the rods and cones. Another type of photoreceptor cell, the ganglion cell, is responsible for contrast perception.[28]

The automatic brightness adaption of the human eye is realized very fast by the change of the pupil diameter via the iris. Due to the two different photo reception cells, there are two luminosity functions describing the sensitivity of the eye to light of different wavelength, namely the photopic function ($V(\lambda)$) and the scotopic function ($V'(\lambda)$) (Fig. 2.3 (c)). Both functions are provided by the CIE [29].

Photometry

In an analogous way to the radiometric quantities, the photometric equivalents can be defined, namely luminous flux Φ_v, luminous intensity I_v, luminance L_v, and illuminance E_v. The index "v" indicates that these are visual quantities weighted by the human eye sensitivity curve $V(\lambda)$. Eqs. (2.2) to (2.9) from radiometry can be applied in the same manner in photometry. Similarly, the term Lambertian emitter is used for a light source which exhibits the same **luminance** L_v in every viewing direction. The relation connecting radiometry and photometry reads:

$$X_\mathrm{v} = K_\mathrm{m} \int_{\lambda_1}^{\lambda_2} X_\mathrm{e}\, V(\lambda)\, \mathrm{d}\lambda, \tag{2.10}$$

where $K_\mathrm{m} = 683$ lm/W is a constant resulting from historical considerations. A summary of the radiometric quantities, their photometric equivalents, and their units is given in Tab. 2.1.

Table 2.1: Summary of radiometric quantities and photometric equivalents as well as their corresponding units.

RADIOMETRY	symbol	unit	PHOTOMETRY	symbol	unit
radiant flux	Φ_e	W	luminous flux	Φ_v	lm
radiant intensity	I_e	W/sr	luminous intensity	I_v	cd
radiance	L_e	W/m²sr	luminance	L_v	cd/m²
irradiance	E_e	W/m²	illuminance	E_v	lx

Since the luminance describes the brightness of a light source, it is a very important quantity for the lighting industry and technology. Table 2.2 gives typical luminance values for lighting applications and natural light sources. At 1 cd/m² the photopic vision sets in and the human being is able to distinguish colors. The brightness requirements for light sources depending on the application are in the range of 100 to 10,000 cd/m². The dazzle limit for the human eye is at around 10,000 cd/m².

Table 2.2: A selection of typical luminance values required for application or given by a natural light source.

	luminance [cd/m²]
displays	100 - 500
indoor lighting	200 - 5,000 [30]
signage	40 - 1,000 [31]
outdoor lighting	1,000 - 10,000
cloudy sky at noon	1,000 [32]
average clear sky	8,000 [32]

2.2 Color Stimulus Specification

As discussed in the previous section, light perceived by the eye and evaluated by the brain underlies a spectral change. This process depends on the ambient light and the human himself making it necessary to define a table of colors. Therefore, the CIE introduced a two-dimensional color space in 1931.[29, 33] For a spectral distribution $s(\lambda)$, the tristimulus values of X, Y, and Z are given by:

$$X = \int s\left(\lambda\right)\bar{x}\left(\lambda\right)d\lambda, \quad Y = \int s\left(\lambda\right)\bar{y}\left(\lambda\right)d\lambda, \quad Z = \int s\left(\lambda\right)\bar{z}\left(\lambda\right)d\lambda, \qquad (2.11)$$

where $\bar{x}(\lambda)$, $\bar{y}(\lambda)$, and $\bar{z}(\lambda)$ are the so-called color matching functions derived from a series of methodical experiments [34] (Fig. 2.4 (a)). The coordinates in the CIE1931 color diagram (Fig. 2.4 (b)) are given by:

$$x = \frac{X}{X+Y+Z}, \quad y = \frac{Y}{X+Y+Z}, \quad z = \frac{Z}{X+Y+Z}, \qquad (2.12)$$

with $x + y + z = 1$ for standardization. The gamut of colors for an average person is given by the horseshoe-shaped color diagram, where the coordinates x and y determine one color. The z value is redundant due to the normalization. By selecting two (three) color points, all colors which are on the connecting line (inside the triangle) can be reached by mixing the two (three) colors.

The closer the color point is positioned to the edge of the diagram, the purer the color is perceived. The spectrum $s^{\mathrm{Planck}}(\lambda, T)$ depending on the wavelength λ and the temperature T of a **Planckian radiator** (black body) can be derived by:

$$s^{\mathrm{Planck}}(\lambda, T) = \frac{2hc}{\lambda^5 (e^{\frac{hc}{\lambda k_{\mathrm{B}} T}} - 1)}, \qquad (2.13)$$

where $k_{\mathrm{B}} = 8.617 \cdot 10^{-5}$ eV/K is the Boltzmann constant. The Planck curve represents the colors of a hypothetical black body at different temperatures T. In Fig. 2.4 (b), the point A (0.448/0.407) represents the spectral distribution of a Planckian radiator

with a temperature of 2856 K and is often referred to as warm white color point, while
E (0.333/0.333) is the point of equal energy which is often referred to as cold white
color point. In Appendix A.1, the spectral emission intensities and the resultant color
coordinates measured for conventional light sources are summarized.
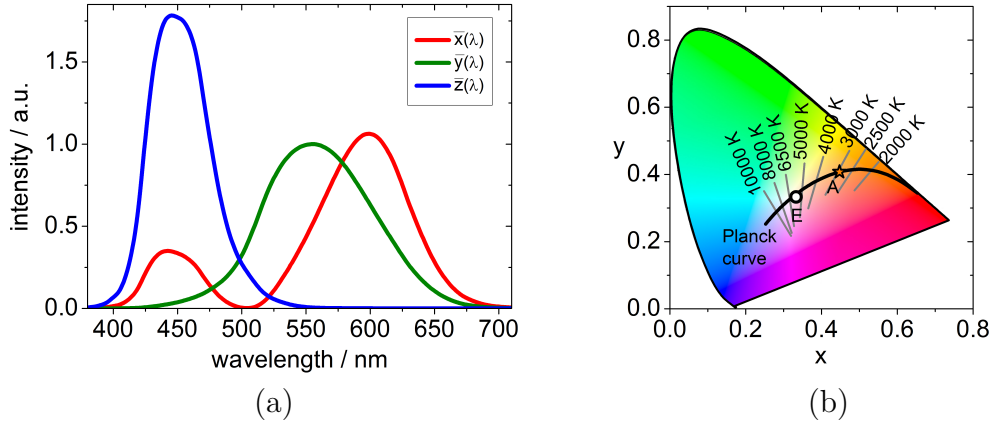
Figure 2.4: Color matching functions (a) representing the light sensitivity of the
different cones. Two dimensional CIE1931 color diagram (b). Every color can be
described by two coordinates x and y. The warm white point A (0.447/0.407) and
the point E (0.333/0.333) of equal energy are plotted. The black line represents the
Planckian radiator and the gray lines the lines of equal correlated temperature.

2.3   White Light

Color correlated temperature

The color correlated temperature (CCT) of a light source is the temperature of the
Planck curve whose perceived color most closely resembles that of the light source. In
Fig. 2.4 (b), the lines of equal correlated temperature are shown. The CCT can be
calculated for every light source, however, it is only meaningful for a small distance of
the color coordinates Δuv from the Planck curve:

$$\Delta uv = \sqrt{\left(u_{\text{source}} - u_{\text{Planck}}\right)^2 + \left(v_{\text{source}} - v_{\text{Planck}}\right)^2}, \tag{2.14}$$

with u and v being the CIE1960 uniform color coordinates of the light source and the
Planckian curve, respectively. The CIE1960 color coordinates have been introduced
to achieve a perceptual uniformity. The uniform color coordinates can be calculated
from the CIE1931 color coordinates using:

$$u = \frac{4x}{-2x + 12y + 3} \text{ and } v = \frac{6y}{-2x + 12y + 3}. \tag{2.15}$$

The CCT allows to distinguish between warm (CCT: 2,500 to 3,300 K), neutral (CCT:
3,300 to 5,000 K), and cold/daylight (CCT: 5,000 to 7,500 K) white light sources.

For example, the light during the sunset/sunrise corresponds to a CCT of 3,200 K, while a sunny day around noon corresponds to a CCT of 5,800 K. Table 2.3 gives an overview of CCTs of different light sources. While incandescent and halogen lamps are restricted to warm white, fluorescent tubes, compact fluorescent lamps, LEDs, and OLEDs cover a CCT range from warm white to cold white.[35, 36]

Color rendering index

In most cases, the impression caused by the reflected light from the illuminated surface is more important than the direct light of a light source. The quality of the reflected light can be quantified by the color rendering index (CRI). The CRI of a light source can be measured by comparing the reflected light of eight test color samples to the reflected light of a Planckian radiator at the same CCT. However, due to the complexity of this measurement, the CRI is nowadays calculated by a convolution of defined reflectivity curves with the spectrum of the light source. The exact calculation can be found in Ref. [37]. In a strict sense, the CRI is only valid if the color coordinates are close to the Planck curve, i.e. a distance $\Delta uv \leq 0.0054$.

The values of the CRI range from 0 to 100, where higher values indicate better color rendering. An incandescent lamp has a CRI of 100 by definition, a CRI above 90 is still very good, between 80 and 90 is good, and a CRI between 60 and 80 is sufficient for most applications. For indoor solid state lighting a minimum CRI of 75 is required. An overview of CRI values for different lights sources are given in Tab. 2.3. For fluorescent tubes, compact fluorescent lamps, LEDs, and OLEDs the CRI can be adjusted by tuning the emission spectrum and very good CRIs are possible (cf. Appx. A.1). [35, 38]

Table 2.3: Summary of color correlated temperatures and color rendering index values for different light sources. While incandescent and halogen lamps are restricted to warm white and have maximum CRI, fluorescent tubes, compact fluorescent lamps, LEDs and OLEDs range from warm white to cold white. The CRI of the four latter ones can be adjusted by tuning the emission spectrum leading to very good CRIs.

light source	CCT [K]	CRI
incandescent [39]	~2,700	~100
halogen [40]	~2,900	~100
fluorescent tube [35, 39]	2,700-8,000	50-95
compact fluorescent [35, 39]	2,700-8,000	80-90
LED [39, 40]	2,650-6,500	70-90
OLED [41]	2,500-6,500	75-90

Energy Star requirements

As indicated in the previous section, a light source is perceived as white if the color coordinates are close to the Planckian curve and a CRI is defined ($\Delta uv \leq 0.0054$ in the CIE1960 color space). However, this definition is arguable, since two lamps can have the same CRI and CCT, but still show differences in appearance. A definition which further includes the tolerance of the human eye to perceive different whites is more useful.[42–44]

Since 2008, there is an ANSI standard based on studies with fluorescent tubes, which is also used by the Energy Star program of the US Environmental Protection Agency and the US Department of Energy to define requirements for solid state lighting.[38] For white light, it is required that the color coordinates fall into one of the eight chromaticity quadrangles in the CIE1931 color diagram (Fig. 2.5), while every quadrangle is assigned to a CCT value. This standard is based on 7-step MacAdam ellipses. That means that the original (1-step) MacAdam ellipses are scaled up by a factor of 7. Here, one ellipse is the region where colors are perceived to be the same.[45] However, it is strongly discussed if this is sufficient since in industry manufacturers already use a much finer binning for white LEDs, e.g. based on 2-step or 4-step MacAdam ellipses.[44]
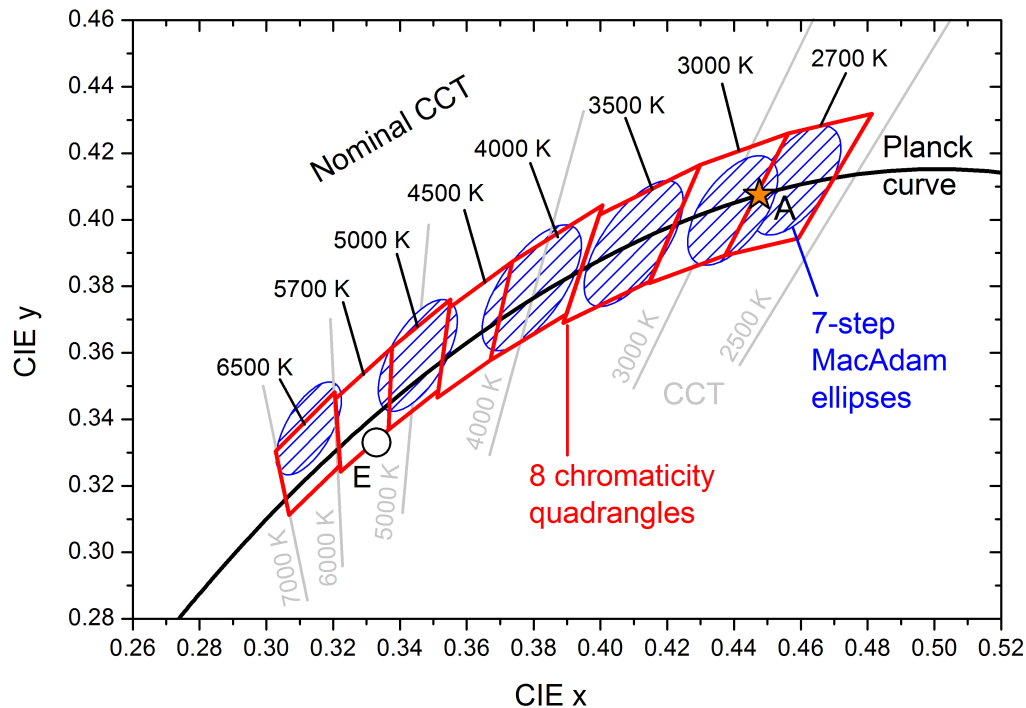
Figure 2.5: CIE1931 diagram including the eight chromaticity quadrangles which define a white light source and their CCT. Each ellipse of the 7-step MacAdam ellipses defines a region, where the colors are perceived to be the same. The Planck curve, and the color points A and E are included for better visualization.

2.4   Light Sources

Another important quantity for the characterization of human-made light sources is the ratio of light power output, corrected to human reception (in lumen), to the electrical power input (in watt). This ratio is called **luminous efficacy** (LE). The maximum LE of an ideal white light source (having a color point A and a CRI of 100) is 240 lm/W. For a warm-white LED (at 3,000K, CRI: 90), a theoretical maximum of 408 lm/W can be estimated.[39] Based on a real device performance and reasonable estimated device improvements, a possible efficacy of 155 lm/W (at 5,000 cd/m²) is calculated for an all-phosphorescent single stack white OLED.[46] A theoretical limit of 250 lm/W for such a white OLED is stated by Tyan[47], assuming that the driving voltage is reduced to a minimum of 2.9 V and no loss mechanisms are present in the device. A second important quantity for light sources is the **external quantum efficiency** (EQE). The EQE is given by the number of photons emitted into air divided by the number of injected electrons.

Incandescent lamp

The incandescent light bulb has been a major light source since the 19th century, in particular for home lighting. A filament wire is heated to a high temperature until it glows. The wire is protected against air by a gas filled or evacuated glass enclosure. Although incandescent lamps emit warm white light and have a high CRI of 100, they are very inefficient. Only 5% of the power is converted to visible light, the rest is emitted as heat. The typical lifetime is below 1,000 h. Filling the glass bulb with halogen gas, the lifetime can be extended to 2,000 h and the efficacy can be increased to 20 lm/W.

Since 2009, the European Union is step-wise forbidding the production and sales of incandescent lamps. Hence, in future the incandescent lamp will be replaced by alternative light sources.[39, 48]

Fluorescent lamp

In the late 1930s, first fluorescent tubes were processed by General Electrics in the USA and are now dominating the lighting in offices and public buildings. Here, UV light is generated between the electrodes at the end of the tube and excites a phosphor which is coated on the inner side of the tube. The phosphor absorbs the UV light and emits light in the visible wavelength regime (down-conversion). Fluorescent tubes have a better efficiency (about 25%) and a longer lifetime than incandescent bulbs (up to 30,000 h), however, most of them contain small amounts of toxic mercury.

About 50 years later the compact fluorescent lamp (CFL) entered the market, which consists of two, four or six small fluorescent tubes and fits into the socket of incandescent bulbs. The main advantage of CFLs is the high efficiency (35-

80 lm/W, 20%), and hence the energy saving. As a result, the environmental pollution (carbon dioxide, nitrogen oxide, and sulfur dioxide) is strongly reduced compared to incandescent bulbs. On the other hand, the amount of mercury in these lamps lowers the advantage of the energy saving issue.

LEDs

Inorganic LEDs providing a nontoxic alternative to fluorescent lamps were first demonstrated in the 1960s.[49] The light emission is based on recombination of electrons and holes at a pn junction of semiconducting materials. Using down-conversion from a blue emitting gallium nitride diode, highly efficient white LEDs are possible (~100 lm/W, 30%). In April 2012, Cree Inc. (Durham, USA) claimed a record efficacy of 254 lm/W.[50] One major difference of the LED to other conventional light sources is the strong forward directed emission, which makes LEDs especially useful for applications where spotlight with high luminance is necessary. The lifetime can be over 25,000 h. Nowadays, LED lighting for the household is still expensive. Nevertheless, LEDs are very promising candidates to replace the incandescent bulb.

OLEDs

In the past years OLEDs became a light source competitive to their inorganic counterparts, despite the fact that intensive research on OLEDs started about 30 years later. In OLEDs, light emission is realized by recombination of charge carriers on organic semiconducting molecules. OLEDs exhibit a large variety of advantages and new features like area emission, processing possibility on flexible substrates, small thickness, and wide viewing angle. On the lab scale, efficacies exceeding that of fluorescent tubes have been already demonstrated (124 lm/W at 1,000 cd/m²).[14] First white OLED tiles and lamps are commercially available, however, the prices are still very high.

One of the first commercial availabe white OLED tile has been sold by OSRAM (ORBEOS, 23 lm/W at 1,000 cd/m²) which cost about 100 € (lifetime ~5,000 h, size ~90 mm diameter, 1.9 mm thickness). Konica Minolta sells OLED panels (45 lm/W at 1,000 cd/m²) for about 1,000 € (lifetime ~8,000 h, size ~74 x 74 x 1.9 mm). A hybrid LED/OLED lamp (Benwirth Licht GmbH) costs between 2,000 and 5,000 €.[51–53]

3 Organic Semiconductors

The variety of organic materials offers the possibility to build light-emitting diodes, solar cells, field effect transistors, and other devices. In this chapter, the physical and chemical properties of organic semiconductors are discussed. Firstly, the formation of molecular orbitals is deduced from the Schrödinger equation. Then, the important radiative transitions of fluorescence and phosphorescence are explained. Furthermore, the respective energy transfer between electrons and between molecules is discussed. This includes diffusion and annihilation processes, which are essential for this work.

3.1 Molecular Orbitals

Comparable to a single atom, molecules composed of n atoms can be generally described by the time independent nonrelativistic **Schrödinger equation**:

$$\hat{H}\,\Psi^{\mathrm{n}}(\vec{r}) = E^{\mathrm{n}}\,\Psi^{\mathrm{n}}(\vec{r}), \tag{3.1}$$

where $\hat{H}$ denotes the Hamilton operator and Ψ^{n} are the eigenfunctions depending on the spatial vector $\vec{r}$, leading to the allowed energy eigenstates E^{n}. In organic films, intermolecular bonds are realized by weak van der Waals forces. Thus, the organic film can be described as an oriented gas and the energy eigenstates are primarily determined by the structure of a single molecule. [54–56]

Several approximations have to be made, since the Schrödinger equation cannot be solved analytically for the many-particle problem. One is the **Born-Oppenheimer approximation** which assumes that motion of electrons (e) is much faster than that of the nuclei (N). Due to the low mass of the electron compared to nuclei, the electrons respond instantaneously to any change of the nuclei formation. The Hamilton operator $\hat{H}$ and the wave function ψ can therefore be separated into:

$$\hat{H} = \hat{H}^{\mathrm{e}} + \hat{H}^{\mathrm{N}} \tag{3.2}$$

$$\psi(\vec{r}, \vec{R}) = \psi^{\mathrm{e}}(\vec{r}) \cdot \psi^{\mathrm{N}}(\vec{R}), \tag{3.3}$$

where ψ^{e} describes the electronic part and ψ^{N} the vibrational part, depending on the electron coordinates $\vec{r}$ and the nuclei coordinates $\vec{R}$, respectively. The energy E of a certain molecular state can therefore be written as:

$$E = E^{\mathrm{el}} + E^{\mathrm{vib}}. \tag{3.4}$$

Disregarding the numerous interactions between single electrons (**Hartree approximation**), allows the total electron wave function to be written as a product of the

wave functions of a single electron ψ_i:

$$\psi^e = \prod_i \psi_i. \tag{3.5}$$

Since electrons are fermions, the wave function has to be antisymmetric under the exchange of two electrons (**Pauli principle**). This is ensured by the Slater determinant:

$$\psi^e = \frac{1}{\sqrt{n!}} \begin{vmatrix} \psi_1(1) & \psi_1(2) & \cdots & \psi_1(n) \\ \psi_2(1) & \psi_2(2) & \cdots & \psi_2(n) \\ \vdots & \vdots & \ddots & \vdots \\ \psi_n(1) & \psi_n(2) & \cdots & \psi_n(n) \end{vmatrix}, \tag{3.6}$$

where $\psi_1(1)$ describes the wave function of electron 1 at the position 1, $\psi_2(1)$ the wave function of electron 2 at the position 1, and so on.

In quantum chemistry the electron wave functions ψ_i describing the molecular orbitals are calculated using the **Linear Combination of Atomic Orbitals (LCAO)** Φ_k:

$$\psi_i = \sum_k c_{i,k}\, \Phi_k. \tag{3.7}$$

By minimizing the energy of the system, the coefficients $c_{i,k}$ can be determined numerically.

Organic semiconducting molecules consist of hydrocarbons with alternating single and double bonds (conjugated system). In benzene (Fig. 3.1 (a)), for example, the molecular orbitals can be assumed to be a superposition of the sp^2 and p_z orbitals of single carbon atoms (Fig. 3.1 (b)). The sp^2 orbitals form the σ bonds in the xy plane (Fig. 3.1 (c)), while the p_z orbitals form a delocalized electron cloud, the so-called π bonds (Fig. 3.1 (d)). The overlap of the p_z orbitals is lower than that of the sp^2 orbitals, which results in a lower energy splitting of the binding π and anti-binding π^* states compared to the σ and σ^* states. Thus, the **Highest Occupied Molecular Orbital (HOMO)** and **Lowest Unoccupied Molecular Orbital (LUMO)** are given by π and π^*, respectively (Fig. 3.1 (e)). Furthermore, the σ bonds are the strongest type of covalent bonds and determine mainly the chemical properties, while the delocalized π system is mainly responsible for the electrical and optical properties.[57]

The energy gap $\triangle E = E_{\text{HOMO}} - E_{\text{LUMO}}$ can be adjusted by the number of aromatic rings as well as by incorporation of various atoms such as nitride, oxygen, sulfur, and others. This allows the design of molecules with band gaps in the range between infrared and UV light, i.e. of molecules that are suitable as emitters or absorbers in OLEDs or OSCs, respectively.

It is common practice to consider these organic solids as "organic semiconductors", although they are rather insulators than semiconductors. The associated semicon-

ducting properties like light absorption, emission, and conduction of charges can be observed. While absorption and emission are indeed intrinsic properties, charges are usually created extrinsically, e.g. via injection by electrodes or dissociation of optically generated electron-hole pairs.
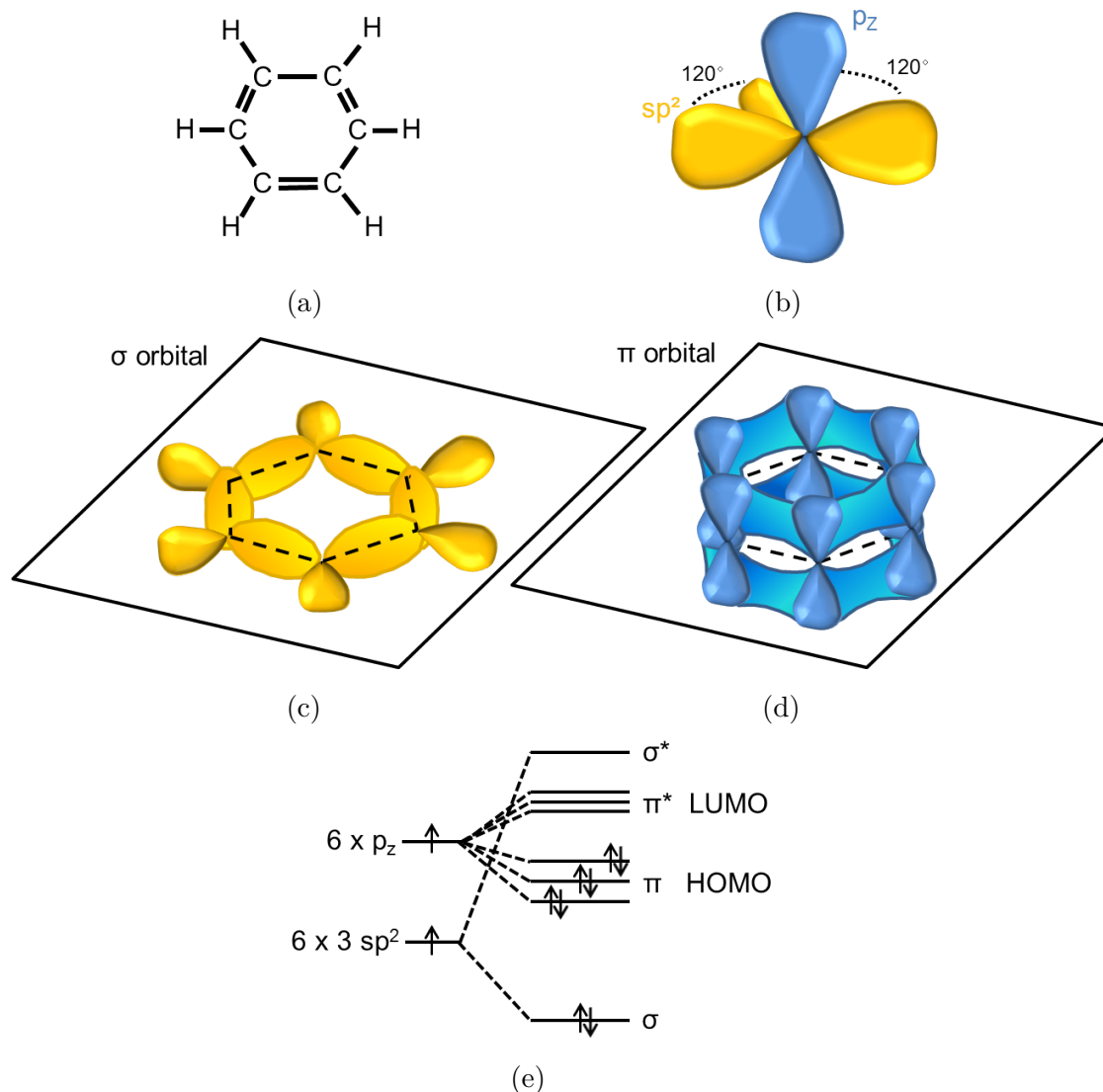
Figure 3.1: The chemical structure of benzene (a), sp^2 hybridization of a single carbon atom (b), the σ orbital/electrons (c), and the delocalized π orbital/electrons (d) of benzene resulting from the linear combination of atomic orbitals of the carbon atoms. A schematic energy level diagram (e). The electrons in the π system form the highest occupied molecular orbital (HOMO) and lowest unoccupied molecular orbital (LUMO). These orbitals are responsible for the electronic and optical properties of organic semiconductors.[57]

Density-functional theory

The technique of constructing the molecular wave function from the electron wave functions is known as **Hartree-Fock (HF)** method, where every electron has to be described by three coordinates. However, in modern quantum chemistry, an alternative approach named **density-functional theory (DFT)** is well established. The advantage of DFT is that it calculates the molecular properties from the electron density, which depends itself only on three coordinates, thus decreasing computation time. Various methods based on HF or DFT have been developed to calculate properties of molecules. However, there is not one ultimate method that works best. Even nowadays, it is common to compare the data found experimentally to the values predicted by the different theoretical approaches, and use the best fitting method for further optimization.[58–62]

   To demonstrate this approach, an example calculation for the simple benzene molecule can be found in Appendix A.2 together with the calculated electron wave functions.

3.2   Fluorescence and Phosphorescence

By excitation of the organic molecule, either optically or electrically, a Coulomb-bound pair of an electron and hole, an (electrically neutral) **exciton**, is formed. In organic semiconductors these excitons are called **Frenkel excitons** and are strongly localized and bound to the molecule with a binding energy of 0.1 eV to 1 eV. This is in sharp contrast to inorganic semiconductors, where Wannier-Mott excitons have a typical size in the order of tens of lattice constants and binding energies in the range of a few meV [63].

   Electrons and holes have a spin of $s = 1/2$, respectively, which leads to a total exciton spin of $S = 0$ (singlet) or $S = 1$ (triplet). In a two particle system the spin wave function of the particles α and β can be written as:

exciton	spin wave function	S	M_s
singlet			
	$\frac{1}{\sqrt{2}}\left\{\alpha_1\beta_2 - \beta_1\alpha_2\right\}$	0	1
triplet			
	$\alpha_1\alpha_2$	1	1
	$\frac{1}{\sqrt{2}}\left\{\alpha_1\beta_2 + \beta_1\alpha_2\right\}$	1	0
	$\beta_1\beta_2$	1	-1

where M_s is the eigenvalue of the z-component of the spin. The index 1 and 2 refer to particle 1 and 2.[64, 65] Excitons have the possibility to end up in either the singlet state or in one of three triplet states. For electrical excitation, taking a random distribution of spins into account, the singlet to triplet ratio is 1:3.

In contrast, optical excitation is a transition from the ground state S_0, which is a singlet state, to an excited state. This transition requires spin conservation, i.e. transitions to the triplet state are forbidden and excitons end up in a singlet state. "Forbidden" is used here in the typical quantum mechanical sense, meaning that the probability of this process is orders of magnitudes lower than of those which are not spin-forbidden. The ratio of optically excited singlets/triplets in organic materials is the range of $10^9 - 10^{10}$ to 1.[57]

By definition, the energy of the ground state S_0 is 0 eV. The radiative transition from a singlet state to the ground state is called **fluorescence** and from a triplet state to the ground state is called **phosphorescence**. The transition probability P from an initial state i into the final state f depends on the matrix dipole moment M and holds:

$$P_{i \to f} \propto \mid M \mid^2 . \tag{3.8}$$

The matrix dipole moment M can be calculated using perturbation theory and **Fermi's Golden Rule**. For details, the reader is referred to Ref. [66]. The energy E_γ of the emitted photon is than simply given by:

$$E_\gamma = h\nu = E_f - E_i. \tag{3.9}$$

Fluorescence

In order to explain the absorption and emission spectra of organic materials, vibronic states (indicated by the index ν) have to be taken into account. The energy difference between vibronic levels is about a factor of ten lower than between electronic states.

Figure 3.2 schematically illustrates the origin of the symmetric behavior between absorption and emission spectra of a molecule **(Frank-Condon diagram)**. Absorption is the transition of an electron from the ground state (S_0, $\nu = 0$) to a vibrational state of an energetically higher electronic state (S_1, $\nu = 0...$k). The transitions between vibrational states are very fast (typically 10^{-12} s). Hence, excitons relax first into the deepest vibronic state (S_n, $\nu = 0$) before they are radiatively back transferred to a vibronic level of the electronic ground state (S_0, $\nu = 0...$k). The typical lifetime of a singlet exciton in a fluorescent system is in the range of $10^{-9} - 10^{-6}$ s (triplets: $10^{-3} - 10^0$ s [67]). During this relaxation the electron dissipates a small amount of energy resulting in an emission at longer wavelength **(Stokes shift)**. The Stokes shift is usually in the range of 1 eV.[68]

The absorption coefficient α in an organic material is given by the **Lambert-Beer** law:

$$I = I_0 \, 10^{-\alpha l}, \tag{3.10}$$

where l is the layer thickness. The ratio between the incident light intensity I_0 and

transmitted light intensity I is given by the transmission $T = I/I_0$. Typical absorption coefficients for organic thin films and crystals are in the range of 10^5 cm^{-1}.[57]
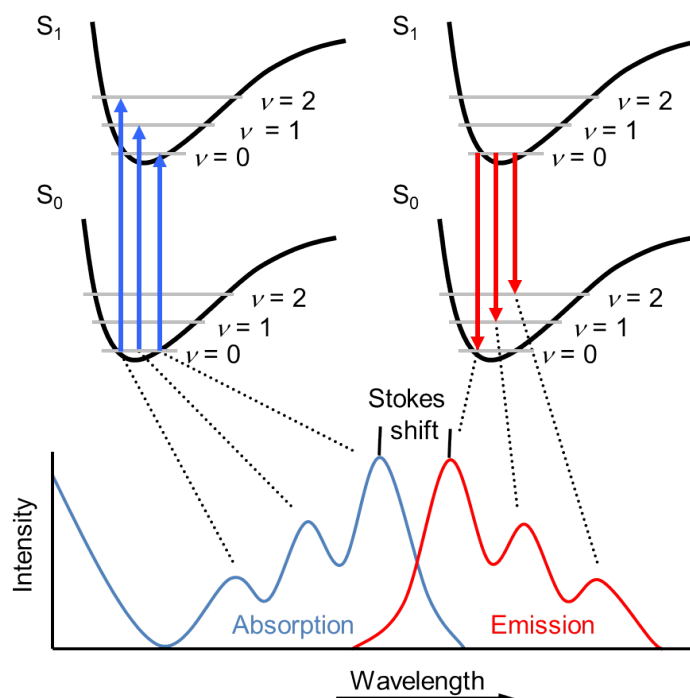

Figure 3.2: Frank-Condon diagram, absorption, and emission spectra of a fluorescent molecule. The transitions between electronic and vibronic states quantitatively describe the symmetric behavior of absorption and emission. The Stokes shift is a result of the energy loss during the stay in an excited state.[69]

Phosphorescence

Transitions between singlet and triplet state are usually spin-forbidden. However, incorporating heavy metals (e.g. platinum, europium, or iridium) into the molecule weakens the spin-orbit coupling and leads to an increased **intersystem crossing (ISC)** rate between the singlet and triplet state. In organo-transition metal triplet emitters, the ISC rate can be very high in the order of $10^{12} - 10^{13}$ s^{-1}. The molecule emits, therefore, efficiently from the triplet state (phosphorescence). The lifetime of the triplet state in phosphorescent materials is about 10^{-6} s. [70]

Figure 3.3 **(Jablonski diagram)** summarizes the most important radiative and nonradiative transitions within an excited molecule. Additionally to absorption, fluorescence, and phosphorescence, nonradiative internal conversion (energy transfer to phonons) can take place.
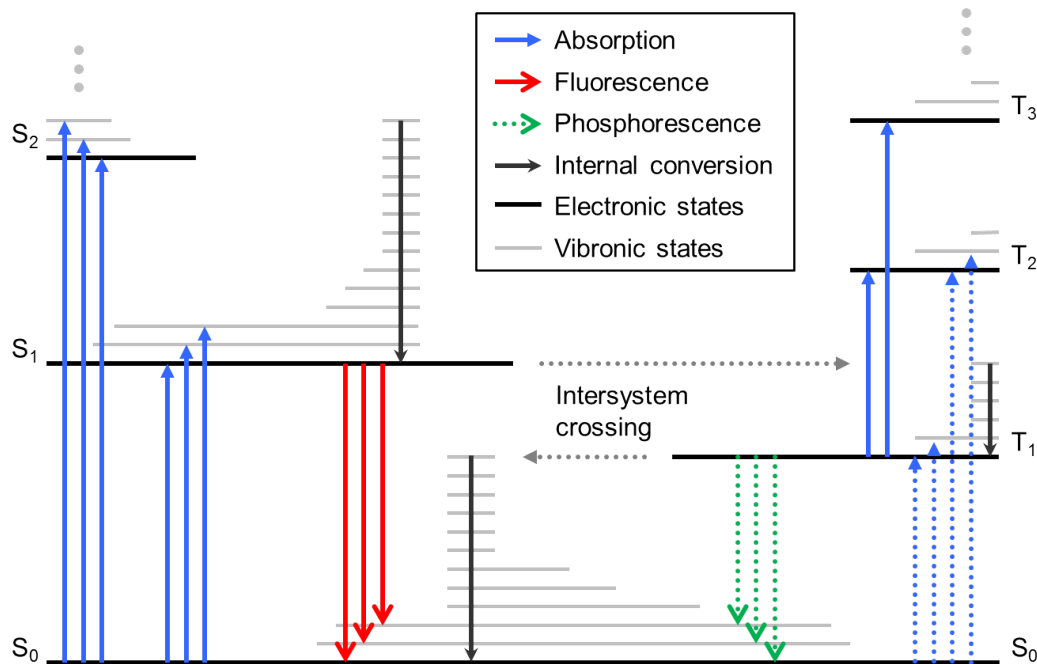
Figure 3.3: Jablonski diagram illustrating the most important radiative and nonradiative transitions in a molecule: absorption, fluorescence, phosphorescence, intersystem crossing, and internal conversion. Spin-forbidden transitions are marked by dotted arrows. However, using materials with a high intersystem crossing rate can lead to efficient phosphorescence from the triplet state.[69]

3.3   Singlet-Triplet Splitting

As stated in the previous section, the optical energy gap between the singlet level S_1 and ground state S_0 is not equal to the energy difference between HOMO and LUMO. It can be calculated using the Coulomb integral K:

$$K = \iint \psi_a^*(\vec{r}_1)\, \psi_b^*(\vec{r}_2)\, \frac{e^2}{4\pi\epsilon_0} \frac{1}{\vec{r}}\, \psi_a(\vec{r}_1)\, \psi_b(\vec{r}_2)\, \mathrm{d}^3\vec{r}_1\, \mathrm{d}^3\vec{r}_2, \tag{3.11}$$

and the electron exchange interaction integral C:

$$C = \iint \psi_a^*(\vec{r}_1)\, \psi_b^*(\vec{r}_2)\, \frac{e^2}{4\pi\epsilon_0} \frac{1}{\vec{r}}\, \psi_b(\vec{r}_1)\, \psi_a(\vec{r}_2)\, \mathrm{d}^3\vec{r}_1\, \mathrm{d}^3\vec{r}_2, \tag{3.12}$$

which is the first-order quantum mechanical correction of the electron-electron repulsion due to the Pauli principle. Both integrals are defined as positive mathematical quantities, i.e. are energy-raising. Here, $e = 1.602 \cdot 10^{-19}$ C denotes the electron charge, $\varepsilon_0 = 8.854 \cdot 10^{-12}$ As V^{-1} m^{-1} is the permittivity in free space, and $\mid r \mid$

the distance between electron a and electron b. The asterisk on the electronic wave function ψ marks an excited state.[71]

The resulting equations for the singlet and triplet energies are:

$$E_\text{S} = K + C \tag{3.13}$$

$$E_\text{T} = K - C. \tag{3.14}$$

Equations (3.13) and (3.14) clearly show that the singlet energy E_S is higher than the triplet energy E_T. The energy difference between both, the singlet-triplet splitting E_ST, is given by:

$$E_\text{ST} = E_\text{S} - E_\text{T} = 2\,C > 0. \tag{3.15}$$

The singlet-triplet splitting depends only on the exchange interaction integral C and scales, therefore, with the overlap of the electron wave functions, i.e. HOMO and LUMO of the molecule. Typical values for the singlet-triplet splitting E_ST of organic materials are in the range of hundreds of meV.[70]

3.4   Energy Transfer Mechanisms

Additionally to the energy transfer between different states of a molecule, energy transfer between molecules can take place in an organic semiconductor. In this section, a molecule providing energy is referred to as donor (D) and a molecule harvesting energy is referred to as acceptor (A). An excited molecule is marked with an asterisk, and the subscripts S and T denote a singlet and triplet state, respectively.

Reabsorption

The process where one molecule emits a photon (due to radiative transition of an electron from an excited state to the ground state) and another molecule subsequently absorbs this photon (resulting in a transition from the ground state to an excited state) is called reabsorption. This photon exchange can be written as a two step process:

$$\begin{aligned} D^* &\rightarrow D + h\nu \\ A + h\nu &\rightarrow A^*, \end{aligned} \tag{3.16}$$

where $h\nu$ is the photon energy. The interaction radius of the reabsorption process is in the range of more than 10 nm. However, due to the Stokes shift in organic semiconductors, this process is mostly negligible.[69]

Förster transfer

The energy transfer from a donor to an acceptor via nonradiative dipole-dipole coupling is known as (long-range) Förster transfer.[72] The transfer energy $E_{\text{Förster}}$ is given by:

$$E_{\text{Förster}} = \frac{1}{1 + \left(\frac{r}{R_0}\right)^6},$$

(3.17)

where r is the distance between donor and acceptor and R_0 is the Förster radius (determined by the distance when the energy transfer efficiency is reduced to 50%):

$$R_0^6 = \frac{9000 \, c^4 \ln 10 \, \kappa^2 \, Q}{128 \, \pi^5 \, n^4 \, N_{\text{A}}} \, J.$$

(3.18)

Here, c is the speed of light in vacuum, κ is the dipole orientation factor (which is often assumed to be 2/3 for isotropic orientation), Q denotes the quantum yield of the donor in absence of the acceptor, n is the refractive index, and $N_{\text{A}} = 6.022 \cdot 10^{23} \, \text{mol}^{-1}$ the Avogadro constant. Furthermore, the Förster radius depends on the overlap between normalized donor emission spectrum $f_{\text{D}}(\tilde{\nu})$ and the acceptor molar extinction coefficient $\varepsilon_{\text{A}}(\tilde{\nu})$, (i.e. the absorption spectrum) with $\nu = \lambda^{-1}$ as wave number. The overlap integral J is given by:

$$J = \int f_{\text{D}}(\tilde{\nu}) \, \varepsilon_{\text{A}}(\tilde{\nu}) \, \frac{1}{\tilde{\nu}^4} \, \mathrm{d}\tilde{\nu} \text{ with } 1 = \int f_{\text{D}}(\tilde{\nu}) \, \mathrm{d}\tilde{\nu}.$$

(3.19)

The Förster transfer can overcome distances of more than 10 nm and plays an important role for matrix-emitter systems.[67]

As a consequence of the pure dipole-dipole interaction, the total spin of each molecule has to be conserved during the energy transfer. This means that a triplet transfer from donor to acceptor is strictly forbidden in Förster theory. The allowed transfers are:

$$D_{\text{S}}^* + A_{\text{S}} \rightarrow D_{\text{S}} + A_{\text{S}}^*$$
$$D_{\text{S}}^* + A_{\text{T}} \rightarrow D_{\text{S}} + A_{\text{T}}^*$$

(3.20)

Dexter transfer

The process based on electron exchange between two neighboring molecules is named (short-range) Dexter transfer and requires an overlap of the molecular orbitals. Thus, the transfer distance is typically shorter than 1 nm.[67, 73]

Here, the total spin of both molecules needs to be conserved, resulting in the allowed Dexter mechanisms:

$$D_{\text{S}}^* + A_{\text{S}} \rightarrow D_{\text{S}} + A_{\text{S}}^*$$
$$D_{\text{T}}^* + A_{\text{S}} \rightarrow D_{\text{S}} + A_{\text{T}}^*$$

(3.21)

Figure 3.4 illustrates Förster and Dexter type transfers schematically. Förster transfer

requires that the electrons remain confined to the same molecule, in contrast to Dexter transfer, where electrons between the two molecules are exchanged. While for triplet-triplet transfer only Dexter transfer is possible, singlet-singlet energy transfer can occur via both, Förster and Dexter energy transfers. For low concentrations of the acceptor in matrix-emitter systems, Förster energy transfer is dominant since it is faster at longer distances.
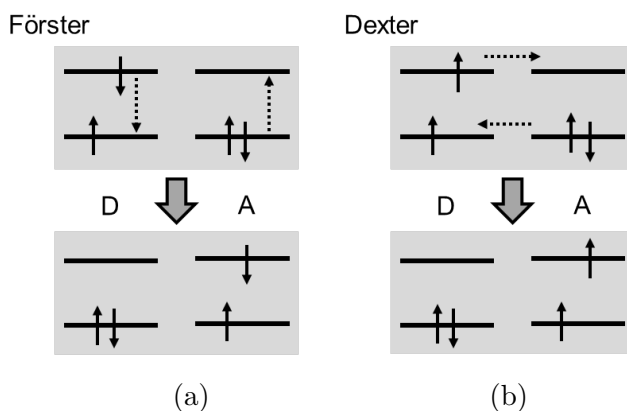
Figure 3.4: Schematic diagram of Förster (a) and Dexter (b) energy transfer between donor and acceptor molecules. The electron transition is indicated by dotted arrows. For Förster transfer the electrons remain at the same molecule, while for Dexter transfer electrons of two molecules are exchanged.

3.5   Exciton Diffusion and Quenching

Exciton diffusion

Exciton diffusion processes can be considered as a series of uncorrelated Förster and Dexter type transfers between molecules as discussed in the previous section. The exciton concentration gradient provides the driving force for exciton migration within the organic semiconductor.

Neglecting quenching processes, the time dependent, one dimensional diffusion equation for the exciton density $n(x,t)$ is given by **Fick's second law**:

$$\frac{\mathrm{d}n\,(x,t)}{\mathrm{d}t} = G\,(x,t) + D\frac{\partial^2 n(x,t)}{\partial x^2} - \frac{n}{\tau}. \qquad (3.22)$$

The first term $G\,(x,t)$ describes the generation of excitons. The second term stands for diffusion with D as diffusion constant. Finally, the third term covers the monomolecular decay where τ is the excited state lifetime. In many cases, the exciton generation zone is assumed to be a delta-shaped profile $G(x,t) = G_0 \cdot \delta(x = 0,t)$.[74–76] Under this condition, the steady-state solution $\mathrm{d}n/\mathrm{d}t = 0$ to Eq. (3.22) reads:

$$n(x) = n_0 \cdot e^{-x/L}, \qquad (3.23)$$

where n_0 is the exciton density at the generation interface and L is the exciton diffusion length according to:

$$L = \sqrt{D\tau}. \tag{3.24}$$

A wide range of values is reported for the diffusion length in organic semiconductors, mostly strongly dependent on the material and the excitation method (optically or electrically). For singlet excitons, the diffusion length ranges from a few nm to several tens of nm. For triplets, which are assumed to have a longer diffusion length due to their longer lifetime, even values in the µm regime have been reported.[77, 78] Precise knowledge of the exciton diffusion length is important, especially for the design of white triplet-harvesting OLEDs where the triplet diffusion is appreciated and singlet diffusion needs to be avoided.[17–19]

Quenching

The annihilation of an exciton due to the interaction with other excitons, charge carriers, surfaces, impurities, or defects is called quenching. Quenching caused by impurities and defects is of minor importance, since nowadays organic materials can be sufficiently purified, for example by vacuum sublimation.[79]

The quenching by electrical charges is called exciton-polaron quenching and is important in OLEDs where charges are injected via the contacts (**singlet-polaron annihilation (SPA), triplet-polaron annihilation (TPA)**). Typical current densities in OLEDs are in the range of 10^{-1} to 10^2 mA/cm² corresponding to polaron densities of about 10^{10} to 10^{13} cm^{-3}. At high current densities the polaron density can exceed 10^{17} cm^{-3}.[80]

Two singlet excitons can annihilate according to:

$$S_1 + S_1 \rightarrow S_0 + S_1, \tag{3.25}$$

meaning that two excited singlets end up in one excited singlet and one singlet in the ground state (**singlet-singlet annihilation, SSA**). However, due to the small lifetime of singlets the quenching by triplet excitons (**singlet-triplet annihilation, STA**) is more likely:

$$S_1 + T_1 \rightarrow S_0 + T_1. \tag{3.26}$$

The interaction of two triplet excitons can lead to the following important mechanisms, known as **triplet-triplet annihilation (TTA)** :

$$\begin{aligned} T_1 + T_1 &\rightarrow S_0 + T_1 \\ T_1 + T_1 &\rightarrow S_0 + S_1 \end{aligned}. \tag{3.27}$$
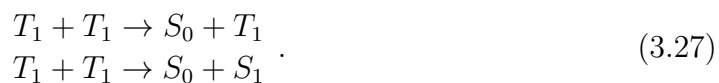
In the first case two excited triplets form an excited triplet state and a singlet in the ground state and in the second case the triplets form a singlet in the ground state and an excited singlet state which is able to decay radiatively (delayed fluorescence). According to quantum statistics, the first process is more likely than the second. The triplet density in the emissive layer of an OLED device under electrical excitation is in the range of 10^{16} to $10^{20}\,\mathrm{cm}^{-3}$. From photoluminescence, it can be deduced that the concentration where TTA sets in is about $10^{18}\,\mathrm{cm}^{-3}$. The number of TTA events scales quadratically with the triplet density.[81, 82]

A combination of several annihilation processes can be observed in OLEDs when driven at high current densities. The result is a decrease in efficiency, known as **roll-off**.[70] This is, of course, an undesired effect, hence the reduction of the roll-off has been a mayor focus of OLED research over the last years. [81, 83–86]

3.6   Charge Carrier Transport

In the previous section, the physics of electrically neutral excitons were discussed. Molecules can, of course, also be charged. An additional electron in the LUMO provides a negative charge, while a HOMO occupied by only one electron provides a positive charge, a hole. When applying an electric field $\vec{F}$, the charge carriers can move. In a first approximation (according to the **Drude model** of inorganic semiconductors) the drift velocity $\vec{v}$ is given by:

$$\vec{v} = \hat{\mu}\vec{F}, \tag{3.28}$$

where $\hat{\mu}$ is the (field-independent) mobility tensor. In amorphous organic layers the mobility can be assumed to be isotropic and thus a scalar quantity.

Usually, organic devices can be regarded to have infinite extension in two directions, which reduces the transport to a one-dimensional problem. The most common experiments used to determine the mobilities for electrons and holes are the time-of-flight method [87], field-effect mobility measurements [88, 89], and the analysis of space-charge limited currents (SCLC)[69, 90]. It is worth noting that the mobility is not an intrinsic material property, but does strongly depend on the sample preparation conditions, the morphology of the substrate, the material purity, and the used experimental method.[91]

Hopping transport

In amorphous organic semiconductors, the electrons and holes are strongly localized and a coupling of π-orbitals is not present. Hence, a band transport like in inorganic semiconductors is not possible. The current flow is instead determined by a series of hopping events of charge carriers between neighboring molecules. The **Gaussian disorder model**, introduced by Bässler describes the hopping transport between

Gaussian distributed density of states.[92] The mobilities reached by hopping transport (10^{-6} to 10^{-2} cm²/Vs [69]) are much lower than for inorganic semiconductors.

If an ohmic contact is given, the layer will then charge at the interface and further hinder the transport. This effect is known as space-charge limited current.[93] The one-dimensional unipolar transport for ohmic injection is described by the **Mott-Gurney law**:

$$j_{\mathrm{MG}} = \frac{9}{8}\varepsilon_0\varepsilon\mu\frac{U}{L^3}, \tag{3.29}$$

where j is the current density, $\varepsilon_0 = 8.854 \cdot 10^{-12}$ As/Vm the permittivity constant, ε the permittivity of the material, U the applied voltage, and L the length/thickness of the layer. The assumption of $\varepsilon = 3$ holds for most organic compounds.[57] The Mott-Gurney law does not consider trap states or the dependence of the mobility on the temperature and the electric field. Additional trap states, mainly caused by impurities, can be described within the trap filled limited current (TFLC) theory.[56, 94] Here, the traps are filled gradually with increasing voltage until the trap filled limit is reached. For an exponential or Gaussian distribution of trap states above this limit, the relationship between current density and voltage is $j \sim U^{l+1}$, while $l = E_{\mathrm{t}}/k_{\mathrm{B}}T$ with E_T the energy depth of the trap states and T the temperature.

At high current densities, the dependence of the mobility on the electric field cannot be neglected anymore.[95] This can be described by the Poole-Frenkel type mobility $\mu(F,T)$:

$$\mu\left(F,T\right) = \mu\left(0,T\right)\,e^{\gamma(T)\sqrt{F}}, \tag{3.30}$$

where $\mu\left(0,T\right)$ is the zero-field mobility and $\gamma\left(T\right)$ the so-called field enhancement factor. The field enhancement factor describes the lowering of the barrier for hopping in the direction of the field. The SCL current density can be approximated to [96]:

$$j_{\mathrm{PF}} = \frac{9}{8}\varepsilon\varepsilon_0\mu\left(0,T\right)\,e^{\gamma(T)\sqrt{\frac{U}{L}}}\frac{U^2}{L^3}. \tag{3.31}$$

Using Eq. (3.31), the zero-field mobility can be evaluated straightforward from the IV-curve, if unipolar transport and ohmic injection are given.

4   Organic Light-Emitting Diodes

Since OLEDs are the focus of this work, their operation principle will be described in detail. Beginning with electroluminescence in a two-layer OLED, the development of a multi-layer pin-OLEDs and the role of phosphorescent emitters are explained. The principle and verification of the triplet harvesting process are described. Furthermore, it will be shown that light outcoupling is an important issue to increase device efficiency. Finally, a brief summary of state-of-the-art white OLEDs is given.

4.1   Electroluminescence

Depending on the used organic material, OLEDs are distinguished into polymer and small-molecule OLEDs. Furthermore, OLEDs are divided into top-emitting (emission away from the substrate) and bottom-emitting (emission through the substrate). In the following, the main focus will be on bottom-emitting small-molecule OLEDs.

Electroluminescence of organic materials has been first published by Pope *et al.*[97], and later by Helfrich and Schneider[98] in the 1960s. They observed luminescence when applying a high voltage (50 to 2,000 V) to anthracene crystals. However, the first so-called "OLED" was demonstrated by Tang and VanSlyke in 1987.[2] They embedded two small-molecule organic materials between a transparent anode and a highly reflective cathode by vapor deposition and observed luminescence already at a driving voltage of less than 5 V. The anode material is indium-doped tin oxide (ITO) which is transparent and conductive at the same time. ITO is still the most common anode material for OLEDs, while the cathode is usually a metal.
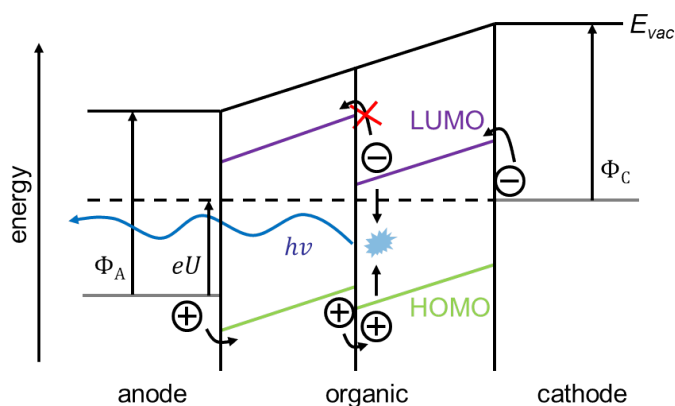
Figure 4.1: General working principle of a two-layer OLED introduced by Tang and VanSlyke.[2, 11] Holes and electrons are injected via the anode and cathode, respectively. At the organic-organic interface charge carriers form excitons which can emit light. The recombination is only taking place in one material. The light is further outcoupled through the semitransparent anode.

The basic working principle of a two-layer OLED is shown in Fig. 4.1. When applying a voltage U to the electrodes, electrons and holes are injected into the two different materials with appropriate transport properties. Additionally to their optical properties, the electrode materials need to be chosen according to their work functions Φ_A and Φ_C to provide sufficient charge injection into the HOMO and LUMO of the organic materials, respectively. The charge carriers accumulate at the interface of the organic layers, where the exciton generation is taking place. The excitons can radiatively decay and generate photons. The transparent anode allows outcoupling of these photons.

The efficiencies reached with this first green OLED were quite low (EQE $< 1\%$, LE ~1.5 lm/W). This is due to the following reasons: (i) the efficient injection and transport of charge carriers is hindered by the SCLC, (ii) the used emitter system is a fluorescent emitter, i.e. all electrically excited triplets are a lost, and (iii) the light outcoupling is not optimized for this thin film structure, i.e. light is trapped inside the OLED. How each of these factors can be mitigated and will be addressed in the following sections.

4.2   The pin Concept

Doping

In analogy to inorganic semiconductors, doping can increase the density of free charge carriers and thus the conductivity in organic materials by several orders of magnitude. Doping of organic materials was first shown by Shirakawa *et al.*[99, 100] for polymers in 1977, and later by Maitrot *et al.*[101] by the use of co-evaporation of small-molecules in 1986. The principle of electrical p- and n-type doping for a matrix:dopant system is shown in Fig. 4.2.
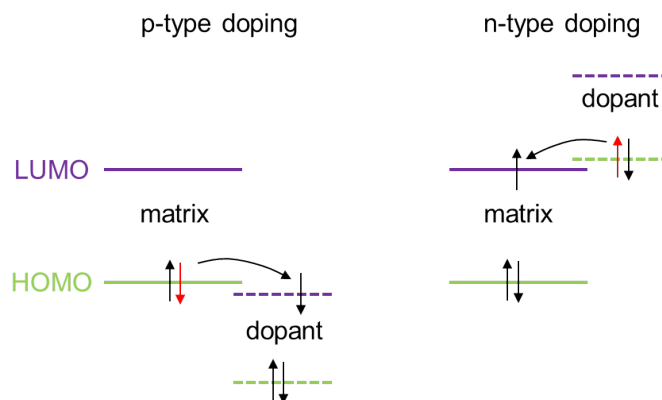
Figure 4.2: Principle of p- and n-type doping of organic materials.[9, 102] The charge transfer between matrix and dopant leads to a strong increase in charge carrier density and thus conductivity of the layer.

For p-type doping, the HOMO of the matrix donates an electron to the unoccupied LUMO of the dopant. This leads to a higher hole density and thus higher conductivity of the layer. This process works similar for n-type doping. Here, the matrix acts as acceptor. By transfer of an electron from the HOMO of the dopant to the LUMO of the matrix, the electron density increases. In OLEDs, the high charge carrier density reduces the voltage drop over the organic layer significantly. Therefore, their thickness can be increased to several hundreds of nanometers without any significant drop in voltage. Hence, the doped layers can be used as charge transport layers to adjust the position of the emission zone inside the OLED cavity to the location that is most favorable from an optical perspective. However, for thick layers it has to be considered that most dopants have a small band gap and thus absorb light from the emitting molecules.

It is far more difficult to find suitable n-dopants rather than p-dopants: The n-dopants need to have a higher HOMO energy than the LUMO energy of the matrix. This requires at the same time that the LUMO energy of the dopant is close to the vacuum energy. Usually these molecules are very sensitive to oxidation, which is the reason why alkali metals are often used for n-type doping instead of organic molecules.[103] The doping concentration c in weight percent [wt%] is given by:

$$c = \frac{m_D}{m_D + m_M} \cdot 100,$$ (4.1)

with m_D and m_M as mass of the dopant and matrix, respectively.

Another important advantage of electrically doped layers becomes relevant, when regarding the charge injection from a metal contact. As indicated in Fig. 4.3, doping leads to an energy level bending towards the Fermi energy E_F and thus a formation of a depletion zone, typically within the first 5 nm of the organic material.[7] This increases the tunneling probability of charge carriers into the organic layer. The tunneling of charge carriers results in an ohmic injection and thus reduces the voltage drop at the metal-organic interface.
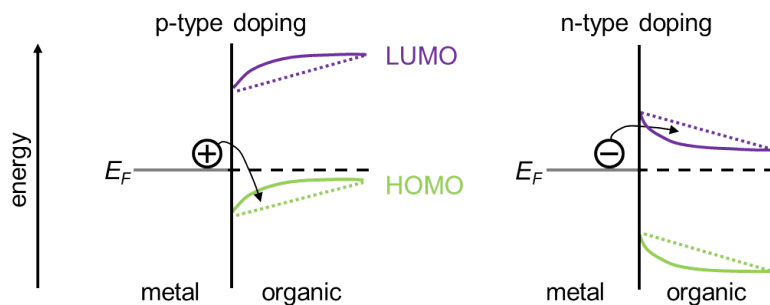

Figure 4.3:   Effect of p- and n-doping at a metal interface.[9, 102] Doping leads to band bending towards the Fermi energy. The formation of a depletion zone increases the tunneling probability of charge carriers into the organic layer.

The pin-OLED

The doping of transport layers in OLEDs has been intensively investigated since the late 1990s and is still an important research aspect.[7, 8, 103–106] In 1998, Bharathan and Yang[107] demonstrated a reduced driving voltage for a polymer OLED with p-doped hole and n-doped electron transport layer. However, here the excitons had been quenched at the dopants, which resulted in a low light intensity.

The intrinsic layer, sandwiched between the p- and n-doped transport layer leads to the name pin-OLED. Exciton blocking layers can help to overcome the quenching of excitons and can additionally be used to confine charge carriers. A five layer small molecule pin-OLED with undoped blocking layers at both sides of the emission layer has been first shown by Huang *et al.*[10] in 2002. The green fluorescent pin-OLED reached a luminance of 1,000 cd/m² at a driving voltage of 2.9 V.

In Fig. 4.4 the working principle of such a multilayer pin-OLED is shown. The different organic layers are named according to their function: the electron transport layer (ETL), the hole blocking layer (HBL), the emission layer (EML), the electron blocking layer (EBL), and the hole transport layer (HTL).
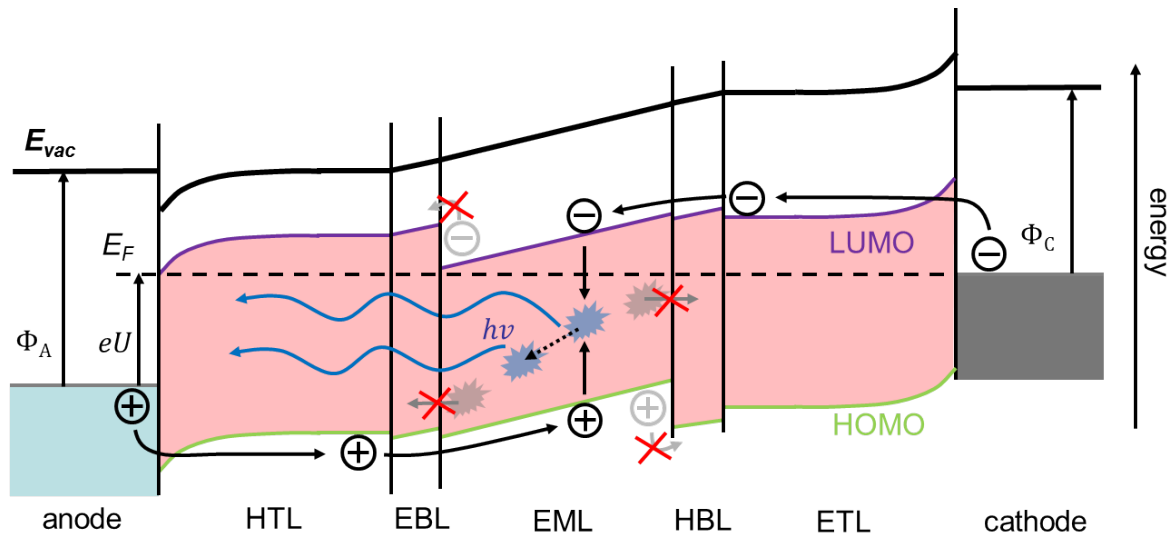
Figure 4.4: Working principle of a pin-OLED. Charge carriers are injected via the contacts into the respective doped transport layers. The charges pass the blocking layers and generate excitons inside the EML. These excitons can underlie diffusion processes before they generate photons. The photons can then be outcoupled through the semitransparent anode. In addition to the charge carrier confinement, the EBL and HBL also hinder the excitons from diffusing into the ETL or HTL.

The mechanisms are the following: (i) electrons and holes are efficiently injected into the respective transport layers, (ii) the electrons/holes are transported through the ETL/HTL and HBL/EBL to the EML, (iii) the blocking layers prevent the charge carriers from traveling through the whole device, (iv) holes and electrons form excitons

in the EML, (v) the excitons can diffuse and generate photons, (vi) the blocking layers ensure that the excitons are maintained within the EML and are thus not quenched at the dopants, and finally, (vii) the photons can be outcoupled.

4.3   Phosphorescent Emitters

In the previous section, it has been explained how the efficiency of an OLED can be enhanced by incorporating blocking and doped transport layers. However, due to the use of fluorescent emitters, the reported EQEs had been rather low ($< 5\%$).[108, 109] The reason is that the electrical excitation leads to a singlet:triplet ratio of 1:3 (cf. Sec. 3.2). Since on a fluorescent emitter, only the singlet excitons recombine radiatively, about 75% of the injected charge carriers are lost (Fig. 4.5).

This problem can be overcome by using phosphorescent emitters, which efficiently emit from the triplet state. In 1998, Baldo *et al.*[110, 111] showed that the incorporation of the heavy metal platinum into an organic compound leads to efficient phosphorescence (yield ~50%). The spin-orbit coupling strongly increases due to the high atomic number of the metal. Furthermore, the ISC rate is increased and leads to an efficient transfer of singlets to the triplet state (Fig. 4.5). This makes it possible to reach phosphorescence yields closed to unity, like reported by Adachi *et al.*[12] using iridium as heavy metal.
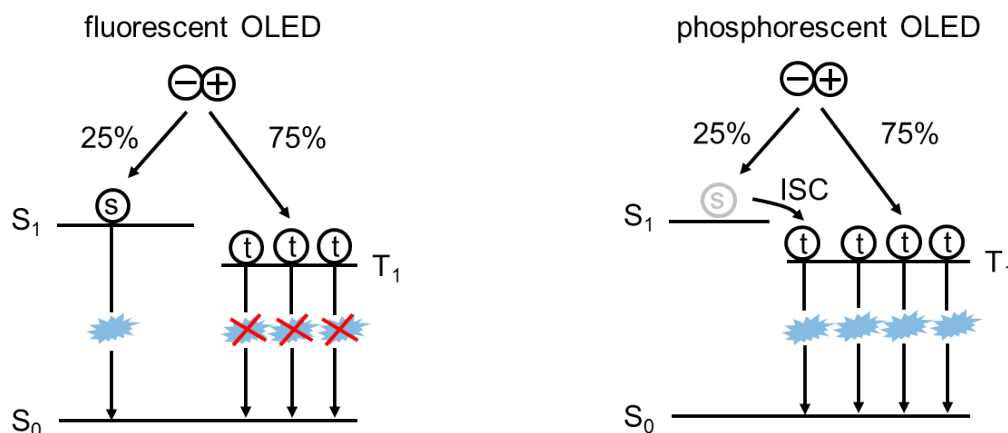
Figure 4.5: Distribution and emission from singlet and triplet state in OLEDs comprising either a fluorescent or a phosphorescent emitter. While in the first case only 25% of the injected charge carriers contribute to the emission, a phosphorescent OLED benefits from the high ISC rate and the efficient emission from the triplet state.

In the following years, the reported EQE values for phosphorescent pin-OLEDs could reach up to 20%.[15, 112] This is consistent with the picture that now both exciton species, singlets and triplets, contribute to the emission, thus leading to a four fold increase in efficiency from the original 5%. However, new problems arise when

using phosphorescent emitters in OLEDs: (i) phosphorescent emitters need to be doped into a suitable matrix material, mostly to avoid concentration quenching, and (ii) due to the long lifetime, the triplet density inside the EML can become very high in comparison to the singlet density in fluorescent OLEDs. Therefore, annihilation processes are more relevant and a stronger roll-off is observed in phosphorescent OLEDs.[46]

In particular, blue phosphorescent emitters have two additional drawbacks: While for red and green phosphorescent emitters, long OLED lifetimes have been reported ($> 100,000$ h at $1,000$ cd/m² [113, 114]), the lifetime of OLEDs with blue phosphorescent emitters is usually very low (< 2 h [14]). Secondly, most phosphorescent blue emitters have a sky-blue emission color and only little emission at the short wavelength end of the visible spectrum which complicates the achievement of high CRIs in white OLEDs.[14] The accomplishment of highly efficient long-living phosphorescent blue OLEDs is challenging since they require a matrix material with a large energy band gap, which usually go side by side with insufficient carrier injection, imperfect exciton confinement, and chemical instability.[15]

Therefore, in the next section, a harvesting concept for triplet excitons will be introduced, which on the one hand allows to benefit from the good properties of blue fluorescent emitters and on the other hand ensures high internal quantum yields.

4.4 Triplet Harvesting

Since this work is focused on triplet harvesting (TH) OLEDs, the basic working principle and different possibility to investigate the TH processes will be explained in detail in the following.

Principle

The term triplet harvesting relates primarily to the fact that triplet excitons are usually lost in a fluorescent emitter system. As shown in Fig. 4.6, the basic idea of this concept is the transfer of these triplets to a phosphorescent emitter, where they can decay radiatively. At the same time, the singlet transfer needs to be hindered. Considering the longer lifetime of triplets, and hence the longer diffusion length, this can be achieved by a spatial separation of the emitters. Of course, for an efficient transfer, the triplet energy level of the phosphorescent emitter needs to be lower than that of the fluorescent emitter.

In the ideal case, all singlet excitons from the fluorescent emitter and all harvested triplet excitons will generate photons. This means that if ideally all triplets are harvested, the internal quantum yield in TH OLEDs can be close to unity.
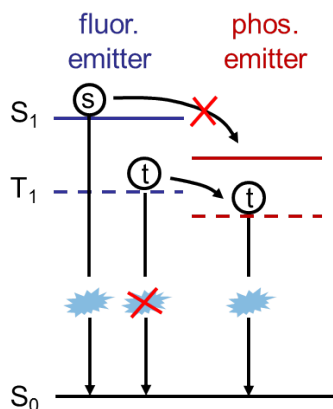
Figure 4.6: Principle of TH. The triplets of the fluorescent emitter can be trans-
ferred to the deeper lying triplet level of a phosphorescent emitter and are therefore
"harvested". At the same time singlet transfer needs to be hindered. This can be
achieved by a spatial separation of the emitters.

In 2006, Sun *et al.*[17] and Schwartz *et al.*[16] first realized TH in OLEDs. Sun
and coworkers used the ambipolar large band gap host material CBP[1] (Fig. 4.7 (a))
as matrix material in the EML (Fig. 4.7 (a)). The blue fluorescent emitter BCzVBi[2]
is doped at a concentration of 5 wt% into two parts of host material next to the
outside of the EML. The singlets generated at CBP are transferred by Förster transfer
to BCzVBi. Due to the low concentration, triplets cannot be efficiently transferred
to this emitter. However, these triplets have a long lifetime and can diffuse to the
green phosphorescent emitter $Ir(ppy)_3$ (cf. Sec. 5.1), which is doped into the middle
of the EML. The singlet transfer to the phosphorescent emitter is hindered by a thin
intrinsic layer of the host material between the two doped regions.

In 2010, Kondakova *et al.*[21] reported TH by doping the deep-blue emitter
MQAB[3] ($T_1 = 2.55$ eV) into the host CBP ($T_1 = 2.61$ eV) at only one side of the
EML (Fig. 4.7 (b)). Similarly, they observed TH by the green phosphorescent emitter
$Ir(ppy)_3$ ($T_1 = 2.49$ eV) using the matrix $Ga(pyimd)_3$[4]($T_1 = 2.71$ eV).

Schwartz *et al.*[18] introduced a slightly different approach. Here, excitons are
generated directly on the fluorescent bulk emitter 4P-NPD ($T_1 = 2.31$ eV) (cf. Sec. 5.1)
(Fig. 4.7 (c)). A direct generation on the blue emitter is beneficial for OLEDs, since
losses occurring from the matrix-emitter transfer, like in the previous case, are avoided.

Furthermore 4P-NPD has a much higher hole mobility than electron mobility
($\mu_h = 6.6 \cdot 10^{-4}$ cm^2/Vs, $\mu_e = 3.6 \cdot 10^{-8}$ cm^2/Vs) which leads to a narrow exciton
generation zone close to the HBL. The red phosphorescent emitter $Ir(MDQ)_2(acac)$
($T_1 = 2.02$ eV) (cf. Sec. 5.1) is doped into the hole-transporting host material NPB

---

[1]4,4'-bis(N-carbazolyl)biphenyl
[2]4,4'-bis(9-ethyl-3-carbazovenylene)-1,1'-biphenyl
[3]difluoro[6-mesityl-N-(2-(1H)-quinolinylidene-κN)-(6-mesityl-2-quinolinaminato-κN1)]boron
[4]tris[2-(2-pyridyl)imidazole]gallium(III)

(cf. Sec. 5.1) at the opposite side of the EML. Like in the structures discussed before, the triplets can diffuse towards the phosphorescent emitter and get harvested. Since the singlet diffusion length is shorter than the diffusion length of triplets, singlets will not reach the phosphorescent emitter. In this manner, the singlet transfer is hindered.

Using a blue fluorescent bulk emitter, two further configurations can be realized to obtain TH. First, the phosphorescent emitter can be doped into the whole EML (Fig. 4.7 (d)).[115, 116] However, very low concentrations (~ 0.2 wt%) are necessary to ensure that singlet transfer is not taking place at any significant rate. The second configuration is similar to Fig. 4.7 (c). Here, the host material is replaced by the blue emitter (Fig. 4.7 (e)).[19]
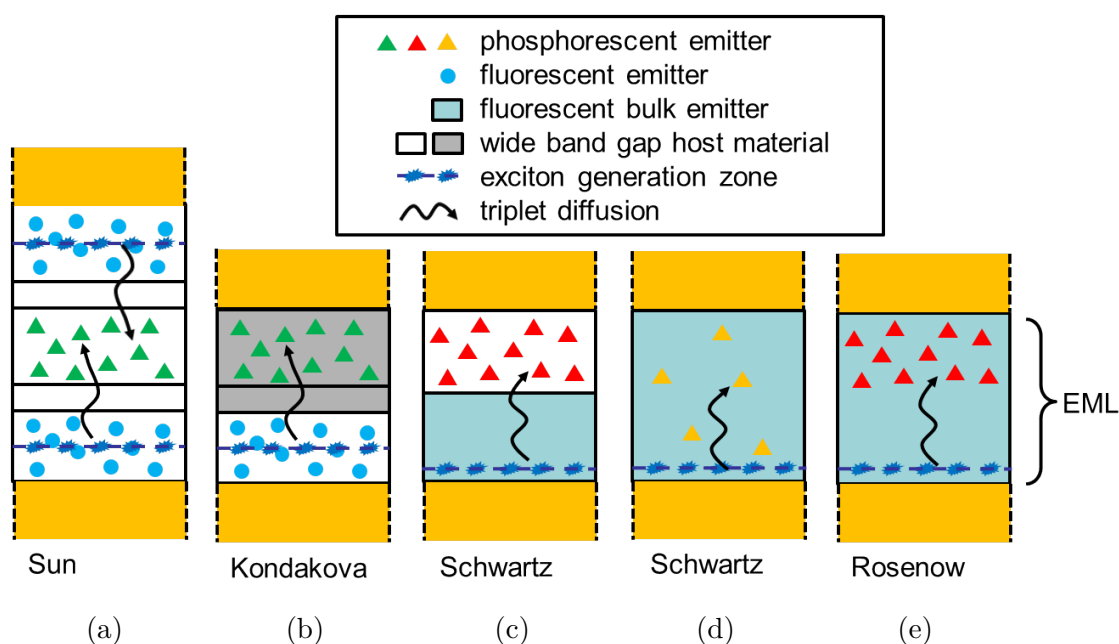
Figure 4.7: Realization of TH in OLEDs using a fluorescent emitter in a matrix material (a,b) or a blue fluorescent bulk emitter (c-e). In the latter case, the phosphorescent emitter can be doped into a different matrix (c), at low concentration into the complete EML (d), or only into a part of the fluorescent emitter (e). The exciton generation zone and the diffusion of triplets are indicated.

Verification of TH

TH can be investigated by the comparison of the spectral emission as well as the EQE of a TH OLED and a reference device without the phosphorescent emitter. In Fig. 4.8 (a) the spectral emission of these OLEDs is shown at constant current density as published by Sun and coworkers.[17] A constant current density ensures the same injection rate of holes and electrons into the OLED and it can be assumed that therefore the exciton generation rate is the same in both devices. The blue emission spectra remains constant, while for the TH device additional green emission is observed. This means that no singlet transfer to the green phosphor is present,

because this would lower the blue emission. Therefore, the generation of triplets is realized either by direct recombination of holes and electrons on the phosphorescent emitter or by TH after diffusion. A direct recombination would reduce the number of holes and electrons available for the recombination on the blue emitter, and thus lower the blue emission in comparison to the reference devices. Since this is not observed, it is concluded that the additional green emission occurs from TH.

When applying TH, the EQE of the considered OLEDs increases from 1.4 to 2.6%. This is a rather small improvement (factor of 1.9), regarding the fact that three times more excitons should be contributing to the emission. The reason is that due to the trapping of triplets on the blue fluorescent emitter, not all triplets reach the phosphorescent emitter, which, of course, reduces the EQE.[117]
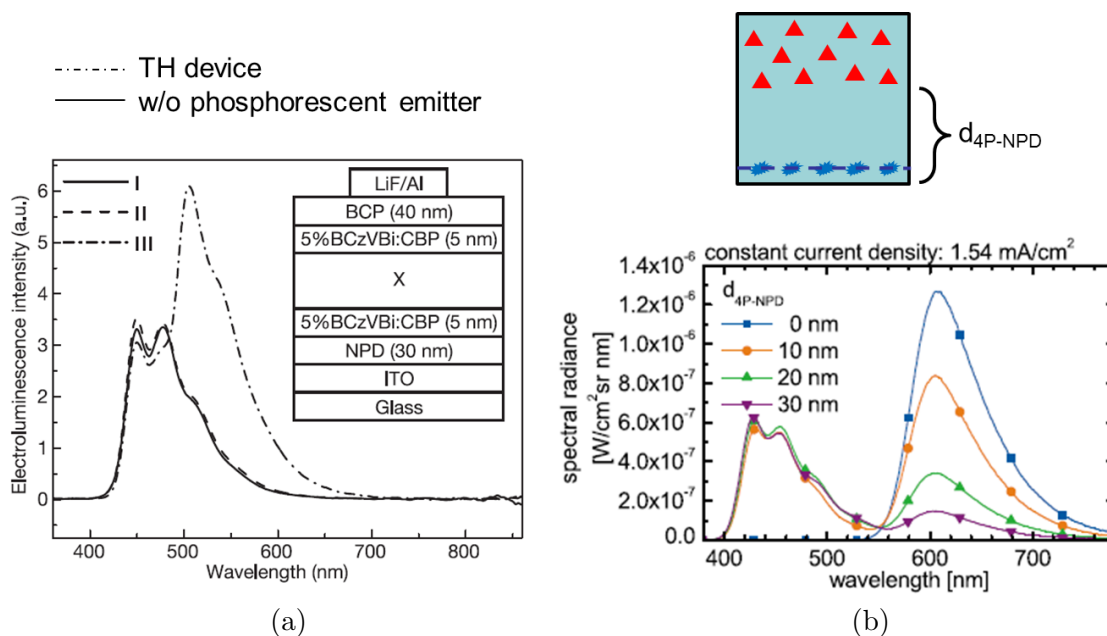
Figure 4.8: Proof of TH using a reference device without the phosphorescent emitter (a) by Sun *et al.*[17] and using a distance variation between exciton generation and TH zone (b) by Rosenow *et al.*[19]. In the TH OLED additional emission of the phosphorescent emitter can be observed, which strongly indicates diffusion based TH as discussed in the text. The reduction of the emission from the phosphorescent emitter with increasing layer thickness in (b) is in agreement with the assumption of a decreasing number of diffusing triplets. In both cases the blue emission remains constant, which proves that the singlet transfer is efficiently hindered. Reprinted by permission from Macmillan Publishers Ltd: Nature [17], copyright 2006, and reprinted with permission from [19]. Copyright 2010, American Institute of Physics.

Another possibility to investigate triplet harvesting in OLEDs is the variation of the distance between the exciton generation and the TH zone. For example, Rosenow *et al.*[19] studied this effect using the highly hole transporting blue emitter 4P-NPD, which ensures the generation zone to be close to the HBL. The phosphorescent red

emitter Ir(MDQ)$_2$(acac) is doped into 4P-NPD only at the EBL side (cf. Fig 4.7 (e)). A thickness variation of the intrinsic 4P-NPD layer is performed (Fig. 4.8 (b)), which changes the distance between exciton generation and TH zone. With increasing thickness of intrinsic 4P-NPD, the spectral emission at a constant current density remains the same for the blue part and decreases steadily for the red part. This is in good agreement with the fact that the diffusion mechanisms of triplets determine the number of harvested triplets. At larger distances, fewer triplets can reach the phosphorescent emitter and thus the red emission decreases. This statement is furthermore supported by the EQE which decreases from 11.0% at a thickness of 10 nm to 4.9% at 30 nm (at 1,000 cd/m²).

The TH principle can be therefore used to investigate the triplet diffusion length in operating OLEDs as demonstrated by Wünsche *et al.*[118], who examined the same emitter system. Interestingly, they found that additionally to the triplet harvesting process, a non-negligible amount of direct recombination events of holes and electrons is taking place on the red emitter. It is noteworthy that the direct recombination does not necessarily lower the internal quantum yield, but reduces the number of available holes and electrons for the recombination on the blue emitter.

The variation of the distance between exciton generation and the TH zone can be also achieved by decreasing the doping concentration of the phosphorescent emitter.[115, 116] In this case the whole EML layer can be doped. However, the required low doping concentrations (< 0.2 wt%) are experimentally challenging.

In addition, qualitative evidence of TH in OLEDs can be found by regarding the time resolved electroluminescence and the emission when applying an electromagnetic field. Kondakova *et al.*[21] investigated both methods using MQAB (doped into the matrix CBP) and Ir(ppy)$_2$pc[5] (in Ga(pyimd)$_3$) as blue and yellow emitter, respectively (cf. Fig. 4.7 (d)). In Fig. 4.9 (a) the emission of the TH OLED is shown as function of time. For this experiment, the OLED is excited by 2 µs long voltage pulses (+5.4 V on state, -10 V off state), and the yellow and blue emission are separated using appropriate filters. While the blue emission rises and decays rapidly, the yellow emission increases and decays slowly. The delay between both emission peaks is about 1 µs, and is independent of the on state and off state driving voltage.

These results indicate that triplets diffuse from a recombination zone to the phosphorescent emitter, which causes a delayed emission. This delay depends on the distance between blue and yellow emitter (spacer thickness) and used materials. The observed linearity between delayed signal and spacer thickness (inset in Fig. 4.9 (a)) suggests a constant diffusion velocity of the triplets.

In Fig. 4.9 (b), yellow and blue emission are shown as function of the strength of an externally applied magnetic field. Interestingly, no change in driving voltage is observed. The yellow emission increases with increasing magnetic field strength,

---

[5]fac-bis(2-phenylpyridyl)(2-pyridylcoumarin)iridium(III)

meaning that more triplets reach the phosphorescent emitter. This can be explained by the fact that the annihilation of triplets by polarons is spin controlled and the annihilation rate can be reduced by applying a magnetic field.[81]

The saturation of the blue emission with increasing magnetic field strength is not fully understood yet. It is interesting that in a conventional OLED containing only the yellow phosphorescent emitter, the magnetic field effect is not present. Kondakova *et al.* stated that this effect seems to be unique for TH OLEDs.[21]
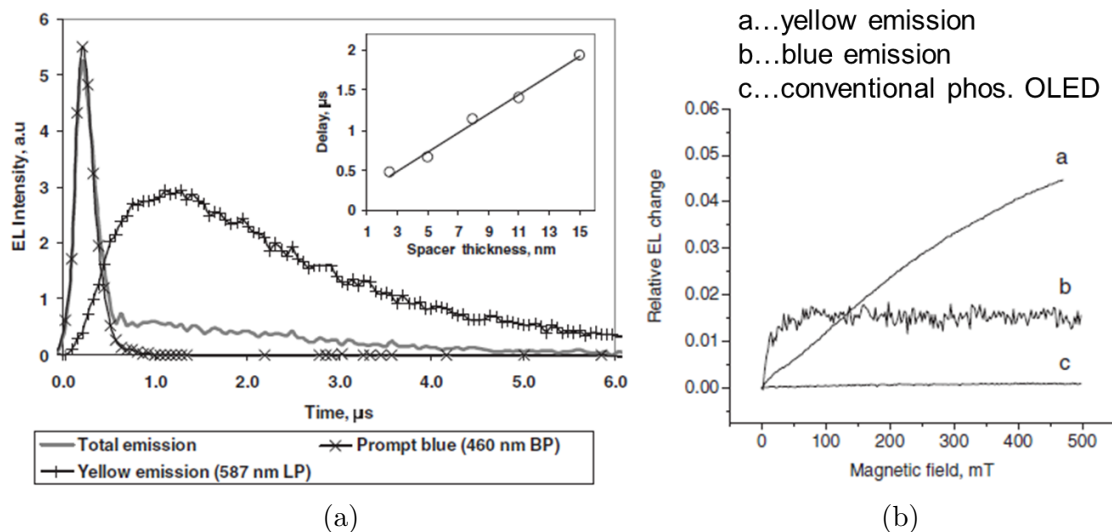
Figure 4.9: Proof of TH using time-resolved electroluminescence (a) and the magnetic field effect (b) by Kondakova *et al.*[21]. The diffusion of triplets leads to a delayed signal of the phosphorescent yellow emitter compared to the blue emitter. The inset shows that the delay time increases with increasing (spacer) distance between the two emitters. The increase of the yellow emission with increasing magnetic field strength results from the reduced triplet-polaron annihilation rate. This increases the number of triplets which are able to reach the phosphorescent emitter and hence increases the emission intensity. Reprinted with permission from [21]. Copyright 2010, American Institute of Physics.

Finally, it is important to mention that TH from a matrix material or a doped blue emitter to a green emitter has been shown several times.[17, 21, 117] However, TH from a blue fluorescent bulk emitter to a green phosphorescent emitter has not been demonstrated up to now. From a luminous efficacy point of view, TH from a bulk emitter is preferred, since the use of a matrix material usually results in higher driving voltages.

The challenge is to find an efficient blue fluorescent bulk emitter with a high triplet energy ($T_1 > 2.4$ eV) and a singlet energy in the range of 2.7 to 2.9 eV. The required reduction of the singlet-triplet splitting can be achieved by localizing the HOMO and LUMO wave functions on different regions of the molecule. Unfortunately, a smaller overlap of the wave functions goes hand in hand with a decrease of the

fluorescence quantum yield. Using up-conversion of triplets into singlets, e.g. by two triplets forming a singlet or by thermally activated delayed fluorescence (TADF), which converts a triplet into an excited singlet state, this issue might be overcome. The research of efficient emitters with small singlet-triplet splitting is in the very beginning.[119] Promising results have been achieved by Endo *et al.*[120] in 2011 using TADF. They demonstrated a fluorescence quantum yield of 39% for the compound PIC-TRZ[6], which exhibits a singlet energy of $S_1 = 2.66$ eV and a triplet energy of $T_1 = 2.55$ eV. Recently the same group obtained even 62% for the triazine derivative having bicarbazole substituents (CC2TA[7]) with $S_1 = 2.52$ eV and $T_1 = 2.46$ eV. The OLED comprising CC2TA as emitting material exhibits a remarkable high EQE of 11% at 0.1 mA/cm².[121]

4.5   Light Outcoupling

Light modes inside the OLED

It is a very strong simplification to describe light propagation in a thin film structure with ray optics. However, it helps to understand how light is lost inside the OLED and how most outcoupling approaches are working. Figure 4.10 shows a scheme of the OLED cavity including the glass substrate. Since organic materials have a similar refractive index of about 1.7 to 2.1 (depending on the wavelength), the single functional layers do not need to be distinguished. The refractive index of ITO ranges from 1.8 to 2.0. Glass has a refractive index of 1.5.
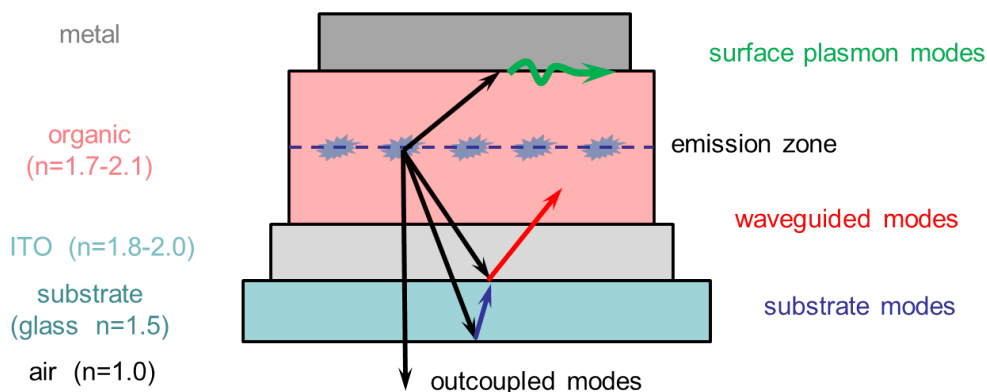
Figure 4.10: Light loss mechanisms inside the OLED resulting from total internal reflection. The light modes can be distinguished into outcoupled, waveguided, and surface plasmon polariton modes. Absorption losses in the ITO and the doped transport layers can be expected to play a minor role. Refraction at the interfaces has been omitted for simplification.

---

[6]2-biphenyl-4,6-bis(12-phenylindolo[2,3-a] carbazole-11-yl)-1,3,5-triazine,
[7]2,4-bis{3-(9H-carbazol-9-yl)-9H-carbazol-9-yl}-6-phenyl-1,3,5-triazine

Light is generated by the emitting molecules which can be assumed to form a thin emission zone close to the center of the organic layer. Due to total internal reflection at the interfaces organic/ITO, ITO/glass, and glass/air, only a certain amount of light is outcoupled into air (refractive index of 1), while the rest is trapped inside the device. Light modes trapped in the organic material and ITO are referred to as waveguided or organic modes. Light modes which cannot escape the substrate are so-called substrate modes.

A further loss mechanism are the surface plasmon polariton (SPP) modes, which are a result of the coupling of the emitting molecules to the metal surface. Absorption may also occur in the ITO and the doped transport layers. However, due to the high transparency of these layers, it can be expected that this forms a minor loss mechanism.

Quantification of light loss mechanisms

Regarding the electrical, excitonic, radiative, and optical processes, the external quantum efficiency η_{EQE} can be split into four terms[12, 122, 123]:

$$\eta_{\mathrm{EQE}} = \gamma\,\eta_{\mathrm{S/T}}\,\eta_{\mathrm{out}}\,\eta_{\mathrm{rad,eff}}, \tag{4.2}$$

where γ is the electrical efficiency (also known as charge balance factor). It describes the ratio of generated excitons to the number of injected electrons. The ratio of singlets/triplets is considered by $\eta_{\mathrm{S/T}}$, with $\eta_{\mathrm{S/T}} = 1$ for phosphorescent emitters, and $\eta_{\mathrm{S/T}} = 0.25$ for fluorescent emitters. The third term is the outcoupling efficiency η_{out}. It accounts for the ratio of outcoupled photons to generated photons. Using ray optics, η_{out} can be estimated using the refractive index of the glass substrate n_{glass} [124, 125]:

$$\eta_{\mathrm{out}} = \frac{1}{2n_{\mathrm{glass}}^2} = 0.22. \tag{4.3}$$

Eq. (4.3) implies that about 80% of the generated light cannot escape the device structure. This is a rather rough estimation, but in good agreement with the fact that the maximum measured EQEs for OLEDs (without using outcoupling enhancement methods) are in the range of 20% and indicates that there is a huge potential for efficiency improvement, if it is possible to outcouple the trapped modes.[15, 112]
The effective radiative efficiency $\eta_{\mathrm{rad,eff}}$ describes the number of generated photons to the number of generated excitons and is given by[13]:

$$\eta_{\mathrm{rad,eff}} = \frac{F\,\eta_{\mathrm{rad}}}{1 - \eta_{\mathrm{rad}} + F\,\eta_{\mathrm{rad}}}, \tag{4.4}$$

with F as Purcell factor and η_{rad} as intrinsic emitter radiative quantum efficiency (or internal quantum efficiency of the emitter). The Purcell factor accounts for the quantum mechanical effect that the radiative efficiency of an emitter depends on the

surrounding. In OLEDs, F ranges values below and above 1. In free space $F = 1$, and the effective radiative efficiency equals the intrinsic emitter efficiency η_{rad} which is given by[126–128]:

$$\eta_{\mathrm{rad}} = \frac{\Gamma_{\mathrm{rad}}}{\Gamma_{\mathrm{rad}} + \Gamma_{\mathrm{nonrad}}}, \tag{4.5}$$

where Γ_{rad} and Γ_{nonrad} are the radiative and nonradiative decay rates of the emitter. To calculate the EQE, the wavelength dependency of the respective efficiencies needs to be considered. Furthermore, the formula has to include the intrinsic emission spectrum of the emitter $s(\lambda)$ (i.e. the photoluminescence spectrum) with $1 = \int s(\lambda) \, \mathrm{d}\lambda$. Finally, the EQE reads[13]:

$$\eta_{\mathrm{EQE}} = \gamma \, \eta_{\mathrm{S/T}} \int s\,(\lambda) \, \eta_{\mathrm{out}}(\lambda) \, \eta_{\mathrm{rad,eff}}(\lambda) \, \mathrm{d}\lambda$$

$$= \gamma \, \eta_{\mathrm{S/T}} \int s\,(\lambda) \, \eta_{\mathrm{out}}(\lambda) \, \frac{F(\lambda) \, \eta_{\mathrm{rad}}}{1 - \eta_{\mathrm{rad}} + F(\lambda) \, \eta_{\mathrm{rad}}}(\lambda) \, \mathrm{d}\lambda. \tag{4.6}$$

In 2012, Furno *et al.*[13] showed that Eq. (4.6) can be used to calculate the intrinsic emitter efficiency η_{rad} and the electrical efficiency γ for pin-OLEDs with one emitter, when the EQE for different ETL thicknesses is known from the experiment. Here, the Purcell factor $F(\lambda)$ and the outcoupling efficiency $\eta_{\mathrm{out}}(\lambda)$ are modeled by treating the emitting molecules as ensemble of emitting dipole antennas. The obtained values for η_{rad} are in the range of 73 to 84% with an error of $\pm 10\%$, while γ lies between 0.90 to 0.94. The investigated emitters were the red phosphorescent emitter $\mathrm{Ir(MDQ)_2(acac)}$, the green phosphorescent emitter $\mathrm{Ir(ppy)_3}$, and the blue fluorescent emitter TBPe (cf. Sec. 5.1).

These validations are done at low exciton densities of the OLEDs, before the roll-off sets in, so that annihilation effects can be excluded. The distribution of the emitting dipoles within the EML is considered as delta-shaped. This is reasonable, since the EML thickness is small compared to the whole device thickness. However, for a complete description, the incorporation of the emission profile might be interesting.

As discussed in the previous section, the emission profile inside the OLED is a result of the recombination profile of electrons and holes, and the diffusion profile of excitons within the device. The study of emission profiles in OLEDs is an important research topic. While for polymer OLEDs several methods are known to obtain the emission profile[129, 130], this topic is hardly investigated for small molecule OLEDs. One reason is that they usually have smaller EML thicknesses.

Nevertheless, it is possible to quantify the loss mechanisms inside the OLED cavity. In the following, a red phosphorescent $(\mathrm{Ir(MDQ)_2(acac)})$ pin-OLED as described in Ref. [131] is considered as an example. The loss mechanisms depending on the ETL thickness are shown in Fig. 4.11.

The outcoupled emission exhibits a strong dependence on EML thickness. This can be understood by regarding the resonance condition inside the OLED cavity for 0°:

$$2\,L = m\,\lambda, \tag{4.7}$$

with $L = nd$ the optical thickness of the cavity (i.e. the cavity length d multiplied by the refractive index n) and m the resonance order. The cavity condition is a result of constructive and destructive interference of the light modes. The calculation of the electromagnetic field confirms this condition.
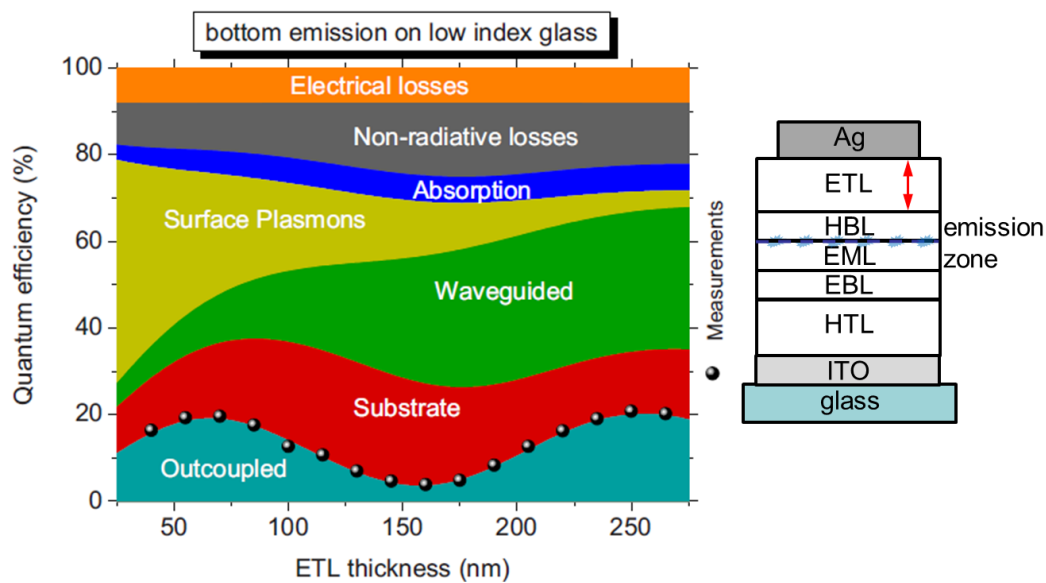
Figure 4.11: Quantified loss mechanisms in a red phosphorescent pin-OLED for different ETL thicknesses by Meerheim *et al.*[131]. The simulated quantum efficiency agrees nicely with experimental results (at low current density of 1.51 mA/cm², configuration as shown on the right side). Reprint with permission from [131]. Copyright 2010, American Institute of Physics.

For the red OLEDs, the calculated field intensity for different cavity lengths and emitter positions is shown in Fig. 4.12. Here, the field is obtained using classical electrodynamics and the transfer matrix method.[13] If the emitting molecules are placed in the maximum of the electromagnetic field, a large number of radiation modes is available, and therefore a strong coupling to the outcoupled modes can be expected. Placing the emitters into the node of the field, in contrast, leads to low outcoupling efficiencies. The influence of the emitter coupling to the field and the Purcell effect on the outcoupling efficiency are often referred to as cavity effects. As indicated in Fig. 4.12, so-called optical maxima of higher order occur when increasing cavity thickness. Hence, in Fig. 4.11 the OLED at 70 nm ETL thickness is called first order device, and the OLED at 250 nm second order device. Interestingly, in

the considered case, the EQE in the second maximum is slightly higher than for the first order device. It can be shown that this effect strongly depends on the intrinsic radiative emitter efficiency.[127, 131]

Regarding the substrate modes in Fig. 4.11, their dependence on the ETL thickness is similar but not as strong as for the outcoupling efficiency. Furthermore, the mode redistribution from SPP to waveguided modes with increasing ETL thickness can be seen in Fig. 4.11. Together, the SPP, waveguided, and substrate modes account for about 60 to 70% of the light loss inside these OLEDs. Since the increase of the doped transport layer thickness does not result in a voltage drop, the electrical efficiency can be assumed to be constant for all layer thicknesses. The electrical, nonradiative, and absorption losses are together in the range of 20 to 30%, which in the end limit the device EQE to about 20%. This is in good agreement with the calculations of Nowy *et al.*[127] and Setz *et al.*[132], who obtained similar results for green OLEDs.
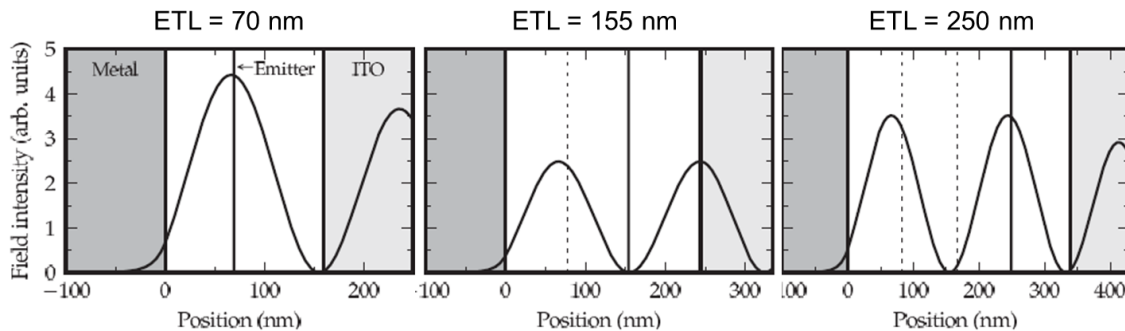
Figure 4.12: Electromagnetic field intensities for the devices shown in Fig. 4.11 at the peak wavelength of the emitter (610 nm, 0°) by Furno *et al.*[13]. Increasing the ETL thickness and thus the cavity thickness shifts the emitting molecules through a first maximum, a minimum, and a second maximum. The coupling of the emitting molecules to the electromagnetic field influences the outcoupling efficiency strongly and explains qualitatively the dependence of the outcoupling efficiency in Fig. 4.11 on the ETL thickness. Reprinted with permission from [13]. Copyright 2012 by the American Physical Society.

Orientation of the emitting dipoles

The outcoupling efficiency η_{out} depends on the orientation of the transition dipoles. This issue has to be considered when modeling η_{out}. Often, the dipole orientation of the emitting molecules is unknown and therefore assumed to be isotropic, i.e. 1/3 vertical (z-direction) and 2/3 horizontal dipoles (xy-plane) (cf. Fig. 4.13 (a)). As shown in Fig. 4.13 (b), a vertical dipole emits only transversal magnetic (TM) light, while horizontal dipoles emit TM and transversal electric (TE) light modes. Only TM modes can couple to surface plasmon modes, meaning that TE modes will more strongly contribute to the outcoupled modes. Hence, a horizontal orientation of emitting dipoles is desired.

The anisotropy factor Θ accounts for the number of vertically orientated dipoles to the number of total dipoles, so that $\Theta = 1/3$ for isotropic orientation, $\Theta = 1$ for completely vertical orientation, and $\Theta = 0$ for completely horizontal orientation.

Recently, it was found that certain emitters provide a preferentially horizontal dipole orientation in small-molecule OLEDs.[133–139] A correlation between molecule length and horizontal orientation (the more planar the molecule, the more horizontal emitters) has been observed[139]. However, there are as well non-planar emitters which show preferential horizontal orientation[138, 140]. Up to now, the reason for this effect is not clear. It might be possible that the orientation depends on the processing conditions, matrix materials, the surface/material below, and so on.

Schmidt *et al.*[138] obtained an anisotropy factor of $\Theta = 0.24$ for the red phosphorescent emitter $Ir(MDQ)_2(acac)$. They further estimated a maximum EQE of 38% (70%, if substrate modes can be outcoupled), assuming $\Theta = 0$, $\gamma = 1$, and $\eta_{rad} = 1$. Controlling the emitter orientation offers the possibility to achieve highly efficient OLEDs. Unfortunately, a method to achieve complete horizontal orientation is not known up to now.

(a)   (b)
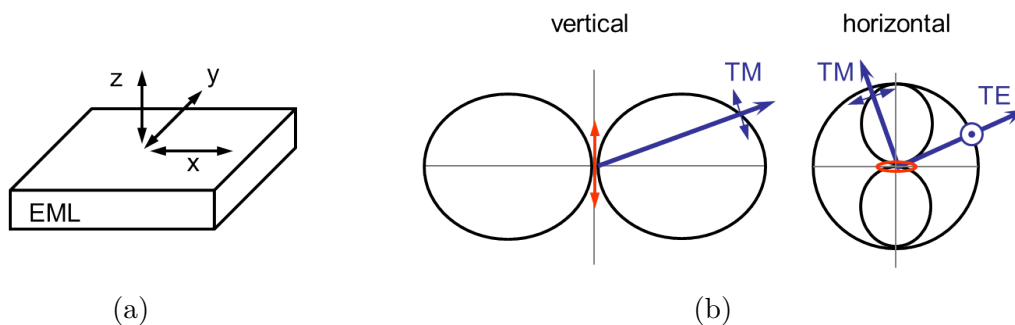
Figure 4.13: Geometry of dipole distribution inside the EML (a) and emission pattern of horizontal and vertical oriented dipoles (b). A vertical dipole emits TM modes, while horizontal dipoles emit TM and TE modes.

Outcoupling enhancement methods

A simple approach to get access to the substrate modes is the attachment of a glass half-sphere (Fig. 4.14 (a) and (b)). Index matching oil is then used to obtain an optical contact between the substrate and the sphere. Modes which would undergo total internal reflection at the glass/air interface are directly coupled into the half-sphere. Due to the shape of the half-sphere, the angle of light incidence becomes now 90° and the former glass modes are converted to outcoupled modes (Fig. 4.14 (b)).

The outcoupling of organic modes can be achieved by the use of a high refractive index (high-n) substrate (Fig. 4.14 (c)). The organic modes can now be transferred into the substrate. Similarly to the low-n case, a half-sphere made of high-n glass is necessary to couple these modes into air.
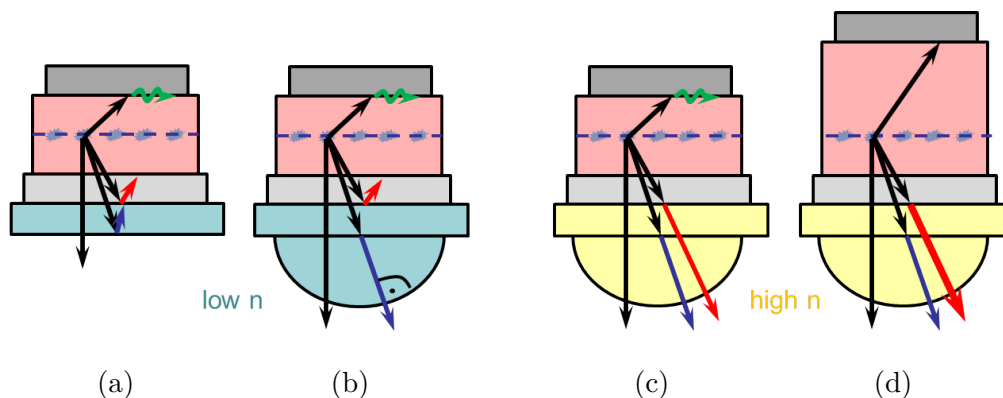
Figure 4.14: Light outcoupling of substrate modes from conventional configuration (a) via an attached glass half-sphere (b). The substrate modes are now coupled into the glass half-sphere and contribute to the outcoupled modes. Using high-n glass, the organic modes can be extracted (c). By increasing the distance between emitting molecules and the metal cathode (d), the SPP modes are strongly reduced and more waveguided modes are generated, which will be outcoupled by the high-n glass. Refraction at the interfaces has been omitted for simplification.

The strength of excited SPP modes depends strongly on the distance of emitter molecules to the metal electrode. Thus, an increase in distance will lower the SPP coupling (Fig. 4.14 (d)). However, it can be observed that the modes which are no longer lost to SPP modes now strongly contribute to waveguided modes. Therefore, a high-n substrate and half-sphere are required to make full use of this approach. Using this simple picture, it is expected that almost all light modes can be outcoupled and high EQEs in the range of 80 to 100% should be possible.

Applying a configuration like the one illustrated in Fig. 4.14 (d), high efficiencies have indeed been demonstrated. In 2009, Mladenovski *et al.*[141] measured an EQE of 42%, corresponding to 183 lm/W (at 1,000 cd/m²) for a green phosphorescent pin-OLED. Meerheim *et al.*[131] achieved even 54% (104 lm/W at 500 cd/m²) with a red phosphorescent pin-OLED. This demonstrates that the index matching approach works well to efficiently enhance outcoupling. However, the experimentally achieved EQEs of about 50% are still significantly lower than the expected 80 to 100%. Despite the fact that perfect index matching cannot be achieved experimentally, this already indicates that ray optics are not sufficient to describe OLEDs quantitatively.

Furthermore, high index glass is very expensive and a half-sphere which needs to have at least the size of the OLED is not very handy. Various other outcoupling methods are therefore in the focus of current OLED research, like the use of micro-lens arrays[142, 143], alternative electrodes (e.g. polymers[144, 145], metallic nanowires[146–148], graphene films[149]), scattering layers[150, 151], gratings structures[17, 152, 153], and others.

4.6   White OLEDs - State-of-the-Art

The possibilities to obtain white emission in OLEDs are manifold.[154, 155] An overview on the existing white OLED layouts is given in Fig 4.15. Depending on the number of emitter materials, the OLEDs can be distinguished into single-color, two-color, three-color, etc. white OLEDs. Single-color white OLEDs (Fig. 4.15 (a)) comprise one emitter with a broad emission spectrum.[156] However, achieving the desired color coordinates might be difficult with this approach. In multi-color OLEDs this can be done more easily by adjusting the emitter contributions. For two-color OLEDs the down-conversion principle is one possible approach (Fig. 4.15 (b)).[157] Here, a part of the blue light is converted into red/yellow light. Since the down-conversion layer is electrically inert, this layer can be placed on the outside of the substrate.

The layouts (c-f) in Fig. 4.15 are shown for three-color white OLEDs, but they are not restricted to three emitters. Nevertheless, white OLEDs based on three emitters are most common.
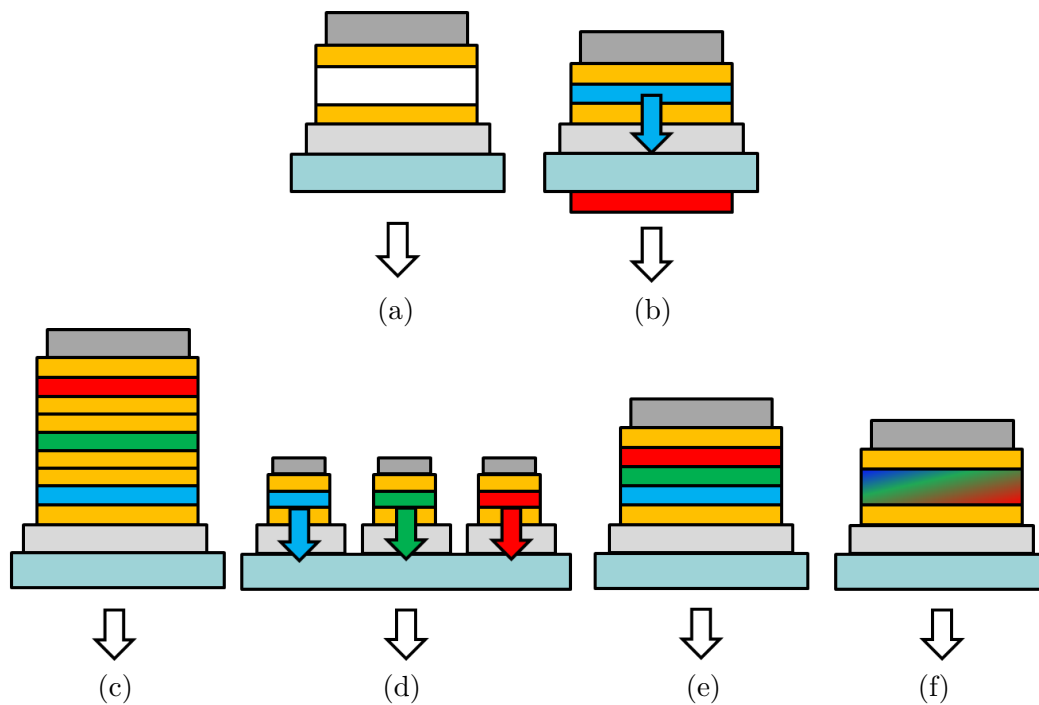
Figure 4.15:   Common layouts for white OLEDs: single-color (a), down-conversion (b), stacked (c), subpixel (d), sublayer EML(e), and multiple doped EML OLEDs (f). Furthermore, white OLEDs can be distinguished by the number of emitters: single-color, two-color, three-color, etc. white OLEDs.

In the last years, tandem (stacked) OLEDs, where two or more OLEDs are built on top of each other came into the focus of interest (Fig. 4.15 (c)).[158] These structures are very efficient, since additional charge carriers are generated at the interfaces between the single OLEDs. In a tandem OLED consisting of two subunits, ideally an internal quantum efficiency of 200% is possible. However, the large cavity complicates light outcoupling, since all emitters need to be placed in their respective field maximum. Since these tandem OLEDs are series connected, the driving voltage is strongly increased in comparison to single-unit OLEDs.[19, 20]

Another possibility to obtain white light is the use of monochrome OLEDs in a subpixel design (Fig. 4.15 (d)).[154] Here, the advantage is that each pixel can be individually optimized. The disadvantage, on the other hand, is that these subpixel OLEDs require a very sophisticated and complicated structuring processes. The last two OLED layouts are either based on a sublayer EML design (Fig. 4.15 (e)) or a multiple-doped EML (Fig. 4.15 (f)).[159, 160]

The most promising methods to achieve highly efficient white OLEDs are the full phosphorescent (PH) and the TH OLED, since both concepts allow very high internal quantum yields (see previous sections). The layouts used for these devices are mostly multi-color sublayer EML (Fig. 4.15 (e)) or stacked OLEDs (Fig. 4.15 (c)).

The advantage of the TH OLED in comparison to PH OLEDs is that due to the use of a blue fluorescent emitter, the common problems with phosphorescent blue emitters (sky-blue color coordinates and low lifetime) can be overcome. Table 4.1 gives an overview of the performance of state-of-the art white OLEDs.

Without outcoupling enhancement, luminous efficacies of more than 30 lm/W (EQE of 10 to 20%) with almost warm white color coordinates and good CRI values are possible with both concepts. Using light outcoupling techniques, the LE and EQE can be strongly enhanced (about 120 lm/W and 45% at 1,000 cd/m²). It is important to mention that when comparing EQEs of tandem units with non-tandem OLEDs, the EQE value should be divided by the number of OLED units to obtain a fair comparison.

It can be also seen from Tab. 4.1 that, as expected, more emitters usually lead to higher CRI values and that more greenish or reddish color coordinates lead to higher efficiencies. Of course, the more emitters are used, the more complicated is the design of OLEDs. Regarding lighting application, further issues, including color stability with current and viewing angle, lifetime, and costs, have to be considered. Nevertheless, these achievements show great promise for white OLEDs to become a general light source (cf. Sec. 2).

Table 4.1: Summary of the performance properties of PH and TH state-of-the-art small-molecule white OLEDs.

group	year	LE¹ lm/W	LE² lm/W	LE³ lm/W	EQE¹ %	EQE² %	EQE³ %	CE³ cd/A	CRI³	CIE³	layout cf. Fig. 4.15
FULL PHOSPHORESCENT											
Sun[161]	2008	37	22	—	15.3	13.6	—	—	~81	~(0.37/0.41)	3-color (e)
		63[a]	37[a]	—	26[a]	23[a]	—	—	—	—	2-color (e)
Su[85]	2008	—	—	44	—	—	24	—	68	(0.34/0.40)	2-color (e)
Reineke[14]	2009	—	—	30	—	—	13.1	—	80	(0.44/0.46)	3-color (e)
		—	—	55[b]	—	—	24[b]	—	—	—	
		—	—	33[c]	—	—	14.4[c]	—	80	(0.45/0.47)	3-color (e)
		—	—	81[d]	—	—	34[d]	—	—	—	
		—	—	124[d]	—	—	46[d]	—	69	(0.41/0.49)	3-color (e)
Sasabe[162]	2010	52.7	—	33.2	19.0	—	15.9	38.7	66	(0.38/0.38)	2-color (e)
		59.9	—	43.3	21.6	—	21.5	49.6	80	(0.43/0.43)	3-color (e)
TRIPLET HARVESTING											
Sun[17]	2006	22.1	—	—	11.0	10.8	—	—	—	~(0.40/0.41)	3-color (e)
		37.6[e]	23.8[e]	—	18.7[e]	18.4[e]	—	—	—	—	
Schwartz[163]	2008	—	—	31.6	—	—	15.2	—	62	(0.49/0.41)	3-color (e)
		—	—	49.2[f]	—	—	24.3[f]	—	—	—	
		—	—	25.4	—	—	11.2	—	82	(0.43/0.43)	3-color (e)
		—	—	40.7[f]	—	—	20.3[f]	—	—	—	
Rosenow[19]	2010	—	—	33.0	—	—	26.0	—	78	(0.51/0.42)	4-color (c)
		—	—	90.5[d]	—	—	75.8[d]	—	81	(0.46/0.43)	4-color (c)
Kondakova[21]	2010	—	—	30.1	15.8	—	13.6	34.8	—	(0.32/0.36)	2-color (e)
		—	—	21.4	—	—	12.6	—	—	(0.32/0.32)	3-color (e)
Ye[116]	2012	67.2	40.1	33.5	26.6	—	21.2	42.6	54	~(0.46/0.44)	2-color (e)

¹ maximum value
² at 500 cd/m²
³ at 1,000 cd/m²

[a] with microlens
[b] with half-sphere
[c] with high-n glass
(no outcoupling enhancement structures)

[d] with high-n glass and half-sphere
[e] with edge emission
[f] with edge emission and microlens foil

5 Experimental and Methods

In this chapter, the materials used for OLEDs investigated in this work are introduced. This includes the substrate, electrodes, transport materials, blocker materials, and fluorescent and phosphorescent emitters. The device fabrication in the ultrahigh vacuum chamber is explained. Furthermore, important measurement setups and characterization methods of OLEDs, such as current-voltage-luminance, spectral emission, angular dependence, efficiencies, and lifetime are described. The time-resolved measurement of the spectral emission of OLEDs using a streak camera is introduced, as well as the photoluminescence setup. At the end, the theoretical methods of optical simulation of OLEDs and the quantum chemistry calculations are briefly discussed.

5.1 Materials

All used materials are commercially purchased from various suppliers as stated below. The organic materials consist of small molecules, having a mass between approximately 300 and 1500 g/mol. All organic materials are available in powder form and are purified by vacuum gradient sublimation before evaporation.[9, 164]

Transport Materials

The transport layers in this work are realized by doping a guest molecule into a matrix material, thus increasing conductivity (cf. Sec. 4.2). As hole transport layer the wide gap matrix material N,N,N',N'-tetrakis(4-methoxyphenyl)-benzidine (MeO-TPD, Sensient) doped with 2,2'-(perfluoronaphthalene-2,6-diylidene)dimalono-nitrile (F6-TCNNQ, Novaled AG) is used. The doping concentration is typically in the range between 2 and 4 wt%.[165, 166]
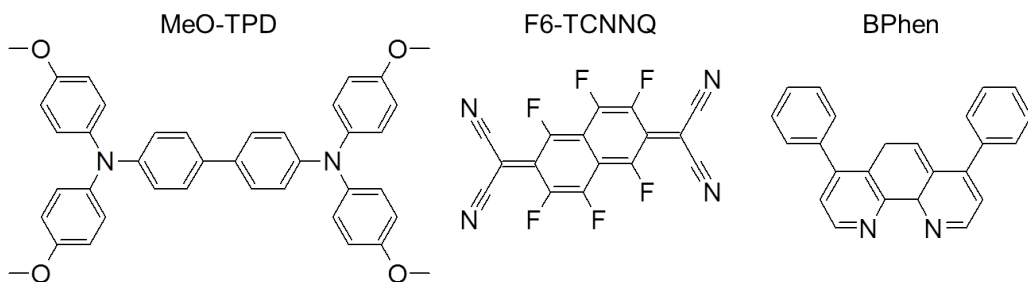
Figure 5.1: Molecular structures of materials used as transport layers. The matrix MeO-TPD and the dopant F6-TCNNQ serve as hole transport layer, and BPhen as matrix for the electron transport layer.

The electron transport layer consists of the wide gap bathophenanthroline; 4,7-diphenyl-1,10-phenanthroline (BPhen, abcr GmbH & Co. KG) doped with the metal cesium (Cs) which has a work function of -2.1 eV.[103] The chemical structures of MeO-TPD, F6-TCNNQ, and BPhen are shown in Fig. 5.1. The doping concentration of Cs is adjusted while performing a conductivity measurement during evaporation with a test sample. Therefore, BPhen and Cs are co-evaporated and the current/conductivity change between two side by side ITO contacts is measured. The temperature of Cs is then set to fulfill a current change of 0.01 nA/(s nm). This leads to a ratio of about one Cs atom per BPhen molecule [167]. Both doped transport layers exhibit a conductivity in the range of 10^5 S/cm [167]. A summary of HOMO, LUMO, singlet, and triplet energies for all materials used in this study is given in Tab. 5.1.

Blocker Materials

For efficient electron (hole) blocking, the respective materials need to have a sufficiently high LUMO energy (low HOMO energy). For efficient exciton confinement, the singlet energy has to be higher than that of the emitter material. In case of phosphorescent emitters, the triplet energy of the blocker needs to be sufficiently higher.
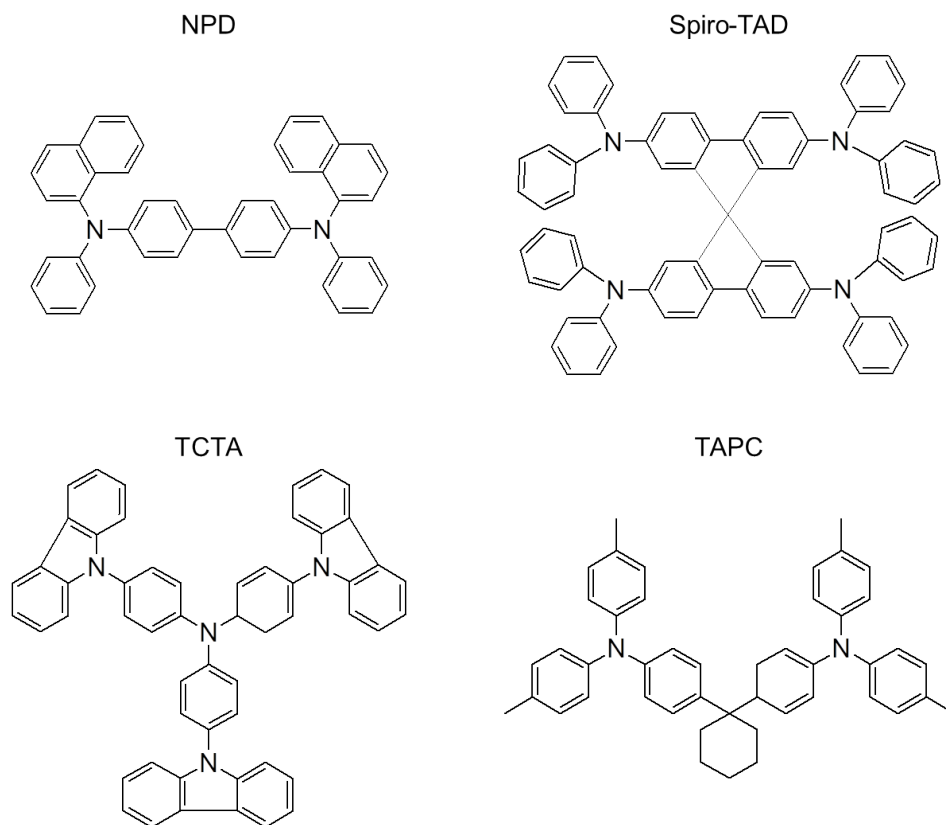
Figure 5.2: Molecular structures of important materials used as electron blocking layers: NPD, Spiro-TAD, TCTA, and TAPC.

The molecular structures of the electron blocking materials used in this study are shown in Fig. 5.2: N,N'-Di(naphthalene-1-yl)-N,N'-diphenyl-benzidine (NPD, Sensient) [111], 2,2',7,7'-tetrakis-(N,N-diphenylamino)-9,9'-spirobifluorene (Spiro-TAD, Lumtec) [168], 4,4',4''-tris(carbazol-9-yl)-triphenylamine (TCTA, Sensient) [169], and di-[4-(N,N-ditolyl-amino)-phenyl] cyclohexane (TAPC, Sensient) [170]. The LUMO energies are in the range of -2.3 to -2.7 eV (cf. Tab. 5.1).

The hole blocking materials are shown in Fig. 5.3: aluminum (III) bis(2-methyl-8-quinolinato)-4-phenylphenolate (BAlq2, Sensient) [171, 172], 2,2',2''-(1,3,5-phenylene)tris(1-phenyl-1H-benzimidazole) (TPBI, Sensient) [173], N,N'-Di(naphthalene-1-yl)-N,N'-diphenyl-benzi-dine2- (diphenyl-phosphoryl)spirofluorene (SPPO1, Lumtec) [174], 1,4-phenylene bis(tri-phenyl-silane) (UGH2, Sigma-Aldrich Co. LLC.) [175], and 2,9-dimethyl-4,7-diphenyl-1,10-phenanthroline (BCP, abcr GmbH & Co. KG) [111]. The HOMO energies of all hole blocking materials are below -6.1 eV (cf. Tab. 5.1). Since BPhen has a low HOMO energy of -6.5 eV, it is also used as HBL.
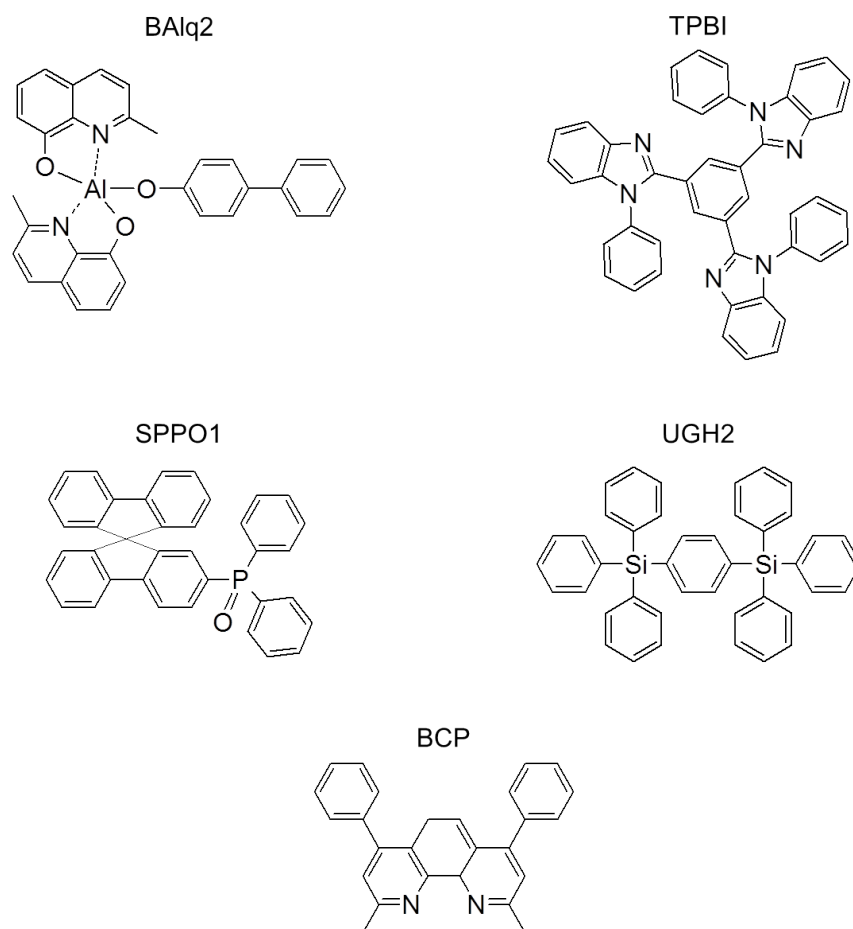
Figure 5.3: Molecular structures of important materials used as hole blocking layers: BAlq2, TPBI, SPPO1, UGH2, and BCP.

Emitter Materials

As blue fluorescent emitter, the bulk emitter N,N'-di-1-naphthalenyl-N,N'-diphenyl-[1,1':4',1":4",1"'-quaterphenyl]-4,4"'-diamine (4P-NPD, Lumtec) is used. This emitter chemically differs from NPD by two additional phenyl rings. 4P-NPD has a deep blue emission (cf. Fig. 5.6) and emits efficiently from the singlet state.[18]

The second blue fluorescent emitter used in this work is 2,5,8,11-tetra-tert-butylperylene (TBPe, Lumtec). In contrast to 4P-NPD, this emitter is embedded into a matrix to avoid concentration quenching. As matrix, the ambipolar wide band gap material 2-methyl-9,10-bis(naphthalen-2-yl)anthracene (MADN, Lumtec) is used.[102]

The chemical structures of fluorescent emitter materials are shown in Fig. 5.4.
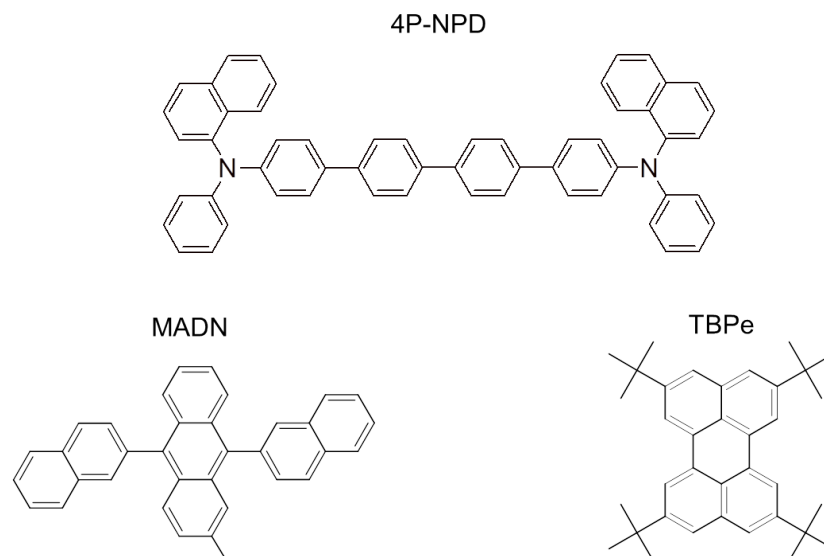
4P-NPD

MADN   **TBPe**

Figure 5.4: Molecular structure of the deep blue fluorescent bulk emitter 4P-NPD and the matrix:emitter system MADN:TBPe.

The phosphorescent emitters used in this work have an iridium atom as heavy metal in their core. This increases the ISC rate dramatically and leads to an efficient emission from the triplet state (cf. Sec. 4.3). Figure 5.5 shows the molecular structure of the phosphorescent emitters: tris(2-phenylpyridine) iridium(III) (Ir(ppy)$_3$, Covion GmbH) [81], bis(2-phenylpyridine)iridium(III) acetylacetonate (Ir(ppy)$_2$(acac), Lumtec) [12, 176], bis(2-(9,9-dihexylfluorenyl)-1-pyridine) (acetylacetonate) iridium(III) (Ir(dhfpy)$_2$(acac), Lumtec) [115], and iridium(III)bis(2-methyldibenzo-[f,h]chinoxaline) (acetylacetonate) (Ir(MDQ)$_2$(acac), American Dye Source, Inc.) [177]. Due to the longer lifetime of triplets compared to singlets, the triplet density becomes high in the EML, and the phosphorescent emitters underlie a strong concentration quenching.[83, 178] Hence, for OLEDs they are doped at low concentration (typically 1 to 10 wt%) into a suitable matrix material (e.g. NPD, TPBI, or TCTA).
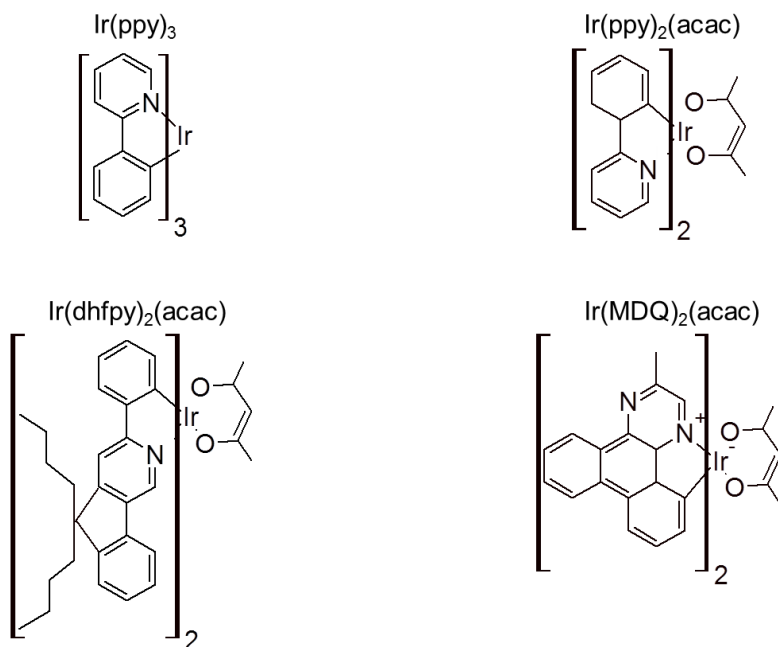
Figure 5.5: Molecular structures of important materials used as phosphorescent emitters Ir(ppy)$_3$, Ir(ppy)$_2$(acac), Ir(dhfpy)$_2$(acac), and Ir(MDQ)$_2$(acac). Due to the iridium core the ISC rate is dramatically increased which leads to an efficient emission from the triplet state.
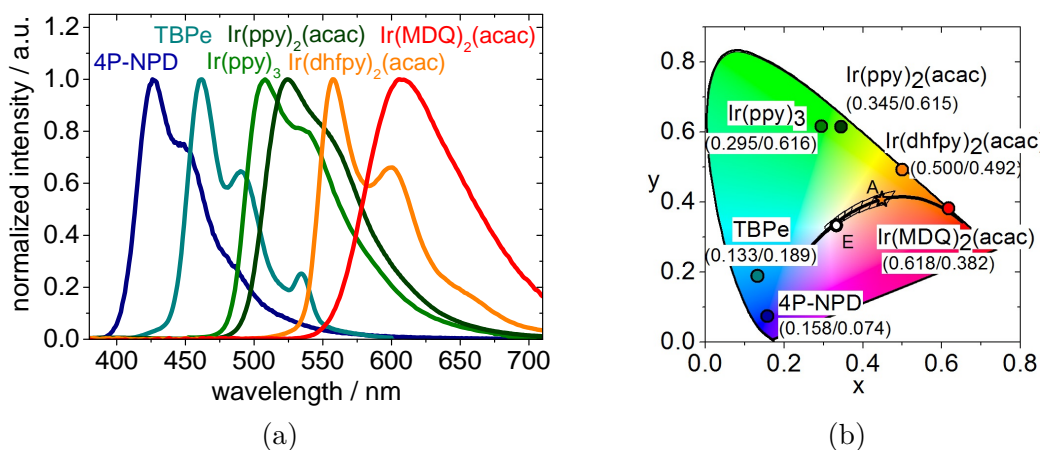
Figure 5.6: Photoluminescence spectra of important emitter materials 4P-NPD (deep blue), TBPe (blue), Ir(ppy)$_3$ (green), Ir(ppy)$_2$(acac) (green), Ir(dhfpy)$_2$(acac) (orange) and Ir(MDQ)$_2$(acac) (red) (a) and CIE color coordinates calculated from the spectral emission (b).

In Fig. 5.6 (a) the photoluminescence spectra [179] of the used emitters are shown. The spectra exhibit a full width at half maximum of 60 to 80 nm and are perceived as monochrome colors, since their color coordinates are close to the edge of the CIE diagram (Fig. 5.6 (b)). The emission color of 4P-NPD is deep blue, blue for

TBPe, green for Ir(ppy)$_3$ and Ir(ppy)$_2$(acac), yellow for Ir(dhfpy)$_2$(acac), and red for Ir(MDQ)$_2$(acac).

Summary of Material Properties

The HOMO, LUMO, singlet, and triplet energy levels of all materials used in this study are displayed in Tab. 5.1. HOMO and LUMO energy are deduced from photoelectron spectroscopy of thin films.[180] Singlet energies are derived from the fluorescence emission peak of thin films.[179] In case of phosphorescent emitters the emission peak yields the triplet energy. The triplet energy of the remaining materials is measured by delayed phosphorescence at 77 K.[46, 181]

Table 5.1: Summary of material properties (HOMO, LUMO, singlet energy S$_1$, and triplet energy T$_1$) of different organic small molecule materials used in this work.

material	HOMO eV	LUMO eV	S$_1$ eV	T$_1$ eV
TRANSPORT MATERIALS				
MeO-TPD	-5.1 [180]	-1.9 [180]	2.53 [179]	—
F6-TCNNQ	-7.8 [166]	-5.4 [166]	—	—
BPhen	-6.5 [180]	-2.9 [180]	3.21 [179]	2.50 [46]
ELECTRON BLOCKING MATERIALS				
NPD	-5.4 [180]	-2.6 [180]	2.81 [179]	2.29 [46]
Spiro-TAD	-5.4 [168]	-2.4 [168]	3.06 [179]	—
TCTA	-5.3 [169]	-2.7 [169]	3.20 [179]	2.83 [46]
TAPC	-5.8 [170]	-2.4 [170]	3.35 [179]	2.87 [170]
HOLE BLOCKING MATERIALS				
BAlq2	-6.1 [180]	-3.2 [180]	2.51 [179]	2.31 [21]
TPBI	-6.3 [180]	-2.8 [180]	3.20 [179]	2.64 [46]
SPPO1	-6.5 [182]	-2.8 [182]	3.52 [179]	2.80 [182]
UGH2	-7.4 [180]	-2.7 [180]	4.40 [175]	3.50 [175]
BCP	-6.5 [180]	-3.0 [180]	—	—
FLUORESCENT EMITTER				
4P-NPD	-5.7 [18]	-2.3 [18]	2.91 [179]	2.31 [18]
TBPe	-5.3 [180]	-2.3 [180]	2.70 [179]	—
MATRIX FOR TBPE				
MADN	-5.5 [180]	-2.6 [180]	2.74 [179]	—
PHOSPHORESCENT EMITTER				
Ir(ppy)$_3$	-5.1 [180]	-2.4 [180]	2.60 [183]	2.40 [179]
Ir(ppy)$_2$(acac)	-5.4 [12]	-2.8 [12]	—	2.38 [179]
Ir(dhfpy)$_2$(acac)	-5.1 [180]	-2.4 [180]	—	2.23 [179]
Ir(MDQ)$_2$(acac)	-5.4 [180]	-2.8 [180]	—	2.02 [179]

Substrates and electrodes

In this work, borofloat glass (Thin Film Devices Inc.) with a thickness of 1.1 mm is used as substrate for OLEDs. The glass substrates are already coated with ITO as bottom contact when received from the manufacturer. The substrates are cleaned by ultrasonic treatment in n-methyl-2-pyrrolidon (NMP), distilled water, and ethanol before device processing. A detailed description of the cleaning procedure can be found in Ref. [184].

The inset in Fig. 5.7 shows a photographical image of a 1 x 1 inch pre-structured ITO glass substrate. The patterned structure consists of four ITO fingers, each serving as anode for one OLED pixel, and an additional rectangular shaped enhancement contact for the top contact. The ITO has a thickness of 90 nm and a sheet resistance of approx. 26 Ohm/sq.[185] The transmission of the glass substrate and ITO is shown in Fig. 5.7 for the visible wavelength regime using air as reference.[186] While the transmission of the ITO-free glass substrate has an average value of 91.6%[8] and is almost wavelength independent (standard deviation of 0.5%), the average transmission for ITO on glass decreases to 84.3% and shows a larger wavelength dependence with a standard deviation of 2.1%. The average transmission of ITO (excluding the glass substrate) over the visible wavelength regime is 92%.

The highly reflective top electrode of the OLED is a metal, either aluminum (Al) or silver (Ag) exhibiting an average reflectivity of about 90 or 95%, respectively. The work function of both metals is -4.3 eV.[187]
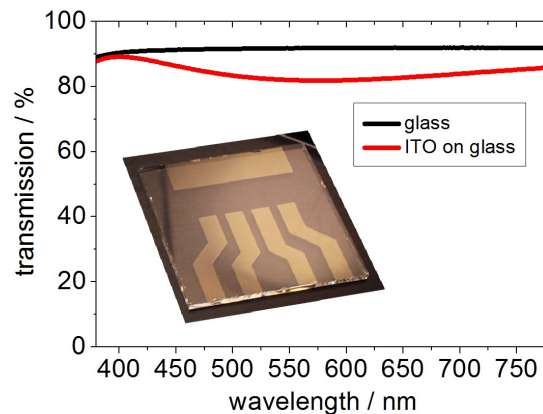
Figure 5.7: Transmission of the substrate with and without ITO. Inset: photographical image of a pre-structured 1 x 1 inch glass substrate with four ITO fingers.

---

[8]Losses mostly originate from Fresnel reflection.

5.2   Device Preparation

All OLEDs are prepared by thermal evaporation of thin layers under ultra high vacuum (UHV) conditions. For device preparation three tools at the IAPP are available, namely UFO2, Lesker A, and Lesker B. The UFO2 can only process small substrates (1 x 1 inch), whereas the Lesker tools can handle larger substrates (6 x 6 inch). This allows the processing of several different OLEDs with equal processing conditions. Since the Lesker tools provide a better comparability and reproducibility, all OLEDs are processed there. The UFO2 is mainly used for single layers and testing, thus avoiding waste of material.

UFO2 and layer deposition

The UFO2 (Fig. 5.8) is a multichamber evaporation cluster system (Bestec), where single chambers are connected via the handler to move the sample from chamber to chamber without braking the vacuum. A load lock is connected to a nitrogen filled glove box and further to a flow box to load in/out the samples. The UFO2 consists of five chambers for organic material evaporation, one metal chamber, one sputter chamber and one storage chamber. Each organic chamber consists of four to eight heat sources for the crucibles, two to four quartz crystal microbalance (QCM), a mask system and a shutter. Fig. 5.9 shows a scheme of the detailed setup of an organic evaporation chamber.
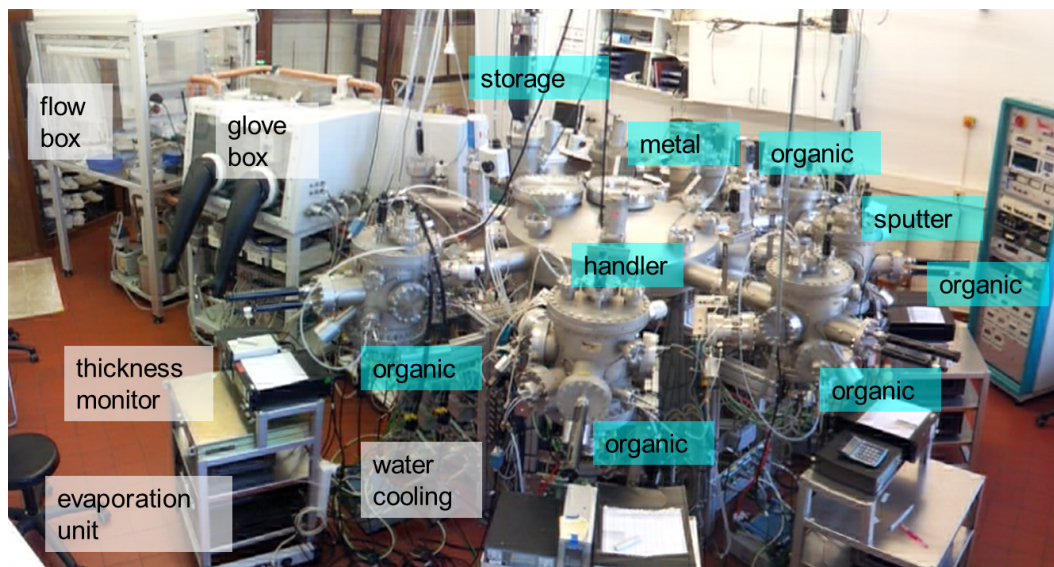
Figure 5.8: Photograph of the multichamber evaporation cluster tool UFO2. The single chambers are connected via a handler system to move the sample from chamber to chamber. A load lock is connected to a nitrogen filled glove box which again is connected to a flow box to load in/out the samples.

The substrate is mounted upside down into the sample holder. When heating the crucible, the organic material starts evaporating and condensates on the sample and at the same time on a QCM, which is mounted above the source. The distance between the substrate and the crucible is about 25 cm. With the QCM, the rate and thickness of the organic material can be obtained by measuring the frequency change of the quartz crystal resonator. Using the QCM and the manual opening/closing of the shutter between crucible and substrate, the thickness of the organic layer can be well controlled. Layer thicknesses in the range of a few nanometer to hundreds of nanometers can be processed. The pressure during evaporation is in the range of $10^{-9} - 5 \cdot 10^{-7}$ mbar. Doping can be achieved by co-evaporation of two or more materials. A mask system allows to structure the layers and the top contact on the substrate.
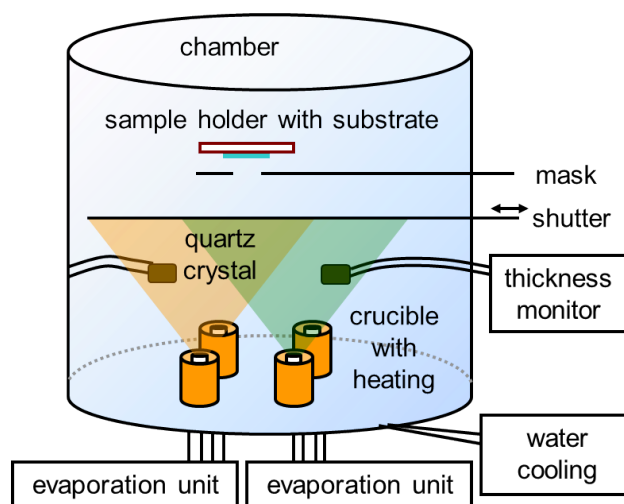
Figure 5.9: Schematic illustration of an organic deposition chamber. The heating of the crucible results in evaporation of organic material. If the shutter is opened, organic vapor condensates on the upside down mounted substrate. Doping is achieved by co-evaporation of two or more materials.

Lesker A, Lesker B, and device layout

The two Lesker tools A and B (Kurt J. Lesker Co.) are single evaporation chambers with comparable performance. Hence, only the Lesker A is described (Fig. 5.10). Lesker A consists of 11 organic sources and three thermal sources for metal evaporation. It is possible to co-evaporate up to four organic materials. The evaporation process is very similar compared to the UFO2. However, here the substrate (or wafer, 6 x 6 inch) does not need to be transferred from chamber to chamber. The availability of a wedge tool allows the processing of thickness/concentration/material variations from sample to sample within one run.
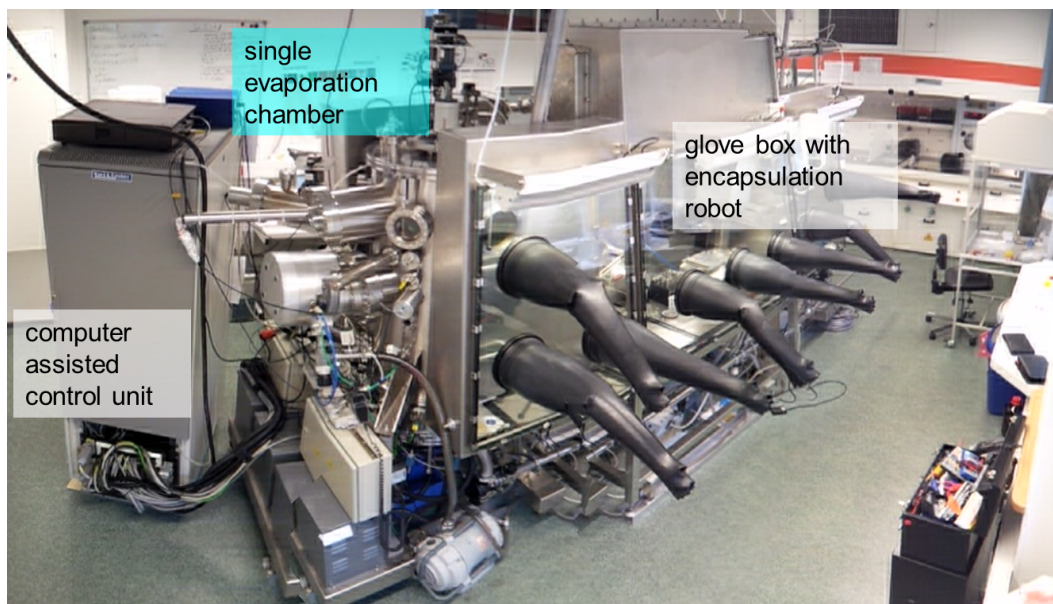
Figure 5.10: Photograph of the single evaporation chamber "Lesker A". The advantage compared to the UFO2 is the possibility to process 16 different OLEDs within one run. This ensures a high comparability.
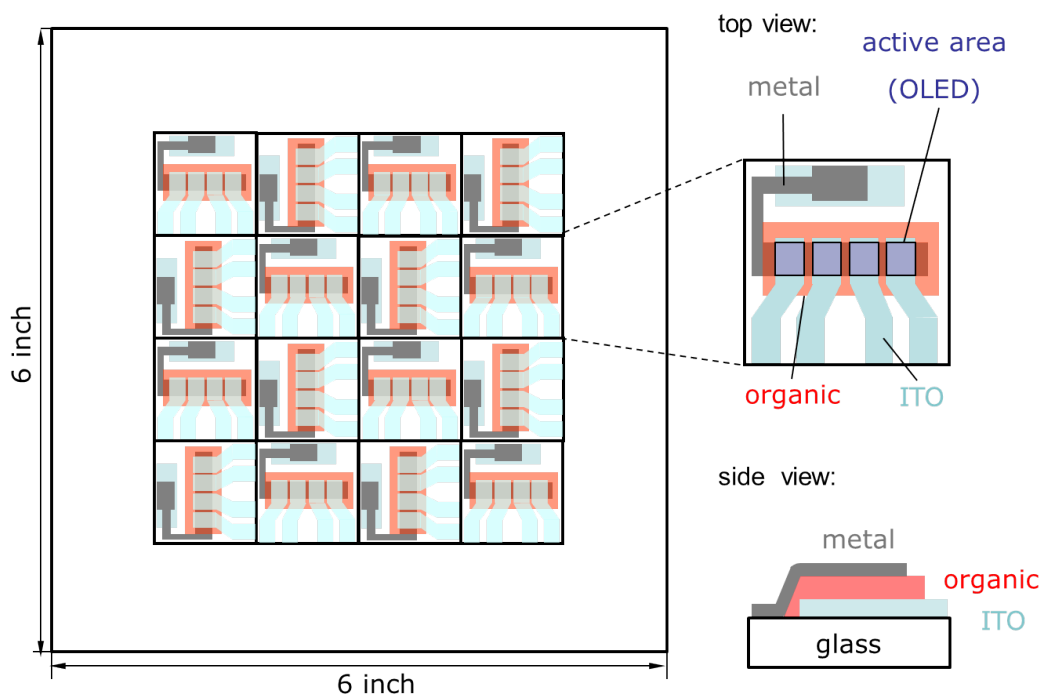
Figure 5.11: Layout of a Lesker OLED wafer. A single sample of a size of 1 x 1 inch is shown in the enlarged section on the right. Due to the pre-patterned ITO electrode, there are four identical OLEDs on one single sample.

Furthermore, the wafer rotates during evaporation leading to a more homogenous layer thickness. The thickness deviation from the center to the corner ranges between 8% to 12%[187]. Hence, OLED processing is taking place only in the 4 x 4 inch inner quadrangle to ensure a thickness gradient $< 3\%$.[188]

Figure 5.11 shows the layout of the samples when looking through the substrate side. A total of 16 samples, each with four (identical) pixels can be obtained. In Fig. 5.11 a single sample is also illustrated. It consist of the four pre-structured ITO-contacts, the organic material, and the metal evaporated on top. Similarly to the UFO2, structuring of the deposited layers is achieved using shadow masks. Finally, the overlap between the ITO area and the top contact defines the active area (6.49 mm^2).

Sample encapsulation

To protect the devices against moisture and air, all OLEDs are encapsulated in the glovebox under nitrogen atmosphere directly after processing. The encapsulation glass consists of a small cavity which includes a getter material. The cavity prevents a direct contact between the evaporated layers and the encapsulation glass. Hence, scratching or damaging of the devices are avoided. The encapsulation glass is attached to the substrate using an epoxy resin (XNR5516Z-L and XNR5590, Nagase Europa GmbH).

5.3   OLED Characterization

After processing, the OLEDs were in most cases characterized within a time span of < 24h. In the following, the most important measurement setups for OLED characterization are explained.

5.3.1   IVL and Spectral Emission

The current-voltage-luminance characteristics (IVL) of OLEDs are recorded with a measurement robot (Fig. 5.12 (a)) from Novaled AG. The whole setup is computer controlled and the measurement is done in an automated fashion. Therefore, the sample/wafer is placed into a moveable tray. Using a SMU2400 (Keithley), the current-voltage characteristic is measured. The luminance in forward direction L_{v}^0 as a function of the current I is recorded with a fast Si-photodiode. A spectrometer (CAS100A, Instrument Systems GmbH) measures the spectral radiance $L_{\mathrm{e}}^0(\lambda)$ at a defined luminance L_{v}^0 (typically at approx. 1,000 cd/m^2).

Before the measurement of a sample, a positioning calibration is performed. Here, the sample luminance is measured while scanning over one OLED pixel in x and y direction. This ensures that the pixel is in the middle of the focus of the spectrometer.

5.3.2   Angular Dependence

To obtain the viewing angle characteristics of OLEDs, a custom-made, computer controlled spectro-goniometer setup is used (Fig. 5.12 (b)).[189] A single sample is therefore mounted on a rotary table (OWIS GmbH) and a positioning is performed to ensure that the active area is placed in the center of rotation. The current and voltage to drive the device are applied via a Keithley SMU2400. A USB4000 fiber optics spectrometer (OCEAN OPTICS) is used to measure the spectral irradiance $E_e(\lambda, \vartheta)$. The setup allows an automatic recording of the spectra for different viewing angles ϑ. For all OLEDs, the angular dependence is measured in 5° steps from 0° to 90°. From the spectral radiance $L_e^0(\lambda)$ measurement at the IVL robot, the absolute spectral radiant intensity $I_e^0(\lambda)$ in forward direction can be calculated using Eq. (2.4). The calibration factor between E_e^0 and I_e^0 is further used to calculate $I_e(\lambda, \vartheta)$ by scaling the goniometer measurement.
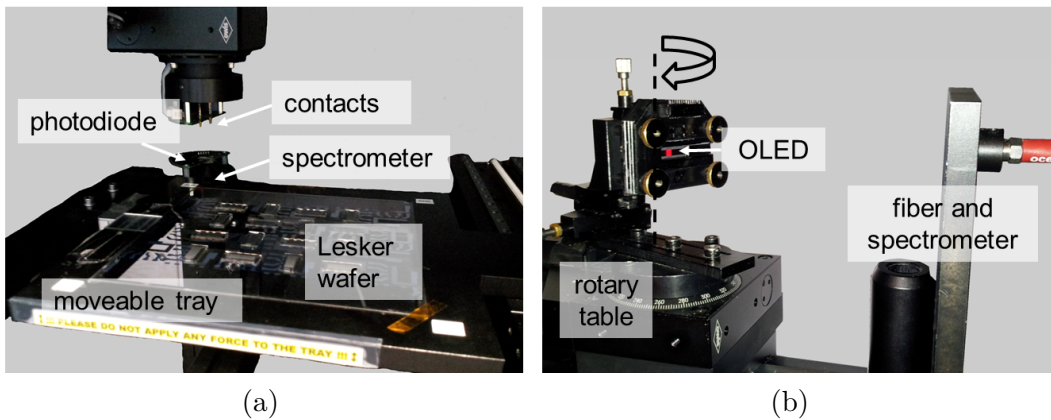
Figure 5.12: Photograph of the IVL robot (a) and the goniometer (b). The IVL characteristics and the spectral emission depending on viewing angle can be recorded in an automated fashion.

5.3.3   Efficiencies

For OLEDs there are three important efficiency terms: current efficiency (CE), external quantum efficiency (EQE), and luminous efficacy (LE). While the first one can be calculated from the forward emission of IVL robot measurements, the latter two require the integrated emission from the whole forward hemisphere. The direct method of determining the external quantum efficiency and luminous efficacy is the measurement in an integrating sphere (EQE^S, LE^S). This method is widely used within the OLED community especially if absolute values are important. Alternatively, the efficiencies can be calculated using (i) the forward emission intensity and the Lambertian assumption (EQE^L, LE^L) or (ii) the angular dependent spectral radiant intensity from goniometer measurement (EQE, LE). All three methods will be described in the following.

Integrating sphere

An ISP 500 Ulbricht sphere (Instrument Systems GmbH) at Novaled AG (Dresden) is available for measuring device efficiencies. Here, the OLED is mounted in the center of the sphere and the edges of the substrate are covered to avoid the recording of edge emission. The current and voltage to drive the OLED are applied via a Keithley SMU2400 and the spectral emission is recorded with a CAS140 CT (Instrument Systems GmbH)) spectrometer. The Ulbricht sphere allows the determination of the external quantum efficiency and luminous efficacy at a constant current density.

For outcoupling enhancement, a microlens array foil (Microsharp) with closed packed hemi-spherical lenses or alternatively a glass half-sphere (Biomedical Optics, n = 1.5, ø = 18 mm) can be attached on the glass surface using index matching oil (Zeiss, Immersol 518F, n = 1.52). It is important that a background and absorption correction is done whenever the integration time or the geometry of the setup has been changed.

However, due to the large sphere diameter (50 cm) the OLED needs to be driven at least at a forward luminance of 1,000 cd/m² and long integration times (> 30 s) are required to ensure a sufficient signal to noise ratio.[189] This makes the setup less suitable for standard device evaluation.

Current efficiency

The current efficiency η_{CE} is widely used in industry and is given by the forward luminance L_v^0 divided by the applied current density j:

$$\eta_{CE} = \frac{L_v^0}{j}. \tag{5.1}$$

The unit is candela per ampere [cd/A] and the current density j is given by the current I through the device divided by the area A:

$$j = \frac{I}{A}. \tag{5.2}$$

Since only the emission in forward direction is considered, the CE is of minor importance in this work.

External quantum efficiency

The external quantum efficiency η_{EQE} is defined as ratio of the number of emitted photons into air n_γ to the number of injected electrons n_e:

$$\eta_{EQE} = \frac{n_\gamma}{n_e}, \tag{5.3}$$

with:

$$n_e = \frac{I}{e} \text{ and } n_\gamma = \frac{1}{hc} \iint \lambda\, I_e\,(\Omega, \lambda)\; d\lambda\, d\Omega. \tag{5.4}$$

In the following, the EQE will be deduced with respect to the OLED geometry. Therefore, polar coordinates ϑ and φ as shown in Fig. 5.13 are used. The solid angle Ω can be written as:

$$\Omega = \iint \sin \vartheta\; d\vartheta\; d\varphi, \tag{5.5}$$

with ϑ spanning from 0 to $\pi/2$, and φ from 0 to 2π. Due to the symmetry of the system, the integration over φ can be executed and the spectral radiant intensity I_e reads:

$$I_e(\Omega, \lambda) = 2\pi\, I_e\,(\vartheta, \lambda)\; \sin \vartheta. \tag{5.6}$$

Finally, using Eqs. (5.4) and (5.6), the EQE reads:

$$\eta_{\text{EQE}} = \frac{2\pi e}{Ihc} \iint \lambda\, I_e\,(\vartheta, \lambda)\; \sin \vartheta\; d\lambda\, d\vartheta, \tag{5.7}$$

while assuming a Lambertian emission ($I_e = I_e^0 \cdot \cos \vartheta$), Eq. (5.7) reduces to:

Figure 5.13: The geometry of the OLED allows emission only into the forward half space. The polar coordinates ϑ and φ, and the symmetry of the system facilitate the calculation of the external quantum efficiency.

$$\eta_{\text{EQE}}^{\text{L}} = \frac{\pi e}{Ihc} \int \lambda\, I_e^0\,(\lambda)\; d\lambda. \tag{5.8}$$

As it can be seen from Eq. (5.8), the calculation of the EQE^L requires the spectral radiant intensity $I_e^0\,(\lambda)$. This is measured by the IVL robot for a constant luminance of approx. 1,000 cd/m². Hence, the EQE can only be calculated for a constant current. Using the $L_v^0 - I$ curve which is recorded with a fast Si-photodiode, the EQE can be derived as function of the current I. This is valid as long as the shape of spectral emission intensity curve is independent of the applied current, i.e. $I_e^0 \neq f\,(I)$. Furthermore, the angular dependent emission characteristics need to be constant with the applied current. While the latter requirement is met in most cases [189], the first one does not need to be fulfilled for white OLEDs. For example, white OLEDs consisting of multiple emitting layers mostly suffer a change of the spectral intensity curve with increasing current. The reason is that the exciton distribution changes with higher excitation energy (e.g. due to TTA), so emission intensities for different emitters are varying. However, recording the spectral emission with the slow

spectrometer would lead to a degradation of the device and cause a larger error than the method described above.

Using the radiant intensity $I_e(\vartheta, \lambda)$ at a constant current from the goniometer measurement, the EQE can be calculated using Eq. (5.7). The EQE-I curve is then obtained by scaling the EQE^L-I curve.

Luminous efficacy

The luminous efficacy η_{LE} describes the ratio between the emitted luminous flux Φ_v and the consumed electrical power P:

$$\eta_{LE} = \frac{\Phi_v}{P} = \frac{\Phi_v}{UI}. \tag{5.9}$$

Strictly speaking, η_{LE} is more a light yield than an efficiency. This can be also seen from the unit lumen per watt [lm/W]. Using Eqs. (5.6) and (5.9), the luminous efficacy is given by:

$$\eta_{LE} = \frac{2\pi K_m}{UI} \iint V(\lambda) \, I_e(\vartheta, \lambda) \, \sin\vartheta \, d\lambda \, d\vartheta. \tag{5.10}$$

Applying the Lambertian assumption leads to:

$$\eta_{LE}^L = \frac{\pi I_v^0}{UI} = \frac{\pi L_v^0 A}{UI}. \tag{5.11}$$

Equation 5.11 does not contain a wavelength dependent quantity. Hence, the LE^L-I curve can be simply obtained by the use of measured forward luminance L_v^0, voltage U, and current I from the IVL robot. Similar to the EQE, the LE at a constant current density can be calculated from the radiant intensity $I_e(\vartheta, \lambda)$ measured with the goniometer and Eq. (5.10). The LE-I curve is then obtained by scaling the LE^L-I curve.

5.3.4   Lifetime

The lifetime $t_{0.5}$ of an OLED is defined as the time after which the forward luminance L_e^0 decreases to 50% of its initial value. Here, the decrease is caused by the degradation of the emitters inside the electrically driven device. Besides the intensive research on improving devices efficiency, processes which cause the degradation in OLEDs are in the focus of investigation.[113, 190–193]

In this work, the lifetime is measured with the "Simple Lifetime" system (Novaled AG). It consists of a power supply to drive the OLEDs at a constant current. A photodiode is used to detect the forward luminance L_e^0 after certain time intervals. Due to the substrate layout, it is possible to apply a different current to each of the four OLED pixels facilitating the measurement. Details about the lifetime setup can be found in Ref. [194]

5.4   Time-Resolved Spectroscopy

Streak camera

For time- and wavelength-resolved measurements, a HPD-TA C5680 (high performance digital temporal analyzer) self-calibrated streak camera (Hamamatsu) is used.[195, 196] The working principle of the streak camera is shown in Fig. 5.14. The incoming photons strike a photocathode after crossing a slit and a lens system. Due to the photoelectric effect, electrons are emitted, magnified by a multichannel plate, and accelerated towards a phosphor screen. Hereby, the electrons pass through a quickly changing electric field generated by two electrodes. This leads to a sweeping of electrons across the phosphor screen and leads to a time resolved image. A monochromator in front of the streak camera ensures the wavelength resolution. Hence, the time resolution is seen on the vertical axis, while the wavelength is connected to the horizontal axis. The CCD camera behind the phosphor screen is used to measure and visualize the streak pattern. The streak camera offers a wide range of time windows, reaching from ns to the ms regime.
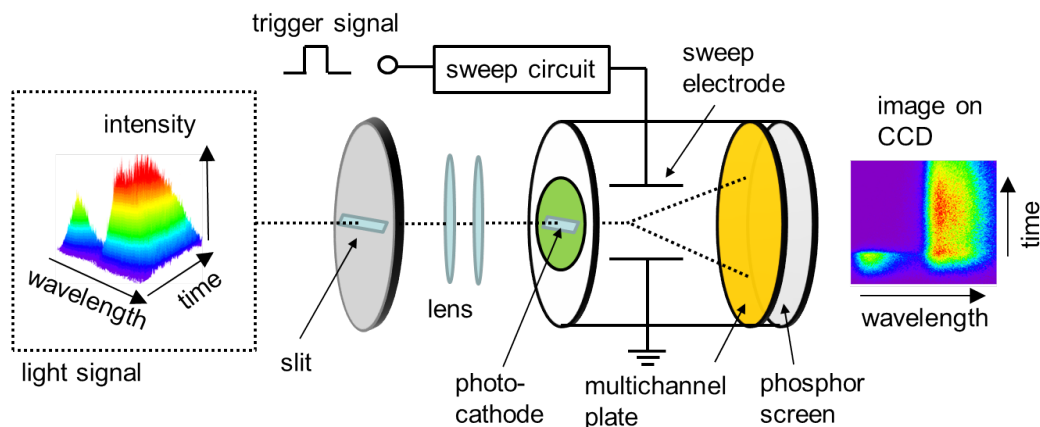
Figure 5.14: Schematic illustration of the working principle of the streak camera. The incoming photons generate electrons when hitting the photocathode. The changing electric field between the electrodes leads to a sweeping of the electrons across the phosphor screen. The time resolution is seen on the vertical axis, while the wavelength is connected to the horizontal axis.[196]

In order to record periodic events, the streak camera is triggered with C4792 trigger unit (Hamamatsu). All streak camera images in this work are background corrected. Furthermore, the response of the monochromator and the CCD are wavelength dependent. This makes it necessary to apply an additional shading correction.[197]

Setup for time-dependent measurements

In order to investigate the time-dependent spectral emission of OLEDs, a configuration as shown in Fig. 5.15 is realized. This setup will be used later to investigate the triplet harvesting process in OLEDs (Chapter 6). A 8114A pulse generator (Hewlett Packard) is used to excite the OLED with a voltage pulse. At the same time this pulse is used to trigger the streak camera. The emitted light from the OLED passes a slit and is focused on the monochromator using a lens system. The time and spectrally resolved intensity is recorded with the streak camera.
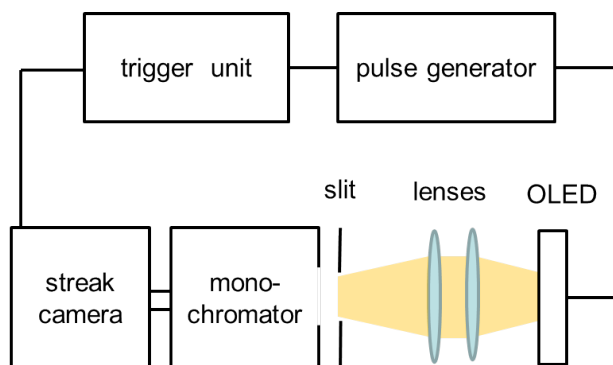
Figure 5.15: Setup for time-dependent spectroscopy of OLEDs. A pulse generator is used to excite the OLED electrically and to trigger the streak camera. With a lens system, the light emitted from the OLED is focused on a monochromator which is placed in front of the streak camera.

5.5 Photoluminescence Setup

The PL setup is shown schematically in Fig. 5.16 and will be used for quenching experiments (Sec. 7.2) to study the singlet diffusion length. The excitation source is the 325 nm UV wavelength of a He-Cd continuous wave (cw) laser (KIMMON, IK series). The substrate is mounted on a translation stage (Thorlabs) to be moved in lateral direction to the laser. This is convenient for the measurement, since sample and reference are on the same substrate. Optionally, neutral density (ND) filters (Thorlabs ND03A, ND05A, and ND10A) can be inserted between the laser and the sample to vary the excitation intensity. The PL emission of the sample is recorded with a calibrated fiber optics USB4000 spectrometer (OceanOptics). A long wave pass filter (laser filter) with a transmission edge at 395 nm (Melles Griot, CG-GG-395-25.QM-1) is mounted between the substrate and the spectrometer to avoid damage to the CCD camera of the spectrometer by the laser. A power meter (Newport, 1935-C) is used to measure the absolute power of the laser at the substrate position.
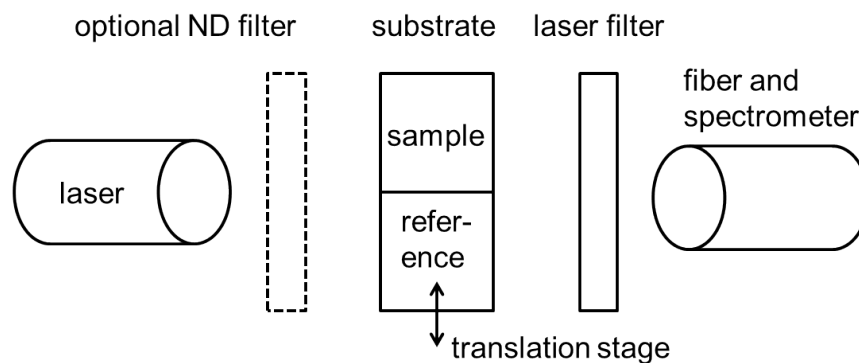
Figure 5.16: Setup for photoluminescence measurements. The sample is excited with a UV cw-laser and its emission can be recorded via a spectrometer. A neutral density filter can optionally be inserted to vary the excitation intensity. The laser filter is important to avoid damage of the spectrometer. Using a translation stage the sample can be moved in lateral direction to the laser.

5.6   Theoretical Calculations

5.6.1   Optical Simulation of OLEDs

In this work the simulation tool SimOLED[9] is used for optical simulations. It is based on the Maxwell equations, thin film optics, and transfer matrix formalism to simulate the optical effects inside an OLED cavity. The emitting molecules are treated as randomly distributed dipoles in a one-dimensional multilayer structure.[198]

As input parameters, the layer sequence, the layer thickness, the optical constants of the used materials (refractive index n and extinction coefficient κ) [199], the photoluminescence spectrum of emitter molecules and the position of radiating dipoles within the layer structure are required. SimOLED than calculates values in arbitrary units for the emission affinity, the spectral radiant intensity, CIE color coordinates, as well as for the photon flux PF and luminous flux LF:

$$PF = \frac{2\pi}{hc} \iint \lambda \, I_{e}\left(\vartheta, \lambda\right) \, \sin\vartheta \, \mathrm{d}\lambda \, \mathrm{d}\vartheta, \text{ and} \tag{5.12}$$

$$LF = 2\pi K_{m} \iint V\left(\lambda\right) I_{e}\left(\vartheta, \lambda\right) \, \sin\vartheta \, \mathrm{d}\lambda \, \mathrm{d}\vartheta. \tag{5.13}$$

It has been shown several times that the software is able to simulate and to some extent predict the angular dependent spectral emission for different types of real pin-OLED devices.[13, 200–202]

Since SimOLED uses a classical description of the emitting dipoles, it is not suitable to calculate absolute values for outcoupling efficiency and the internal quantum

---

[9]Mauro Furno has also developed the code for SimOLED and OLEDPower at the IAPP. He now works at Novaled AG (Dresden).

efficiency. These calculations are done by Mauro Furno using a quantum physical model that is numerically implemented in the software OLEDPower.[13]

5.6.2   Calculation of Molecular Orbitals

All theoretical calculations of molecular properties are performed by Regina Luschtinetz at the *Institut für Physikalische Chemie und Elektrochemie* (TU Dresden). It would be beyond the scope of this work to describe the different methods. For details, the reader is referred to Refs. [58–62].

The abbreviations of the methods used in this thesis are summarized in Tab. 5.2. Five possibilities to calculate the energy levels of molecular orbitals are applied: (i) HF // B3LYP, (ii) B3LYP // B3LYP, (iii) HF // TD-SCC-DFTB, (iv) SCC-DFTB // B3LYP, and (v) SCC-DFTB // TD-SCC-DFTB. Here, the first term denotes the method used to optimize the geometry of the molecule and the second term is the method used to calculate the energy levels.

The used software for geometry optimization are Gaussian03[203] (B3LYP,HF), DFTB+[204] (SCC-DFTB), and NG-DFTB[205] (TD-DFTB). The geometry of the molecule itself is constructed via the software MOLDEN[206], and the program VMD[207] is used to visualize the molecular orbitals resulting from the DFTB calculations.

Table 5.2: Abbreviations of the used theoretical models for calculating molecular properties.

abbreviation	method
HF	Hartree-Fock
B3LYP	hybrid-functional of Hartree-Fock and density-functional theory
SCC-DFTB	self-consistent-charge density-functional based tight-binding method
TD-SCC-DFBT	time dependent self-consistent-charge density-functional based tight-binding method

6 Triplet Harvesting

The choice of the blue emitter material is crucial to realize effective triplet harvesting in OLEDs. In this chapter, the fluorescent emitter 4P-NPD is investigated in detail. First, the orientation of the transition dipoles is determined using optical excitation of a single layer on the one hand, and by electrical excitation in an OLED structure on the other hand. As a next step, the triplet harvesting process using different phosphorescent emitters is studied and two-color white OLEDs are obtained. Furthermore, two new blue fluorescent emitters 8M-4P-NPD and 8M-4P-FPD are introduced and investigated in terms of triplet harvesting. Using 8M-4P-NPD, three-color white OLEDs are demonstrated where the green and red emission result from triplet harvesting.

6.1 The Emitter 4P-NPD

6.1.1 Orientation

Determination by optical excitation

Due to the stretched shape of the 4P-NPD (Fig. 6.1) molecule, a preferentially horizontal orientation of the emitting dipoles is likely. In a collaboration with the University of Augsburg (Germany), this issue is investigated. Therefore, a single layer of 10 nm 4P-NPD on glass is excited with a 375 nm laser. A glass half-sphere is mounted on the glass substrate and the angular (from 0° to 90°) and polarization dependent PL emission is measured. Details about the measurement method can be found in Ref. [136].
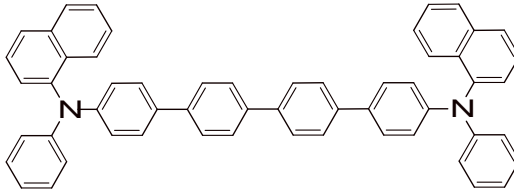
Figure 6.1: Molecular structure of 4P-NPD. Due to the elongated shape, it is expected that the transition dipoles show a preferred horizontal orientation.

The analysis of the p-polarized light yields information about the number of vertical and horizontal dipoles. The simulation of the PL spectra for completely horizontal and completely isotropic orientation, as well as the experimentally obtained spectra are shown in Fig. 6.2. Comparing the simulation results, a change in orientation is preferentially seen at high viewing angles (45° to 80°). Since vertical dipoles emit preferentially at large viewing angles, the emission at these angles is reduced for completely horizontal orientation (Fig. 6.2 (a) and (b)). It can be clearly seen that the experimental data (Fig. 6.2 (c)) implies an orientation somewhere between random and horizontal.
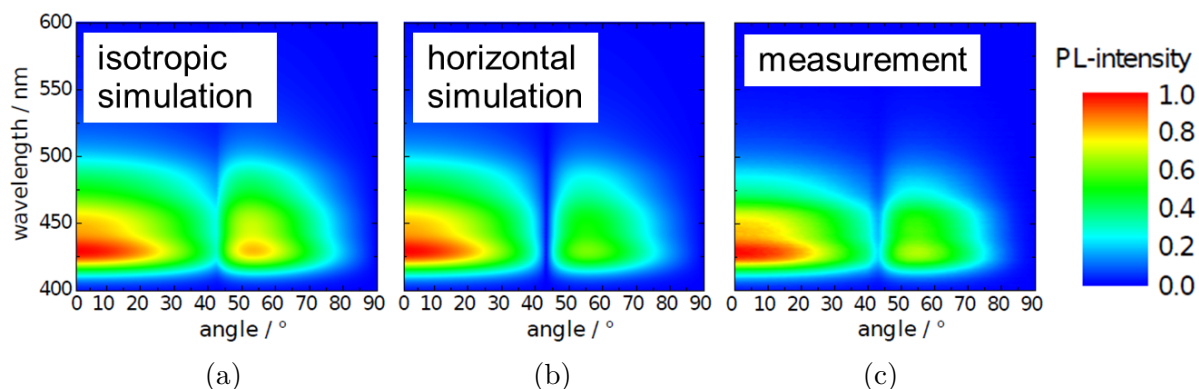
Figure 6.2: Simulated emission spectra for completely isotropic (a) and completely horizontal orientation (b) of the 4P-NPD molecules. Comparing the simulation results, a change in orientation is preferentially observed at large viewing angles (45° to 80°). Relating the measured p-polarized spectra (c) to the simulated spectra indicates that the 4P-NPD transition dipole moments are primarily horizontally oriented.
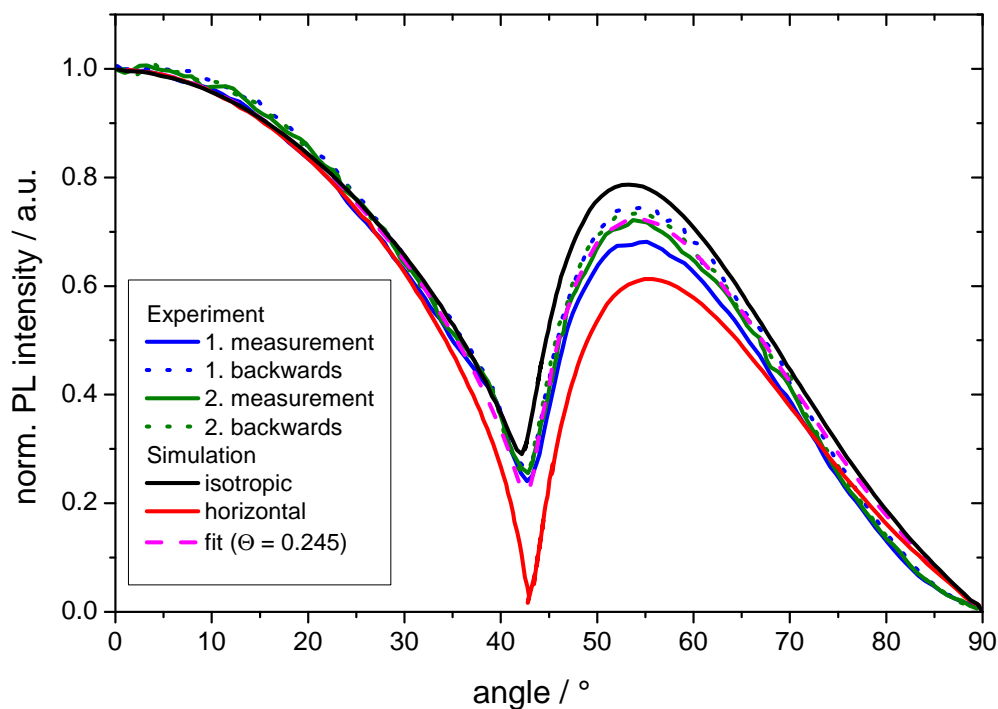
Figure 6.3: Cross section of the p-polarized measured spectrum at 420 nm. The differences between first and second measurement, as well as the forward (0° to 90°) and backward measurements (90° to 0°) are due to intrinsic degradation of 4P-NPD during the measurement. By fitting the second measurement, an anisotropy factor of $\Theta = 0.245$ is obtained.

To estimate the anisotropy factor Θ, the cross section through the plots in Fig. 6.2 is taken for a constant wavelength and the simulation is fitted to the measured data using Θ as free parameter (Fig. 6.3). By this means, $\Theta = 0.245$ at 420 nm and $\Theta = 0.222$ at 430 nm are found indicating a preferentially horizontal orientation of the 4P-NPD transition dipoles. However, degradation of 4P-NPD during the measurement was observed. This can be seen, not only by the repeated measurement, but also if the spectra are measured in backward direction from 90° to 0°. The degradation of 4P-NPD means that the intensity at high viewing angles is reduced compared to the case when no degradation would be present. This shifts the measured data towards the simulated curve of horizontal orientation. Thus, degradation of a 4P-NPD during the measurement leads to an overestimation of the number of horizontal dipoles.

It is worth noting that the extracted anisotropy factors have to be taken with care, since these results were not reproducible. In repeated experiments, i.e. for different 4P-NPD films, the material showed a preferentially random orientation. The reason might be different processing parameters (evaporation temperature, evaporation rate, pressure, rotation of the substrate), since in the first experiment the sample has been processed in the UFO2 and for the latter experiment the sample was processed at Lesker A.

Determination by electrical excitation

It is further possible to determine the dipole orientation by using electrical excitation of the material under investigation within an OLED structure. Since the growth of material and hence the alignment of the emitting dipoles may depend on the underlying materials, this method is seen as more meaningful compared to the previously described measurement of the PL-spectra of a single layer. Details about the electrical excitation method are described in Refs. [134, 135, 140]. Again the analysis of the p-polarized light yields information about the number of vertical and horizontal dipoles.

Using the goniometer setup (described in Sec. 5.3.2), the p-polarized angular dependent emission of an OLED containing 4P-NPD as EML is measured (Fig. 6.4 (d)). Here, the transport layer thicknesses are chosen to place the emitter into the optical minimum (Fig. 6.4 (b)), where the relative contribution of the TM modes emitted from vertical dipoles (and coupled into air) to the overall emission is relatively high, thus enabling a precise determination of the number of vertically oriented dipoles.

The smallest deviation between the measured emission intensities and simulated intensities is obtained for $\Theta = 0.14$.[10] However, comparing the emission patterns the difference between experiment and simulation remains rather large (Fig. 6.4 (d) and (e)). Especially the emission in the range of 450 to 500 nm is not sufficiently well reproduced by the simulated spectra. The main reason is most likely the degradation of 4P-NPD during the measurement.

---

[10]Measurement and simulation are performed by Philipp Liehm at the IAPP.

To obtain a sufficient signal to noise ratio, the driving current needs to be as high as 46.2 mA/cm² in this experiment. The goniometer measurement from 0° to 90° in 1° steps takes 605 s. However, at 46.2 mA/cm² the lifetime of 4P-NPD OLEDs is only 437 s (Fig. 6.4 (c)).
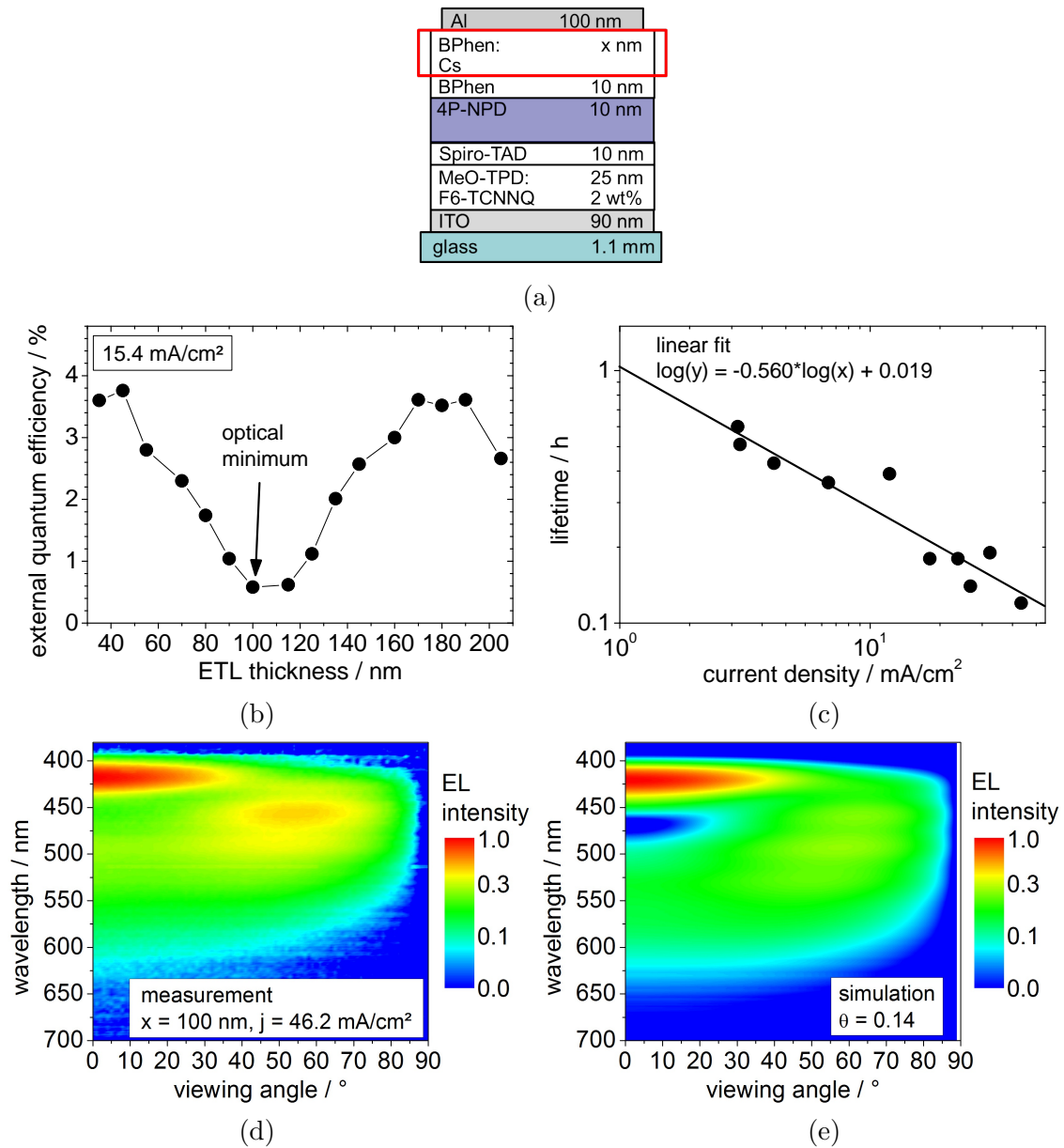
Figure 6.4:   Layer architecture of the OLEDs used to determine the optical minimum experimentally (a), EQE versus ETL thickness (b), lifetime versus current density (c). The measured p-polarized spectral emission (d) exhibits a strong deviation from the simulated emission pattern (e) for which an anisotropy factor of $\Theta = 0.14$ reveals the best fit. The spectral deviation between experiment and simulation is mainly attributed to the degradation of the 4P-NPD OLED during the goniometer measurement. For better visualization, a logarithmic intensity scale is used (d,e).

As in the previous experiment using optical excitation, degradation of 4P-NPD remains a major problem, when determining the orientation. A possibility to overcome this issue is the correction of the angular dependent emission intensity using a time dependent intensity curve. This will be presented in the next subsection.

Electrical excitation using lifetime correction

Since the luminance drop over time is not simultaneously recorded during the goniometer measurement, a simple exponential decrease of the luminance is assumed. To take the degradation of 4P-NPD into account, the measured spectral radiant intensity $I_e(\vartheta, \lambda)$ (data shown in Fig. 6.4 (d)) is corrected using:

$$I_e^{corr.}(\vartheta, \lambda) = I_e(\vartheta, \lambda) / \left(\frac{1}{2}\right)^{-\frac{t}{t_{50}}\frac{\vartheta}{90°}}, \tag{6.1}$$

with $t = 605$ s and $t_{50} = 437$ s. The result is presented in Fig. 6.5 (a). The lifetime correction of the intensity leads to enhanced emission at higher viewing angles (later times) (cf. Fig. 6.4 (d)).

An anisotropy factor of $\Theta = 0.32$ offers the best fit to the corrected data (Fig. 6.5 (b)). This suggests an isotropic orientation for 4P-NPD. Like in the PL experiment, degradation induces an overestimation of the number of horizontal dipoles. However, a comparison to the simulated intensity pattern using $\Theta = 0.24$ (as derived from PL experiments) shows only very small differences (red marked in Fig. 6.5). While region 1 fits better to $\Theta = 0.24$ (Fig. 6.5 (c)), regions 2 and 3 are in good agreement with $\Theta = 0.32$ (Fig. 6.5 (b)). It is therefore important to analyze the whole spectral region rather than a wavelength cross section.

Interestingly, the blue marked region 4 in Fig. 6.5 cannot be reproduced by any of the simulations. In the experiment the emission in this region is higher than expected from the simulation. This phenomenon is observed for several emitters and the origin of this problem is not fully understood.[140] It is believed that differences in emission result from insufficient knowledge of simulation parameters, like the recombination profile, which is generally assumed to be a delta-shaped profile. Also scattered light due to insufficient coverage of the sample might cause differences.

The emission pattern of the extreme cases of completely horizontal ($\Theta = 0$) and vertical ($\Theta = 1$) orientation are given in Fig. 6.5 (d) and (e), respectively. Comparing these cases to the experimental data, it can be nicely seen that the horizontal dipoles contribute mainly to the emission at small angles (0°-30°), while the vertical dipoles contribute mainly to emission at large viewing angles (30°-80°). In the end, the experimental data cannot be clearly assigned to one of two extreme cases, i.e. 4P-NPD does not have a completely horizontal or completely vertical orientation.
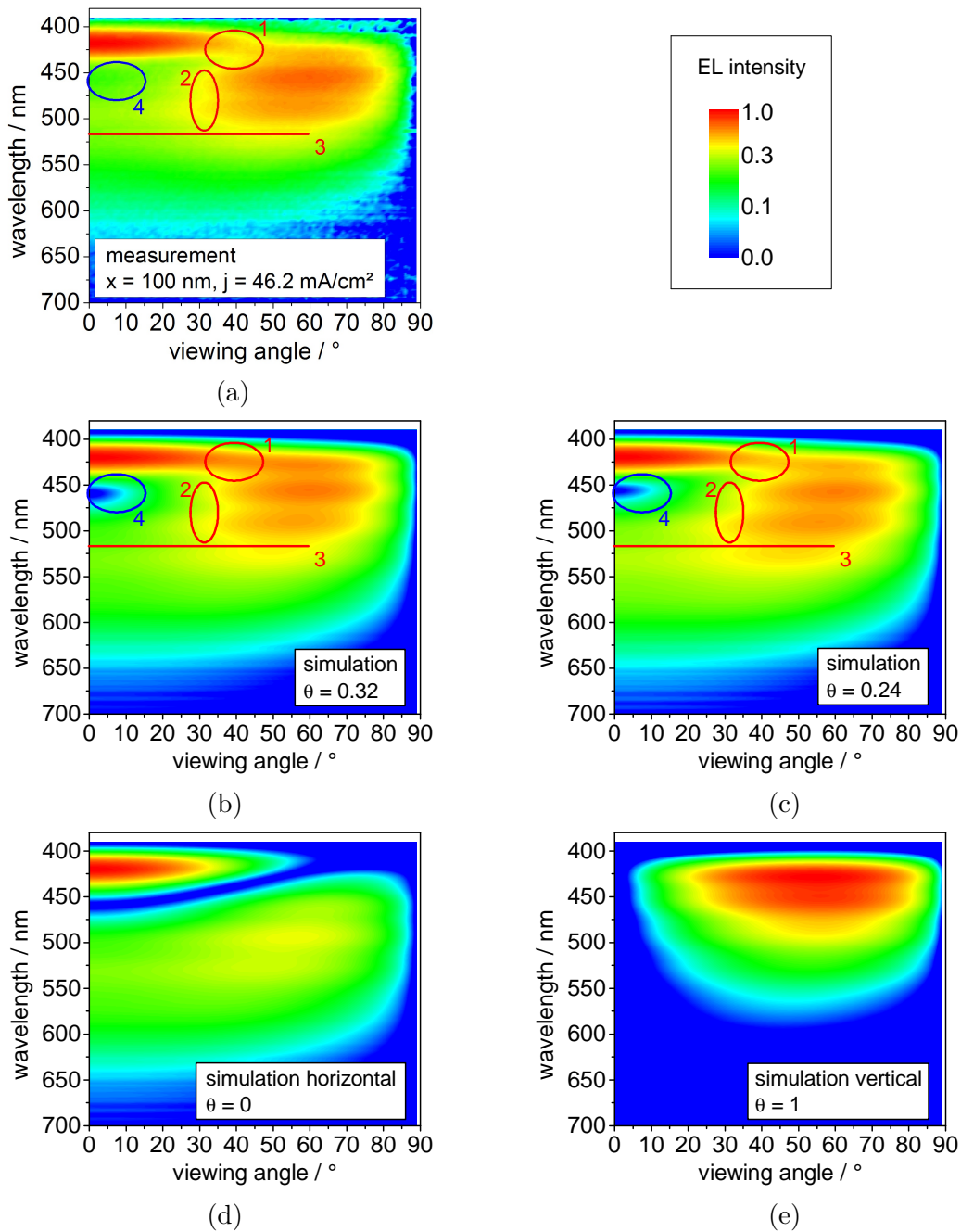
Figure 6.5: Lifetime corrected angular dependent emission pattern using Eq. 6.1 (a) for the 4P-NPD OLED with 100 nm ETL thickness (cf. Fig. 6.4 (a)) and simulated emission intensities for different dipole orientations (b-e). A logarithmic intensity scale is used for better visualization. An anisotropy factor of $\Theta = 0.32$ (b) yields the best fit to the experimental data. However, the spectral differences to $\Theta = 0.24$ (c), as derived from PL experiments, are rather small. For comparison, the simulated emission patterns of completely horizontal (d) and completely vertical (e) aligned dipoles is given.

Summary: Orientation of 4P-NPD

The orientation of 4P-NPD transition dipoles was studied by optical excitation of a single layer and electrical excitation inside an OLED structure. By comparing the experimentally obtained angular dependent emission intensities to simulation results, anisotropy factors of $\Theta_{PL} = 0.24$ and $\Theta_{EL} = 0.14$ were obtained, respectively. These results indicate a preferred horizontal orientation of 4P-NPD as expected due to the linear shape of the molecule. However, in both experiments degradation of 4P-NPD was observed, which did not only impede the determination of the orientation, but also led to an overestimation of the number of horizontal dipoles.

Using the lifetime measurement of the intensity, the OLED emission pattern were revised and $\Theta_{EL,corr.} = 0.32$ was obtained, i.e. 4P-NPD showed isotropic orientation. Nevertheless, this value has to be taken with care, since the emission pattern has also a spectral region which indicated a preferred horizontal orientation.

In 2011, Yokoyama *et al.*[139] reported a random dipole orientation for NPD, a material chemically differing from 4P-NPD only by two phenyl rings. Furthermore, they claimed that planar or linear shaped molecules show a preferred horizontal orientation. However, this could not be confirmed for 4P-NPD within this thesis.

6.1.2 Exciton Harvesting

As described in Sec. 4.6, TH is a suitable approach to design highly efficient white OLEDs. Therefore, the blue fluorescent emitter has to fulfill certain requirements. From previous studies it is known that 4P-NPD is a beneficial material for TH.[19, 102, 115, 163, 208] In Fig. 6.6, the principle of TH is shown, using 4P-NPD as bulk emitter and simultaneously as matrix material for a phosphorescent emitter.
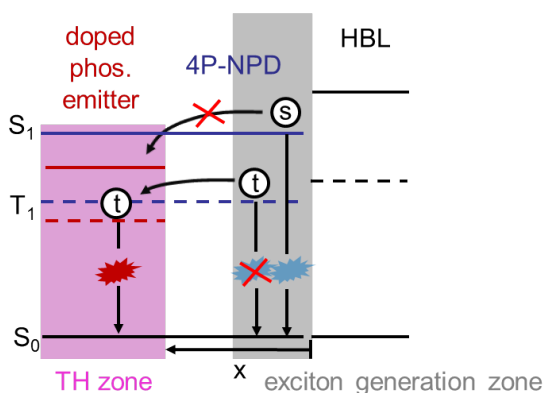
Figure 6.6: Principle of TH using 4P-NPD. Since 4P-NPD is primarily hole transporting, excitons are generated next to the HBL interface. Due to their long lifetime, triplets can diffuse towards a phosphorescent dopant and decay radiatively. The relatively short lifetime of singlets prevents a singlet transfer by applying a sufficient distance x between exciton generation zone and TH zone.

Due to the high hole mobility compared to the electron mobility ($\mu_h = 6.6 \cdot 10^{-4}$ cm²/Vs, $\mu_e = 3.6 \cdot 10^{-8}$ cm²/Vs)[115], exciton generation is expected to take place next to the hole blocking layer interface in OLEDs based on 4P-NPD emission layers. At the other side of the EML, 4P-NPD is doped with a phosphorescent emitter. Triplets formed at the HBL interface can then diffuse via Dexter transfer towards the phosphorescent dopant. If the triplet energy of the phosphorescent dopant is lower than that of 4P-NPD, triplets are harvested by the phosphorescent emitter. Singlets, on the other hand, have a shorter diffusion length compared to triplets due to their shorter lifetime. Thus, they do not reach the phosphorescent emitter and decay on the 4P-NPD molecules, generating blue emission.

To verify this principle, a series of TH OLEDs with different phosphorescent emitters (Ir(ppy)$_3$, Ir(dhfpy)$_2$(acac), and Ir(MDQ)$_2$(acac)) is investigated (Fig. 6.7 (a)). An OLED where the phosphorescent emitter is omitted is used as reference. A proposed energy diagram is given in Fig. 6.7 (b). As described previously, the exciton generation zone is close to the BPhen hole blocking layer. Due to the higher singlet and triplet energy of BPhen ($S_1 = 3.2$ eV, $T_1 = 2.5$ eV) compared to 4P-NPD ($S_1 = 2.9$ eV, $T_1 = 2.3$ eV), BPhen provides a sufficient energy barrier for both exciton species. Hence, excitons are not able to diffuse into the HTL. The triplet energies of Ir(ppy)$_3$, Ir(dhfpy)$_2$(acac), and Ir(MDQ)$_2$(acac) are 2.40, 2.23, and 2.02 eV, respectively.

Taking a triplet energy of 2.3 eV for 4P-NPD into account, TH should be possible using Ir(MDQ)$_2$(acac) or Ir(dhfpy)$_2$(acac). For Ir(ppy)$_3$, however, TH is not expected since the triplet energy of Ir(ppy)$_3$ is higher than that of 4P-NPD.

The IV-curves of the four OLEDs under investigation do not show any significant difference (Fig. 6.7 (c)). This indicates that the phosphorescent emitter plays a minor role concerning charge transport or direct recombination, i.e. the recombination of holes and electrons on the phosphorescent emitter. However, the LV-curves differ strongly: For Ir(ppy)$_3$, the luminance is decreased compared to the reference device, while for Ir(dhfpy)$_2$(acac) and Ir(MDQ)$_2$(acac) the luminance is strongly enhanced. This can be understood when considering the emission spectra (Fig. 6.7 (d)). The blue emission spectrum (400 to 525 nm) represents the emission from 4P-NPD (singlets). 4P-NPD emission is decreased for the OLEDs with a phosphorescent emitter compared to the reference OLED. This indicates singlet transfer to the phosphorescent emitter, resulting in reduced blue emission. Since singlet diffusion depends on the distance between exciton generation zone and the TH zone, i.e. the layer thickness of the intrinsic 4P-NPD, a variation of this distance/layer thickness can be used to verify this statement. This will be investigated in the next subsection.

Furthermore, additional emission in the yellow and red wavelength regime is observed for the Ir(dhfpy)$_2$(acac) and Ir(MDQ)$_2$(acac) OLEDs, respectively. Since direct recombination is excluded, this additional emission is a result of harvested excitons. This and the fact that the EQE is strongly enhanced for the Ir(dhfpy)$_2$(acac) and Ir(MDQ)$_2$(acac) OLEDs are strong indications for TH (Fig. 6.7 (f)).
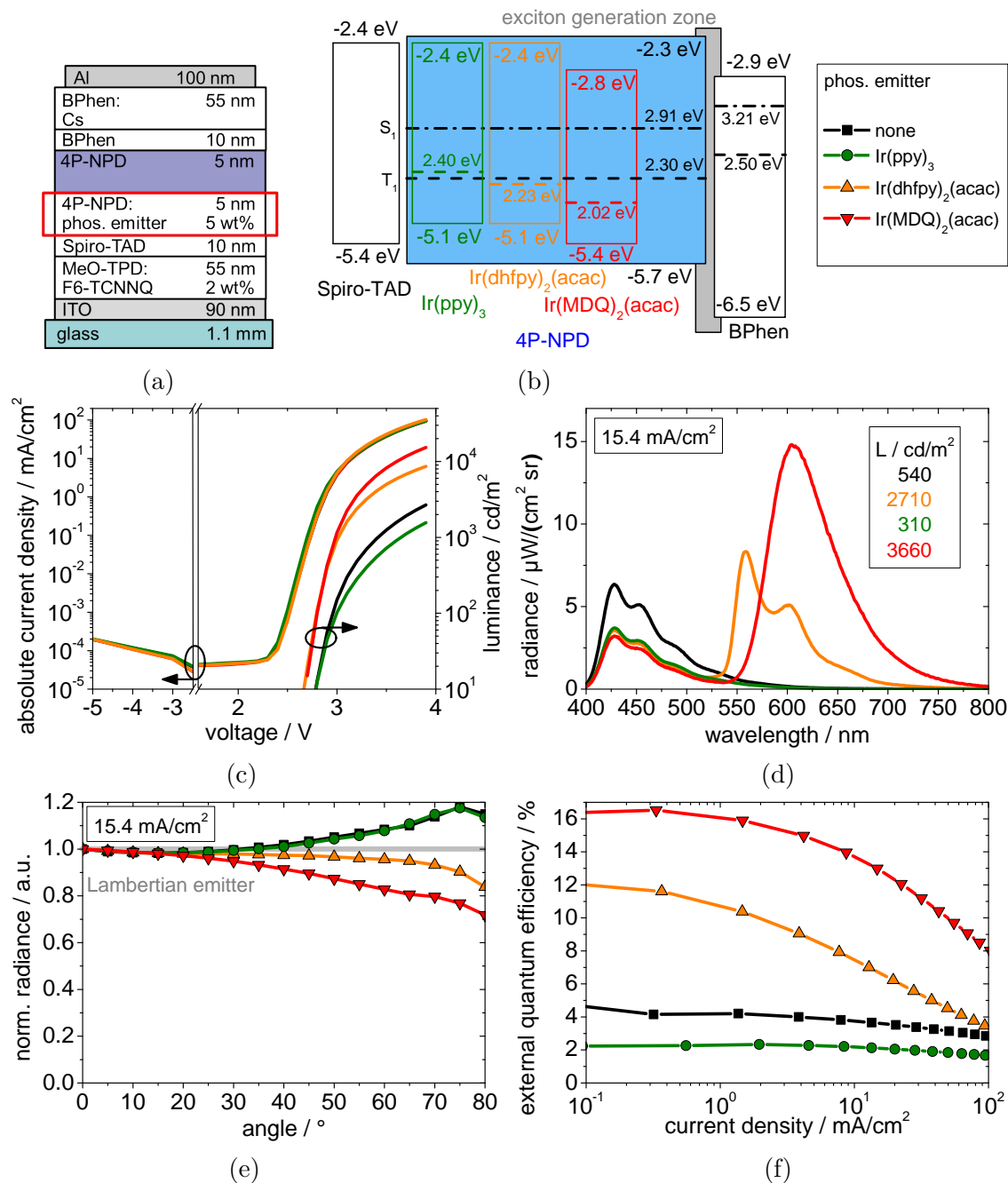
Figure 6.7: OLED layer structure (a), proposed energy level diagram (b) and performance (c-f) of the TH OLED using different phosphorescent dopants. Due to TH, OLEDs doped with $Ir(dhfpy)_2(acac)$ and $Ir(MDQ)_2(acac)$ show additional yellow and red emission (c), respectively, and the EQE (f) is strongly enhanced compared to the reference sample without the phosphorescent dopant. However, for the green emitter, no TH is observed since the triplet energy of $Ir(ppy)_3$ is higher than that of 4P-NPD (b).

In case of Ir(dhfpy)$_2$(acac), the EQE is more than doubled compared to the reference and for Ir(MDQ)$_2$(acac) the EQE shows a three fold enhancement at low current density. This is in agreement with the singlet/triplet ratio of 1/3 which, without taking wavelength dependent outcoupling efficiency into account, would lead to a three fold enhancement of the EQE in an ideal TH OLED. The difference in EQE between the two emitters can be assigned to different outcoupling efficiencies and IQEs.

As expected, additional emission and enhancement in EQE is not observed in case of the green emitter Ir(ppy)$_3$, since TH is not possible due to the energetic situation. The different emission spectra result in small changes of the radiance versus viewing angle characteristics (Fig. 6.7 (e)). Since the spectral emission is the same for the reference OLED and the Ir(ppy)$_3$ OLED, their curves are overlapping.

Thickness variation of the intrinsic 4P-NPD layer

As described previously, a distance variation between exciton generation zone and TH zone is helpful to prove TH. This variation is realized by an increase of the intrinsic 4P-NPD layer thickness x (cf. Fig. 6.6). The OLED layer structure and the spectral emission at a constant current density of 15.4 mA/cm² for different phosphorescent emitters are shown in Fig. 6.8. The emission of the reference OLED without the phosphorescent emitter is almost constant for all layer thicknesses. Only the $x = 3$ nm sample exhibits a slight decrease of the spectrum compared to longer distances.

In contrast, for all OLEDs with phosphorescent dopants, the 4P-NPD emission decreases steadily with decreasing distance. This can be explained by a singlet transfer to the phosphorescent dopant which is based on singlet diffusion and a Förster transfer from 4P-NPD to the phosphorescent emitter. It can be concluded that the singlet level of all phosphorescent emitters is lower than that of 4P-NPD (S$_1$ = 2.9 eV). Due to the high ISC rate of phosphorescent emitters, no emission from the singlet state occurs. Hence, the singlet energy level is generally difficult to extract. For Ir(ppy)$_3$ a singlet level of 2.6 eV[183] is reported which is below that of 4P-NPD.

Like in the previous experiment, the Ir(ppy)$_3$ OLED shows only 4P-NPD emission, but no emission of Ir(ppy)$_3$. Clearly triplets are not harvested by the Ir(ppy)$_3$ emitter due to its high triplet level. However, singlets transferred to Ir(ppy)$_3$ will be further transferred to the triplet level of Ir(ppy)$_3$ and should end up in Ir(ppy)$_3$ emission. Since Ir(ppy)$_3$ emission is not observed, it can be concluded that the Ir(ppy)$_3$ triplets resulting from diffusing 4P-NPD singlets are back-transferred to the triplet level of 4P-NPD. A scheme of the proposed exciton transfer processes is shown in Fig. 6.9 (a). The incorporation of Ir(ppy)$_3$ is beneficial to study the singlet diffusion length in 4P-NPD. The effects of these distance dependent quenching experiment are presented in Sec. 7.1.

(a)

(b)

(c)

(d)

(e)
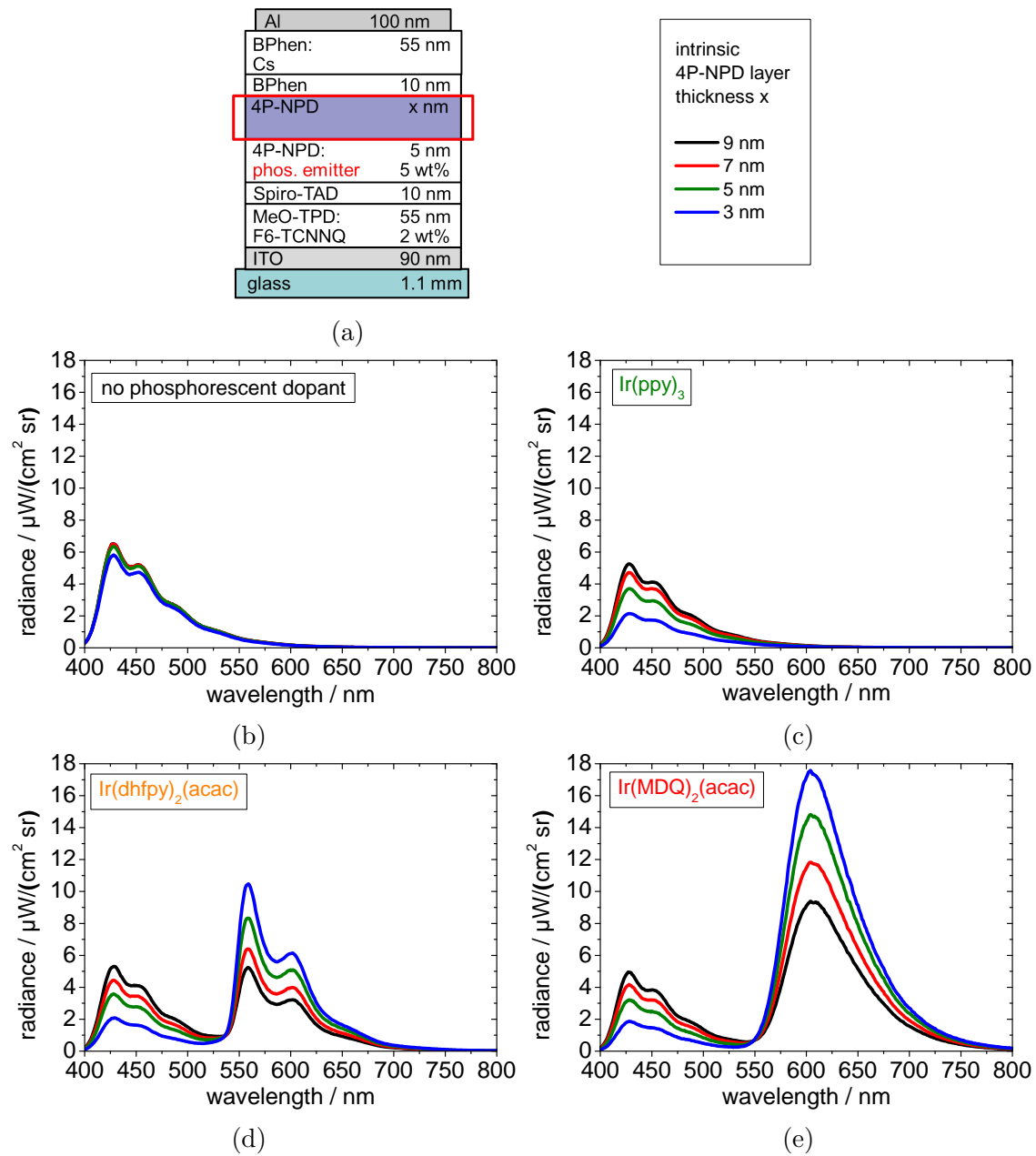
Figure 6.8: OLED layer structure (a) and emission spectra at 15.4 mA/cm² for varying intrinsic 4P-NPD layer thickness x and different phosphorescent emitters (b-e). While the sample with no phosphorescent dopant shows a constant 4P-NPD emission spectrum (b), the 4P-NPD emission decreases steadily with decreasing layer thickness if a phosphorescent emitter is incorporated (c-e). For the OLEDs doped with Ir(dhfpy)$_2$(acac) and Ir(MDQ)$_2$(acac) the additional emission in the yellow and red wavelength regime increases with decreasing 4P-NPD thickness (d,e), which confirms TH.
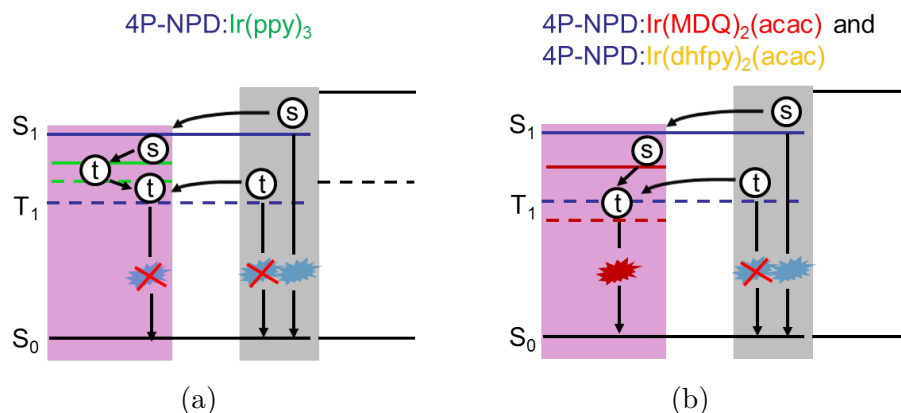
Figure 6.9: Exciton transfer processes in TH OLEDs incorporating the blue fluorescent emitter 4P-NPD and the phosphorescent dopants Ir(ppy)$_3$ (a) and Ir(dhfpy)$_2$(acac)/Ir(MDQ)$_2$(acac) (b). Due to the different positions of the energy levels, singlets reaching Ir(ppy)$_3$ are transferred to the nonradiative triplet state of 4P-NPD (a), while singlets and triplets reaching Ir(dhfpy)$_2$(acac)/Ir(MDQ)$_2$(acac) are transferred to the radiative triplet level of the phosphorescent emitter (b).

For Ir(dhfpy)$_2$(acac) and Ir(MDQ)$_2$(acac), the additional emission at higher wavelength decreases with increasing 4P-NPD thickness. Emission from Ir(dhfpy)$_2$(acac) or Ir(MDQ)$_2$(acac) resulting from a direct recombination was excluded in the previous experiment. Therefore, a diffusion based process such as singlet and triplet diffusion has to take place. Diffusive singlets which are converted into triplets when reaching the phosphorescent emitter cannot be transferred back to 4P-NPD, because the triplet level of the phosphorescent emitter Ir(dhfpy)$_2$(acac) and Ir(MDQ)$_2$(acac) is lower than that of 4P-NPD (cf. Fig. 6.7 (b)). Thus, they will end up in the emissive triplet state of the phosphorescent emitter (Fig. 6.9 (b)).

Finally, the design of an efficient TH OLED is a trade-off between singlet loss and triplet gain. Avoiding singlet losses due to diffusion would be possible if the phosphorescent emitter has a higher singlet energy than 4P-NPD. However, at the same time, the triplet energy has to be lower than that of 4P-NPD to realize TH. This means a phosphorescent emitter with a singlet-triplet splitting of > 0.6 eV is required. An emitter which fulfills these requirements is not known at present.

Also a singlet blocking layer between intrinsic 4P-NPD and the doped 4P-NPD layer would avoid singlet diffusion, but again, the blocking material would need a higher singlet-triplet splitting than 4P-NPD. Furthermore, it would be necessary to ensure that the hole transport is not effected by this blocking layer.

Time- and spectrally-resolved measurements

The changes in the emission spectrum of the previously described OLEDs comprising 4P-NPD and Ir(dhfpy)$_2$(acac) in response to short electrical pulses are investigated by time-resolved measurements using a streak camera. During electrical excitation, singlet and triplet excitons are generated at the same time. Due to the short lifetime of singlets, fluorescence of 4P-NPD is expected to decay relatively fast, and will be followed by the delayed and extended Ir(dhfpy)$_2$(acac) phosphorescence signal. The delay of the second signal is related to the triplet diffusion to the phosphor, i.e. by the distance x between the exciton generation zone and the TH zone. If TH is present, an increase of the distance x should result in an increased delay time.

In Fig. 6.10 (a) the time- and spectrally resolved emission following a voltage pulse (3.6 V for 2.5 µs) is shown for a device containing 4P-NPD and Ir(dhfpy)$_2$(acac) (OLED layer structure is given in Fig. 6.8 (a)).

(a)   (b)
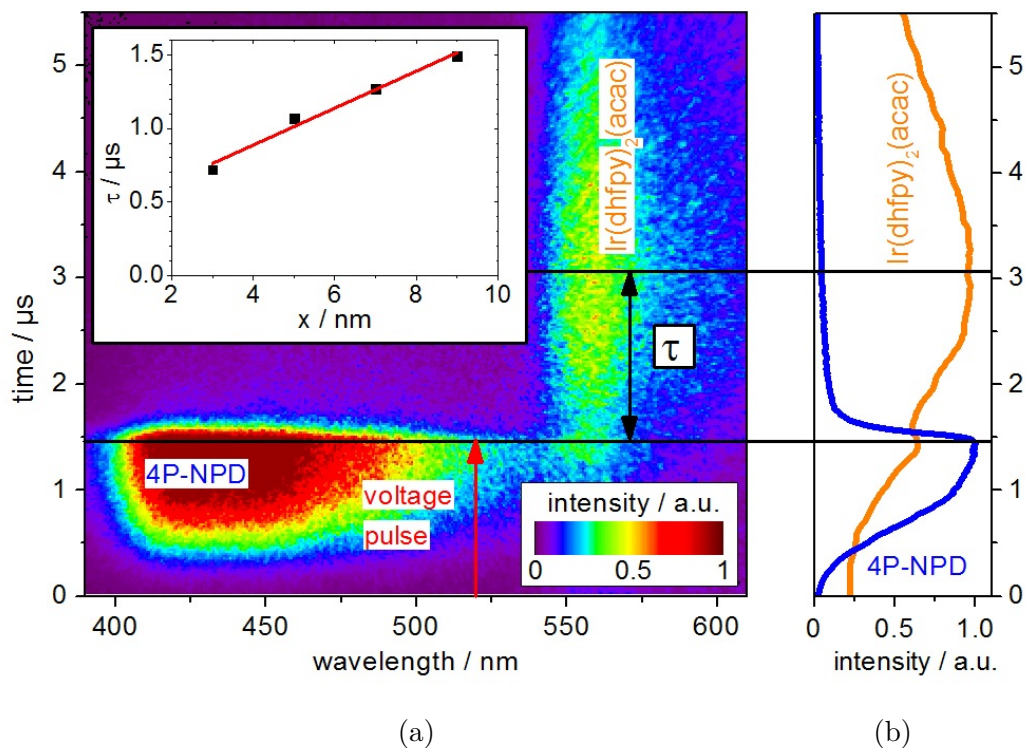
Figure 6.10: Normalized time- and spectrally-resolved intensity (a) after application of short electrical pulses (red arrow) of 2.5 µs and 3.6 V to the 4P-NPD:Ir(dhfpy)$_2$(acac) OLED shown in Fig. 6.8 (a) with a 4P-NPD layer thickness of $x = 9$ nm and normalized integrated intensity for both emitters (b), obtained by integrating the 390 nm to 540 nm and 540 nm to 610 nm wavelength range, respectively. The delay time τ is defined as the time between the emission maxima. Inset: delay time τ versus 4P-NPD layer thickness x. The delay time τ increases linearly with increasing distance x, which is further evidence for the presence of TH.

Both emitters can be distinguished not only by wavelength, but also by their different transient behavior after the pulse is switched off. Emission at small wavelengths shows a short decay and can be attributed to 4P-NPD; the signal at longer wavelengths is characterized by a slow decay and is associated with $Ir(dhfpy)_2(acac)$ emission. Integrating the measured intensity of the two different wavelength regimes (from 390 nm to 540 nm for 4P-NPD and 540 nm to 610 nm for $Ir(dhfpy)_2(acac)$), temporal profiles for each emitter (Fig. 6.10 (b)) are obtained.

The delay time τ is defined as the time between the maximum emission intensity of the fluorescent and phosphorescent emitter. For $x = 9$ nm, a delay time of $\tau = 1.5$ µs can be found. As expected, the delay between fluorescent and phosphorescent signal increases with increasing distance x (inset in Fig. 6.10 (a)), which is further evidence for the presence of TH. This is also in good agreement with the results of Kondakova *et al.*[21]. They obtained as well a linear behavior of the delay time for the emitters MQAB and $Ir(ppy)_2(pc)$ (cf. Sec. 4.4 and Fig. 4.9 (a)).

Interestingly, the emission of $Ir(dhfpy)_2(acac)$ shows an intermediate maximum at 1.4 µs (Fig. 6.10 (b)). It is difficult to clearly assign this peak to one of the emitters; on the one hand, emission from 4P-NPD is not zero at wavelengths larger than 540 nm and on the other hand, singlet transfer may lead to prompt emission from $Ir(dhfpy)_2(acac)$. Due to the short lifetime of singlets compared to triplets, the singlet transfer can be expected to occur at much shorter timescales than the triplet transfer. Further investigations would be necessary to quantify the amount of direct recombination events, transferred singlets, and harvested triplets.

6.1.3   Two-color white TH OLED

Since the use of two complementary colors exhibits the possibility to achieve white OLEDs, a detailed investigation of the TH system $4P-NPD:Ir(dhfpy)_2(acac)$ is presented in this section. In Sec. 6.1.2, it has been shown that a thickness variation of the intrinsic 4P-NPD layer can be used to vary the spectral contributions of each emitter. Figure 6.11 exhibits a closer look on the performance of these TH OLEDs.

For a constant voltage, increasing the intrinsic layer thickness of 4P-NPD leads to a continuous decrease in current density and, even more dramatically, in luminance (Fig. 6.11 (b)). The reduced current is attributed to a reduction in electric field within the thicker EML. The strong decrease in luminance can be explained by considering the change in emission spectrum between devices of this series (Fig. 6.11 (c)). The luminance is calculated using the V-lambda luminosity curve. The maximum of this curve is at 555 nm which almost matches the emission peak of $Ir(dhfpy)_2(acac)$ (557 nm). With increasing 4P-NPD layer thickness the emission of $Ir(dhfpy)_2(acac)$ and, as a result, the luminance decreases significantly. At the same time, blue emission from 4P-NPD increases but this affects the measured luminance to a lesser extent due to the small overlap of the blue emission with the V-lambda curve.

(a)

(b)

(c)

(d)

(e)

(f)
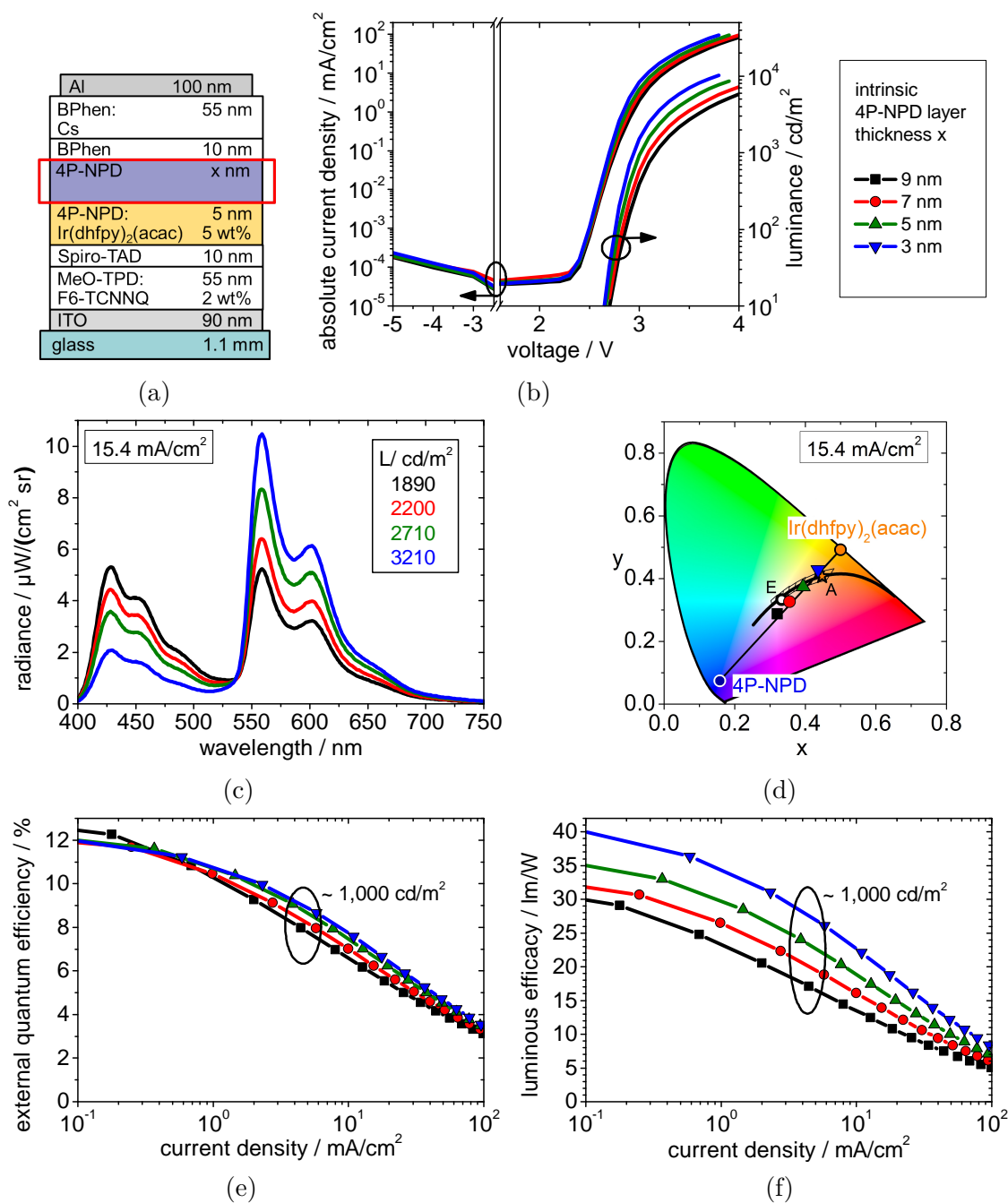
Figure 6.11: OLED layer structure (a) and performance (b-f) of the two-color white TH OLEDs for different 4P-NPD layer thicknesses. With increasing layer thickness the IV- and LV-curves become more flat (a). The different contribution of the blue and yellow emitter to the spectrum (c) allows the adjustment of the CIE color coordinates along the connection line between the color coordinates of the PL-emission of 4P-NPD and Ir(dhfpy)$_2$(acac) (d). At 1,000 cd/m^2, the OLEDs show EQEs and LEs in the range of 8% and 30 lm/W, respectively (e,f).

The spectral behavior can be explained when considering the singlet and triplet harvesting processes, which has been intensively discussed in Sec. 6.1.2. Interestingly, these spectral differences allow a shift of the CIE color coordinates among a line of the PL-emission of 4P-NPD and Ir(dhfpy)$_2$(acac) (Fig. 6.11 (d)). This is beneficial for the design of white OLEDs, since the color can be precisely adjusted. Emission close to the warm white color point A can be obtained for a 4P-NPD layer thickness of 3 nm and 5 nm.

The EQE and LE tend to decrease with increasing 4P-NPD thickness (Fig. 6.11 (e) and (f)). This behavior can again be understood by considering properties of TH: At small thickness, a larger number of triplets (and singlets) can diffuse towards Ir(dhfpy)$_2$(acac) and lead to additional yellow emission. When increasing the distance, triplets will undergo annihilation processes or decay non-radiatively before they reach Ir(dhfpy)$_2$(acac). Consequently, the efficiency will drop with increasing 4P-NPD thickness. This is also reflected in the roll-off of the different devices: The roll-off for the OLED with a 9 nm 4P-NPD layer is stronger than for the OLED with 3 nm, which is attributed to the longer diffusion path and bigger interaction volume for triplets. This is in contrast to the situation in phosphorescent monochrome OLEDs where thicker EMLs tend to reduce the roll-off. It is worth noting that the simple two color white OLED shows efficacies in the range of 30 lm/W at 1,000 cd/m² which is comparable to other state-of-the-art white OLEDs.

Dependence of the CIE coordinates on the applied current density

From an application point of view, it is important that the color does not change with the luminance, i.e. current density. As seen in Fig. 6.11 (d), the OLEDs with 4P-NPD layer thickness of 3 nm and 5 nm exhibit color coordinates which are close to the warm white color point A. For these OLEDs the CIE color coordinates are shown as function of the applied current density in Fig. 6.12. The corresponding luminance and CRI values are given in square brackets.

Increasing current density leads to a shift towards the blue region of the CIE diagram. This can be explained by the spectral emission (inset in Fig. 6.12). For comparison the spectra are divided by the applied current. While the blue emission is almost independent of the current density, the contribution of the yellow emitter decreases steadily. The reason is that, as typically for phosphorescent emitters, the triplets on the matrix or on the yellow emitter underlie stronger annihilation processes (TTA, TPA) than the singlets of fluorescent blue emitter. A reduction of the TTA and TPA annihilation rates would increase the color stability with applied current density. Nevertheless, for $x = 5$ nm the CIE coordinates remain almost within one chromaticity quadrangle for a wide luminance range (417 to 2714 cd/m²). This means that the color shift ($\Delta\text{CIE}_{417\rightarrow2714\,\text{cd/m}^2} = (0.04/0.05)$) cannot be perceived by the human eye (cf. Sec. 2.3).

A color rendering index in the range of 40 to 50 can be obtained by this simple two-color white OLEDs. However, this is too low for indoor lighting applications which require a CRI of > 75, but in good agreement with two-color white OLEDs realized by other groups. For example, Ho *et al.*[209] obtained CRI values from 50 to 60 for two-color white TH OLEDs.
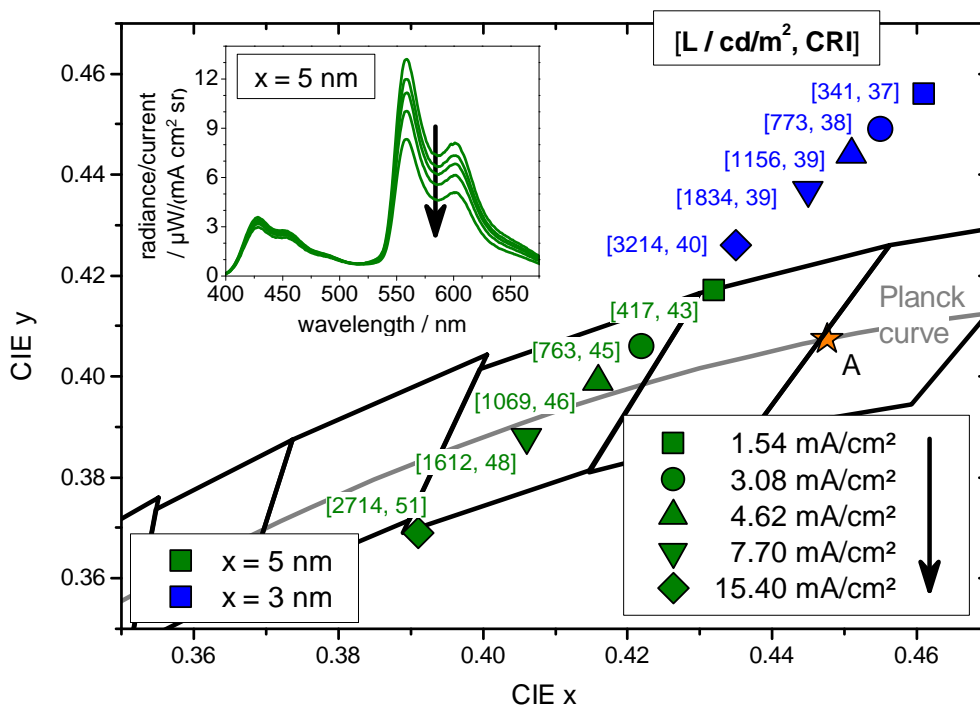
Figure 6.12: CIE color coordinates for the two-color white TH OLEDs at different applied current densities for 4P-NPD layer thicknesses of 3 and 5 nm, respectively. Corresponding luminance and CRI values are given in square brackets. For a wide luminance range (417 to 2714 cd/m²) the CIE coordinates of the OLED with $x = 5$ nm remain almost within one of the chromaticity quadrangles. Inset: spectral radiance divided by applied current for the OLED with $x = 5$ nm. While the blue emission is almost independent of the current density, the contribution of the yellow emitter decreases steadily.

Angular dependent emission and internal quantum efficiency

The spectral radiant intensity of the OLED with the 5 nm 4P-NPD layer is shown in Fig. 6.13 (a) for viewing angles between 0° and 80°. The spectra are taken at 15.4 mA/cm². With increasing viewing angle, blue and yellow emission decrease by similar amounts. Using optical simulations the spectra can be fitted (open circles). The agreement between simulation and experiment is remarkably good. The layer thicknesses used to fit the experimental data are the same as given in Fig. 6.11 (a), except for the HTL and ETL where values of 75 nm and 50 nm are assumed, respectively.

It is interesting to analyze the optical field profiles calculated at the peak emission wavelength of the emitters (428 nm for 4P-NPD, 557 nm for Ir(dhfpy)$_2$(acac)) at 0° (Fig. 6.13 (b)). The emitters are in very close proximity to their respective field maximum, indicating that at best a slight efficiency enhancement can be expected when further optimizing the transport layer thicknesses.

Furthermore, the radiance versus viewing angle characteristics are shown in Fig. 6.13 (c) for the TH OLEDs differing in 4P-NPD thickness. All devices exhibit nearly Lambertian emission characteristics with small differences at high viewing angles ($> 50°$). This confirms that the OLED structure is close to the optical efficiency maximum. These OLEDs have a negligible color shift with viewing angle (Fig. 6.13 (d)). For example, from 0° to 70°, the color shift of the CIE coordinates is $\Delta\mathrm{CIE}_{0°\to70°} = (0.02/0.01)$ for a 4P-NPD layer thickness of 5 nm.
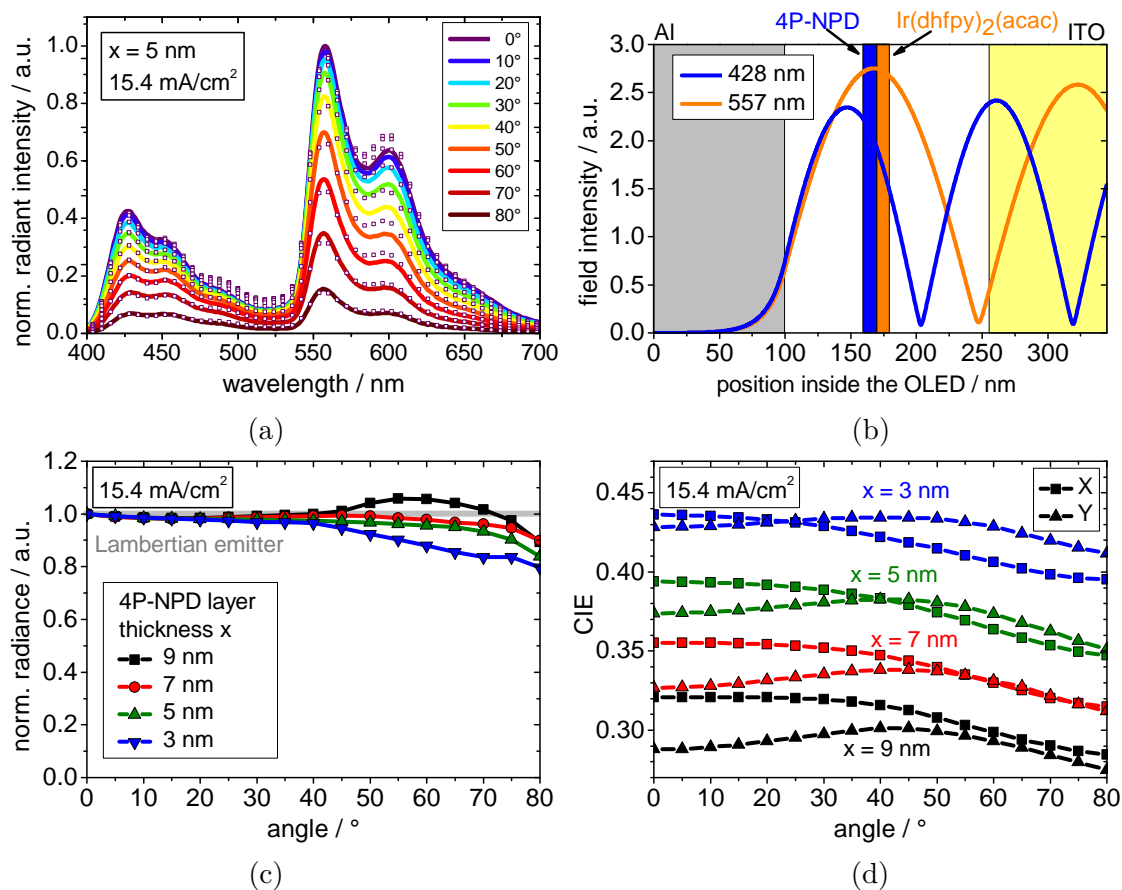
Figure 6.13: Measured (lines) and simulated (dots) spectral radiant intensity for viewing angles between 0° and 80° (a) and the corresponding simulated optical field profiles inside the OLED with 5 nm 4P-NPD thickness (b). All 4P-NPD:Ir(dhfpy)$_2$(acac) TH OLEDs exhibit emission close to a Lambertian emitter (c) and a small change of the CIE color coordinates with viewing angle (d).

By a fit of the 0° spectra, the photon contributions ω_B and ω_Y , and the outcoupling efficiencies $\eta_{out,B}$ and $\eta_{out,Y}$ for each emitter can be obtained for the OLEDs under study. The subscripts B and Y indicate the blue and yellow emitter, respectively. For both emitters an isotropic dipole orientation is assumed. The total outcoupling efficiency η_{out} is given by:

$$\eta_{out} = \omega_B \eta_{out,B} + \omega_Y \eta_{out,Y}. \tag{6.2}$$

Furthermore, the internal quantum efficiency η_{IQE} can be calculated using:

$$\eta_{IQE} = \frac{\eta_{EQE}}{\eta_{out}}, \tag{6.3}$$

where η_{EQE} is the experimentally measured EQE^S at 1.54 mA/cm². The superscript S indicates that the EQE^S is measured in an integrating sphere. The low current density is chosen since annihilation processes, which lead to a decrease in IQE, are negligible here. Tab. 6.1 summarizes the obtained efficiencies and simulation results for the OLEDs under study. Since the optical cavity is only changed by a few nanometers, the outcoupling efficiencies $\eta_{out,B}$ and $\eta_{out,Y}$ are almost similar for all thicknesses x. Also the total outcoupling efficiency η_{out} is only slightly decreased for thicker 4P-NPD layer thicknesses. The ratio between the photon contributions ω_B and ω_Y reflect the singlet/(harvested) triplet ratio inside the OLED. It was previously believed that a ratio of ~ 0.33 is necessary to realize a high IQE.[102] However, here an almost constant IQE for different ratios between ω_B and ω_Y is demonstrated. The reason is that in previous studies, the effect of singlet harvesting, i.e. 4P-NPD singlets are converted into emissive triplet state of the phosphorescent emitter, has been neglected. Since the amount of diffusing excitons is exponentially reduced with the distance between generation zone and TH zone, it is expected that the IQE will strongly decrease with further increasing 4P-NPD thickness x.

Table 6.1: Summary of the photon contribution ω and the outcoupling efficiency η_{out} for the blue (B) and yellow (Y) emitter, respectively. The superscript S indicates that the EQE^S (at 1.54 mA/cm²) is measured in an integrating sphere. The internal quantum efficiency η_{IQE} is almost independent of the 4P-NPD layer thickness x.

x nm	ω_B	ω_Y	$\eta_{out,B}$ %	$\eta_{out,Y}$ %	η_{out} %	EQE^S %	η_{IQE} %
3	0.167	0.833	16.58	24.48	23.16	11.3	48.79
5	0.278	0.722	16.38	24.70	22.39	10.9	48.68
7	0.364	0.636	16.21	24.85	21.52	9.9	46.00
9	0.437	0.563	16.05	24.92	21.05	9.5	45.13

An IQE of about 50% for TH OLEDs with 4P-NPD:Ir(dhfpy)$_2$(acac) is considerably lower than 73%[19] when using 4P-NPD:Ir(MDQ)$_2$(acac). It is believed that this arises from fact that the radiative efficiency of Ir(dhfpy)$_2$(acac) is lower than that of Ir(MDQ)$_2$(acac). Further investigations, e.g. the triplet transfer efficiency from 4P-NPD to the phosphorescent emitter, are necessary to confirm this. However, our results suggest that the EQE could be doubled if internal losses, due to non-perfect charge balance and non-unity radiative efficiency, could be overcome. This would also increase the LE significantly.

Table 6.2 summarizes the most important properties of the two-color white TH OLEDs. For $x = 3$ nm an LE^S (EQE^S) of 32.6 lm/W (10.2%) is achieved at 1,000 cd/m², which can be strongly enhanced to 55.4 lm/W (14.9%) when using a glass half-sphere. Furthermore, it can be seen that the design of white OLEDs is a trade-off between white color coordinates, high color rendering index, and high efficiencies.

Table 6.2: Summary of highly efficient two-color white TH OLED properties at a luminance of 1,000 cd/m². The superscript S indicates that the values are obtained in an integrating sphere.

x nm	U_{on} V	U V	j $\frac{mA}{cm^2}$	CIE	CRI	CCT K	CE cd/A	EQE^S %	LE^S lm/W
3	2.6	2.9	3.5	(0.46/0.45)	38	3050	28.4	10.2	32.6
								14.9[a]	55.4[a]
5	2.6	3.0	4.3	(0.42/0.40)	46	3310	23.4	9.4	27.1
								15.2[a]	46.1[a]

[a] with half-sphere

Summary: Triplet harvesting using 4P-NPD

Applying the phosphorescent emitters Ir(ppy)$_3$ (green), Ir(dhfpy)$_2$(acac) (yellow), and Ir(MDQ)$_2$(acac) (red) as dopants, TH from the blue bulk emitter 4P-NPD was investigated. By a careful analysis of the IVL-curves, the emission spectra, and the efficiencies, TH by the emitters Ir(dhfpy)$_2$(acac) and Ir(MDQ)$_2$(acac) was found. A distance variation between exciton generation zone and TH zone showed that, at small distances, singlet transfer could be identified as second transfer mechanism. For Ir(dhfpy)$_2$(acac), time- and spectrally-resolved measurements gave further evidence that TH is taking place.

Using 4P-NPD and Ir(dhfpy)$_2$(acac), two-color white TH OLEDs were realized. Here, the emission color could be nicely tuned towards the warm white point A by varying the distance between exciton generation zone and TH zone. Luminous efficacies in the range of 30 lm/W at 1,000 cd/m² were achieved, which are comparable to state-of-the-art white OLEDs. However, due to the absence of green and red emission, the CRI of these OLEDs was very low. Furthermore, the devices showed a good color stability with applied current density. Using optical simulation, an IQE of about 50% was obtained for the OLEDs under investigation, suggesting that strong improvement is possible if electrical, radiative, excitonic, and optical losses can be overcome. Since radiative losses, in conjunction with optical losses, are seen as key issue, materials with higher intrinsic quantum yield are necessary to enhance the efficiency.

TH was not possible using 4P-NPD and Ir(ppy)$_3$. The reason is that Ir(ppy)$_3$ has a higher triplet energy than 4P-NPD, thus preventing a triplet transfer. An emitter with similar singlet energy like 4P-NPD (S_1 = 2.9 eV), but a higher triplet energy ($T_1 > 2.4$ eV) would be beneficial for the design of white OLEDs. The development of such emitters will be described in the next section.

6.2   Development of Blue Emitters

As described in the previous section, there is a need for efficient blue emitter materials with a high triplet energy to realize TH by a green phosphor. This will also be helpful for the development of efficient white OLEDs. The requirements for a new blue emitter are:

- a singlet energy S_1 between 2.5 and 3.1 eV (400 and 500 nm),

- a triplet energy T_1 higher than 2.4 eV (515 nm) to ensure TH by $Ir(ppy)_3$,

- and an efficient emission from the singlet state when used as a bulk emitter, i.e. a high radiative efficiency.

Furthermore, preferential hole or electron transporting properties rather than bipolar transport is helpful to ensure that the exciton generation zone is close to one of the blocking layers. In addition, a horizontal alignment of the transition dipoles is desired. These two issues as well as a long lifetime are desirable but not necessary conditions.

Since the emitter 4P-NPD is a convenient TH material for yellow and red emitters, its structure is used as a starting point. Based on quantum chemical calculations of the singlet/triplet splitting, two new emitters "8M-4P-NPD" and "8M-4P-FPD" were synthesized and sublimated by Markus Hummert and Annette Petrich, respectively, in the IAPP chemistry group. The properties and performance of these two new emitters, especially with focus on TH by a green emitter, are presented here.

For the new emitters various properties had to be determined. The employed measurement techniques are briefly described here: HOMO energies were measured by Markus Hummert using cyclic voltammetry (CV). Since LUMO energies were not measurable with CV for the investigated compounds, the LUMO energy is estimated using the HOMO energy and the optical gap derived from transmission measurements of thin films performed with a Perkin Elmer Lambda 900 spectrophotometer. Singlet energies were calculated from the first PL-emission peak. PL-spectra of thin films were obtained by an Edinburgh F900 fluorescence spectrometer. The same spectrometer was used to measure the PL-QY in solution (THF[11], concentration ~1.9-2.9 mol/l) by Sylke Furkert. Densities were calculated from thickness measurements of thin films using a Veeco Dektak 150 profilometer. All these measurements were done at the IAPP. In collaboration with the University of Durham (England), phosphorescence spectra (at < 100 K) and the PL-QY of thin films were measured. Triplet energies were calculated from the peak of the phosphorescence signal.

---

[11]Tetrahydrofuran

6.2.1 8M-4P-NPD

Preliminary theoretical considerations

One possibility to increase the triplet level of 4P-NPD is the reduction of the singlet/triplet splitting E_{ST}. To decrease E_{ST}, a stronger separation of the molecular orbitals of HOMO and LUMO is desired (cf. Eqs. 3.12 and 3.15). It is expected that this can be achieved by a twist of the inner phenyl rings of the 4P-NPD molecule, since this interrupts the π-system of the material.[102]

Figure 6.14 shows the calculated singlet and triplet energies for different rotation angles φ between the planes of the phenyl rings P1 and P2. The same rotation angle is found between the planes of P3 and P4. An angle of $\varphi = 0°$ describes a planar structure. When optimizing the molecular structure for 4P-NPD using SCC-DFTB // TD-SCC-DFTB (cf. Sec. 5.6.2) an angle of $\varphi = 27°$ is obtained. In this calculation, the inner phenyl rings P2 and P3 are fixed to a planar position for simplification.
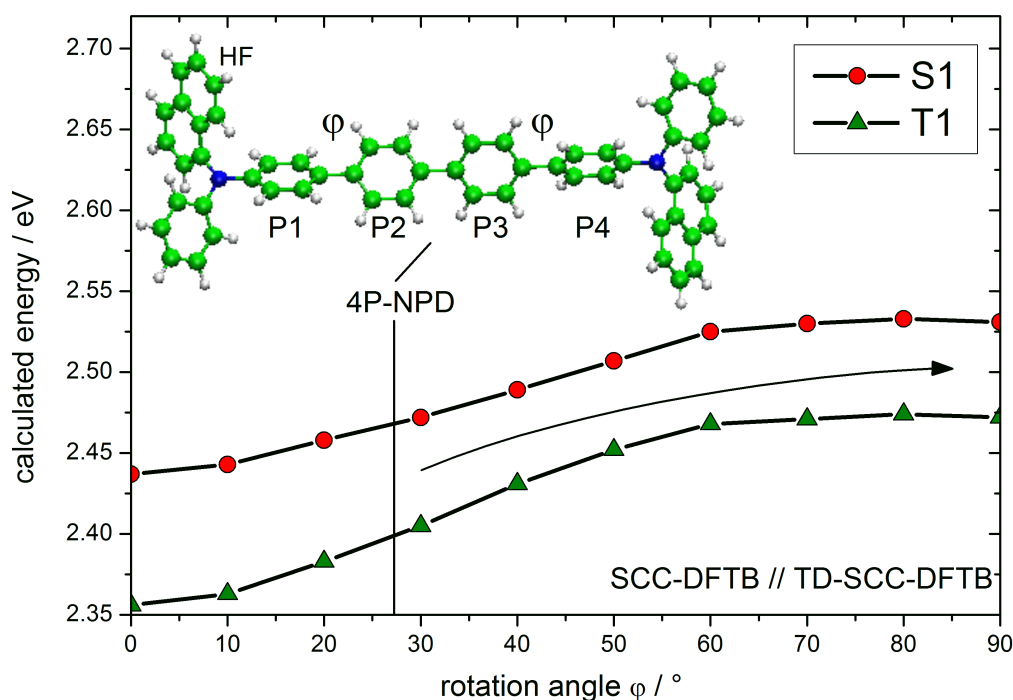
Figure 6.14: Calculated singlet and triplet energy levels of 4P-NPD depending on the rotation angle φ between the plane of the phenyl rings P1 and P2 and accordingly between P3 and P4. An angle of $\varphi = 0°$ describes a planar structure. For the calculations, P2 and P3 are fixed to a planar position. The molecular structure of 4P-NPD as a result of HF calculations is shown. Energies are calculated using SCC-DFTB // TD-SCC-DFTB for which 4P-NPD exhibits $\varphi = 27°$. An increase of φ leads to a rise in singlet and triplet energy.

As illustrated in Fig. 6.14, a stronger twist of the inner phenyl rings does not reduce the singlet-triplet splitting E_{ST} significantly, but leads in fact to a rise in singlet and triplet energy. This is an improvement since finally a rise in triplet energy needs to be achieved. The additionally predicted increase of the singlet energy is not desired but tolerable as long as the emission is still in the blue wavelength regime.

The simulation indicates an increase of the triplet energy by 0.07 eV from 2.40 to 2.47 eV, when φ increases from 27° to 90°. The triplet energy of 4P-NPD known from literature is 2.3 eV[18], indicating that the absolute values predicted by the simulation are not reliable. The same applies to the singlet energy which is known to be 2.91 eV[18]. Here the simulation predicts a value of 2.46 eV.

In order to allow TH by Ir(ppy)$_3$, the required increase in triplet energy is 0.1 eV. This is only 0.03 eV more than predicted by the simulation and indicates that developing a new material with a slightly different molecular structure than 4P-NDP is a promising route.

By incorporation of repulsive methyl groups to the inner phenyl rings, a twist of these rings close to $\varphi = 90°$ is expected. Figure 6.15 shows the molecular structure and orbitals of 4P-NPD and the new material "8M-4P-NPD" with eight additional methyl groups.

It is interesting to analyze the calculated distribution of the HOMO and LUMO of the molecules (Fig. 6.15). While the HOMO of 4P-NPD is extended over the whole molecule, the LUMO is more strongly localized on the naphthalene side groups. For 8M-4P-NPD, the HOMO shows less electron density on the inner phenyl rings (P2 and P3) compared to 4P-NPD. Interestingly, the LUMO of 8M-4P-NPD is only located on one naphthalene group.

The fact that the LUMO is not symmetric with respect to the 8M-4P-NPD molecule structure results from the 90° rotation of the outer phenyl rings since this leads to a splitting of the HOMO and LUMO, respectively (cf. Appendix A.3). For 8M-4P-NPD the LUMO and the second lowest unoccupied molecular orbital (LUMO+1) have the same energy. The same applies to the HOMO and the second highest occupied molecular orbital (HOMO-1). Therefore, it is reasonable to consider the superposition of LUMO and LUMO+1 (HOMO and HOMO-1) when investigating the overlap of HOMO and LUMO in 8M-4P-NPD. In comparison to 4P-NPD, the HOMO and LUMO of 8M-4P-NPD are distributed by similar amount on the naphthalene groups but less on the four phenyl rings which indicates a reduction of HOMO-LUMO overlap and thus the singlet-triplet splitting E_{ST}.

This is in contradiction to the results obtained by the considerations from Fig. 6.14. The reason is seen in the different calculation methods and the fact that the methyl groups are considered in the calculation of the molecular orbitals, which was not the case for the calculations of the singlet and triplet energy level in Fig. 6.14.

To study the significance of the reduction of E_{ST}, further quantum chemical calculations of the energy eigenvalues are carried out and will be presented in Sec. 6.3.
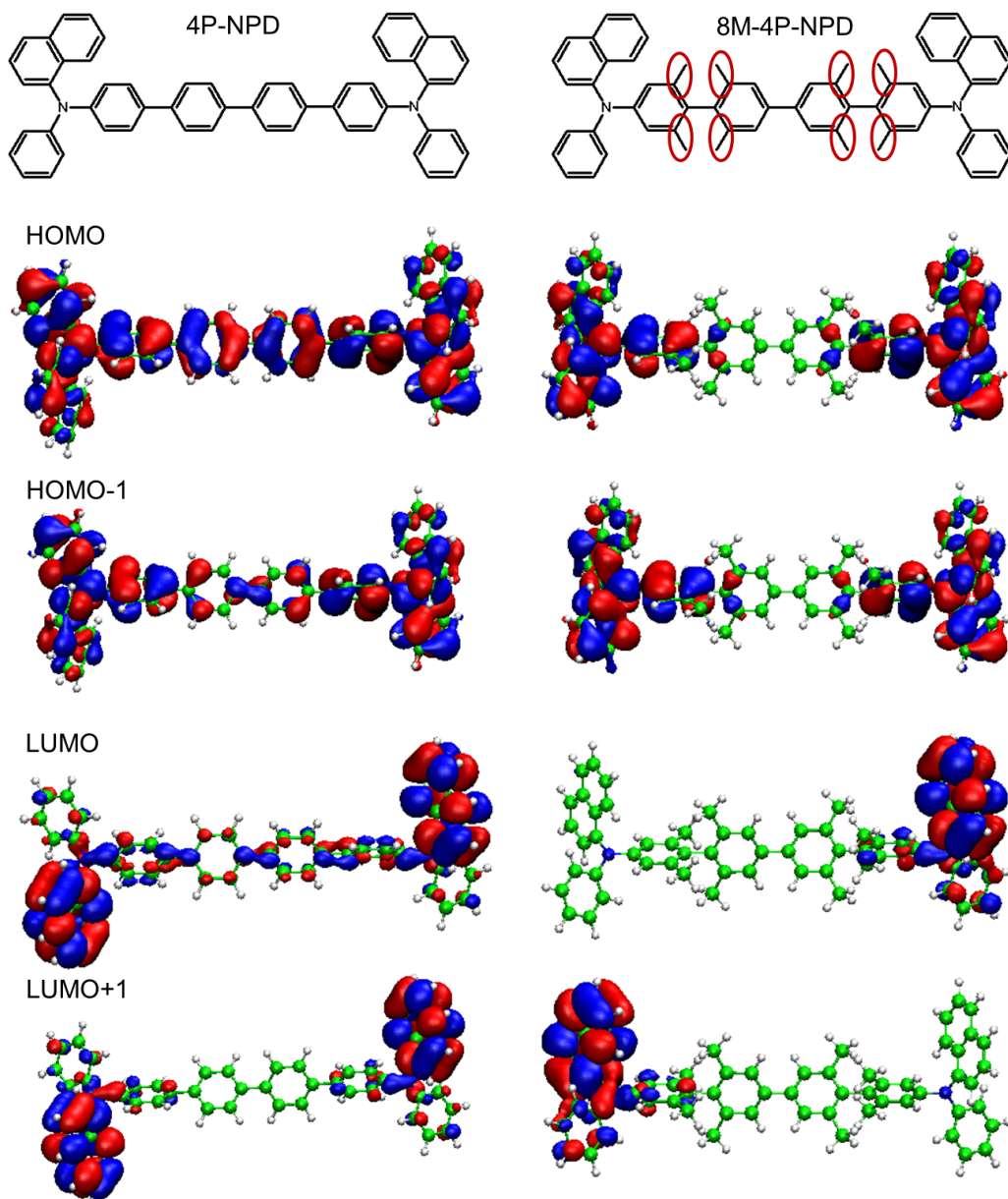
Figure 6.15: Molecular structure and orbitals of 4P-NPD and methylized 4P-NPD (8M-4P-NPD) calculated with HF // SCC-DFTB. The eight repulsive methyl groups (marked with red circles) are expected to twist the corresponding phenyl rings and hence to an increase of the triplet energy (cf. Fig. 6.14). The fact that the LUMO is not symmetric with respect to the 8M-4P-NPD molecule structure results from the 90° rotation of the outer phenyl rings since this leads to a splitting of the HOMO and LUMO, respectively.

Thin film properties and energy levels

Excitation scans and PL spectra of 10 nm 4P-NPD and 8M-4P-NPD evaporated on a glass substrate are shown in Fig. 6.16 (a) and (b). The excitation scans are taken at the peak emission wavelength of both emitters (420 nm for 8M-4P-NPD and 428 nm for 4P-NPD). The absorption maximum at 368 nm for 4P-NPD is maintained in 8M-4P-NPD as a side peak, but the main band shows a new absorption edge at 306 nm. The emission peaks of 4P-NPD and 8M-4P-NPD are at 428 nm and 420 nm, respectively, yielding singlet energies of $S_1^{4P-NPD} = 2.90$ eV and $S_1^{8M-4P-NPD} = 2.95$ eV. For 8M-4P-NPD, the whole spectrum is shifted towards smaller wavelengths and the 4P-NPD shoulder at 449 nm vanishes completely. This is the second vibronic transition of the PL. In the twisted molecule, rotation modes are activated much more due the disturbed molecular geometry. This leads to a widening of the PL vibronic subbands and blurs the shape of the PL spectrum. The second vibronic transition is still there but hidden in the broad peak. This leads to a deeper blue emission color (Fig. 6.16 (c)) for 8M-4P-NPD. Furthermore, the PL-QY of both materials is very similar ($41 \pm 13\%$ for 4P-NPD, $42 \pm 13\%$ for 8M-4P-NPD) making 8M-4P-NPD a promising candidate as a blue OLED emitter.

In terms of TH, the position of the triplet level is important. The phosphorescence spectra determined at < 100 K are shown in Fig. 6.16 (d). Indeed, the phosphorescence of 8M-4P-NPD sets in at smaller wavelengths than for 4P-NPD leading to triplet energies of $T_1^{4P-NPD} = 2.19$ eV and $T_1^{8M-4P-NPD} = 2.27$ eV. Since the triplet energy of 8M-4P-NPD is lower than that of Ir(ppy)$_3$ ($T_1^{Ir(ppy)_3} = 2.4$ eV), TH by Ir(ppy)$_3$ is unlikely.

The triplet energy of 4P-NPD of 2.19 eV obtained within this work is considerably lower than 2.30 eV measured by Schwartz *et al.*[115]. Schwartz and coworker doped 4P-NPD into a polystyrene matrix, while in this work a neat film was used. The peak of the phosphorescence spectrum obtained by these two methods might be considerably different due to interactions with the polystyrene or different triplet relaxation in the triplet density of states. Furthermore, the measurement temperature and the delay time after which the phosphorescence was measured play an important role. In literature, triplet energies for the same material vary by similar amount of energy (~0.1 to 0.2 eV). For example, for the well-known material NPD, values in the range between 2.2 eV and 2.4 eV are reported.[21, 81, 210]

Finally, singlet and triplet energy levels of 8M-4P-NPD are increased in comparison to 4P-NPD. Furthermore, E_{ST} remains the same ($E_{ST}^{4P-NPD} = 0.71$ eV, and $E_{ST}^{8M-4P-NPD} = 0.70$ eV). This is in good agreement with the trends predicted by the quantum chemical calculations presented above. However, absolute energy values between experiment and simulation are not comparable. Nevertheless, 8M-4P-NPD is an interesting material for (TH) OLEDs, and its application as EML is investigated in the following section.
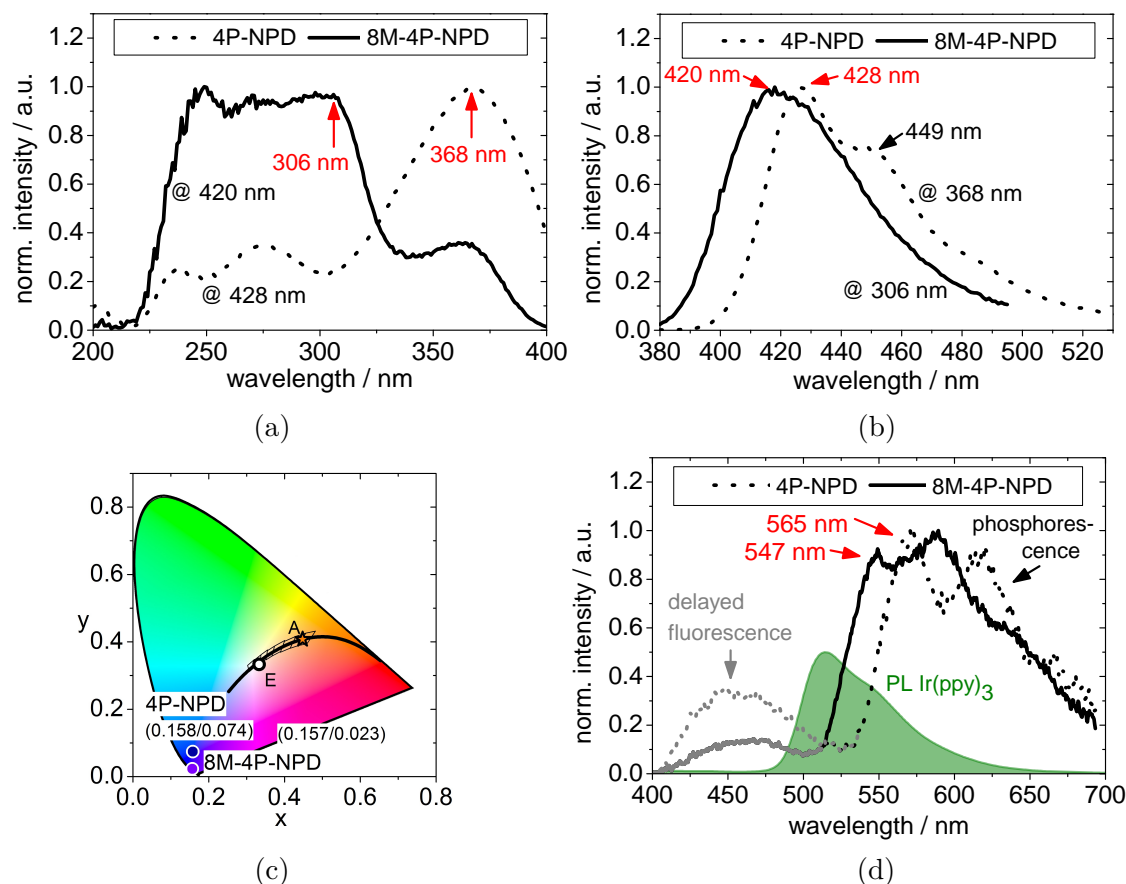
Figure 6.16: Excitation scan (a) and PL emission (b) of 4P-NPD and 8M-4P-NPD single layers. Peak wavelengths are indicated with an arrow and the detection wavelength and excitation wavelength are given, respectively. Due to the shift of emission spectrum towards smaller wavelengths, 8M-4P-NPD exhibits a more deep blue emission color (c) than 4P-NPD. The phosphorescence spectra (d) of 8M-4P-NPD is also shifted towards smaller wavelengths, confirming a rise in triplet energy.

Blue OLEDs - variation of blocker materials

In the next step, 8M-4P-NPD is investigated as EML in an OLED structure. Therefore, different blocker materials are applied. TAPC, Spiro-TAD, and TCTA are used as EBL, while TPBI and BPhen are used as HBL. The results are presented in Fig. 6.17. Also, BAlq2 was tested as HBL. These results are not shown, since only emission from BAlq2 was observed, which results from the fact that the singlet level of BAlq2 (2.51 eV) is lower than that of 8M-4P-NPD (2.95 eV). This also indicates that the exciton generation zone is close to the HBL interface.

Due to the high HOMO energy of 8M-4P-NPD (-5.1 eV), the injection of holes through any of the EBLs should be easy. In contrast, the injection of electrons is strongly hindered since the LUMO energy of -1.6 eV leads to a high injection barrier of more than 1 eV with respect to the HBLs tested here (Fig. 6.17 (b)).

(a)

(b)

(c)

(d)

(e)

(f)
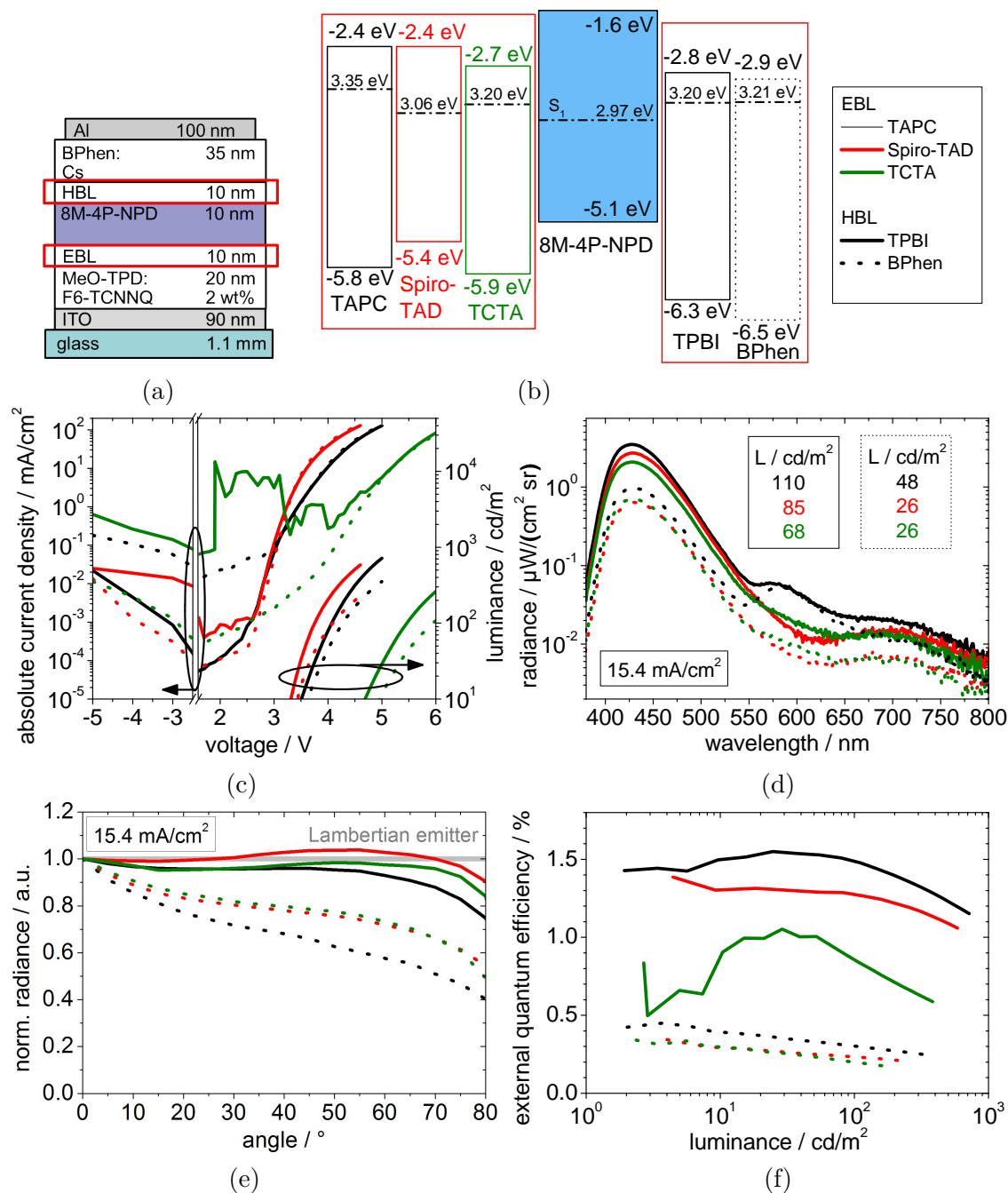
Figure 6.17: OLED layer structure (a), proposed energy level diagram (b), and performance (c-f) of the OLEDs using 8M-4P-NPD as emitter. Different blocking materials are applied. The combination of Spiro-TAD/TPBI exhibits the best IVL performance (c). For all OLEDs emission > 550 nm is observed (d), which indicates the presence of exciplexes. Due to degradation of the BPhen OLEDs during the goniometer measurement, the radiance (e) at high viewing angles is strongly decreased compared to the TPBI OLEDs. This leads to an apparent reduction in EQE (f) for the BPhen OLEDs. In terms of EQE, the blocker combinations TAPC/TPBI and Spiro-TAD/TPBI are most beneficial.

All OLEDs exhibit high leakage currents in the range of 10^{-2} to 1 mA/cm² (Fig. 6.17 (c)). The reason might be that with 20 and 35 nm, respectively, the transport layers are thinner than in other studies. The choice of these thin transport layer thicknesses is motivated because they enable a large outcoupling efficiency in the blue wavelength region[13] (also cf. Fig. 6.4 (b)).

In forward direction, the IV-curves show a strong dependence on the applied EBL, while the use of different HBLs does not have a significant influence. The second aspect is expected since TPBI and BPhen only differ by 0.1 eV in their LUMO energy. Due to the high LUMO energy of 8M-4P-NPD, none of the EBLs is able to block electrons efficiently. It is expected that the forward IV-curve coincides with the HOMO energy of the EBL materials. A high HOMO energy close to that of 8M-4P-NPD should result in best hole injection and steepest IV-curve. This is confirmed by the experiment: The OLED with Spiro-TAD which has the highest HOMO energy of -5.4 eV (TAPC (-5.8 eV), TCTA (-5.9 eV)) shows the steepest IV- and also LV-curve. Interestingly, the difference between the IV-curves of the OLEDs with TAPC and TCTA is rather large, although they have a similar HOMO energy.

The spectral emission at 15.4 mA/cm² is shown in Fig. 6.17 (d) on a logarithmic scale. All OLEDs exhibit 8M-4P-NPD emission. However, when using TAPC as EBL, additional emission at 575 nm can be seen. Since this emission is independent of the HBL material and cannot be observed for Spiro-TAD or TCTA, it is likely that this emission arises from an exciplex formed by 8M-4P-NPD and TAPC. Furthermore, an emission maximum at 700 nm is observed. Emission from the blockers is excluded because their singlet levels are higher than that of 8M-4P-NPD (cf. Fig. 6.17 (b)). Therefore, this emission is also assigned to exciplexes.

The investigation of the angular dependent emission (Fig. 6.17 (e)) shows that for TPBI, the radiance is very close to a Lambertian emitter, while for BPhen, the radiance apparently decreases strongly with increasing viewing angle. It is clear that these differences cannot have an optical origin, since transport layer thicknesses are constant for all devices and a shift in the recombination zone would not change the radiance in such a dramatic way. Instead, the decrease in radiance for the BPhen OLEDs is caused by degradation of the emitter 8M-4P-NPD during the goniometer measurement.

The maximum EQE achieved with the blocker combination of TAPC and TPBI is about 1.5% (Fig. 6.17 (f)). This is rather low, compared to the performance of 4P-NPD, where EQEs > 4% were obtained (cf. Sec. 6.1.1 and Sec. 6.1.2). The reasons for the differences in EQE between 4P-NPD and 8M-4P-NPD are discussed in the following.

8M-4P-NPD and 4P-NPD are both fluorescent emitters. Since their PL-QYs are similar, the same radiative efficiency can be assumed. Differences in the outcoupling efficiency are unlikely: 4P-NPD and 8M-4P-NPD exhibit almost the same blue emission spectra, for the OLEDs similar (transport) layer thicknesses are used, and a strong

difference in the orientation of the transition dipoles is not expected because both materials have a similar length. Thus, the only remaining parameter with an influence on the EQE is the charge balance (cf. Eq. 4.2). It is very likely that the charge balance is different for 4P-NPD and 8M-4P-NPD OLEDs since both materials differ strongly in HOMO and LUMO energy values. While 4P-NPD has a HOMO (LUMO) energy of -5.7 eV (-2.3 eV), 8M-4P-NPD exhibits -5.1 eV (-1.6 eV). Especially the high LUMO of 8M-4P-NPD impedes an efficient injection of electrons. This leads to a charge carrier accumulation at the EML/HBL interface and causes generation of exciplexes[211, 212] which is indeed observed for 8M-4P-NPD OLEDs (cf. Fig. 6.17 (d)). Hence, the charge balance and the effective radiative efficiency are reduced. Since HBL materials with LUMO energies in the range of -1.6 eV are not available, an alternative possibility to increase the EQE is doping 8M-4P-NPD into a suitable matrix material. If exciton generation occurs on the matrix material and the singlets are efficiently transferred to 8M-4P-NPD, a better charge balance might be achieved, and formation of exciplexes might be avoided. Due to their high singlet and triplet energy, TCTA and TPBI might be good matrix materials, however, using 8M-4P-NPD as dopant has not been carried out within this thesis.

Finally, the lifetime of the OLEDs comprising TPBI is investigated and the results are shown in Fig. 6.18. For unknown reasons, the OLED with TCTA shows an untypical behavior: Usually, the lifetime-current density dependence shows a fixed negative slope in a log-log plot.
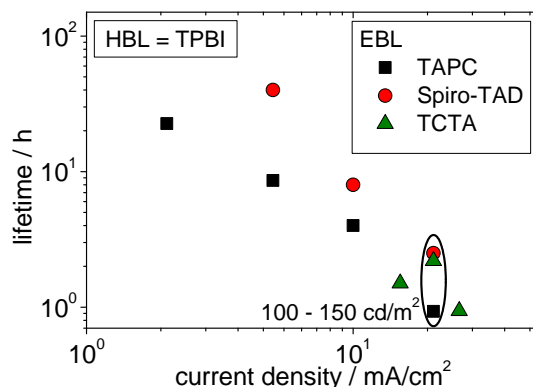
Figure 6.18: Lifetime of 8M-4P-NPD OLEDs comprising TPBI as HBL. For Spiro-TAD as EBL the best lifetime performance is reached. The lifetime is remarkably high compared to 4P-NPD OLEDs. At 10 mA/cm² the lifetime is about 8 h. In contrast, OLEDs comprising 4P-NPD as EML showed a lifetime of ~ 18 min (cf. Fig. 6.4 (c)). At a luminance of about 100 to 150 cd/m² 8M-4P-NPD OLEDs comprising Spiro-TAD or TCTA exhibit lifetimes of about 2 h (4P-NPD OLEDs: < 30 min, 150 cd/m²).

Comparing TAPC against Spiro-TAD, the highest lifetimes are achieved if Spiro-TAD is used. At 10 mA/cm² the lifetime is about 8 h. In contrast, OLEDs comprising 4P-NPD as EML showed a lifetime of ~ 18 min (cf. Fig. 6.4 (c)). At a luminance of about 100 to 150 cd/m², 8M-4P-NPD OLEDs comprising Spiro-TAD or TCTA exhibit lifetimes of about 2 h (4P-NPD OLEDs: < 30 min, 150 cd/m²). The improved lifetime of 8M-4P-NPD as EML in comparison to 4P-NPD is not investigated in detail. As a compromise of IVL, spectral emission, EQE, and lifetime, the blocker combination of Spiro-TAD/TPBI is used in further experiments.

TH OLEDs

The motivation for the development of a new blue emitter is the construction of an OLED where triplets can be harvested by the green emitter $Ir(ppy)_3$, allowing the design of an efficient single stack white TH OLED. As discussed previously, it appears that the triplet energy of 8M-4P-NPD (2.27 eV) is too low to allow this process. Here, a TH OLED is fabricated to verify this assumption. According to the TH experiments with 4P-NPD (Sec. 6.1.2), the same OLED layout is chosen for 8M-4P-NPD (Fig. 6.19 (a) and (b)), except that TPBI is used as HBL instead of BPhen as derived from the previous experiment. It is assumed that the exciton generation zone, like in the case of 4P-NPD, is close to the HBL interface, so that triplets can diffuse towards the phosphorescent emitter which is doped into 8M-4P-NPD at the other side of the EML. In this experiment, the phosphorescent emitters $Ir(MDQ)_2(acac)$ and $Ir(ppy)_3$ are used, respectively, and an OLED without a dopant is taken as reference. Since a comparison to the emitter 4P-NPD is meaningful, the data of the 4P-NPD OLED (from Sec. 6.1.2, no dopant) is also shown. As the same transport layers thicknesses are used, this 4P-NPD OLED is an optical analogon to the 8M-4P-NPD OLED without any phosphorescent dopant.

The IV-characteristics of the OLEDs under study are shown in Fig. 6.19 (c). In comparison to the blocker variation experiment described previously, the leakage currents are lower. Here, current densities are in the expected range of 10^{-4} mA/cm², while previously 10^{-2} to 1 mA/cm² (cf. Fig. 6.17 (c)) were obtained. In this experiment, the thicker transport layers compensate the roughness of the ITO electrode, thus preventing local shorts and reducing leakage currents significantly.

While for the $Ir(MDQ)_2(acac)$ OLED, the forward IV-curve is identical to the reference, the IV-curve of the $Ir(ppy)_3$ OLED is slightly steeper, indicating that $Ir(ppy)_3$ does have an impact on the charge transport. This is very likely as seen in the proposed energy scheme (Fig. 6.19 (b)). The HOMO energy of $Ir(ppy)_3$ is the same as that of 8M-4P-NPD (-5.1 eV) allowing hole transport, and increasing the probability for direct recombination on $Ir(ppy)_3$. In contrast the HOMO energy of $Ir(MDQ)_2(acac)$ is 0.3 eV lower, thus inducing a preferred hole transport on 8M-4P-NPD rather than on $Ir(MDQ)_2(acac)$.

Regarding the spectral emission intensity (Fig. 6.19 (c)), surprisingly Ir(ppy)$_3$ emission (indicated with a black arrow) is found. This means that triplets can decay radiatively on Ir(ppy)$_3$. This is interesting since for 4P-NPD OLEDs no green emission was observed as the low triplet level causes a transfer of triplets to 4P-NPD (cf. Sec. 6.1.2). However, the intensity of the green peak is significantly lower (factor of 10) compared to the red peak of the Ir(MDQ)$_2$(acac) OLED. It is unlikely that is results from differences in radiative efficiency or outcoupling efficiency. (The radiative efficiency of Ir(ppy)$_3$ is 0.76 and 0.84 for Ir(MDQ)$_2$(acac).[13]) Therefore, it is believed that the main amount of Ir(ppy)$_3$ triplets is indeed transferred to 8M-4P-NPD, while some triplets decay on Ir(ppy)$_3$.

In comparison to the reference OLED, the blue peak is slightly reduced for the Ir(MDQ)$_2$(acac) OLED and Ir(ppy)$_3$ OLED (Fig. 6.19 (c)). This effect has been already observed for the 4P-NPD TH OLEDs (Sec. 6.1.2) and can be assigned to singlet diffusion and transfer. The fact that the blue emission is almost maintained in comparison to the reference and additional emission at higher wavelength is observed, indicates TH. Furthermore, the assumption that the exciton generation zone is close to the TPBI (HBL) is confirmed, otherwise the blue emission would be strongly quenched by the green or the red phosphorescent emitter.

The angle-dependent emission of the devices under study is very close to a Lambertian emitter (Fig. 6.19 (e)), except for the Ir(MDQ)$_2$(acac) OLED which shows a sub-Lambertian behavior due to wavelength dependent outcoupling. More interestingly, the EQE at low current densities (10^{-1} - 1 mA/cm²) is enhanced in comparison to the reference OLED by a factor of about 2 in case of Ir(ppy)$_3$ and > 5 in case of Ir(MDQ)$_2$(acac). This strong enhancement for Ir(MDQ)$_2$(acac) is not surprising. Although the singlet emission of the blue 8M-4P-NPD OLED yields only a low EQE of max. 1.5%, triplets are still efficiently transferred to Ir(MDQ)$_2$(acac).

In comparison to the 4P-NPD OLED (black dotted line in Fig. 6.19), 8M-4P-NPD shows a significant deterioration. The main reason is the high LUMO energy of 8M-4P-NPD which impedes electron injection into the EML, thus increasing driving voltage, as well as reducing emission intensity and EQE.

Finally, the IV-curves indicate that emission resulting from direct recombination of electrons and holes on Ir(ppy)$_3$ is very likely, while for Ir(MDQ)$_2$(acac) direct recombination can be neglected. The presence of TH from 8M-4P-NPD to Ir(MDQ)$_2$(acac) can be confirmed due to the significant contribution of red emission to the spectrum. For Ir(ppy)$_3$, this contribution is considerably lower. This does not exclude the presence of TH, but indicates that in case of Ir(ppy)$_3$ direct recombination is the primarily responsible process for light emission.
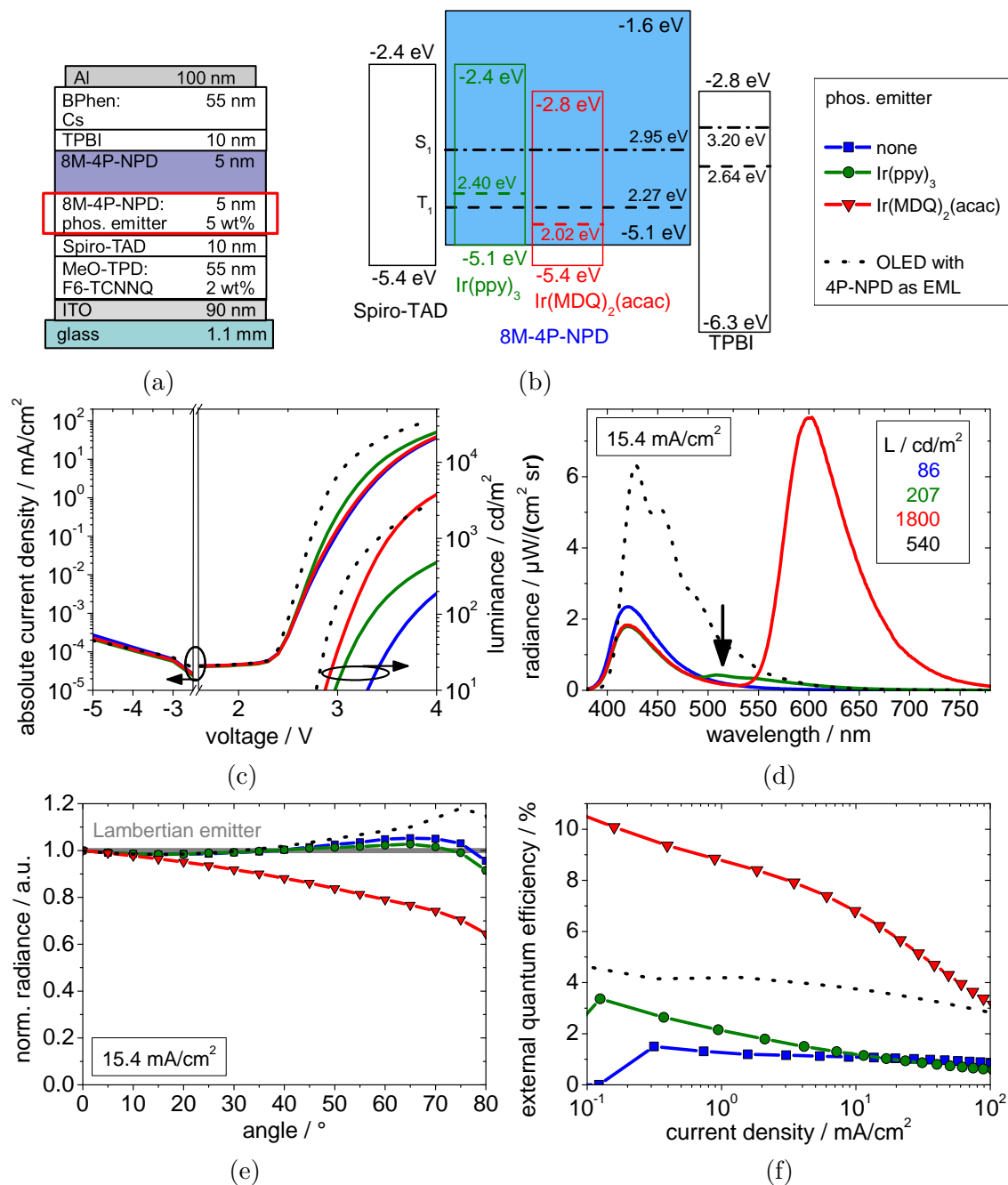
Figure 6.19: OLED layer structure (a), proposed energy level diagram (b) and performance (c-f) of the TH OLEDs using 8M-4P-NPD as emitter. Ir(ppy)$_3$ and Ir(MDQ)$_2$(acac) are applied as phosphorescent emitters, respectively. Furthermore, a reference OLED without a dopant is shown. For comparison, the data of the 4P-NPD OLED from Sec. 6.1.2 is given by a black dotted line. 8M-4P-NPD as EML cannot reach the performance of 4P-NPD OLEDs. Interestingly, green emission from Ir(ppy)$_3$ can be observed (black arrow in (d)).

Thickness variation of the intrinsic 8M-4P-NPD layer

Similarly to the experiments with 4P-NPD, a thickness variation of the intrinsic 8M-4P-NPD layer is meaningful to investigate TH (Fig. 6.20). According to the experiments presented in Sec. 6.1.2, this thickness is correlated to the distance between exciton generation zone and TH zone.
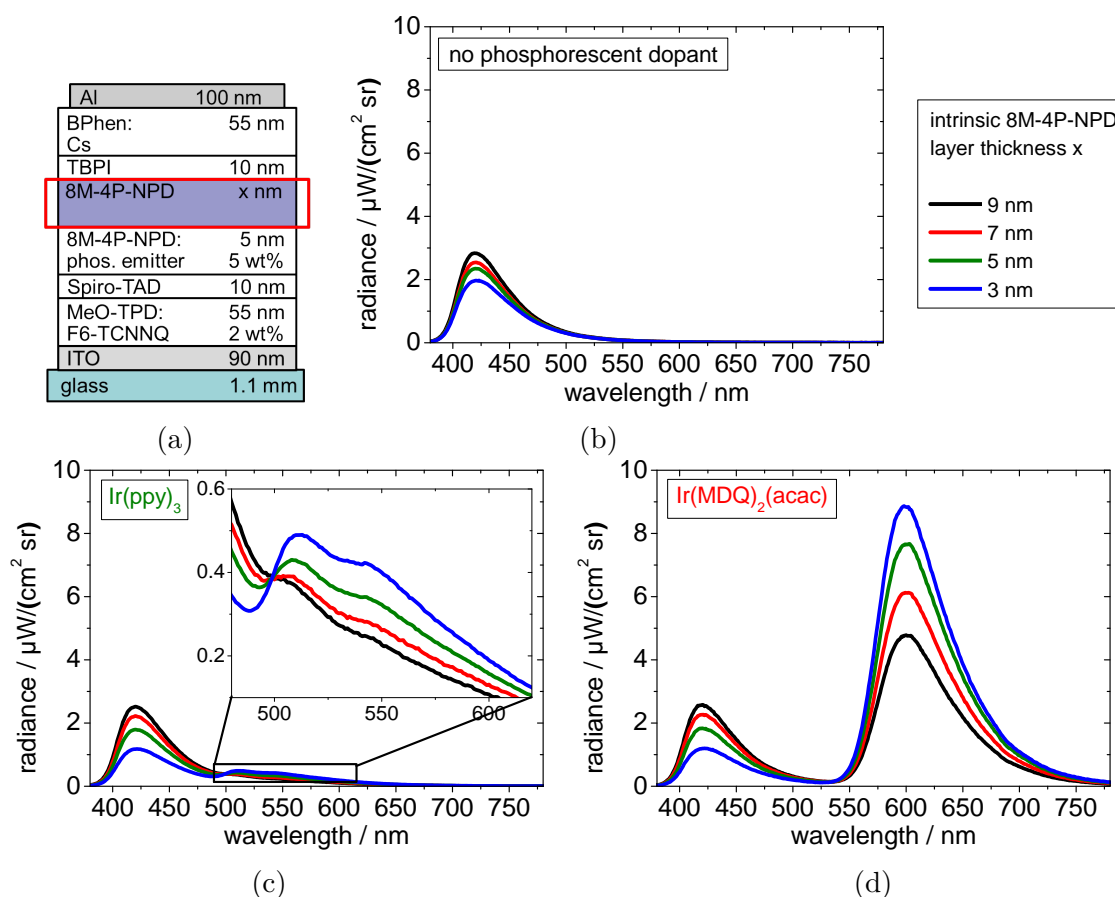
Figure 6.20: OLED layer structure and emission spectra at 15.4 mA/cm² for varying 8M-4P-NPD layer thickness x and different phosphorescent emitters (b-d). For the Ir(ppy)$_3$ OLEDs, the green emission is enlarged for better visibility. Emission from 8M-4P-NPD decreases steadily with decreasing layer thickness x (b-d). For the OLEDs doped with Ir(ppy)$_3$ and Ir(MDQ)$_2$(acac), the additional emission in the green and red wavelength regime increases with decreasing 8M-4P-NPD thickness.

The reference OLEDs without the phosphorescent dopant show a steady increase of the emission spectrum with increasing thickness x (Fig. 6.20 (b)). This is in contrast to previous experiments using 4P-NPD (cf. Fig. 6.8 (b)) where the blue emission was rather constant. A change in charge carrier balance is seen as main reason for this effect: While for 4P-NPD charge injection is quite balanced since the HOMO and LUMO energy levels are in good alignment to that of the surrounding blocking layers (cf. Fig. 6.6 (b)), the electron injection into 8M-4P-NPD is strongly hindered,

due to its high LUMO energy (cf. Fig. 6.19 (b)). Furthermore, holes are efficiently blocked by the TPBI blocking layer. Hence, there is a hole accumulation at the 8M-4P-NPD/HBL interface. Increasing the 8M-4P-NPD thickness slows down the hole transport and leads to an improved charge carrier balance which enhances the emission intensity.

With increasing thickness x, typical TH behavior is observed for both phosphorescent emitter systems: Blue emission increases and additional emission at longer wavelength decreases (Fig. 6.20 (c) and (d)). This confirms that TH is taking place from 8M-4P-NPD to $Ir(MDQ)_2(acac)$. However, the decrease of $Ir(ppy)_3$ emission with increasing x can be as well a result of direct recombination since a thinner 8M-4P-NPD layer enhances the probability for electrons to reach $Ir(ppy)_3$.

Time- and spectrally resolved measurements

So far, it is open if $Ir(ppy)_3$ emission in the TH OLEDs occurs only due to direct recombination and singlet transfer, or if TH is present to some extent. Therefore, a streak camera measurement is performed. In Fig. 6.21 (a) the time- and spectrally resolved emission following a voltage pulse (4 V for 2.5 µs) is shown for a device containing 8M-4P-NPD and $Ir(ppy)_3$ (OLED layer structure is given in Fig. 6.20 (a)).

Similarly to the experiment using 4P-NPD and $Ir(dhfpy)_2(acac)$ described in Sec. 6.1.3, the prompt emission of the blue fluorescent emitter remains. In contrast, the emission of the phosphorescent emitter in this experiment is much stronger in the time range between 0 and 2.5 µs than at later times when the pulse is switched off. This prompt emission of $Ir(ppy)_3$ is assigned to direct recombination and singlet harvesting. The delayed component of $Ir(ppy)_3$ emission (3.2 to 5.5 µs) is allocated to emission resulting from TH because it is rather constant and can be well distinguished from the natural exponential decay of the phosphorescent emitter. The fraction of TH emission is rather low compared to that of the direct recombination. Unfortunately, the amount of TH emission is too low to determine a maximum and study the dependence of the delay time on the intrinsic layer thickness x of 8M-4P-NPD like in the case of 4P-NPD:$Ir(dhfpy)_2(acac)$.

In conclusion, the fact that delayed emission is observed within the streak-camera measurements proves that TH by $Ir(ppy)_3$ is taking place. However, $Ir(ppy)_3$ emission is essentially caused by direct recombination and singlet harvesting.

It is interesting that TH by $Ir(ppy)_3$ is present since this was not expected due to the lower triplet level of 8M-4P-NPD (2.27 eV) in comparison to $Ir(ppy)_3$ (2.4 eV). This can be understood by regarding again the phosphorescence spectrum of 8M-4P-NPD and the $Ir(ppy)_3$ PL emission spectrum (Fig. 6.16 (d)). Here, the onset of the phosphorescence spectrum coincides with the peak of the $Ir(ppy)_3$ emission spectrum. This allows that a few 8M-4P-NPD triplets at the high energy end of the triplet density of states can be harvested by $Ir(ppy)_3$.

(a)   (b)
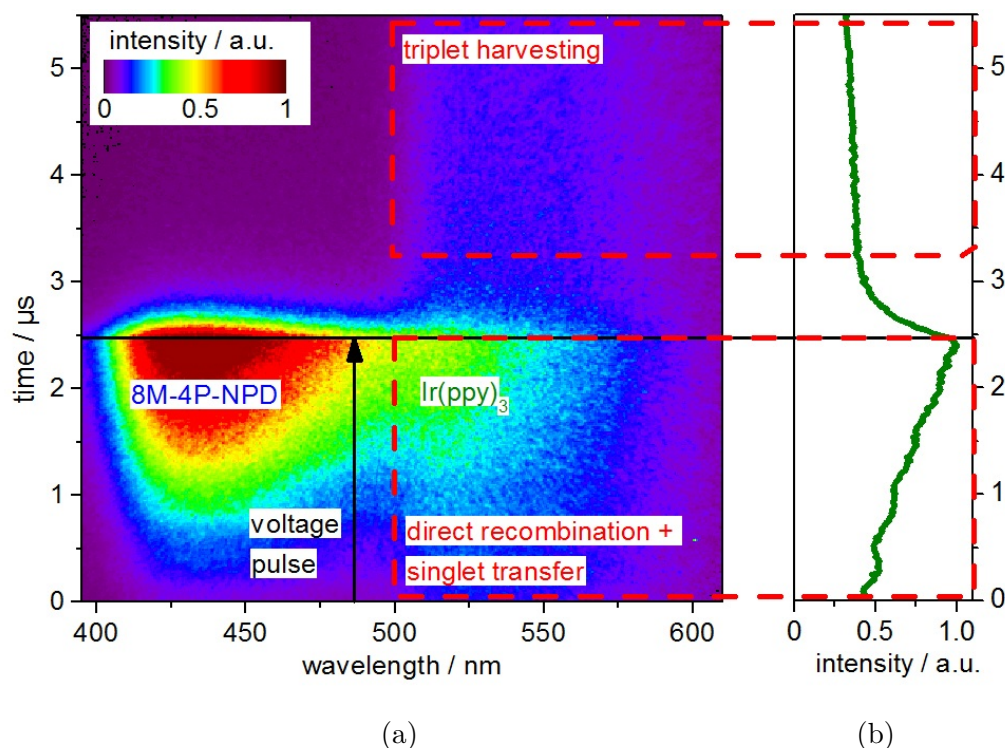
Figure 6.21: Normalized time- and spectrally-resolved intensity (a) after application of short electrical pulses (black arrow) of 2.5 µs and 4 V to the 8M-4P-NPD:Ir(ppy)$_3$ OLED shown in Fig. 6.20 (a) with a 4P-NPD layer thickness of $x =$ 5 nm and normalized integrated intensity (b), obtained by integrating from 500 nm to 620 nm. Processes of direct recombination as well as singlet transfer and TH by Ir(ppy)$_3$ are indicated by red boxes.

Two-color white TH OLED

According to the experiments in Sec. 6.1.3, the yellow emitter Ir(dhfpy)$_2$(acac) is doped partially into the bulk emitter 8M-4P-NPD to design white TH OLEDs. The intrinsic 8M-4P-NPD layer thickness x is varied to adjust the emission ratio between blue and yellow emission (Fig. 6.22). Basically the same trends are observed compared to white TH OLEDs based on 4P-NPD (cf. Sec. 6.1.3): With increasing x, the IVL-curves become flatter (Fig. 6.22 (b)), the blue emission increases while the yellow emission decreases (Fig. 6.22 (c)), and all devices exhibit a Lambertian type emission behavior (Fig. 6.22 (d)). The EQE and LE decrease consistently with increasing x (Fig. 6.22 (e) and (f)).

The spectral emission characteristics confirm TH as discussed several times. One difference between the 8M-4P-NPD OLEDs and the 4P-NPD OLEDs occurs when regarding the EQE at low current density (0.1 mA/cm²). While for 4P-NPD the EQE is rather constant (Fig. 6.11 (e)), it decreases with increasing x for 8M-4P-NPD (Fig. 6.22 (e)). It is believed that changes in charge balance are causing these differences.
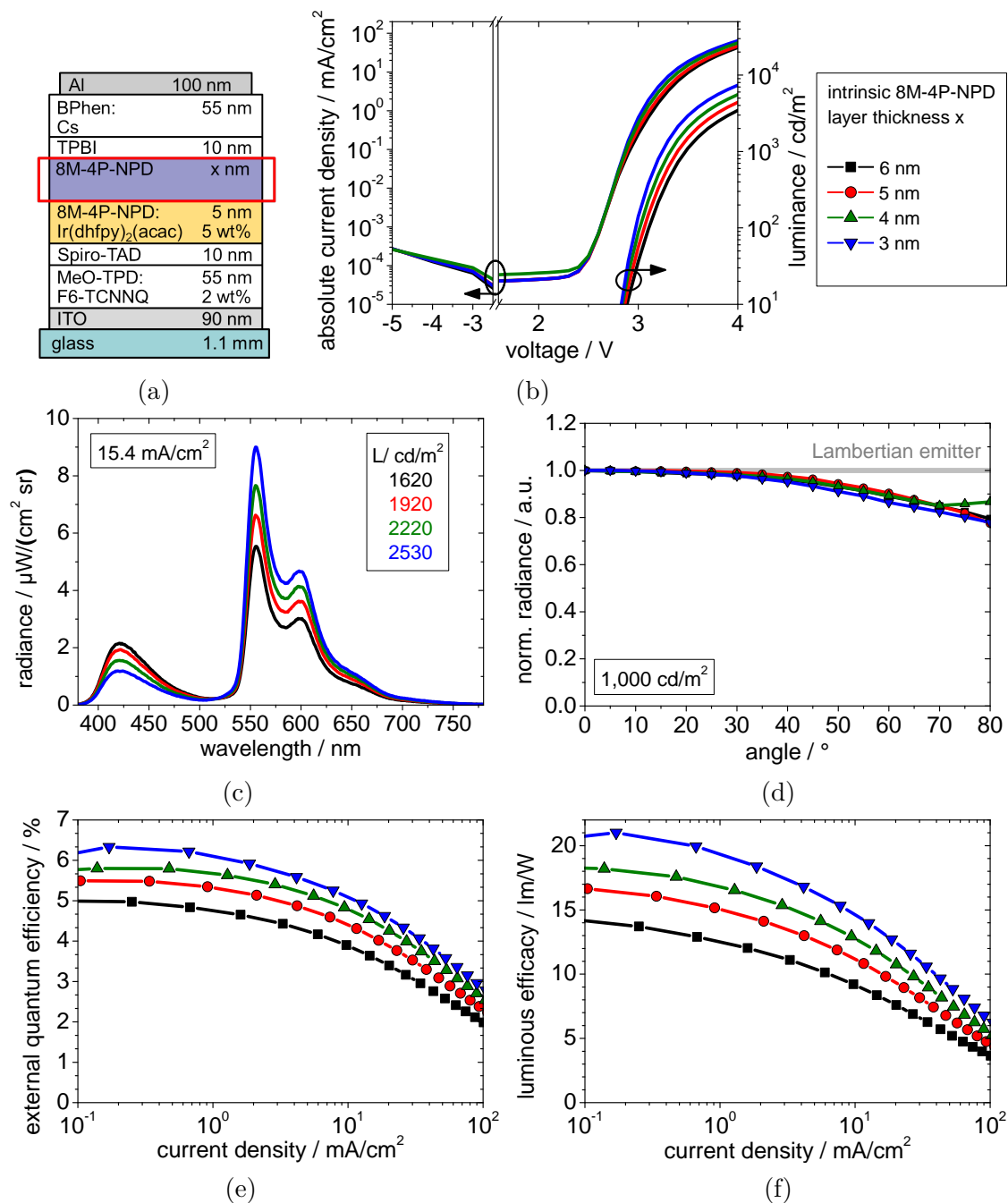
Figure 6.22: OLED layer structure (a) and performance (b-f) of the two-color white TH OLEDs using 8M-4P-NPD and Ir(dhfpy)$_2$(acac) as emitters. The trends for varying 8M-4P-NPD are comparable to the TH OLEDs presented in Fig. 6.11 where 4P-NPD is used as blue fluorescent emitter: With increasing x, the IVL-curves become flatter (b), the blue emission increases while the yellow emission decreases (c), and all devices exhibit Lambertian type emission behavior (d). The EQE and LE decrease consistently with increasing x (e,f).

More importantly, the OLEDs with layer thickness $x = 5$ and 6 nm show white color coordinates (Fig. 6.23). The corresponding luminance and CRI values are given in square brackets. It was expected that color coordinates closer to the warm white point A can be obtained using 8M-4P-NPD instead of 4P-NPD, since 8M-4P-NPD has a deeper blue emission (cf. Fig. 6.16 (c)). However, the opposite trend is observed owing to the emission spectrum of Ir(dhfpy)$_2$(acac): In 8M-4P-NPD OLEDs the second peak of the Ir(dhfpy)$_2$(acac) spectrum at 600 nm is less pronounced than in 4P-NPD OLEDs. This is an unexpected behavior, since the 4P-NPD and 8M-4P-NPD OLEDs comprise the same optics due to the use of same transport layer thicknesses which lead to the same position of the recombination zone inside the device. It is assumed that due to the higher triplet level of 8M-4P-NPD compared to 4P-NPD, the triplet transfer to the first vibronic of Ir(dhfpy)$_2$(acac) is more favorable for 8M-4P-NPD. This enhances the intensity of the first emission peak of Ir(dhfpy)$_2$(acac) at 557 nm in comparison to the second peak at 600 nm.
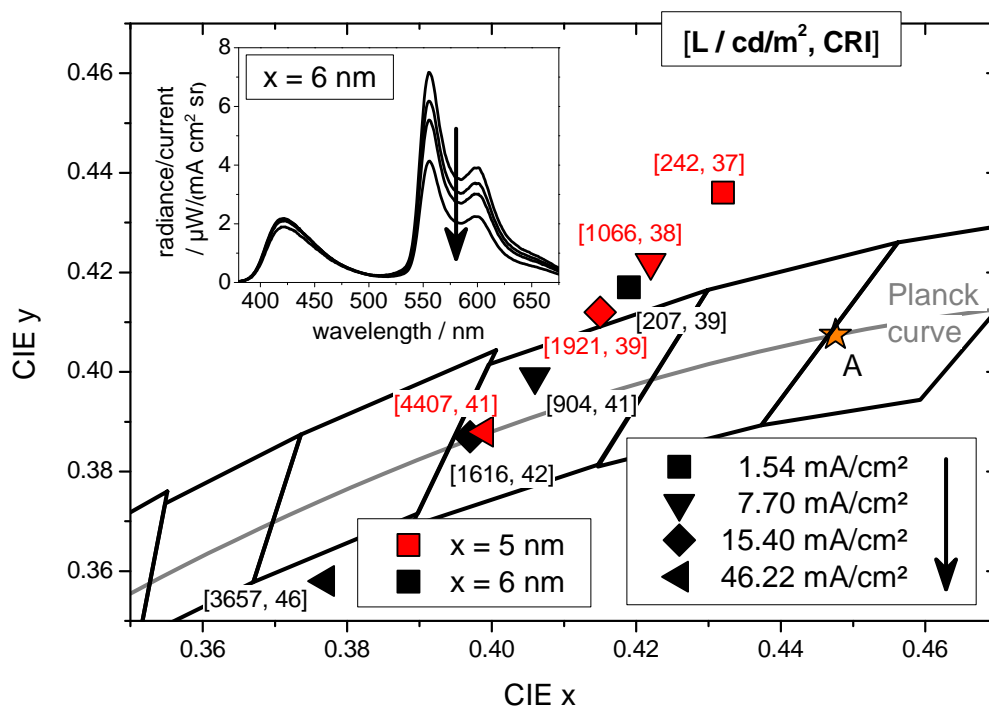
Figure 6.23: CIE color coordinates for the two-color white TH OLEDs at different applied current densities for 8M-4P-NPD layer thicknesses of 5 and 6 nm, respectively. Corresponding luminance and CRI values are given in square brackets. Inset: spectral radiance divided by the applied current for the OLED with $x = 6$ nm. While the blue emission is almost independent of the current density, the contribution of the yellow emitter decreases steadily.

The color shift with applied current density towards blue color coordinates is a result of quenched $Ir(dhfpy)_2(acac)$ triplets which is more pronounced than for the 8M-4P-NPD singlets. This is shown by the radiance divided by the applied current (inset in Fig. 6.23): While the 8M-4P-NPD emission is roughly constant, the fraction of $Ir(dhfpy)_2(acac)$ emission decreases strongly with increasing current density. The achieved CRIs are low, in the range between 37 and 46.
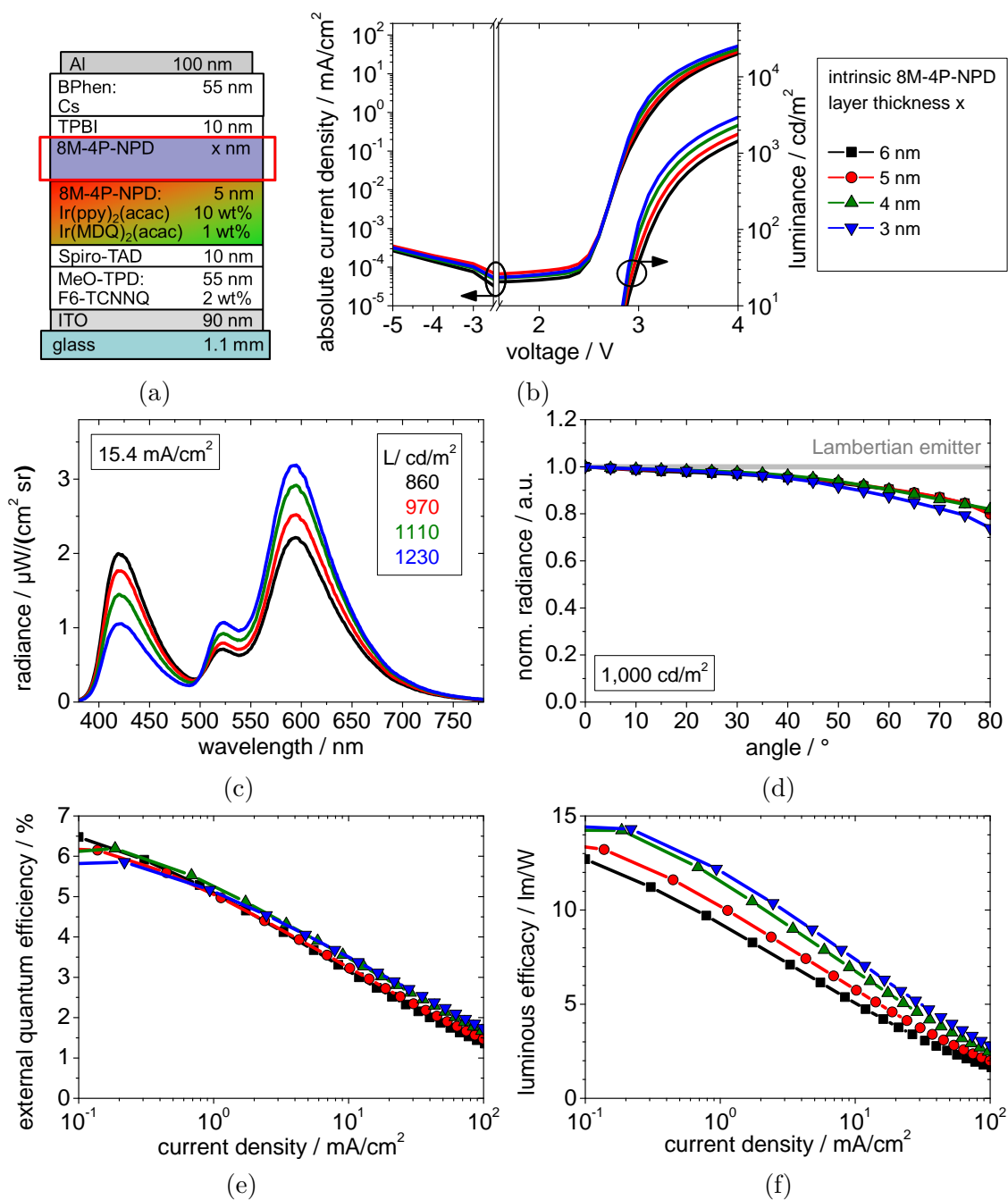
Three-color white TH OLED

Since the development of a new blue emitter is motivated by the fact that TH by the green phosphorescent emitter $Ir(ppy)_3$ is not possible using 4P-NPD, a white OLED is investigated where TH from 8M-4P-NPD to a green and red emitter is present. Despite the fact that TH from 8M-4P-NPD to $Ir(ppy)_3$ is feasible, a strong fraction of direct recombination processes on $Ir(ppy)_3$ was observed. The reason is that the HOMO energies of 8M-4P-NPD and $Ir(ppy)_3$ are nearly identical (-5.1 eV, cf. Fig. 6.19 (b)) which favors hole transfer on the $Ir(ppy)_3$ molecules.

To exclude this effect, the green phosphorescent emitter $Ir(ppy)_2(acac)$ is used instead of $Ir(ppy)_3$. $Ir(ppy)_2(acac)$ has a HOMO energy of -5.4 eV which should efficiently prevent hole injection and transport on this emitter. The triplet energy of $Ir(ppy)_2(acac)$ is 2.38 eV, very similar to $Ir(ppy)_3$ (T_1 = 2.40 eV). Hence, TH from 8M-4P-NPD to $Ir(ppy)_2(acac)$ is possible. Furthermore, $Ir(ppy)_2(acac)$ exhibits a slightly higher EQE than $Ir(ppy)_3$ when used as emitter doped into a matrix material inside an OLED structure. Due to a smaller molecular dipole moment, $Ir(ppy)_2(acac)$ has a lower probability to form aggregates in mixed films, thus exhibiting a better roll-off characteristic.[213] Recent findings indicate that one additional reason for the higher EQE is based on the fact that the $Ir(ppy)_2(acac)$ transition dipoles show a preferred horizontal orientation $\Theta = 0.23$, while $Ir(ppy)_3$ has an almost isotropic orientation $\Theta = 0.29$.[140]

To simultaneously harvest by $Ir(ppy)_2(acac)$ and $Ir(MDQ)_2(acac)$, both emitters are doped into 8M-4P-NPD. The layer structure of the investigated OLEDs is shown in Fig. 6.24 (a). For $Ir(ppy)_2(acac)$ a concentration of 10 wt% is used, while for $Ir(MDQ)_2(acac)$ the concentration is 1 wt%. These concentrations are chosen to avoid a triplet transfer from $Ir(ppy)_2(acac)$ to $Ir(MDQ)_2(acac)$, which otherwise would result in a loss of green emission. Again, the layer thickness x of the intrinsic 8M-4P-NPD is varied to adjust the singlet/harvested triplet ratio and thus the contributions of the emitters to the spectrum. For the IVL-curves, the typical flattening is observed with increasing x (Fig. 6.24 (b)).

TH by both phosphorescent emitters is proven by the fact that additionally to the blue emission, significant emission from the phosphorescent emitters is observed. As typically for TH, the blue peak in the emission spectrum increases with increasing thickness x, while the green and the red peaks decrease (Fig. 6.24 (c)).

Figure 6.24: OLED layer structure (a) and performance (c-f) of the three color white TH OLEDs using 8M-4P-NPD as fluorescent, and $Ir(ppy)_2(acac)$ and $Ir(MDQ)_2(acac)$ as phosphorescent emitters. As typical for TH OLEDs, the layer thickness x of the intrinsic 8M-4P-NPD can be used to adjust the contributions of the emitters to the spectrum (c). The efficiencies (e,f) exhibit a pronounced roll-off, indicating strong quenching effects of the phosphorescent emitters.

All OLEDs show a Lambertian like emission characteristic (Fig. 6.24 (d)). At low current density (0.1 mA/cm²), the EQE is about 6% for all OLEDs (Fig. 6.24 (e)) which is in good agreement with the EQEs for the two-color white OLEDs using 8M-4P-NPD and Ir(dhfpy)$_2$(acac) (cf. Fig. 6.22 (e)) ranging from 5% to 6.5%. However, the roll-off is much stronger for the three-color white OLEDs: While for the two-color white OLEDs the EQE is reduced to 3% at 100 mA/cm², the EQE for three-color white OLEDs is already reduced to 3% at 10 mA/cm². Knowing that the roll-off is determined by the phosphorescent emitters rather than by the fluorescent emitter, the roll-off characteristics might be improved by a decrease of the doping concentrations of the phosphorescent emitters. However, the doping concentration needs to be sufficiently high to ensure an adequate contribution of the emitters to the white spectrum. The strong roll-off for the three-color white OLEDs is also reflected in the LE-curves (Fig. 6.24 (f)).

The CIE color coordinates of the OLEDs with $x = 3$ and 4 nm are shown in Fig. 6.25 for different current densities. The corresponding luminance and CRI values are given in square brackets.
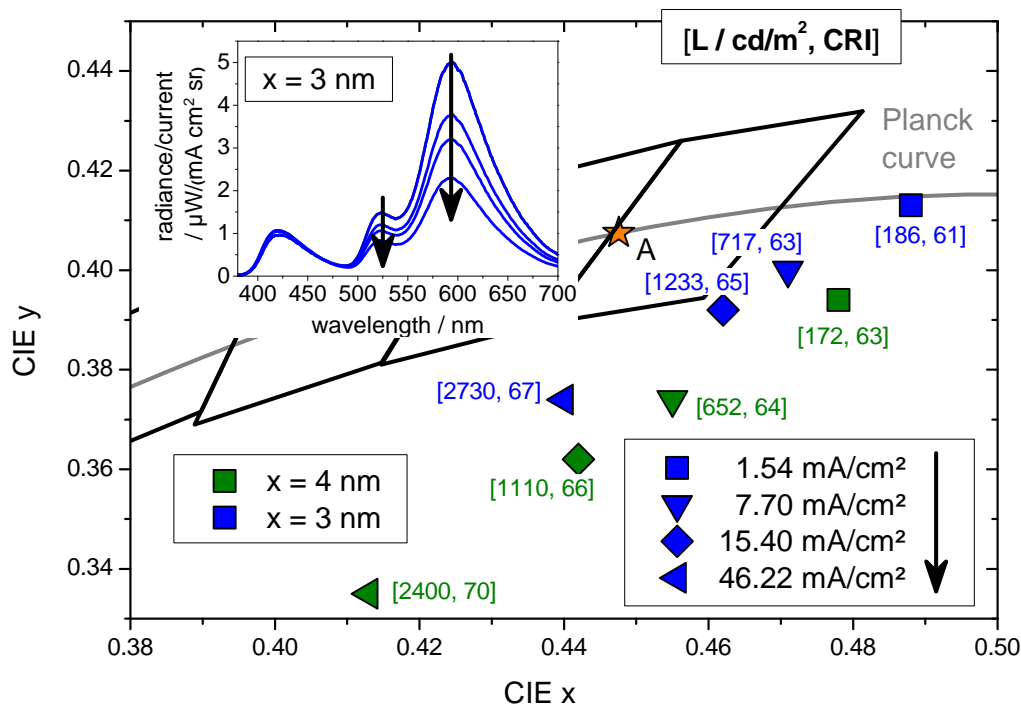
Figure 6.25: CIE color coordinates for the three-color white TH OLEDs at different applied current densities for 8M-4P-NPD layer thicknesses of 3 and 4 nm, respectively. Corresponding luminance and CRI values are given in square brackets. Inset: spectral radiance divided by the applied current for the OLED with $x = 3$ nm. While the blue emission is almost independent of the current density, the contribution of the green and red emitter decreases steadily.

For $x = 3$ nm, the color coordinates are closest to the warm white color point A. However, the color is slightly reddish. Enhancing the green emission would help to shift the color coordinates even further towards A. This would also be beneficial for the efficiency, since usually more greenish color coordinates go side by side with higher luminous efficiencies. A stronger contribution of the green emitter could be realized by further reducing x or increasing the concentration of Ir(ppy)$_2$(acac).

The blue shift of the CIE coordinates with increasing current density results from a reduced emission of the green and red peak in comparison to the constant blue emission. This is indicated in the inset in Fig. 6.25 where the radiance is divided by the applied current. The reduction of the green and red emission at high current densities is mainly caused by TTA. As expected, the CRI is strongly enhanced (up to 70) in comparison to the two-color white OLEDs which showed much lower CRIs in the range between 37 and 46 (cf. Fig. 6.23).

Summary: White TH OLEDs using 8M-4P-NPD

Table 6.3 summarizes the most important properties of the two-color and three-color white TH OLEDs at a luminance of 1,000 cd/m². The thickness x of the intrinsic 8M-4P-NPD determines the distance between exciton generation and TH zone and its variation is useful to adjust the emission color towards warm white color coordinates. In comparison to the experiments in Sec. 6.1.3 where 4P-NPD is used as emitter, the efficiencies for the two-color white OLEDs are much lower (about a factor of 2 to 3). With 4P-NPD as EML, efficiencies close to 30 lm/W (8% EQE) were obtained. It is believed that the difference in EQE between 4P-NPD and 8M-4P-NPD OLEDs is caused mainly by the poor charge balance in the 8M-4P-NPD OLEDs which also limits the efficiency in TH OLEDs.

Using three emitters instead of a two-color system, the CRI can be enhanced. However, the achieved efficiencies are again rather low (~7 lm/W, ~3%).

Table 6.3: Summary of two-color and three-color white TH OLED properties comprising 8M-4P-NPD as blue emitter at a luminance of 1,000 cd/m².

x nm	U_{on} V	U V	j $\frac{mA}{cm^2}$	CIE	CRI	CCT K	CE cd/A	EQE %	LE lm/W
Two-color white									
8M-4P-NPD:Ir(dhfpy)$_2$(acac)									
5	2.8	3.4	7.1	(0.41/0.40)	41	3580	14.0	4.0	11.9
6	2.8	3.5	8.7	(0.42/0.42)	38	3390	11.5	4.6	9.4
Three-color white									
8M-4P-NPD:Ir(ppy)$_2$(acac):Ir(MDQ)$_2$(acac)									
3	2.8	3.4	11.8	(0.47/0.40)	64	2500	8.5	3.4	7.0
4	2.8	3.5	13.2	(0.45/0.37)	66	2530	7.6	3.3	6.2

6.2.2   8M-4P-FPD

In a next step, it is intended to increase the radiative efficiency of 8M-4P-NPD. This would positively influence the EQE of blue and white OLEDs. To increase the radiative efficiency, the fluorescence quantum yield needs to be enhanced. Intuitively, it is believed that this could be achieved by adding fluorenyl groups at the side of the 8M-4P-NPD molecule because fluorene systems usually show strong fluorescence. A scheme of the molecular structure and the HOMO, HOMO-1, LUMO and LUMO+1 of the new material "8M-4P-FPD" is illustrated in Fig. 6.26. As in case of 8M-4P-NPD, it is reasonable to consider the superposition of LUMO and LUMO+1 (HOMO and HOMO-1) when investigating the overlap of HOMO and LUMO (cf. Appendix A.3). In comparison to 8M-4P-NPD (cf. Fig. 6.15), the overlap of HOMO and LUMO is not strongly effected by the fluorenyl groups.

Quantum chemical calculations of the energy eigenvalues are carried out after material testing and will be presented in more detail in Sec. 6.3.
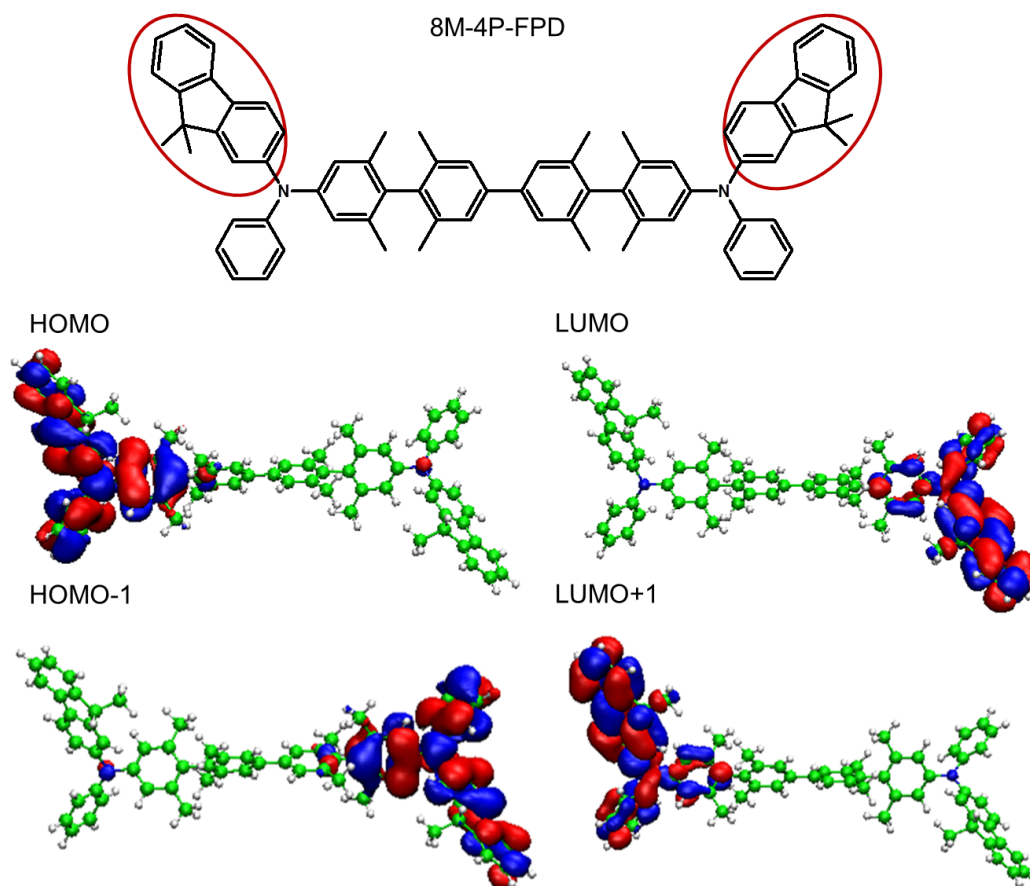
Figure 6.26: Molecular structure of 8M-4P-FPD and distribution of HOMO, HOMO-1, LUMO and LUMO+1 calculated using HF // SCC-DFTB. The additional fluorenyl groups (red marked) are expected to increase the fluorescence quantum yield and hence the radiative efficiency.

Thin film properties and energy levels

A PL spectrum of 8M-4P-FPD is shown in Fig. 6.27 (a) in comparison to the materials 4P-NPD and 8M-4P-NPD. For 8M-4P-FPD, the measurement of the PL emission has been performed at 360 nm which corresponds to the peak absorption of 8M-4P-FPD. The peak emission of 8M-4P-FPD is at 390 nm which corresponds to a singlet energy of $S_1^{8M-4P-FPD} = 3.18$ eV. This is about 0.2 eV higher than the singlet energy of 8M-4P-NPD. Furthermore, 8M-4P-FPD shows emission below 380 nm, which is not in the visible wavelength regime and thus a loss mechanism for conventional OLED applications. From the phosphorescence spectrum (Fig. 6.27 (b)) it can be seen that the spectrum of 8M-4P-FPD is shifted to smaller wavelengths compared to 4P-NPD and 8M-4P-NPD. This leads to a triplet level of $T_1^{8M-4P-FPD} = 2.39$ eV. The singlet/triplet splitting of 8M-4P-FPD is $E_{ST}^{8M-4P-FPD} = 0.79$ eV and therefore slightly higher than that of 8M-4P-NPD and 4P-NPD ($E_{ST}^{4P-NPD} = 0.71$ eV, $E_{ST}^{8M-4P-NPD} = 0.70$ eV). The PL-QY of 8M-4P-FPD is $14 \pm 4\%$. This is about a factor of 3 lower than that of 8M-4P-NPD ($42 \pm 13\%$). Due to the low PL-QY, a significant improvement in EQE compared to 8M-4P-NPD is not expected when 8M-4P-FPD is used as EML inside an OLED structure. However, due to increased triplet level in comparison to 8M-4P-NPD, 8M-4P-FPD is a promising candidate for TH by a green emitter.
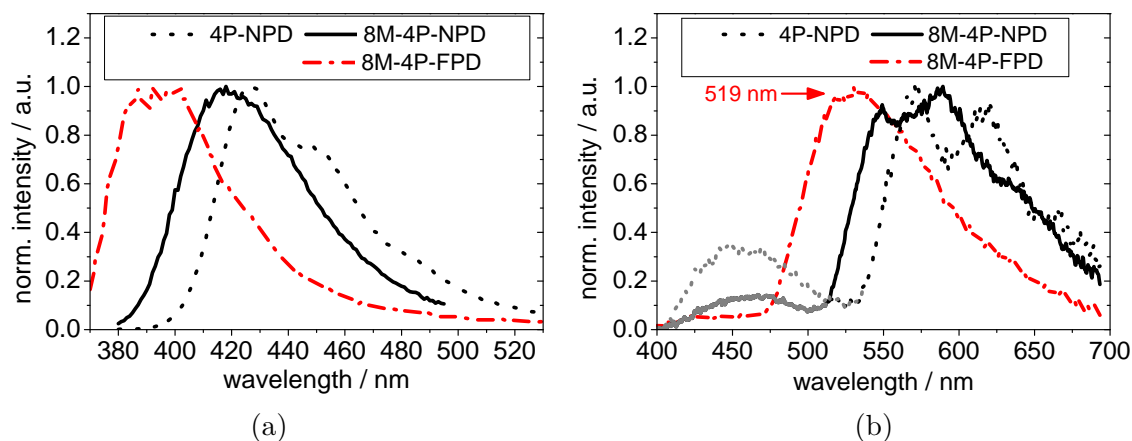

Figure 6.27: PL spectrum (a) and phosphorescence spectra (b) of single layers of 8M-4P-FPD in comparison to 4P-NPD and 8M-4P-NPD. The spectra of 8M-4P-FPD are shifted to smaller wavelength, leading to increased singlet and triplet energy levels compared to 4P-NPD and 8M-4P-NPD.

Blue OLEDs - variation of blocker materials

Despite the fact that 8M-4P-FPD is not a very promising material with regard to its emission spectrum and PL-QY, it is worth to be tested as EML in an OLED structure because of its potential for TH applications. The HOMO and LUMO energies of 8M-4P-FPD are -5.12 eV and -1.6 eV, respectively. These are exactly the same values

as obtained for 8M-4P-NPD. It can be expected that like in case of 8M-4P-NPD, the electron injection into 8M-4P-FPD is hindered and that the exciton recombination zone is close to the HBL interface. As HBL, the materials TPBI, BPhen, SPPO1, and UGH2 are tested, while the EBL is varied among TAPC and TCTA. The choice of blocker materials is motivated by the singlet energy level, which needs to be higher than that of 8M-4P-FPD to ensure singlet confinement in the EML. The used OLED structure and a proposed energy level diagram are shown in Fig. 6.28 (a) and (b).
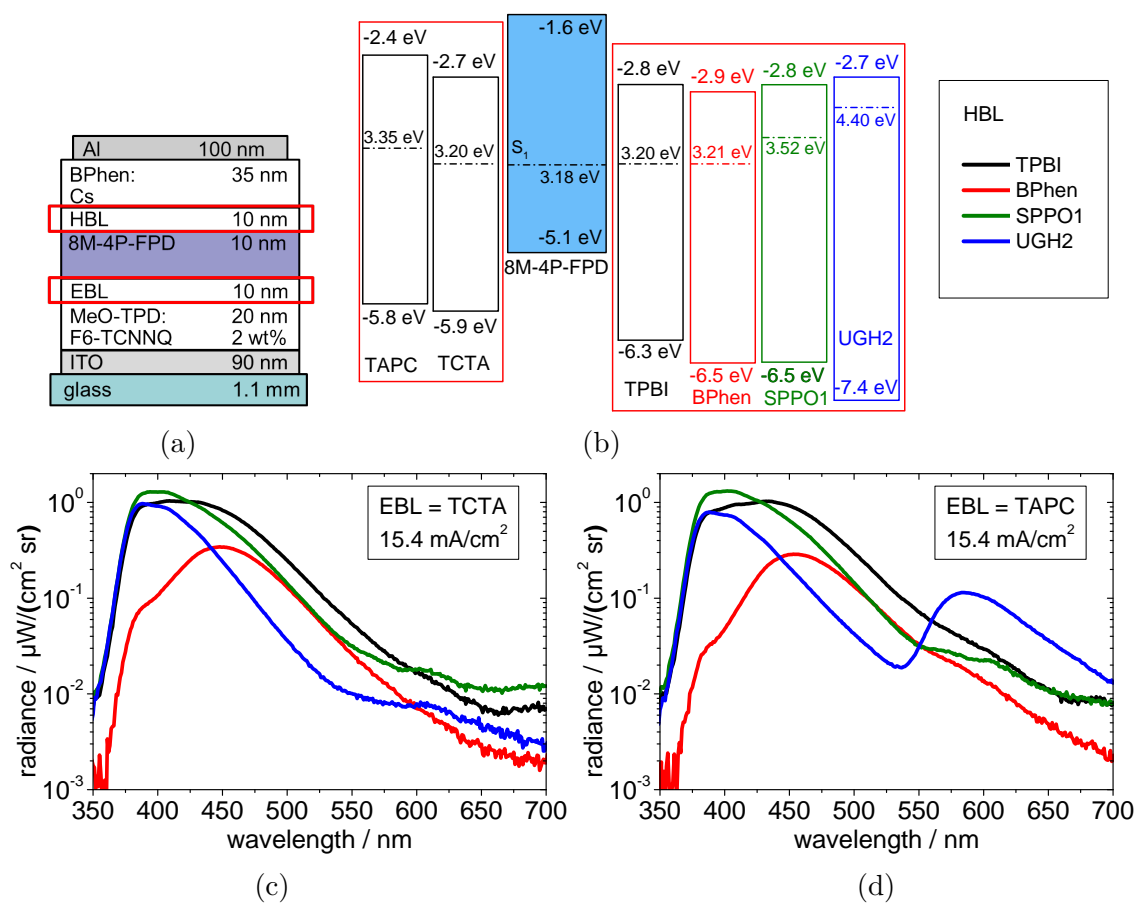
Figure 6.28: OLED layer structure (a), proposed energy level diagram (b), and spectral emission (c,d) of 8M-4P-FPD blue OLEDs using different HBLs and EBLs. For TPBI and BPhen, emission from exciplexes is observed rather than from 8M-4P-FPD. Highest intensities are observed for the SPPO1 OLEDs.

It is interesting to analyze the spectral emission (Fig. 6.28 (c) and (d)): When TPBI is used as HBL, the emission spectra show a peak emission at 430 nm, which is independent of the EBL material. However, the singlet level of TPBI is 3.2 eV which corresponds to a wavelength of 388 nm. Hence, this emission cannot result from TPBI, but is rather expected to result from an exciplex formed by TPBI and 8M-4P-FPD. This confirms the assumption that the exciton generation zone is close

to the HBL interface. A similar observation is obtained for the BPhen OLEDs. Here, the emission peak is at 450 nm. Again this does not fit to the singlet level of BPhen (3.21 eV) and indicates emission from an exciplex.

Using SPPO1, the highest emission intensity of all blocker variations is obtained. The emission peak is at 390 nm, i.e. emission from 8M-4P-FPD is present. At about 600 nm, very weak emission can be observed, which is again assigned to emission from an exciplex formed by SPPO1 and 8M-4P-FPD. For UHG2 which has the highest LUMO energy of -2.9 eV and should lead to best electron injection with respect to the here tested blocker materials, emission from 8M-4P-FPD can be observed for both EBLs TCTA and TAPC. In case of TAPC a strong contribution of orange light at 590 nm is observed, while for TCTA this additional exciplex emission is very weak in comparison to the 8M-4P-FPD emission. It is not clear, why exactly for the UGH2 OLEDs the exciplex emission is so strongly dependent on the choice of the EBL material since for the HBLs BPhen and TPBI no influence on the emission intensity of the exciplex on the EBL is observed.

In conclusion, only SPPO1 OLEDs showed reasonable emission spectra which correspond to 8M-4P-FPD emission. Hence, it is only meaningful to investigate the lifetime and efficiency of these devices as shown in Fig. 6.29 for a constant current density of 4 mA/cm² which corresponds to a luminance of about 15 cd/m².

(a)   (b)
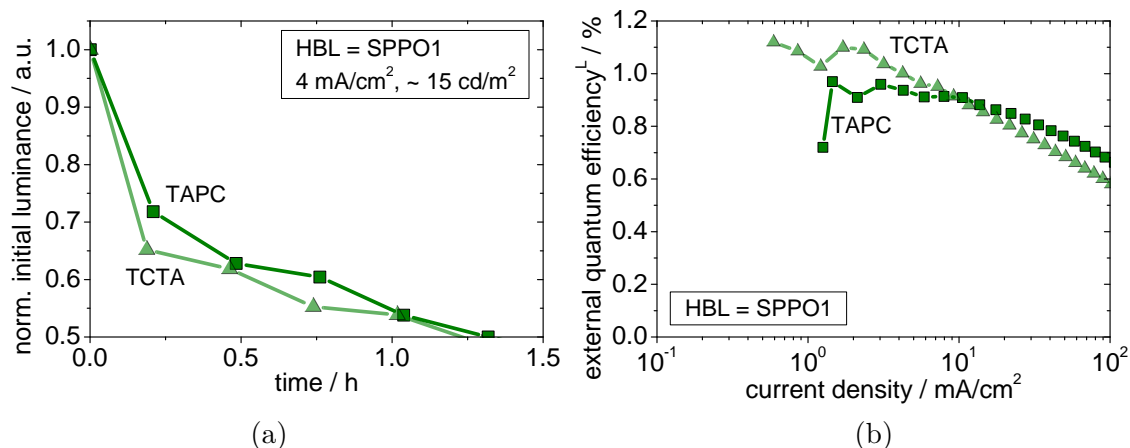
Figure 6.29: Normalized luminance versus time (a) and EQE^L versus current density for the 8M-4P-FPD OLEDs comprising SPPO1 as HBL and TCTA or TAPC as EBL. The superscript L indicates that the efficiency is calculated using the assumption of a Lambertian emission characteristic.

The luminance drop over time is not significantly influenced by the use of the EBL. Both blockers, TCTA and TAPC provide a lifetime of 1.3 h. This is better than OLEDs comprising 4P-NPD, which show a lifetime of less than 30 min at 4 mA/cm² (cf. Fig. 6.4 (c)). Nevertheless, degradation during the goniometer measurement is

observed for the 8M-4P-FPD OLEDs[12]. Therefore, the efficiencies (Fig. 6.29 (b)) are calculated using the assumption of a Lambertian emission characteristic, which is indicated by the superscript L. For low current densities (< 10 mA/cm²), the TCTA OLED shows a slightly higher efficiency. But due to the stronger roll-off, the TAPC OLED exhibits a higher EQE at high current densities. However, the maximum absolute EQE^{L} is in the range of 1% and therefore lower than the 1.5% achieved with 8M-4P-NPD (cf. Fig. 6.19 (f)).

TH by Ir(ppy)$_3$

Since the aim of the development of new blue emitters is TH by a green phosphorescent emitter, TH OLEDs comprising Ir(ppy)$_3$ with a thickness variation of the intrinsic 8M-4P-FPD layer are studied (Fig. 6.30).

Regarding the spectral emission at 15.4 mA/cm² (Fig. 6.30 (b)), the typical TH behavior of increasing green emission with decreasing layer thickness can be observed. Thus, TH from 8M-4P-FPD to Ir(ppy)$_3$ is probable. Interestingly, the green emission is very strong compared to the case of 8M-4P-NPD (cf. Fig. 6.20 (c)). It is most likely that this is due to a better triplet transfer from 8M-4P-FPD to Ir(ppy)$_3$, since the triplet level (2.39 eV) is resonant with that of Ir(ppy)$_3$ (2.40 eV), while for 8M-4P-NPD the triplet level (2.27 eV) is significantly lower.

For $x = 3$ nm a max. EQE^{L} of 10% is obtained. This is much higher than the 3% for the 8M-4P-NPD:Ir(ppy)$_3$ OLED presented in Sec. 6.2.1 (Fig. 6.19 (f)), and indicates a better TH efficiency.
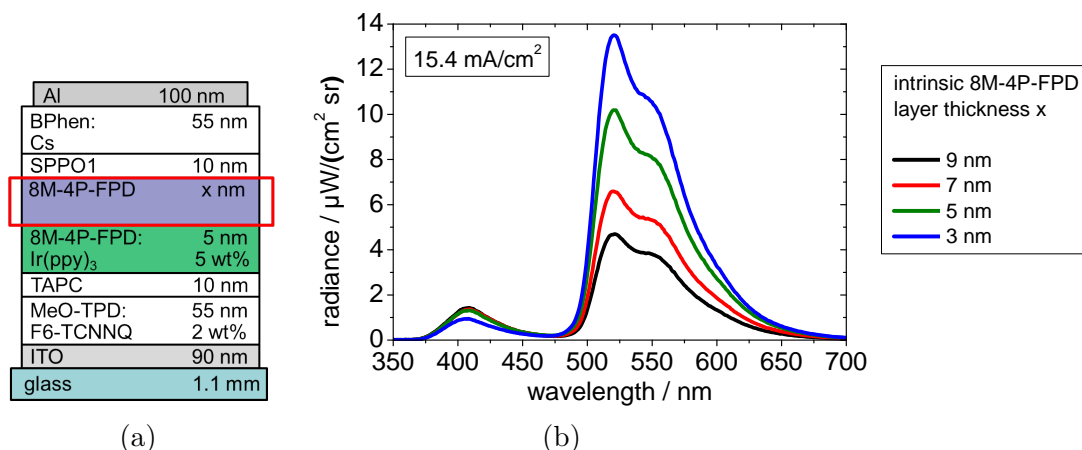
Figure 6.30: OLED layer structure (a) and spectral emission (b) of the TH 8M-4P-FPD OLEDs with varying intrinsic 8M-4P-NPD layer thickness x. The typical TH behavior of decreasing phosphorescent (green) emission with increasing x proves the presence of TH from 8M-4P-FPD to Ir(ppy)$_3$.

---

[12]Due to the lower luminance, 8M-4P-FPD OLEDs need a higher driving current than the 4P-NPD OLEDs to ensure a sufficient signal-to-noise ratio.
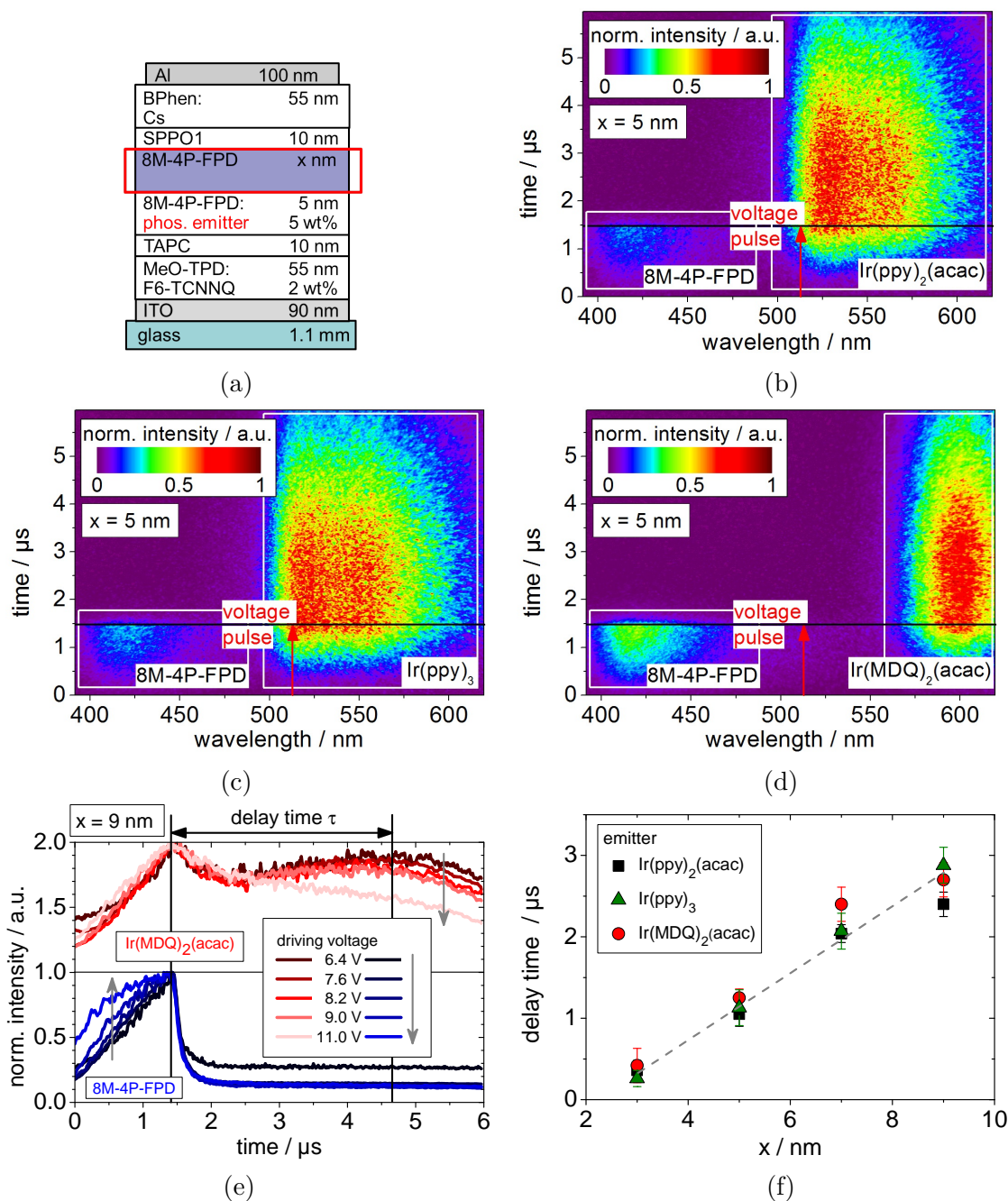
Time- and spectrally-resolved measurements

To further investigate the TH process for 8M-4P-FPD, a study of time- and spectrally-resolved emission using the streak-camera and TH OLEDs with different phosphorescent emitters, similarly to the experiments presented in Sec. 6.1.2 (Fig. 6.10), is performed. A voltage pulse of 2 µs and a voltage of 7.6 V (with a frequency of 30 kHz) is used in this experiment. $Ir(ppy)_2(acac)$, $Ir(ppy)_3$, and $Ir(MDQ)_2(acac)$ are applied as phosphorescent emitters, respectively. Simultaneously, the intrinsic layer thickness x of 8M-4P-NPD is varied (3, 5, 7, and 9 nm). Figure 6.31 (a) shows the layer structure of the OLEDs under investigation. The thickness x describes the distance between exciton generation zone and TH zone.

The normalized time- and spectrally-resolved streak camera images are shown in Fig. 6.31 (b-d) at $x = 5$ nm for $Ir(ppy)_2(acac)$, $Ir(ppy)_3$, and $Ir(MDQ)_2(acac)$, respectively. The duration of the voltage pulse is indicated with a red arrow. The two different emitters emitter can be nicely distinguished by wavelength and transient behavior. While the signal at small wavelengths (390 to 490 nm) and with the short decay belongs to 8M-4P-FPD, the delayed and extended signal at longer wavelengths (490 to 620 nm) is associated with the phosphorescent emitter. The strong emission of the phosphorescent emitters after the voltage pulse is switched off results from TH from 8M-4P-FPD. This is not surprising, since TH from 8M-4P-FPD to $Ir(ppy)_3$ was shown previously (cf. Fig. 6.30). Due to the fact that $Ir(ppy)_2(acac)$ and $Ir(MDQ)_2(acac)$ have a lower triplet energy than $Ir(ppy)_3$, TH was also expected.

It is interesting to analyze the delay time τ between the fluorescent and the phosphorescent signal (cf. Fig. 6.10). As an example, the integrated intensity profiles for different applied voltages are given in Fig. 6.31 (e) for the $Ir(MDQ)_2(acac)$ OLED with $x = 9$ nm. The used wavelength ranges for the integrated intensities are indicated with white rectangles in Fig. 6.31 (d). Furthermore, the intensity profiles of the two different emitters are normalized and vertically displaced for clarity. For the blue emitter 8M-4P-FPD, a relative increase in emission intensity is observed with increasing voltage. The reason is that with higher driving voltage (field), the charge carrier mobility increases and the electrons and holes meet and recombine at earlier times in the EML.[214] For 6.4 V the intensity curve of 8M-4P-FPD shows a constant offset after 1.5 µs compared to the intensity curves at other voltages. This is an indication of a poor signal-to-noise, and has no physical relevance.

The intensity profile of the red emitter $Ir(MDQ)_2(acac)$ is shown in Fig. 6.31 (e). Similarly to the blue emitter, a first maximum at about 1.5 µs can be found, which results either from direct recombination on $Ir(MDQ)_2(acac)$ or from singlet transfer. More importantly, the second maximum is at about 4.6 µs. As discussed in Sec. 6.1.2, this delayed maximum results from emission of triplets after diffusion and can be correlated to TH. With higher voltage, this second maximum vanishes since annihilation process become more relevant which are reducing the relative triplet emission.

(a)

(b)

(c)

(d)

(e)

(f)

Figure 6.31: OLED layer structure (a) and time- and spectrally-resolved intensities for different phosphorescent emitter ($Ir(ppy)_2(acac)$, $Ir(ppy)_3$, and $Ir(MDQ)_2(acac)$) at $x = 5$ nm (b-d) using a voltage pulse of 2 µs and 7.6 V. The normalized integrated intensity profiles (integration range indicated with a white rectangle in (d)) for $x = 9$ nm and the OLEDs comprising $Ir(MDQ)_2(acac)$ indicate that the delay time τ (= time between the peak emission of the two emitters) is independent of the applied voltage (e). The spectra of different emitters in (e) are vertically displaced for clarity. The delay time τ increases with increasing distance x, proving TH by $Ir(ppy)_2(acac)$, $Ir(ppy)_3$, and $Ir(MDQ)_2(acac)$, respectively (f).

The position of the emission maxima and therefore the delay time τ is independent of the driving voltage, i.e. the diffusion of triplets is not influenced by charge carriers.

The dependence of the delay time τ on the distance x for the different phosphorescent emitters is shown in Fig. 6.31 (f). The typical linear increase of τ with increasing x is obtained. Taking errors of the determination of the position of the maximum into account, the slope of the line is independent of the phosphorescent emitter system. For the emitter 8M-4P-FPD the slope is steeper than for 4P-NPD (cf. Fig. 6.10), indicating a slower triplet transport than on 4P-NPD.

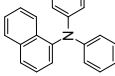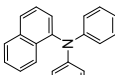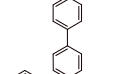## 6.3   Comparison to Quantum Chemical Calculations

A summary of different simulated and experimentally found properties of the four materials NPD, 4P-NPD, 8M-4P-NPD, and 8M-4P-FPD is given in Tab. 6.4. NPD is included in this comparison, since the latter three emitters are all NPD derivatives. The data which is within a 10% error in comparison to any of the experimentally found values is red marked. For the theoretical calculations five methods are available to calculate HOMO, LUMO, singlet, and triplet energy (cf.Sec. 5.6.2). For 8M-4P-FPD the calculations using method 2 could not be completed within this work. Furthermore, a comparison of the absolute values to the preliminary results obtained in Sec. 6.2.1 should be taken with care, since there the influence of the methyl groups was neglected. Although the experimental values are in some cases very close to the simulated ones, none of the theoretical methods is able to describe the energies of all four emitters simultaneously with sufficient accuracy. Especially the prediction of the LUMO energy seems to be problematic.

Most important for this study is the prediction of the singlet and triplet energies: For the singlet level, the methods 2, 3, and 4 show a good agreement with the experimental data. Also the experimentally observed trend of increasing singlet energy (from NPD, 4P-NPD, 8M-4P-NPD to 8M-4P-FPD) is more or less reproduced. Only the triplet energies of method 4 are within the 10% error compared to the experimental data for all materials under study. However, method 5 exclusively predicts the experimentally observed increase in triplet energy from NPD, 4P-NPD, 8M-4P-NPD to 8M-4P-FPD.

The comparison between simulation and experimental values is further hindered by the contradicting experimental data. For example, the triplet energy of 4P-NPD is reported to be 2.3 eV[115], but is found to be 2.19 eV in this study.

Table 6.4 also lists properties like density, evaporation temperature, PL-QY in solution and thin film, and the highest experimentally achieved EQE, when the material is used as a bulk emitter inside an OLED structure. For unknown reasons, the density of 8M-4P-FPD (1.3 g/cm²) is higher than that of the other materials (1.0 to 1.1 g/cm²). The evaporation temperature increases with increasing molecular size.

Table 6.4: Summary of calculated and measured properties of the materials NPD, 4P-NPD, 8M-4P-NPD, and 8M-4P-FPD to theoretical calculations. Data marked in red is within a 10% error in comparison to any of the experimentally found values.

	NPD	4P-NPD	8M-4P-NPD	8M-4P-FPD
molecular structure				
theo. HOMO [eV]*	-5.02[1]/-4.94[2]/-4.88[3]/-4.84[4]/-4.84[5]	-5.17[1]/-5.08[2]/-5.04[3]/-4.95[4]/-4.97[5]	-5.20[1]/-5.15[2]/-4.99[3]/-5.03[4]/-4.94[5]	-5.05[1]/—/-4.96[3]/-4.92[4]/-4.89[5]
exp. HOMO [eV]#	-5.5[a][115]	-5.7[b][115]	-5.12[b]	-5.12[b]
theo. LUMO [eV]*	-1.29[1]/-1.43[2]/-2.38[3]/-1.48[4]/-2.54[5]	-1.33[1]/-1.50[2]/-2.41[3]/-1.60[4]/-2.61[5]	-1.26[1]/-1.39[2]/-2.35[3]/-1.39[4]/-2.46[5]	-1.00[1]/—/-1.98[3]/-1.09[4]/-2.09[5]
exp. LUMO [eV]	-2.4[115]	-2.3[b][115]	-1.6[c]	-1.6[c]
theo. $\Delta E_{\text{HOMO-LUMO}}$ [eV]	3.73[1]/3.06[2]/1.50[3]/3.00[4]/1.94[5]	3.84[1]/3.58[2]/2.63[3]/3.35[4]/2.36[5]	3.94[1]/3.76[2]/2.64[3]/3.64[4]/2.48[5]	4.05[1]/—/2.98[3]/3.83[4]/2.80[5]
exp. $\Delta E_{\text{HOMO-LUMO}}$ [eV]	3.10	3.40	3.52	3.52
theo. S_1 [eV]*	3.19[1]/3.00[2]/2.54[3]/2.86[4]/2.38[5]	3.27[1]/3.07[2]/2.64[3]/2.89[4]/2.41[5]	3.28[1]/3.14[2]/2.64[3]/3.05[4]/2.48[5]	3.56[1]/—/2.98[3]/3.34[4]/2.80[5]
exp. S_1 [eV]	2.78[d][115]/2.81[d]	2.91[d][115]/2.90[d]	2.97[d]	3.18[d]
theo. T_1 [eV]*	2.66[1]/2.45[2]/2.49[3]/2.27[4]/2.27[5]	2.68[1]/2.46[2]/2.61[3]/2.28[4]/2.33[5]	2.67[1]/2.47[2]/2.61[3]/2.31[4]/2.43[5]	2.82[1]/—/2.80[3]/2.57[4]/2.75[5]
exp. T_1 [eV]§	2.26[115]/2.18[e]	2.30[115]/2.19[e]	2.27[e]	2.39[e]
theo. E_{ST}	0.53[1]/0.55[2]/0.05[3]/0.59[4]/0.11[5]	0.59[1]/0.61[2]/0.03[3]/0.61[4]/0.08[5]	0.61[1]/0.67[2]/0.03[3]/0.74[4]/0.05[5]	0.74[1]/—/0.18[3]/0.77[4]/0.05[5]
exp. E_{ST}	0.63	0.71	0.70	0.79
density [g/cm³][f]	1.1	1.1	1.0	1.3
evap. temp. [°C]	150-190	220-270	~240	~280
PL-QY (sol.) [%]$	12	42	10	30
PL-QY (film) [%]§	26±8	41 ±13	42 ±13	14 ±4
EQE [%][g]	—	4.5	1.5	1.0
TH by Ir(ppy)₃	—	no	yes	yes

[1] HF // B3LYP
[2] B3LYP // B3LYP
[3] HF // TD-SCC-DFTB
[4] SCC-DFTB // B3LYP
[5] SCC-DFTB // TD-SCC-DFTB

[a] UPS
[b] CV
[c] HOMO + opt. gap (transmission measurement)
[d] peak of thin film fluorescence spectrum
[e] peak of thin film phosphorescence spectrum (< 100 K)
[f] profilometer
[g] max. EQE when used as bulk emitter in an OLED structure

* calculations performed by Regina Luschtinetz (Dresden University)
# measured by Markus Hummert (IAPP)
§ measured by Vygintas Jankus (Durham University)
$ measured by Sylke Furkert (IAPP)

The comparison of the PL-QYs and the EQE is interesting, since the radiative efficiency should go hand in hand with the PL-QY. The EQE depends on the charge balance, singlet/triplet ratio, outcoupling efficiency, and radiative efficiency. The radiative efficiency and EQE are proportional and thus also the PL-QY and the EQE.

It can be expected that PL-QY determined from thin films leads to better comparison than a PL-QY determined from solution, since the emitters inside an OLED structure exist also as thin film.

However, the trend of decreasing EQE from 4P-NPD, 8M-4P-NPD to 8M-4P-FPD coincides only partly with the PL-QY: The PL-QY measured in solution of 4P-NPD is 42% and reduced by a factor of 4 for 8M-4P-NPD (10%). This is more or less in agreement with the EQE, which is reduced by a factor of 3. For 4P-NPD and 8M-4P-FPD the PL-QY of a thin film is 41% and 14%, respectively which fits nicely to the EQEs of 4.5% and 1.0%. However, in case of 8M-4P-NPD (8M-4P-FPD) the PL-QY for thin films (solution) does not show the same trend as the EQE which is most likely an effect of poor charge balance as discussed in Sec. 6.2.1.

6.4 Summary and Outlook

In this chapter, the blue bulk emitter 4P-NPD was intensively studied concerning its orientation of transition dipoles, the ability of harvesting triplets, and the potential to build highly efficient white OLEDs. The determination of the orientation of the transition dipoles was found to be isotropic. However, the error of the spectral analysis of the emission of an OLED in the optical minimum was rather large which impeded the exclusion of a preferred horizontal orientation. A reduction of the error is expected, if the forward intensity would be recorded simultaneously with the angular dependent spectra. This would offer a more sophisticated possibility to correct the error introduced by the degradation of the OLED.

Since TH from 4P-NPD by the green emitter Ir(ppy)$_3$ had not been possible due to the lower triplet level, two new emitters 8M-4P-NPD and 8M-4P-FPD were introduced. Quantum chemical considerations showed that these are promising candidates to allow TH by Ir(ppy)$_3$. The investigation of the (time-resolved) spectral emission of TH OLEDs verified these calculations. For the first time TH OLEDs (using 8M-4P-NPD or 8M-4P-NPD as EML) were shown, where TH occurred from a blue bulk emitter to a green phosphorescent emitter. Measurement of the triplet energies supported these findings to some extent. Unfortunately, both new emitters had significant disadvantages compared to 4P-NPD, which impeded the design of highly efficient white OLEDs.

In monochrome OLEDs, 8M-4P-NPD as EML showed relatively low EQE values of almost 1.5% compared to 4.5% of 4P-NPD OLEDs although both materials have a similar PL-QY of about 41%. It is most likely that the reason for the low EQE is the fact that the charge carrier balance in 8M-4P-NPD OLEDs was dramatically decreased

due to the high LUMO energy barrier between the EML and HBL interface (> 1 eV). White TH-OLEDs comprising 8M-4P-NPD as blue bulk emitter and efficiencies up to 11.9 lm/W (4% EQE) at 1,000 cd/m² were demonstrated. Doping 8M-4P-NPD into a suitable matrix material, which allows good injection of both charge carrier species and a good singlet transfer to 8M-4P-NPD might be a possibility to increase the EQE further to the level of 4P-NPD. As a result, this would also lead to higher efficiencies for white TH OLEDs.

In addition to a low EQE of 1%, the OLEDs with the second new blue emitter 8M-4P-FPD exhibited low lifetimes. Together with fact that the emitter showed emission below 380 nm, which is not detectable with the human eye, 8M-4P-FPD is seen as a less promising material for efficient white TH OLEDs.

It is suggested that the orientation of 8M-4P-NPD and 8M-4P-FPD transition dipoles, as well as the singlet and triplet diffusion length should be determined in future experiments.

Theoretical calculations are a helpful tool which can to some extent predict trends or energy values, if experimental data of materials with a similar chemical structure is available. However, no simulation method simultaneously predicted all relevant energy values (HOMO, LUMO, S_1, T_1) in a satisfying manner for the materials used in this work. Theoretical calculations, in conjunction with the synthesis and test of new blue fluorescent (bulk) emitters, are seen as a promising route to achieve highly efficient white TH OLEDs.

These emitters should be designed and investigated with respect to:

- a singlet energy S_1 between 2.5 and 3.1 eV (500 and 400 nm),

- a triplet energy T_1 higher than 2.4 eV (515 nm) to ensure TH by Ir(ppy)$_3$ or higher than 2.38 eV (521 nm) to ensure TH by Ir(ppy)$_2$(acac)

- an efficient emission from the singlet state when used as a bulk emitter, i.e. a high PL-QY ($> 40\%$) and a high radiative efficiency,

- suitable LUMO (-2.3 $\pm$ 0.2 eV) and HOMO (-5.3 $\pm$ 0.2 eV) energies providing good charge injection for electrons and holes, and leading to a charge carrier balance close to unity.

Again, preferentially hole or electron transporting properties to ensure that the exciton generation zone is close to one of the blocking layers would be beneficial for the design of TH OLEDs. Also, a horizontal alignment of the transition dipoles is desired. These two latter issues as well as a long lifetime are preferred but are not conditional requirements.

7 Singlet Diffusion Length

In this chapter, the singlet diffusion in 4P-NPD is studied based on singlet quenching and spectral emission intensity of OLEDs. First, the working principle of these OLEDs and quenching mechanisms are discussed. To fit the experimentally obtained emission, a model is introduced to solve the diffusion equation analytically. The influence of fit parameters, including the exciton generation zone width and direct charge carrier recombination, are discussed. Finally, the singlet exciton diffusion length for a series of applied current densities is investigated. In the second part of this chapter, an approach to determine the singlet diffusion length in a pure layer is investigated. The emission of an optically excited 4P-NPD layer containing one or two quenching layers is studied by a simulation of different diffusion profiles.

In the previous chapter, the importance of understanding and controlling excitonic processes in OLEDs to achieve high efficiencies has been discussed. Clearly, the triplet diffusion length is important in TH OLEDs. However, avoiding singlet transfer from the fluorescent emitter to the phosphorescent emitter is crucial for the design of efficient TH OLEDs. Therefore, the knowledge of the singlet diffusion length is also mandatory.

The common methods to determine the exciton diffusion length are based on optical excitation, like photo-current measurements[215–219] and time- or spectrally-resolved PL quenching[220–228]. However, these techniques have certain disadvantages resulting in a wide spread of the reported values of the diffusion length, even for well known materials. Additionally, optical excitation leads to a broad generation zone of the excitons, the profile of which is usually an unknown parameter, complicating the analysis. Also, when using an additional quenching layer, optical interference effects and energy transfer to the quencher have to be taken into account.[229] Typically, the singlet diffusion length is in the range of a few to some tens of nanometers. However, values above 1 μm have also been reported.[230]

In contrast, electrical generation of excitons in an adequate OLED structure can lead to a thin and well controllable generation zone adjacent to one of the blocking layers.[118, 231–233] Furthermore, the use of an OLED reflects the real-world situation for excitons more closely than PL experiments, where e.g. polaron quenching is not present.

In 2009, Julia Wünsche investigated the triplet diffusion length in 4P-NPD using TH OLEDs at IAPP.[118, 234] The usually lost triplets of 4P-NPD diffuse through a spacer layer towards a phosphorescent dopant $(Ir(MDQ)_2(acac))$, are transferred to the lower lying triplet level of the dopant, from which they subsequently emit light. By varying the thickness of the spacer and measuring the emission of the dopant, the triplet diffusion length is calculated and found to be 11 ± 3 nm. Here, the weak

micro-cavity effects were overcome by an appropriate adjustment of the transport layer thickness, which kept the emission zone at a constant position inside the device. However, one problem was that the phosphorescent emitter also shows direct charge carrier recombination, resulting in additional emission, which has to be considered in the analysis. Furthermore, it turned out to be important to take into account that the generation zone has a non-negligible width.

For singlets, this technique has rarely been used so far and in addition the width of the exciton generation zone was not considered in previous studies.[74, 75]

7.1   Electroluminescence Quenching

7.1.1   Working principle of the device

The experiments performed are motivated by the results of the TH OLEDs in Sec. 6.1.2 (Fig. 6.8). There, a reduction of 4P-NPD emission was observed, if a phosphorescent emitter is placed in proximity to the exciton generation zone: the closer the distance, the stronger the reduction of 4P-NPD emission. The reason is singlet diffusion and transfer from 4P-NPD to the phosphorescent emitter. This transfer is observed independently for all three phosphorescent emitters ($Ir(ppy)_3$, $Ir(dhfpy)_2(acac)$, and $Ir(MDQ)_2(acac)$). In order to investigate the singlet diffusion length in 4P-NPD, the incorporation of $Ir(ppy)_3$ as phosphorescent dopant is most beneficial since only 4P-NPD emission and no additional emission due to TH is observed.

A proposed energy level scheme of the devices under investigation is shown in Fig. 7.1 (a). Charge carriers are injected via ITO and Al into the doped transport layers. Passing the thin blocking layers, the charges reach the EML. As 4P-NPD is a primarily hole transporting material, the exciton generation zone can be assumed to be close to the HBL. According to spin statistics, 25% singlets and 75% triplets are generated. Both exciton species can diffuse before they recombine.

Triplets formed on 4P-NPD can diffuse towards $Ir(ppy)_3$. Since the triplet energy of $Ir(ppy)_3$ is higher than that of 4P-NPD, triplets will remain on 4P-NPD molecules. Because 4P-NPD is a fluorescent emitter, they will decay nonradiatively. Singlets have the possibility to decay radiatively before they reach $Ir(ppy)_3$. The generated photons might be coupled out and contribute to the emitted spectrum. A singlet diffusion into the BPhen blocking layer is not possible, due to the 0.3 eV higher singlet level. As indicated in Fig. 7.1 (b), singlets reaching $Ir(ppy)_3$ are transferred to its lower lying singlet level. Due to the strong spin orbit coupling, the singlet excitons undergo intersystem crossing to the triplet state of $Ir(ppy)_3$. Finally, these triplets are then back-transferred to the 4P-NPD host, where they undergo a nonradiative decay. In this manner, the 4P-NPD singlets are quenched by the phosphorescent dopant. Hence, the 4P-NPD:$Ir(ppy)_3$ layer is referred to as quenching layer (QL). A variation of the EML thickness d will lead to a different intensity of outcoupled

emission from singlets and the emitted spectra can be used to determine the singlet diffusion length. By using a reference device where the dopant $Ir(ppy)_3$ is omitted, the number of quenched singlets can be obtained. In total, 16 OLEDs with eight different thicknesses d are investigated. Subtracting the emission of the $Ir(ppy)_3$ OLED from the reference OLED leads to the number of quenched singlets. The use of reference devices furthermore offers the advantage to overcome micro-cavity effects.
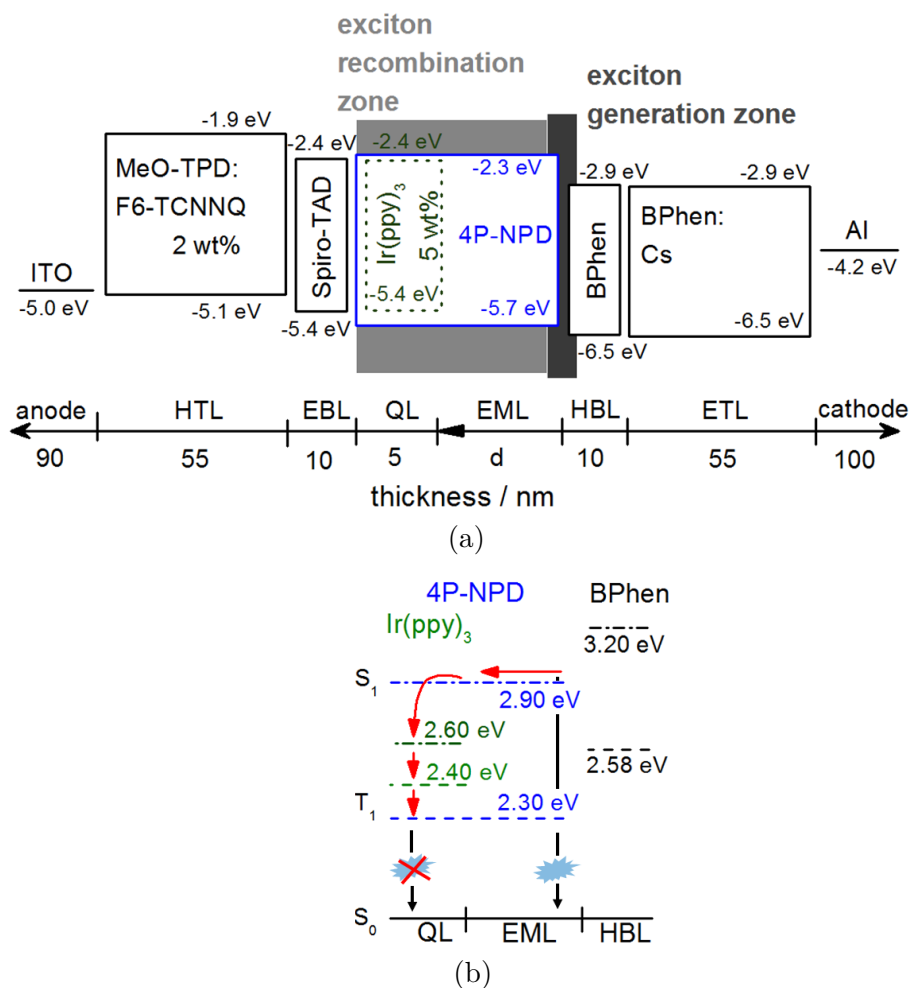
Figure 7.1: Proposed energy level diagram (a) and singlet transfer processes (b) of the blue fluorescent OLEDs. Due to the high hole mobility of 4P-NPD, the exciton generation zone (dark gray box) is assumed to be located at the 4P-NPD/BPhen interface. The singlets can diffuse in the direction of $Ir(ppy)_3$, and can decay anywhere in the 4P-NPD layer (light gray box). Singlets reaching $Ir(ppy)_3$ will be transferred to the singlet level of $Ir(ppy)_3$. The singlet exciton undergoes intersystem crossing to the triplet state of $Ir(ppy)_3$. Finally, the triplet is back-transferred to the 4P-NPD host and decays nonradiatively.

7.1.2   Theoretical Considerations

In this section, an analytical model based on boundary conditions to calculate the singlet diffusion length in 4P-NPD is presented using thickness dependent emission measurements of the operating OLEDs. The model is adopted from Refs. [118, 231]. For singlet excitons, the one-dimensional steady state diffusion equation (cf. Eq. (3.22)) is given by

$$D\frac{\mathrm{d}^2 n(x)}{\mathrm{d}x^2} - \frac{n(x)}{\tau} + G_0 e^{-x/g} = 0. \tag{7.1}$$

The first term describes the diffusive transport, the second the monomolecular decay, and the third the generation of excitons along the diffusion direction x. Here, $n(x)$ is the singlet exciton density and D is the diffusion coefficient, which is assumed to be isotropic and constant in the whole 4P-NPD layer. The diffusion length L and the diffusion coefficient D are connected via the exciton lifetime τ:

$$L = \sqrt{D\tau}. \tag{7.2}$$

It is very likely that the generation zone in OLEDs is not a delta-shaped peak at the interface where holes and electrons meet, but somewhat smeared out. The generation rate at $x = 0$ is given by G_0, and g is the distance from the interface when G_0 is decreased by a factor of $1/e$. Annihilation mechanisms such as SSA, STA, or SPA are neglected. Furthermore, the singlet exciton current density $j_s(d)$ (or singlet flux) into the QL is given by:

$$j_s(d) = -D\frac{\mathrm{d}n(x)}{\mathrm{d}x}. \tag{7.3}$$

Because the BPhen layer exhibits an efficient energy barrier for 4P-NPD singlets (cf. Fig. 7.1 (b)), it can be assumed that the singlet exciton current through BPhen is negligible, which results in the first boundary condition:

$$\frac{\mathrm{d}n(0)}{\mathrm{d}x} = 0. \tag{7.4}$$

This implies that there is no concentration gradient for the exciton current, so excitons can still exist at the EML/HBL interface. The second boundary condition is obtained by the assumption of perfect quenching of singlets on $Ir(ppy)_3$ molecules. The quenching will be investigated experimentally and results are presented in Sec. 7.1.3 to confirm this assumption. At the interface to the quenching layer, the number of singlets is therefore:

$$n(d) = 0. \tag{7.5}$$

Using the two boundary conditions, Eq. (7.4) and Eq. (7.5), the solution of the

steady state equation (Eq. (7.1)) reads[118]:

$$n(x) = \frac{gG_0\tau}{L^2 - g^2}\left(2\frac{Le^{-d/L} + ge^{-d/g}}{e^{d/L} + e^{-d/L}}\cosh\frac{x}{L} - Le^{x/L} - ge^{-x/g}\right). \tag{7.6}$$

To derive the singlet diffusion length L, the calculated singlet exciton current density $j_s(d)$ needs to be connected to the experimentally accessible radiance of the OLED devices. From the measured radiance $L_e(\lambda, 0°)$ in forward direction, the photon flux PF (number of outcoupled photons) can be calculated using the assumption of Lambertian emission characteristics:

$$PF = \frac{\pi A_{\mathrm{OLED}}}{hc}\int_{380\mathrm{nm}}^{780\mathrm{nm}}\lambda L_e(\lambda, 0°)\mathrm{d}\lambda, \tag{7.7}$$

where A_{OLED} is the active area of the device, λ denotes the wavelength, h the Planck constant, and c the speed of light in vacuum. The Lambertian assumption is chosen to simplify the method. It will be shown in Sec. 7.1.3 that the Lambertian emission is an appropriate simplification. PF of the reference devices without $\mathrm{Ir(ppy)_3}$ represents the number of all singlets, whereas PF of the devices containing $\mathrm{Ir(ppy)_3}$ represents the number of singlets which do not reach the QL. Hence, the singlet flux into the QL for a certain EML thickness d is proportional to the difference:

$$j_s(d) \propto PF_{\mathrm{w/o\,Ir(ppy)_3}}(d) - PF_{\mathrm{w/\,Ir(ppy)_3}}(d). \tag{7.8}$$

The final equation used to fit the data resulting from the spatial derivative of the exciton distribution in Eq. (7.6) reads:

$$j_s(d) = -A\left[\left(e^{\frac{d}{L}} + \frac{g}{L}e^{-\frac{d}{L}}\right)\tanh\frac{d}{L} - e^{\frac{d}{L}} + e^{-\frac{d}{g}}\right] + B. \tag{7.9}$$

The term A is a proportionality constant, including the first factor in Eq. (7.6) and the diffusion coefficient. The additional term B is motivated by direct recombination processes as shown in the work of Wünsche *et al.*[118], who demonstrated a non-negligible electron current through these kind of devices. Furthermore, term B compensates possible changes in charge balance between the $\mathrm{Ir(ppy)_3}$ OLEDs and the reference OLEDs.

7.1.3   Results

Influence of quenching layer thickness

In a preliminary experiment, the optimum thickness for the Ir(ppy)$_3$ doped QL is investigated. Complete quenching of singlets at the QL/EML interface is required to ensure that the second boundary condition (Eq. (7.5)) is fulfilled. In Fig. 7.2 (a), the OLED structure under investigation is shown. Since it is expected that the singlet diffusion length is in the few nanometer regime, an intrinsic 4P-NPD layer thickness of $d = 5$ nm is chosen to ensure a sufficient singlet flux into the quenching layer. The thickness c of the QL is varied between 3, 5, 8, and 12 nm. To ensure equal outcoupling efficiencies for all devices, the p-doped HTL layer thickness is reduced accordingly.

At high voltages, a voltage drop over thicker quenching layers can be observed (Fig. 7.2 (b)), which is expected since the thickness of an intrinsic layer is increased. For a QL thickness of 3 nm, the EQE is slightly higher than for thicker layers (Fig. 7.2 (c)). Accounting for an experimental error of 5%, the EQE curves for 5, 8, and 12 nm overlap and the EQE does not decrease any further. This means that 3 nm are not sufficient to quench 4P-NPD singlets, mainly because there are not enough Ir(ppy)$_3$ molecules. However, at thicknesses $c > 3$ nm, the overlapping EQE curves indicate that no additional quenching effects are present. Therefore, it is concluded that 5 nm QL thickness are enough to sufficiently quench 4P-NPD singlets.

(a)   (b)   (c)
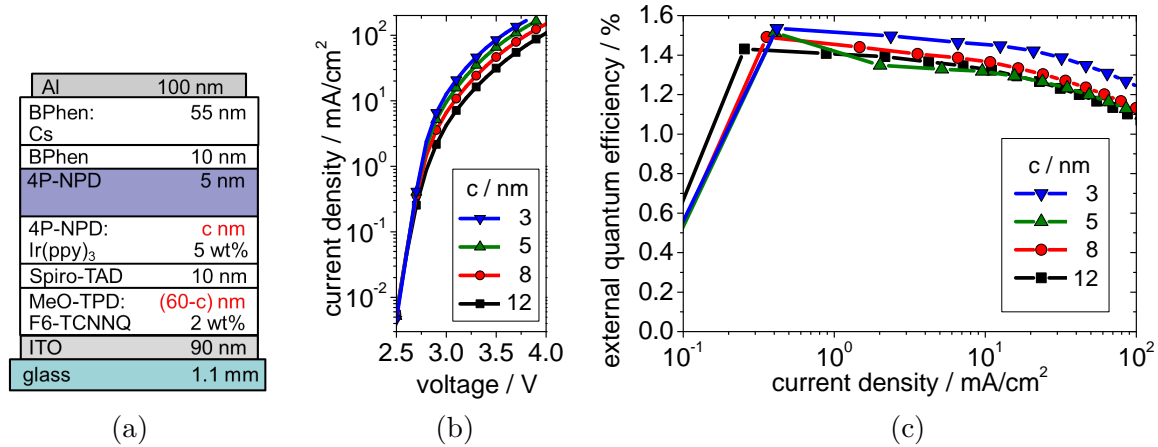
Figure 7.2: OLED architecture (a), IV-characteristics (b), and EQE vs. current density (c) for different QL thicknesses. The variation of the QL thickness c is regarded in terms of quenching properties. For 5, 8, and 12 nm the EQE curves overlap, indicating that a saturation of quenching effects is present, when increasing the number of quenching molecules by using a thicker QL.

IV and spectral emission

In the main experiment, the thickness d between the exciton generation zone and the quenching layer is varied to determine the singlet diffusion length (cf. Fig. 7.1 (a)). To overcome the influence of the optical cavity, a reference device (without $Ir(ppy)_3$) for each thickness d is designed. The IV-characteristics of these devices are shown in Fig. 7.3 (a). The IV curves for one specific distance are in good agreement for the $Ir(ppy)_3$ OLED and for the reference. For high current densities (> 60 mA/cm²), the voltage is slightly higher for the devices containing $Ir(ppy)_3$, which might be a result of hole injection and transport on the $Ir(ppy)_3$ molecules since Spiro-TAD and $Ir(ppy)_3$ have the same HOMO energy of -5.4 eV.

   Figure 7.3 (b) shows the radiance in forward direction for all 16 OLEDs when driven at a current density of 15.4 mA/cm². It can be nicely seen that the radiance decreases significantly with decreasing thickness for the devices containing $Ir(ppy)_3$, which results from the quenching of singlets. On the other hand, the devices without $Ir(ppy)_3$ show a slight increase in emission intensity. This might be a result of a possible change in charge balance and/or an optical effect of the larger cavity. Since one can assume that the same effects are present in the devices with $Ir(ppy)_3$ and the references, this is not a crucial issue. As discussed in Sec. 7.1.1, emission from $Ir(ppy)_3$ is not observed in the measured spectra. This simplifies the presented method, as the photon flux can be directly quantified by the 4P-NPD emission spectrum without any corrections.
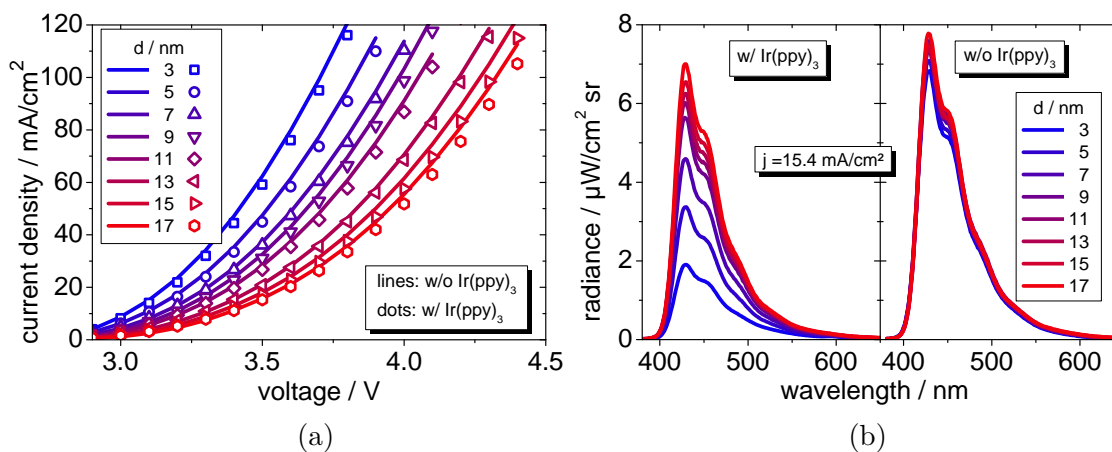
Figure 7.3: IV curves (a) and spectral radiance (b) of the OLEDs under investigation for different ETL thicknesses d. For the IV curves, reference devices (no $Ir(ppy)_3$) are presented by lines and the devices with $Ir(ppy)_3$ are presented by dots. For one specific distance d, the IV curves of the devices with and without $Ir(ppy)_3$ are almost overlapping. The increase in emission with EML thickness for devices containing $Ir(ppy)_3$ results from the lower number of quenched singlets. In contrast, the emission in devices without $Ir(ppy)_3$ is slightly enhanced.

In Fig. 7.4 (a), the normalized emission is shown for different current densities for the reference sample with $d = 3$ nm as an example. The normalized emitted spectra in forward direction do not change significantly with applied current. The angular emission characteristics are expected to be independent of the applied current, since the emission zone is kept at a constant position inside the cavity. Indeed the devices show very similar angular dependent emission intensities at a current density of 15.4 mA/cm² (Fig. 7.4 (b)), further substantiating the fact that optical effects are of minor importance. The angular emission is very close to that of a Lambertian emitter and thus justifies the use of Eq. (7.7) to calculate the photon flux.
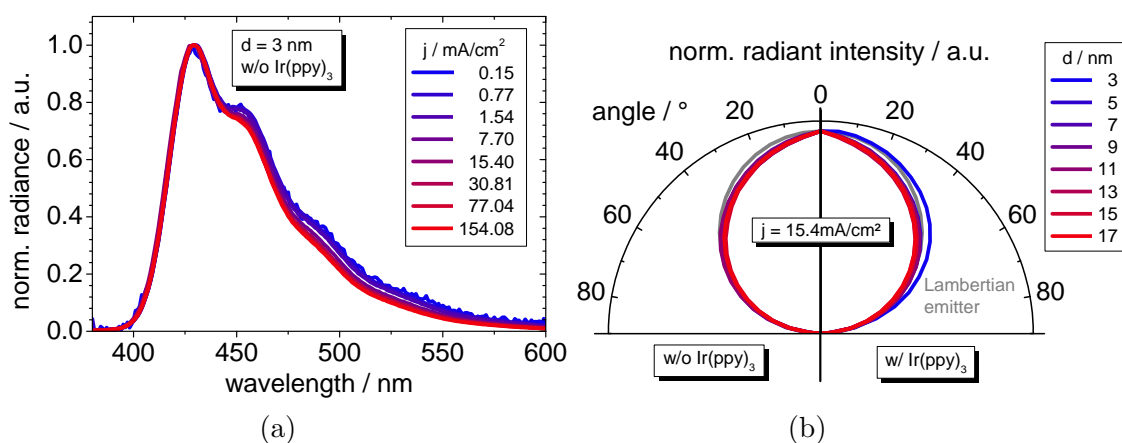

Figure 7.4: Normalized spectral radiance (a) for the device without Ir(ppy)$_3$ and $d = 3$ nm in forward direction for different current densities and normalized radiant intensity in dependence of the viewing angle (b) at a current density of 15.4 mA/cm². The emission spectra do not depend significantly on the applied current and all devices exhibit a similar angular dependence close to a Lambertian emitter.

Width of the generation zone and other fit parameters

In order to investigate the influence of the generation zone width g, the photon flux and the exciton current of non-quenched singlets for different thicknesses d are calculated using Eq. (7.7) and the spectral radiance measurements. The generation zone is the region where holes and electrons meet and the exciton generation takes place. One has to distinguish between generation zone and emission profile. The emission profile results from the radiative decay of the excitons after possible Förster or Dexter transfers, i.e. after diffusion. The generation zone cannot be directly deduced from the emission profile.

Due to the high hole mobility of 4P-NPD, the generation zone is expected to be very narrow in comparison to the whole EML layer thickness and close to the 4P-NPD/BPhen interface. As shown in Fig. 7.5, the photon flux decreases with increasing distance d from the exciton generation zone.

The decrease of PF confirms that the exciton generation takes place next to the HBL. The lines are fits using Eq. (7.9). The width of the generation zone g is varied between 0.1, 0.5, 1, 1.5, and 2 nm. It can be clearly seen that the peak of the fits is shifted to larger distances with increasing g. The other three parameters, the diffusion length L, A, and B are adjusted to fit the experimental data. Basically, A defines the absolute magnitude of the fit, L is responsible for the slope, and B for the non-mono-exponential tail. From $g = 0.1$ to 1 nm, the parameters do not change significantly, and a good fit to the experimental data can be obtained. The diffusion length L varies between 4.2 and 4.3 nm. However, for $g = 1.5$ and 2 nm, the fits deviate more from the experimental data, especially for small distances (3 to 7 nm), and the diffusion length decreases (inset of Fig. 7.5). Therefore, it is concluded that the generation zone has to be smaller than 1.5 nm. In further calculations $g = 0.5$ nm will be used. This corresponds to only one monolayer of 4P-NPD molecules at the EML/HBL interface.
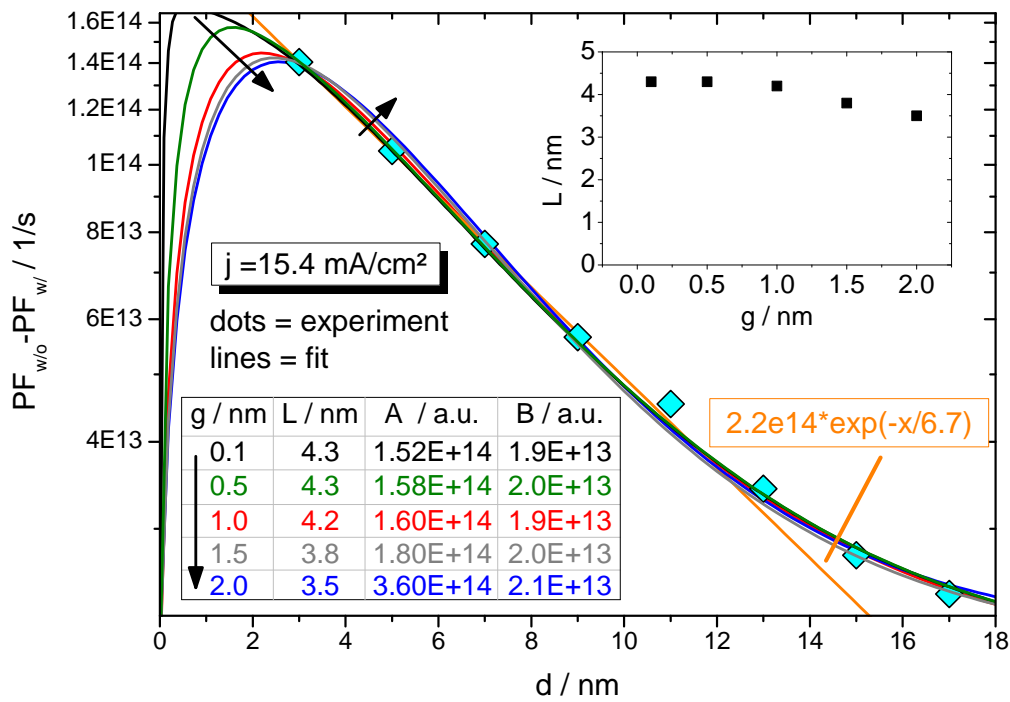
Figure 7.5: Photon flux depending on the distance d at a current density of 15.4 mA/cm² (dots). The fits (lines) according to Eq. (7.9) are describing different broadness g of the generation zone. The fit parameters are given in the table. A simple exponential decay (orange straight line) leads to an overestimation of the diffusion length. Inset: Dependence of the diffusion length L on the width of the generation zone g.

This is lower than $g = 3$ nm obtained by Wünsche *et al.*[118], but still in agreement with the fact that values from 0 to 7 nm lead to reasonable fits for the triplet diffusion length in 4P-NPD. As the generation of singlets and triplets is the result of gathering holes and electrons, the generation zone width should not depend on the exciton species. One reason for the reduced g in this work might be the fact that the EML is significantly thinner (3-18 nm) than in the work of Wünsche *et al.* (10-65 nm).

Using a mono-exponential decay fit (Fig. 7.5, orange line), i.e. assuming a delta-shaped generation zone and no direct recombination processes, a singlet diffusion length L of 6.7 nm is obtained. Underestimating the width of the generation zone and neglecting direct recombination leads to an overestimation of the singlet diffusion length. A more detailed analysis of the width of the generation zone might be obtained from additional experimental data in the small distance regime ($d = 1$ to 3 nm). However, the closer the QL is placed towards the generation zone, the more singlets are quenched and the detectable emission is dramatically lowered.

It is important to mention that this method can give access to the emission profile, which is an important parameter for device modeling and usually hardly accessible in OLEDs. For example, a method to investigate the emission profile claiming nanometer spatial resolution was introduced by Mensfoort *et al.*[130] in 2010, but requires the experimental effort of measuring angle and polarization resolved emission spectra as well as exact optical modeling.

Using the experimental data given in Fig. 7.5, an error of the singlet diffusion length L can be estimated. In Fig. 7.6 (a), the fits for three different values of L are shown. Here, the generation zone width is fixed to $g = 0.5$ nm, and the parameters A and B are adjusted to obtain the best possible fit close to the experimental data. It can be seen that $L = 4.3$ nm provides a good fit, while for 3.8 and 4.8 nm the fits significantly deviate from the experimental values, especially in the range of $d = 5$-13 nm. Therefore, an error of $\pm$ 0.5 nm is a reasonable estimation for the singlet diffusion length L.

It is furthermore interesting to investigate the influence of the fitting parameter B which represents the direct recombination processes of holes and electrons on Ir(ppy)$_3$ (Fig. 7.6 (b)). Again, the same experimental data as in Fig. 7.6 (a) is used and the generation zone width is fixed to $g = 0.5$ nm. First, the singlet diffusion length L is kept constant to 4.3 nm and B is assumed to be $1.9 \cdot 10^{13}$ and 0, respectively (green and red curve in Fig. 7.6 (b)). While the first fit is in good agreement with the experimental data, the second shows a strong linear decrease leading to a significant deviation for $d > 5$ nm. As a logical consequence, the diffusion length L needs to be increased (which leads to a lower slope) to improve the fit. This is intended by the choice of $L = 4.8$ nm (blue curve in Fig. 7.6 (b)) and leads to a slightly improved fit compared to $L = 4.3$ nm. However, the linear decrease at large distances ($d > 7$ nm) remains, demonstrating the necessity of the parameter B.

Keeping the diffusion length $L = 4.8$ nm constant, a fit using $B = 1.6 \cdot 10^{13}$ leads to

reasonable curve close to the experimental data (gray curve in Fig. 7.6 (b)). However, this fit is not as close to the experiment as the first one (green curve) with $L = 4.3$ nm and $B = 1.9 \cdot 10^{13}$. This confirms that the previously estimated error of ± 0.5 nm for the singlet diffusion length is a reasonable value.
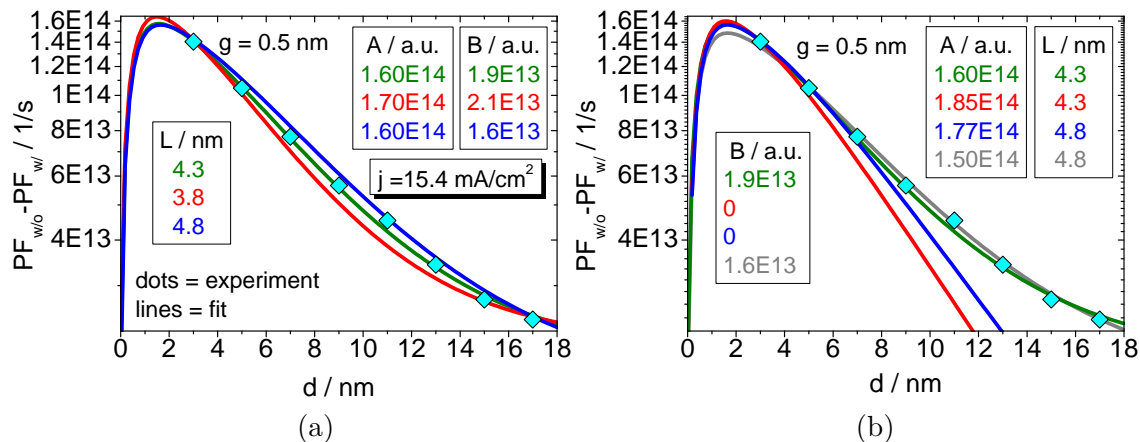

Figure 7.6: Photon flux depending on the distance d at a current density of 15.4 mA/cm² (dots). The fits (lines) according to Eq. (7.9) describe a variation of the singlet diffusion length L (a) and the fit parameter B (b). An error of ± 0.5 nm is a reasonable estimate for the singlet diffusion length L.

Influence of excitation density

The photon flux fitted by Eq. (7.9) is shown in Fig. 7.7 (a) for different applied current densities. As motivated previously, $g = 0.5$ nm is chosen as the width of the generation zone. L, A, and B are adjusted to fit the experimental data. Good fits are obtained for a wide range of current densities. The fitting parameters are summarized in Tab. 7.1 and plotted in Fig. 7.7 (b). The diffusion length L slightly decreases from 4.6 to 4.0 nm for increasing current density, i.e. the exciton density.

In the presented model, the singlet diffusion length should be independent of the applied current. However, at a higher current density, several annihilation processes (STA, SPA, SSA) are present, which lower the exciton current into the quenching layer and explain the decrease in singlet diffusion length. The small decrease with increasing excitation density indicates that secondary effects like annihilation processes, as well as a change in charge balance and a change in generation zone width, which were neglected in the presented model, indeed play a minor role. As shown in the inset of Fig. 7.7 (b), the parameter A increases linearly with current density, while the parameter B (including effects of direct recombination and changes in charge balance) differs slightly for high current densities from the slope of 1. At a low current density of 0.15 mA/cm², a singlet diffusion length of 4.6 ± 0.5 nm is found for 4P-NPD, which is in good agreement with the value of 5.1 ± 1.0 nm obtained by Lunt *et al.*[228] using spectrally-resolved PL measurements for NPD.
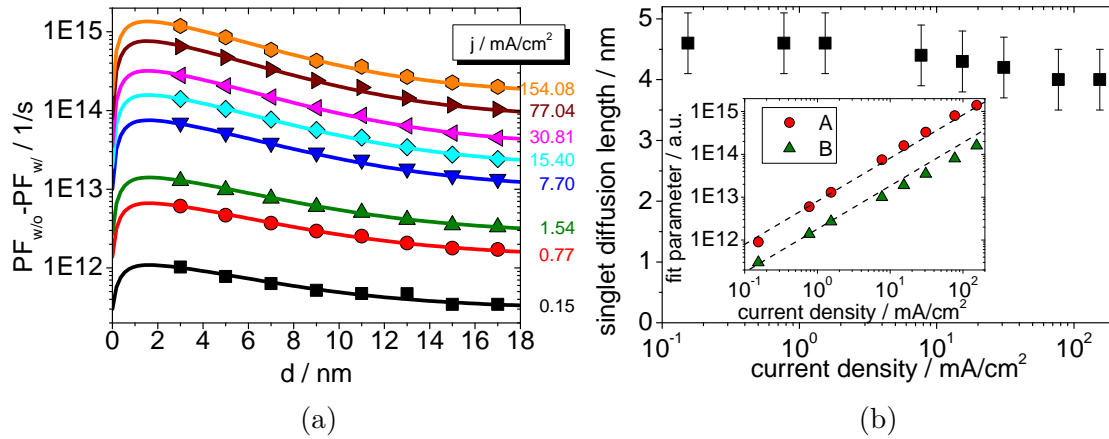
Figure 7.7: Photon flux versus distance d for different current densities (symbols) and fitted emission profiles (lines) using Eq. (7.9) for different current densities (a). A generation zone width of $g = 0.5$ nm is applied. The extracted singlet diffusion length (b) shows a slight dependency on the current density. The inset shows the obtained values for the parameters A and B. The dotted lines represent lines with a slope of 1.

Table 7.1: Fit parameter values from Fig. 7.7 for different applied current densities, according to Eq. (7.9). A describes the emission layer intensity and B the direct charge carrier recombination. L is the singlet diffusion length. The width of the generation zone g is fixed to 0.5 nm for all fits.

j [mA/cm^2]	0.15	0.77	1.54	7.70	15.40	30.81	77.04	154.08
L [nm]	4.6	4.6	4.6	4.4	4.3	4.2	4.0	4.0
A $\times\ 10^{13}$ [a.u.]	0.09	0.60	1.3	7.5	16	33	80	140
B $\times\ 10^{13}$ [a.u.]	0.03	0.14	0.27	1.3	1.9	3.5	8.0	16

7.2 Photoluminescence Quenching
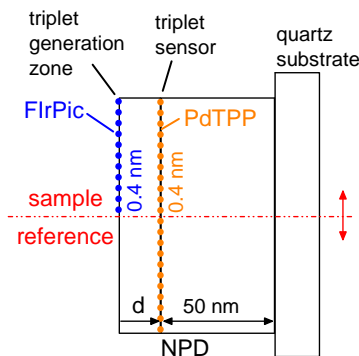
7.2.1 Preliminary Considerations

In order to compare the singlet diffusion length obtained by electrical excitation inside an OLED structure (cf. Sec. 7.1) to the diffusion length inside a pure layer, PL experiments are of interest.

Recently, Mikhnenko *et al.*[76] showed a smart method to measure the triplet diffusion length in NPD via optical excitation of a pure layer. The usual problem of the broad exciton generation zone is overcome by using a thin layer (0.4 nm) of the phosphorescent emitter FIrPic[13] as triplet generation zone on top of NPD (Fig. 7.8). FIrPic has a higher triplet energy than NPD, hence triplet transfer to NPD molecules is likely. As triplet sensor, a thin layer (0.4 nm) of PdTPP[14] is inserted in the NPD layer. PdTPP has a lower triplet energy than NPD and a radiative triplet state. When diffusing triplets reach it, PdTPP emits light. The triplet diffusion length is obtained by a variation of NPD thickness between the FIrPic and PdTPP layer, which defines the distance between the triplet generation zone and triplet sensor. To distinguish between diffusing triplets from FIrPic and triplets generated by other means (i.e. via ISC from the singlet state of PdTPP), the emission from a reference sample without the FIrPic layer is subtracted.

Figure 7.8: Sample geometry for the determination of the triplet diffusion length in NPD as presented by Mikhnenko *et al.*[76]. The working principle is described in the main text.

At low excitation density, the emission intensity of PdTPP decreases exponentially with NPD thickness. Using a mono-exponential fit, a triplet diffusion length of 87.0 ± 2.7 nm is obtained for NPD. This is significantly higher than 11 ± 3 nm measured by electrical excitation for the chemically similar compound 4P-NPD.

It is attempted to use Mikhnenko's method to measure the singlet diffusion length in 4P-NPD. Basically, for the singlet generation layer a material with a higher singlet energy than 4P-NPD ($S_1 = 2.9$ eV) is required, while for the sensing layer a material with a smaller singlet energy is required. To ensure a similar situation to the electrical excitation experiments from Sec. 7.1 , $Ir(ppy)_3$ is used as a sensing/quenching layer.

First tests were carried out using 0.5 nm of TPBI ($S_1 = 3.2$ eV) and TCTA ($S_1 = 3.2$ eV) as generation layers, respectively. However, the recorded emission was identical to that of the reference sample, where the TPBI/TCTA layer was omitted. Since no emission from TPBI/TCTA has been observed, it can be concluded that

---

[13]iridium(III)bis(2-(4,6-difluorephenyl)pyridinato- N,C2)

[14]meso-tetratolylporphyrin-Pd

these singlets were transferred to 4P-NPD molecules. Apparently, the amount of singlets in the generation layer is too small to be distinguished by the amount of singlets generated in the whole 4P-NPD layer.

Therefore, a different idea is carried out: Instead of the generation layer, a second quenching layer is applied. Also, the part of the substrate previously referred to as sample is now considered to be the reference and *vice versa*. A scheme of the used sample geometry is shown in Fig. 7.9 (a).
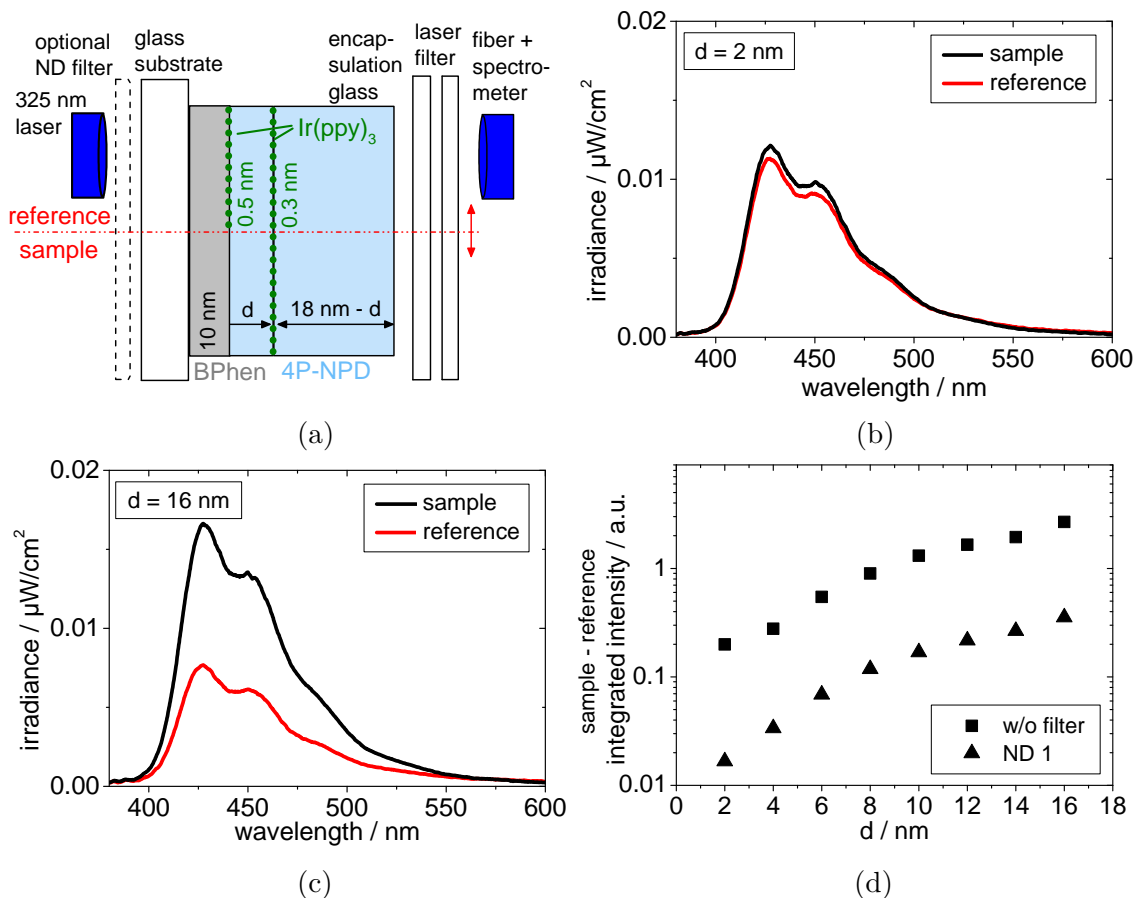
Figure 7.9: Geometry of sample and reference to measure the singlet diffusion length in 4P-NPD using optical excitation (a). The working principle is described in the main text. The spectral emission intensities for $d = 2$ nm (b) and $d = 16$ nm (c) show a stronger emission of the sample than of the reference, indicating a higher singlet generation at the 4P-NPD/BPhen interface for the sample. The difference in integrated spectral intensities between sample and reference (d) leads to an increase in intensity with increasing distance d.

To obtain a similar situation like in the OLED based experiments described in Sec. 7.1, 10 nm of BPhen are used as buffer layer on top of the glass substrate. The BPhen layer is followed by 18 nm of 4P-NPD. A thin layer of 0.3 nm $Ir(ppy)_3$ is used as sensing/quenching layer and inserted at different positions d within the 4P-NPD layer. The reference device additionally contains 0.5 nm of $Ir(ppy)_3$ at $d = 0$. The excitation is performed with a 325 nm cw-laser through the glass substrate and the emission of the sample through the encapsulation glass is recorded with a spectrometer. A variation of excitation density is achieved using neutral density filters between laser and substrate (cf. Sec. 5.5).

In comparison to the experiments of Mikhnenko, the working principle of these devices should be the following: Singlets are generated everywhere within the organic layers according to the absorption of the respective layers. 4P-NPD emits efficiently from its singlet state, hence these singlets can be directly detected by the spectrometer. More singlets should radiatively decay in the sample than in the reference, since the second 0.5 nm layer of $Ir(ppy)_3$ efficiently quenches singlets at the 4P-NPD/BPhen interface. This can indeed be confirmed: In Fig. 7.9 (b) and (c), the emission of two distances $d = 2$ nm and $d = 16$ nm are shown as examples. The fact that the sample emission is stronger than that of the reference holds for all distances d, meaning that for the sample more singlets exist at 4P-NPD/BPhen interface than for the reference devices.

These additional singlets can now diffuse away from the BPhen interface into the 4P-NPD layer and get quenched if they reach the 0.3 nm layer of $Ir(ppy)_3$. By a subtraction of the integrated intensity of the reference from the sample, the number of diffusing singlets at a certain position d can be obtained and should lead a mono-exponential curve. The integrated intensity is shown in Fig. 7.9 (d) for two different filter configurations, i.e. excitation densities. A non-mono-exponential intensity increase is observed with increasing distance d. The reason for this effect is not known so far. Since only minor differences in the shape of the intensity curve are observed for low and high excitation densities, effects occurring from a too high excitation energy, which would cause SSA, can be excluded. To investigate the increase in intensity in more detail, the emission of the reference and the sample is studied separately. The results are presented in the following.

7.2.2   Reference Devices

To understand the previously discussed intensity behavior, a closer look on the emission of the references is performed. The references only comprise one quenching layer and are thus somewhat easier to analyze (Fig. 7.10 (a)). The emission spectra for different distances d are shown in Fig. 7.10 (b) if no filter between laser and substrate is used. Although the BPhen layer is also excited, no significant emission from BPhen is observed. According to the singlet level of BPhen, emission would have been expected

at about 380-400 nm. The fact that only 4P-NPD emission is found indicates that
the singlets generated inside the BPhen layer play a minor role.

In Fig. 7.10 (c), the spectral intensities from Fig. 7.10 (b) are integrated over
wavelength (from 380 to 600 nm) and normalized to the integrated intensity at
$d = 2$ nm. First, the intensity decreases until $d = 8$ nm and than increases again.
This behavior is not dependent on the excitation density. To investigate the excitation
density in more detail, an input/output power measurement is performed for the
device with $d = 6$ nm (Fig. 7.10 (d)).
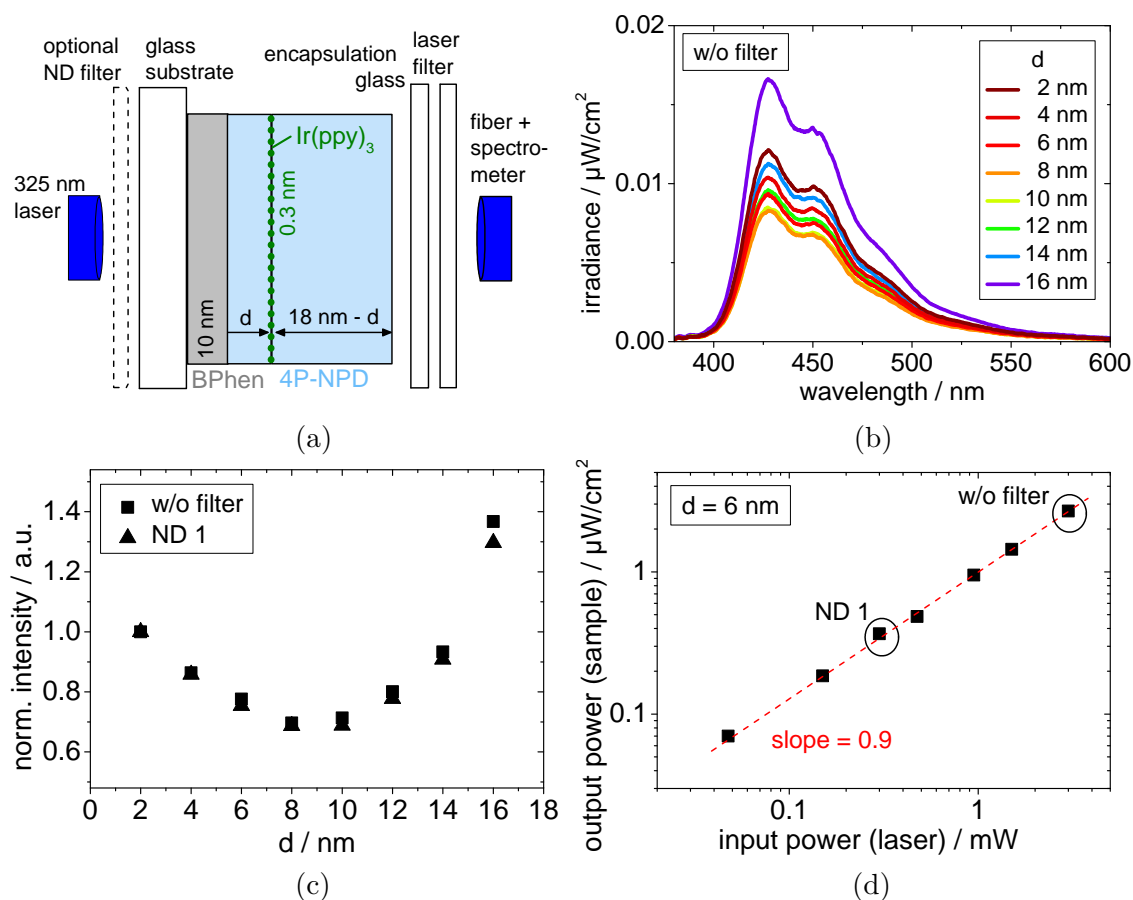
Figure 7.10: Geometry of reference devices (a). By varying d, the Ir(ppy)$_3$
quenching layer is shifted through the whole 4P-NPD layer. The spectral emission
intensity resulting from the optical excitation (b) corresponds to the emission of
4P-NPD. The integrated emission of these spectra is shown in (c) for two different
filter configurations. The integrated intensity is normalized to $d = 2$ nm. The power
input/output characteristic (d) reveals a linear behavior with a slope of 0.9.

The input power of the laser is varied using different ND filters between laser and the substrate. The output power is the integrated 4P-NPD emission intensity of the reference. On a log-log plot, the input/output power characteristic follows a linear curve with the slope of 0.9. The deviation from the expected slope of 1 is most likely a result of singlet-triplet interactions: $Ir(ppy)_3$ singlets (either generated by optical excitation or by transfer from 4P-NPD) are directly converted into $Ir(ppy)_3$ triplets and further converted into 4P-NPD triplets. Although the number of 4P-NPD triplets should be rather small compared to the number of 4P-NPD singlets, the triplet lifetime is much longer than that of singlets, thus enhancing the probability for singlet-triplet quenching. Significant singlet-singlet-annihilation processes can be excluded to a large extent since SSA reduces the number of singlets by a factor of 2, which would lead to a slope of 0.5 in Fig. 7.10 (d).

Influence of the BPhen layer

Despite the fact that emission from the BPhen layer is not observed in the PL spectra, singlets diffusing from the BPhen layer to the 4P-NPD layer might influence the intensity-distance dependency. The influence of BPhen can be studied using excitation through the encapsulation glass (Fig. 7.11 (a)). This is simply achieved by turning the device, without changing the configuration of the setup.

(a)   (b)
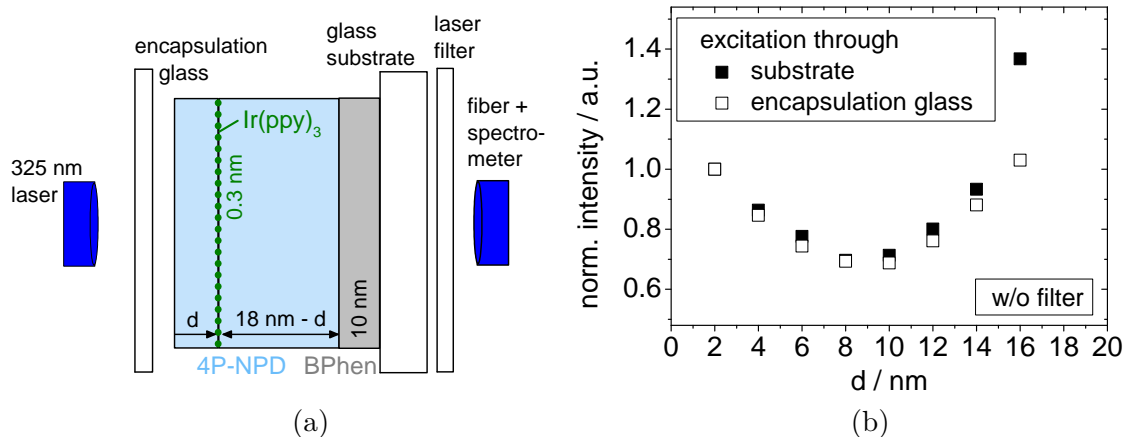
Figure 7.11: Measurement configuration to study the influence of the BPhen buffer layer (a). In contrast to the previous configuration (Fig. 7.10 (a)), the excitation occurs now from the encapsulation glass side. The normalized integrated intensity for different distances d is compared to the results from Fig. 7.10 (c) where excitation occurs through the substrate. The almost identical course of the intensity curves provides evidence for an optically inert BPhen buffer layer.

To ensure comparability, d now represents the distance from the air/4P-NPD interface to the quenching layer. Figure 7.11 (b) shows the normalized integrated intensity in comparison to the experimental data from Fig. 7.10 (c) where excitation occurs through the substrate.

Interestingly, the intensity-distance dependence is almost identical for both cases. Only at $d = 16$ nm a significant deviation in intensity between the excitation through the encapsulation and the substrate glass is observed. It is not fully understood what causes this difference. Nevertheless, the overlap of the intensity curves provides evidence that the BPhen buffer layer is optically inert.

Simulation of Diffusion Profiles

To understand the quenching of the Ir(ppy)$_3$ molecules in more detail, it is intended to model the intensity-distance curve presented in Fig. 7.10 (c). Therefore, the following assumptions are made: The BPhen layer has no influence on the intensity profile. The lateral absorption $I(x)$ of 4P-NPD with the thickness x is given by the Lambert-Beer law (cf. Sec. 3.2):

$$I(x) = 10^{-\alpha x}. \tag{7.10}$$

The absorption coefficient α of 4P-NPD[15] at 325 nm (= laser excitation wavelength) is 0.0062 nm^{-1}. The absorption of 4P-NPD is represented by a blue curve in Fig. 7.12 (a). The diffusion profile which results from (diffusing) singlets quenched by Ir(ppy)$_3$ molecules is assumed to have an exponential shape with a certain width L at a certain position d extended to both sides of the quenching layer. The diffusion profile is weighted with the absorption of 4P-NPD:

$$I(x) = (1 - e^{\frac{-|x-d|}{L}}) \cdot 10^{-\alpha x}, \tag{7.11}$$

The diffusion profile is indicated by the green area in Fig. 7.12 (a). It is believed that the area below the absorption curve of 4P-NPD minus the area of the diffusion profile is proportional to the measured emission intensity of 4P-NPD. This area is red marked in Fig. 7.12 (a). Now the diffusion profile is shifted from $d = 0$ nm to 18 nm through the whole 4P-NPD layer. Via integration of the 4P-NPD absorption and the diffusion profile curves, the area corresponding to the emission of 4P-NPD is calculated. These simulations are done for different widths L of the diffusion profile and are presented together with the experimental data in Fig. 7.12 (b). For the purpose of comparison, the curves are normalized to the intensity at $d = 2$ nm. L is varied between 1 and 30 nm in 1 nm steps.

---

[15]The absorption coefficient is calculated from transmission measurements of a 70 nm 4P-NPD layer on quartz substrate, where a transmission of 36.8% at 325 nm has been measured. This transmission value is already corrected by the substrate transmission.
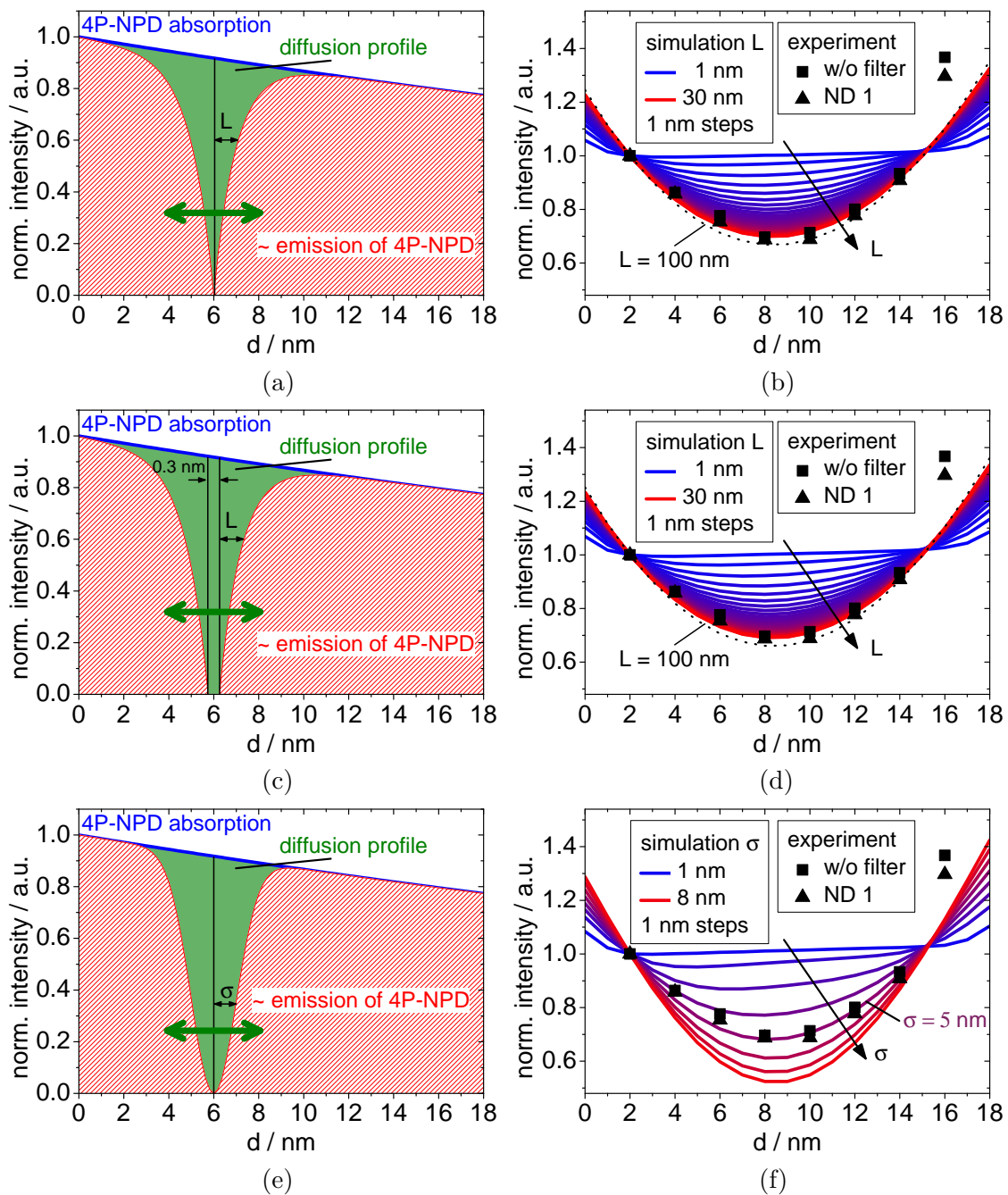
Figure 7.12: Illustration of an exponential (a), extended exponential (b), and Gaussian (c) diffusion profile at a position of $d = 6$ nm inside 4P-NPD (shown for $L = 1$ nm and $\sigma = 1$ nm) . The red marked area represents the emission of 4P-NPD and is shown as simulation result in (b), (d), and (f) for different widths L and σ of the diffusion profile. All diffusion profiles can provide simulation curves close to the experimental data.

With increasing L, the simulation approaches the experimental data. For L larger than 30 nm, the simulation curves do not change significantly. This fact is supported by the black dotted line which represents the simulation for $L = 100$ nm. For large L ($\geq$ 30 nm) the simulation is in good agreement with the experiment.

However, accounting for the fact that the Ir(ppy)$_3$ layer has a thickness of 0.3 nm, a diffusion profile width of more than 30 nm (which is also more than the thickness of the 4P-NPD layer) is implausible. Therefore, two other diffusion profiles are studied: an exponential profile, which is extended by 0.3 nm, and a Gaussian shaped profile. The situation of these two conditions are shown in Fig. 7.12 (c) and (e), respectively. The equations for the diffusion profiles are:

$$I(x) = (1 - e^{\frac{-|x-d-0.15|}{L}}) \cdot 10^{-\alpha x} \text{ and} \tag{7.12}$$

$$I(x) = (1 - e^{-\frac{1}{2}(\frac{x-d}{\sigma})^2}) \cdot 10^{-\alpha x}. \tag{7.13}$$

As presented in Fig. 7.12 (d), the extension of the exponential diffusion profile does not change the simulation results significantly when compared to the non-extended case (cf. Fig. 7.12 (b)). Furthermore, the Gaussian diffusion profile using a width of $\sigma = 4$ to 5 nm provides as well a good agreement with the experimental data (Fig. 7.12 (f)).

Taking the simulation and experimental intensity results into account, a Gaussian profile seems to represent the diffusion of 4P-NPD singlets and quenching by the Ir(ppy)$_3$ molecules in a better fashion than an exponential diffusion profile.

Influence of the absorption coefficient of 4P-NPD

In this paragraph, the influence of the absorption coefficient on the intensity is investigated. Therefore, the simulation using a Gaussian diffusion profile is carried out for $\alpha = 0.01$ nm^{-1} and $\alpha = 0.0043$ nm^{-1} which correspond to a transmission of 20% and 50%, respectively. The results are shown in Fig. 7.13 (a) and (b) for an α of 0.01 nm^{-1} and 0.0043 nm^{-1}, respectively.

It can be seen that the absorption coefficient influences the broadness of the curves rather than their height. Only very slight differences can be seen between Fig. 7.13 (a) and Fig. 7.13 (b): The trend of a more distinct minimum with increasing diffusion profile width σ is observed for both absorption coefficients. The experimental data can be fitted slightly better by an α of 0.0043 nm^{-1}, especially for large d (> 8 nm). However, the small differences between the simulation results suggest that the absorption coefficient plays a minor role when determining the diffusion profile width.
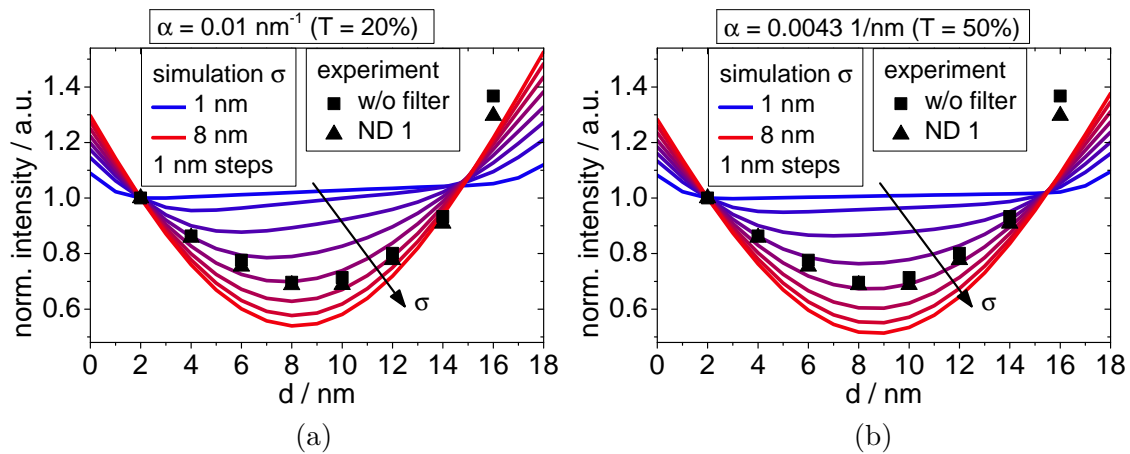
Figure 7.13: Influence of the absorption coefficient α on the simulated intensity. For $\alpha = 0.01$ nm^{-1} (a) and $\alpha = 0.0043$ nm^{-1} (b) only very small differences are visible, suggesting a minor importance of α when determining the diffusion profile width σ.

7.2.3   Sample Devices and Discussion

In order to confirm the assumption of a Gaussian shaped diffusion profile, the intensity of the sample devices from Sec. 7.2.1, which contain two quenching layers, is simulated. The geometry of these samples is shown in Fig. 7.14 (a). A similar model as in the previous section is used with the assumption of a second Gaussian shaped diffusion profile at $d = 0$ nm (Fig. 7.14 (b)). For the reason of simplicity, the width σ of both diffusion profiles is chosen to be the same. Again, the area under the absorption curve of 4P-NPD minus the area of the diffusion profiles (red marked in Fig. 7.14 (b)) is assumed to be correlated to the measured intensity of the 4P-NPD emission.

The simulation curves for different σ together with the experimental data normalized to the intensity at $d = 2$ nm is presented in Fig. 7.14 (c). The experimental data can be very well fitted for $\sigma = 5$ nm, except for one data point at $d = 16$ nm. The good agreement between experiment and simulation shows again that a Gaussian shaped diffusion profile is a valid assumption to describe the emission intensity of 4P-NPD.

This is further supported by the fact that in case of two exponential diffusion profiles (Fig. 7.14 (d)) the simulated intensity approaches the experimental data only for large L (Fig. 7.14 (e)). However, the fit is not as suitable as in case of the Gaussian diffusion profile.
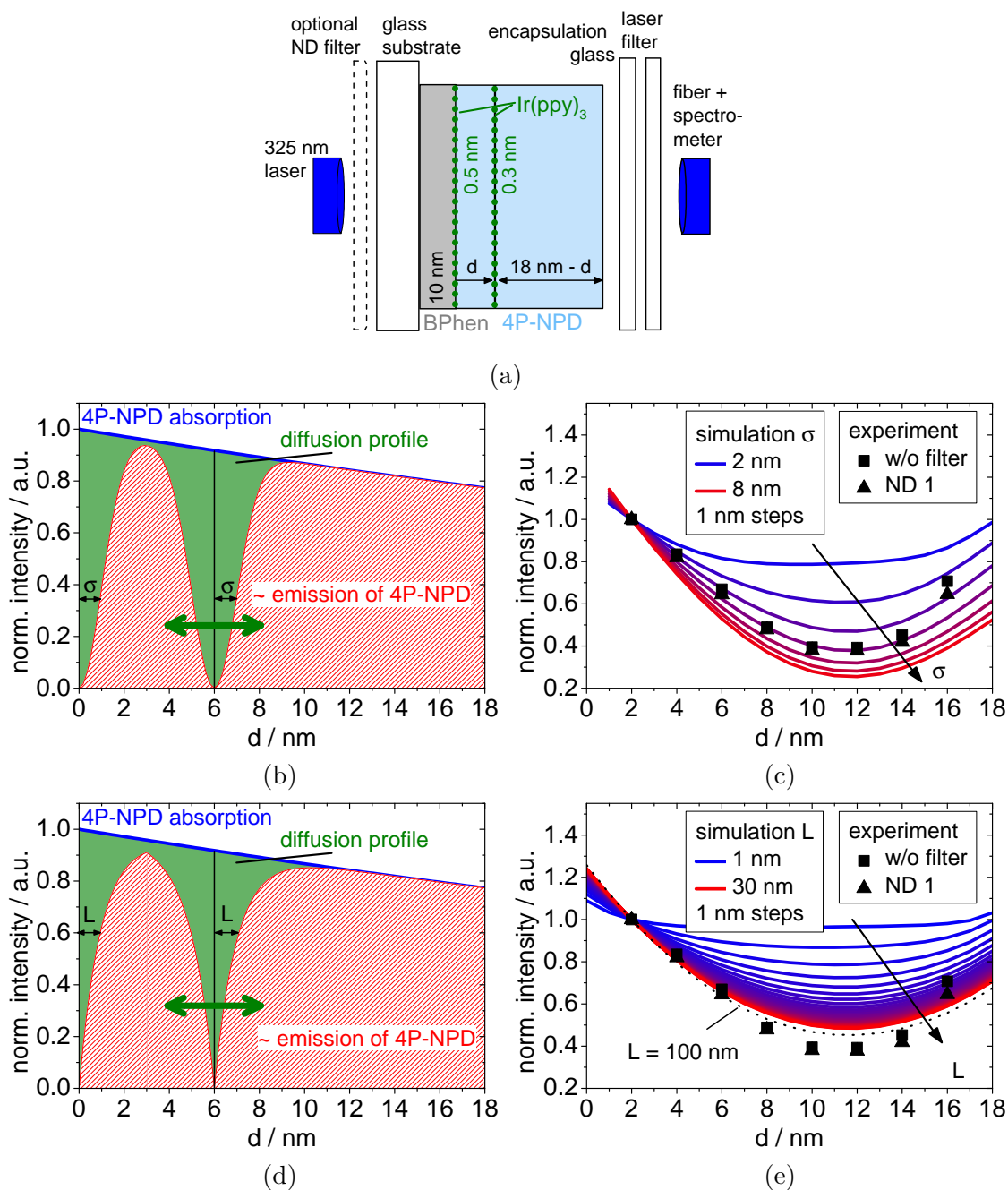
Figure 7.14: Geometry of the sample devices with two quenching layers (a), illustration of Gaussian diffusion profiles (shown for $\sigma = 1$ nm) (b), and simulated 4P-NPD emission intensities (c) for different σ normalized to the intensity at $d = 2$ nm. For comparison, exponential shaped diffusion profiles (shown for $L = 1$ nm) are illustrated in (d) and the simulated 4P-NPD emission intensities for different L normalized to the intensity at $d = 2$ nm are shown in (e). The experimental data can be described best by the simulated intensity curves using Gaussian diffusion profiles and $\sigma = 5$ nm.

Discussion

The model of a Gaussian diffusion profile explains the emission intensity of the samples and references under investigation in a reasonable manner. Using this information, it is indeed possible to simulate the difference in intensity between sample and reference from the experiments presented in Sec. 7.2.1, Fig. 7.9 (d). The simulated intensity curves using Gaussian diffusion profiles are shown in Fig. 7.15 for $\sigma = 4$, 5, and 6 nm, respectively. For these fits, the curves are normalized using the measured intensity of the reference and the sample at $d = 2$ nm, respectively. Again, a σ of 5 nm provides the best fit to the experimental data.
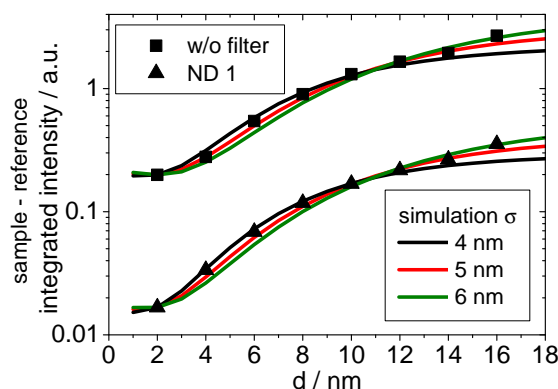
Figure 7.15: Simulation (curves) of intensities of the experimental data (dots) from Fig. 7.9 (d). Using Gaussian shaped diffusion profiles with $\sigma = 5$ nm, the increase in intensity can be well described by the simulation.

Unfortunately, the Gaussian shaped diffusion profile introduced by the $Ir(ppy)_3$ layers complicates the use of the Mikhnenko method, which assumes a delta shaped generation and sensor zone. When subtracting the intensity of the sample with triplet generation zone from the intensity of the sample without generation zone, the number of diffusing triplets from the generation zone can be determined.

In the experiments presented in this work, the generation zone and the sensor are replaced by thin $Ir(ppy)_3$ quenching layers. However, for singlets the assumption of a delta-shaped generation and sensor zone is not valid, as demonstrated by the simulations of the diffusion profiles. For small distances between the two quenching layers, the diffusion profiles are overlapping. Hence, a subtraction of these intensities cannot provide a reasonable value of additionally generated singlets. The approach of Mikhnenko using thin layers of $Ir(ppy)_3$ in 4P-NPD is therefore not meaningful.

However, the width of the simululated diffusion profile in this work is correlated to the singlet diffusion length. It is difficult to say to what extent σ is correlated to the singlet diffusion length since the diffusion length is usually determined using an exponential law. For the samples and the reference devices, a σ of 5 ± 1 nm provides a good fit to the experimental data. The half width when the maximum of

the Gauss-curve is reduced by a factor of $1/e$ may offer a better comparison to the diffusion length. For $\sigma = 5$ nm, this value is 7 nm.

7.3   Summary and Outlook

In the first part of this chapter, it was shown that the quenching of the fluorescence in OLEDs provided a simple and accurate method to measure the singlet diffusion length in 4P-NPD. Using a carefully chosen OLED structure with a narrow singlet generation zone and a suitable quenching material ($Ir(ppy)_3$), the singlet diffusion length for a range of current densities was obtained considering an analytical model based on the boundary conditions of ideal blocking and quenching of singlets. Here, the expansion of the generation zone, as well as the amount of direct recombination processes, were crucial parameters when calculating the diffusion length. By these means, a singlet diffusion length of $L = 4.6 \pm 0.5$ nm was obtained for 4P-NPD at a low current density of 0.15 mA/cm².

Furthermore, this method provided an estimate of the emission profile in the EML, which is otherwise hardly accessible in small-molecule OLEDs. The presented method can be applied to other materials as long as the OLED structure ensures a narrow generation zone close to one of the blocking layers and an efficient quenching of excitons. Thus, the dependence of the singlet diffusion length on the ambient temperature and different material parameters, like crystal orientation, fluorescent yield, and others, can be investigated in the future.

Inspired by the work of Mikhnenko *et al.*[76], who investigated the triplet diffusion length in NPD, a method to determine the singlet diffusion length via optical excitation was carried out in the second part of this chapter. In the experiments presented in this work, the generation layer and the sensing layer were replaced by thin $Ir(ppy)_3$ quenching layers and the method was applied accordingly. However, compared to the experiments of Mikhnenko different trends were observed, which could be explained using the simulation of diffusion profiles. A Gaussian shaped diffusion profile with a width of $\sigma = 5 \pm 1$ nm provided a good agreement with the experimental data.

A σ of 5 nm corresponds to a width of 7 nm (i.e. the position where the intensity is reduced to $1/e$ of the maximum) and correlates best to a diffusion length. This singlet diffusion length of 7 nm in a pure 4P-NPD layer is larger than the 4.6 nm obtained by using 4P-NPD as EML inside an OLED structure. The reason for the reduced diffusion length by electrical excitation might be that inside an OLED, the diffusion is hindered due to interaction with polarons and triplets, which can be neglected when optical excitation is used.

In future studies, the reason for the Gaussian diffusion profile, and the correlation between σ and the singlet diffusion length should be investigated. Especially the difference between optical excitation and electrical excitation and their influence on the shape of the generation and quenching zone are interesting topics.

So far, the Förster transfer radius from 4P-NPD to Ir(ppy)$_3$ (see illustration in Fig. 7.16) was not included in any of the calculations, thus introducing an overestimation of the real value of the diffusion length. The use of a quencher material with a smaller transfer radius would lead to a more precise value of the singlet diffusion length. Therefore, the new quencher requires a smaller overlap between the 4P-NPD emission and the absorption of the new material compared to Ir(ppy)$_3$ (cf. Sec. 3.4). Furthermore, the resonant HOMO energy of 4P-NPD and Ir(ppy)$_3$ of -5.1 eV induces hole trapping on the Ir(ppy)$_3$ molecules, which favors direct recombination and changes the charge balance inside OLEDs. Here, Ir(ppy)$_2$(acac) might be an interesting candidate since its triplet energy is similar to that of Ir(ppy)$_3$, but its HOMO energy is -5.4 eV preventing a hole transfer.

In the presented methods, the decrease of 4P-NPD emission was used to determine the diffusion length. Alternatively, the emission of the sensor could be used to measure the diffusion length. This would provide the advantage that the emission of the sensor can be directly associated to the number of diffusing singlets. Here, the red fluorescent emitter DCM[16], which can be used as dopant, is suggested. For a red fluorescent emitter, emission contributions due to TH can be neglected. Therefore, a red fluorescent emitter is better suited to determine the diffusion length than a phosphorescent emitter, especially if electrical excitation is used.
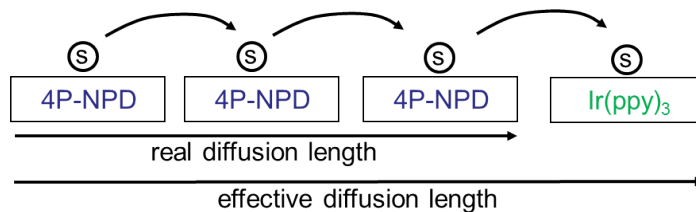
Figure 7.16: Illustration of the effective and real singlet diffusion length. In this work, the effective diffusion length was studied, where the transfer radius from 4P-NPD to Ir(ppy)$_3$ is included in the diffusion length. In future studies this radius should be accounted for in the analysis.

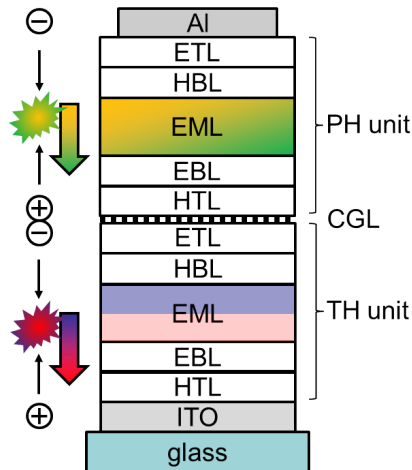[16]4-dicyanomethylene-2-methyl-6-p-dimethylaminostyryl-4H-pyran

8 Tandem OLEDs

In this chapter, the development of a highly efficient white tandem OLED is described. With regard to previous work, the single units of the tandem OLED are investigated in terms of efficiency enhancement, roll-off reduction, and a study on the device lifetime. Furthermore, the charge generation layer material and the hole blocking layer material are varied and, finally, a highly efficient white tandem OLED with a blue/red triplet harvesting unit and green/yellow phosphorescent unit that includes a double emission layer is demonstrated.

8.1 Previous Work

Since TH from 4P-NPD to $Ir(ppy)_3$ is not possible, a tandem OLED structure has been introduced and optimized by Thomas Rosenow[17] with the aim to overcome this problem and to design a highly efficient white OLED structure.[19, 102] As indicated in Fig. 8.1, the tandem OLED contains a green/yellow (GY) PH unit which is stacked on a blue/red (BR) TH unit. Rosenow has optimized both units separately in terms of materials, emitter concentrations, and layer thicknesses. Furthermore, the efficiency of the tandem OLED has been enhanced by a variation of the transport layer thicknesses. The working principle of the tandem unit is the following: when charge carriers are injected via the contacts, an additional electron-hole pair is simulta-

Figure 8.1: Principle of a tandem OLED. The injected charges generate an additional electron hole pair at the CGL. Light from both OLED units can be obtained.

neously generated at the charge generation layer (CGL) (cf. Fig. 8.1). Like in a single unit OLED, these charge carriers are transported to the emission layers and recombine. It has been shown that the charge generation at the CGL can be improved by inserting a thin layer of Al (0.5 nm).[102] With this system an LE of 33.0 lm/W (EQE 26%, CIE (0.51/0.42)) at 1,000 cd/m² has been achieved by Rosenow.[19]

Furthermore, an efficiency analysis has been performed for this particular tandem OLED. An outcoupling efficiency of 20% is calculated, which yields in 130% of possible

---

[17]Thomas Rosenow has been working on the topic of white TH OLEDs at the IAPP until May 2010. He now works at Novaled AG (Dresden).

200% internal quantum efficiency when the measured EQE of 26% is taken into account. This results suggest that the CGL works to some extent in providing charge carriers and that the efficiency can be strongly enhanced by a reduction of electrical, excitonic, and outcoupling losses.[20]

This chapter is organized as follows. Based on the tandem OLED of Rosenow, the structure is further investigated and optimized. This includes the single units as well as the tandem OLED. To reduce the roll-off in the TH OLED, a spacer material is doped into the EML. For the PH OLED a double emission layer is introduced to increase the efficiency. The lifetime for both single units is investigated. As a next step, the double emission layer is applied to the tandem OLED, which is optimized in terms of the CGL material, HTL thicknesses, and HBL material. Finally, a comparison to the work of Rosenow is given.

8.2   Triplet Harvesting Unit

As discussed in Sec. 6.1.3, the roll-off in a TH OLED can be reduced by using a thinner 4P-NPD layer. However, this reduces the amount of blue emission at the same time, which is undesirable when designing white OLEDs. The roll-off is a result of the annihilating triplets on their path from the generation zone to the phosphorescent emitter $Ir(MDQ)_2(acac)$ due to the long triplet lifetime of 4P-NPD.

It has been shown by Zhang $et\ al.$[235] that the insertion of a triplet manager can be used to reduce singlet-triplet annihilation in fluorescent OLEDs. Here, ADN[18] is doped into the matrix:emitter system Alq_3[19]:DCM2[20]. ADN is chosen as triplet manager, since it has a large singlet-triplet splitting, so that the singlet energy is above that of Alq_3 and the triplet energy is below that of DCM2. Triplets which would usually decay on DCM2 are trapped on ADN molecules. Here, the interaction/annihilation with DCM2 singlets is less because of the reduced overlap of singlet emission and triplet absorption. As a result, the OLED with incorporated ADN showed a lower roll-off than the reference OLED without ADN. It is intended to adopt this idea to reduce TTA in TH OLEDs.

To reduce TTA and hence the roll-off, the redistribution of triplets to a suitable triplet managing material is necessary. Ideally, this material should have a higher singlet energy than 4P-NPD ($S_1 = 2.91$ eV) to avoid singlet quenching and a triplet energy between those of 4P-NPD ($T_1 =2.31$ eV) and $Ir(MDQ)_2(acac)$ ($T_1 = 2.02$ eV). It would be beneficial if the HOMO energy of the triplet manager would be lower than that of 4P-NPD (HOMO = -5.7 eV) to ensure that hole transfer and exciton generation is taking place on the 4P-NPD molecules. Furthermore, the triplet diffusion

---

[18]9,10-di(naphtha-2-yl)anthracene
[19]tris(8-hydroxyquinoline) Al
[20]4-(dicyanomethylene)-2-methyl- 6-julolidyl-9-enyl-4H-pyran

length needs to be same or longer than that of 4P-NPD (L_T = 11.3 nm[21][118]), so that triplets are efficiently transported to Ir(MDQ)$_2$(acac). A short triplet lifetime of the triplet manager is desired to reduce TTA. Unfortunately, a material which simultaneously fulfills all these requirements is not known (cf. Table 5.1).

In this work, NPD (S_1 = 2.81 eV, T_1 = 2.29 eV, HOMO = -5.4 eV, L_T = 11.8 nm[22] [183]) is chosen as most promising material for the triplet manager, and is therefore doped into the intrinsic 4P-NPD layer of a TH OLED using different concentrations (0 wt%, 20 wt%, 40 wt%, and 60 wt%). Since the singlet energy is lower and the HOMO energy is higher than that of 4P-NPD, it is expected that the amount of singlets which are generated on the 4P-NPD molecules will be lowered with increasing NPD concentration. However, due to the nearly resonant triplet energy, a triplet transfer to NPD should be possible and might reduce the efficiency roll-off. The layer structure, the proposed energy diagram, and the performance of the OLEDs under investigation are shown in Fig. 8.2.

The IVL-characteristics are identical for all four OLEDs indicating that NPD does not trap charges. However, the spectral emission at a constant current density of 15.4 mA/cm² differs. While for increasing NPD doping concentration the blue emission is reduced, the red emission is enhanced. The decrease in blue emission can be explained by the fact that with increasing NPD concentration, the charge/exciton transport becomes more probable on NPD and hence the recombination/decay rate on 4P-NPD is decreased. Furthermore, an increase of NPD emission can be seen in the normalized emission spectra (Fig. 8.2 (e)). This confirms that charge and exciton transport is increasingly taking place on the NPD molecules as the NPD concentration increases. The fact that the red emission is increased leads to the conclusion that either the triplet transfer is more effective on NPD than on 4P-NPD, or that the exciton generation zone is shifted towards Ir(MDQ)$_2$(acac). Since the hole mobilities of NPD and 4P-NPD are comparable[115], the former is more probable.

As the cavity length is constant for all four devices, no significant change in the angular emission characteristics is expected. This is indeed the case as shown by the radiance over viewing angle curves in Fig. 8.2 (f).

Despite the fact that exciton transfer occurs partly on the NPD molecules, the expected improvement of the efficiency roll-off is not observed (Fig. 8.3 (a)). The most likely explanation is that NPD and 4P-NPD have similar triplet lifetimes and TTA rates. The role of TTA can be studied by investigating the transient decay of triplets. However, such experiments are far beyond the scope of this work, but might be an interesting research topic for future investigations. Because an undesirable reduction of blue emission has been observed in this experiment, an intrinsic 4P-NPD layer will be used for the TH OLED in further experiments in this thesis.

---

[21]measured via electrical excitation in an OLED structure
[22]photo current measurement
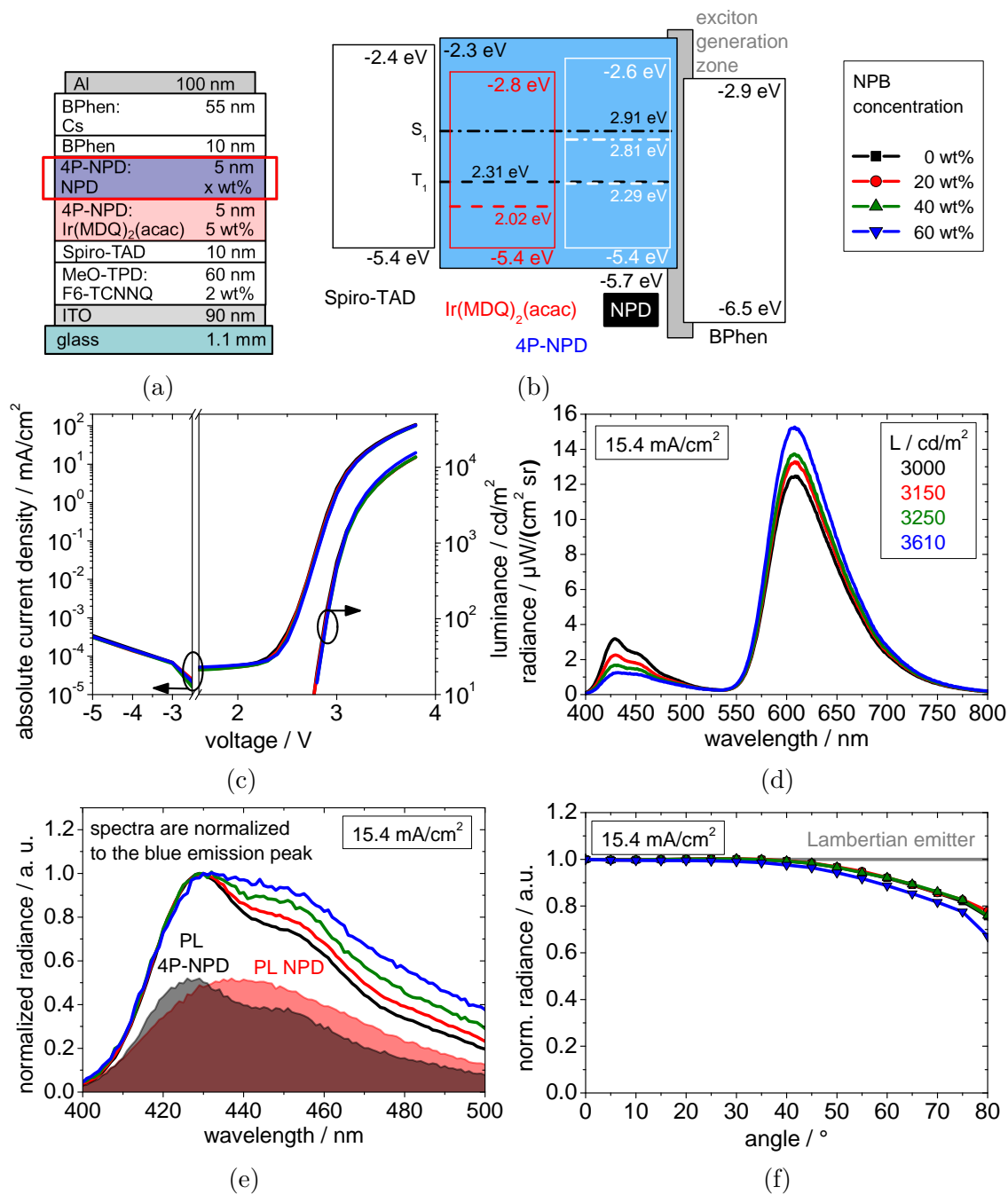
Figure 8.2: OLED layer structure (a), proposed energy diagram (b), and performance (c-f) of the TH OLEDs for different NPD doping concentrations. The IVL-curves (c) and the viewing angle characteristics (f) show no significant dependence on the NPD concentration. However, with increasing concentration, emission from 4P-NPD is reduced and additional emission of NPD is observed (e).
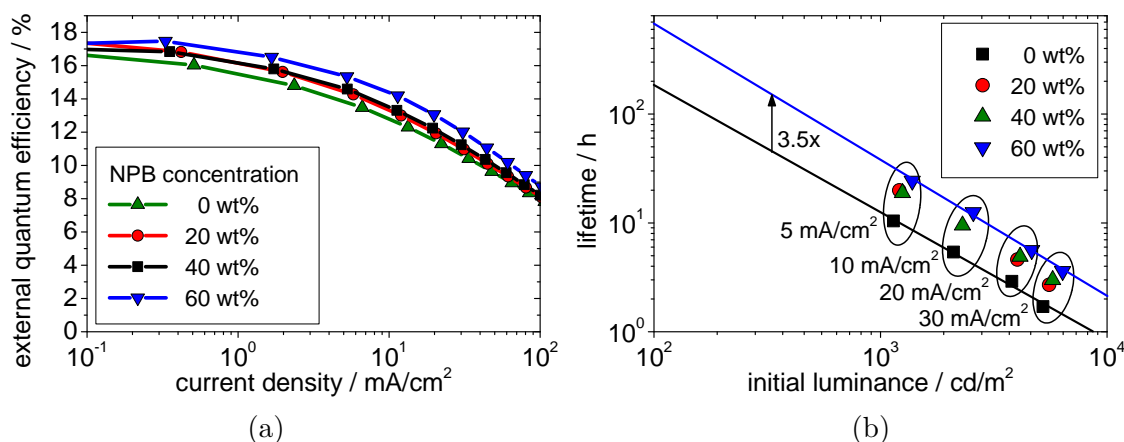
Figure 8.3: EQE (a) and lifetime (b) of TH OLEDs for different NPD doping concentrations. While the roll-off is not significantly changed, the lifetime can be enhanced by a factor of 3.5 when comparing the 60 wt% OLED to the reference with 0 wt%.

As a result of the charge transport on the NPD molecules, the lifetime can be increased up to a factor of 3.5 with increasing NPD concentration (Fig. 8.3 (b)). However, the lifetime at 1,000 cd/m² is still less than a day, and hence much too low for practical applications.

8.3 Full Phosphorescent Unit

It has been demonstrated several times that a double emission layer (DEML) is beneficial for OLEDs, since it avoids charge accumulation at the interface between the EML and one of the blocking layers.[102, 112, 213] Usually, the DEML leads to a better charge balance and a broader emission zone which improves efficiency, lifetime, and roll-off. To improve the PH unit, a double emission layer system using TPBI and TCTA as matrix materials is applied. The comparison to the performance of single emission layer (SEML) OLED is shown in Fig. 8.4. Here, the total thickness of the EML is kept constant (10 nm) to ensure comparability. A slight flattening of the IVL-characteristics for the DEML can be seen which is attributed to a change in charge carrier balance.

Regarding the spectral emission intensity, the Ir(ppy)$_3$ emission is enhanced for the DEML structure, while the Ir(dhfpy)$_2$(acac) emission does not change significantly. Since the thickness of the EML has been kept constant this can be attributed to a increased IQE of Ir(ppy)$_3$. As Ir(ppy)$_3$ and Ir(dhfpy)$_2$(acac) have the same HOMO and LUMO energy it is expected that the emission of both emitters would increase if the charge balance is improved. Since this is not the case, it is believed that the energy transfer from TPBI to Ir(ppy)$_3$ is more efficient than from TCTA to Ir(ppy)$_3$.

The angular dependent emission characteristics are close to a Lambertian emitter (Fig. 8.4 (d)), with a slight increase for the DEML OLED at higher viewing angles.

This occurs from the spectral difference and the fact that the emission zone is shifted inside the cavity. For the SEML OLED, the emission zone can be assumed to be at the HBL interface since TCTA is primarily a hole transporting material. Because TPBI is an electron transporting material, the emission zone of the DEML OLED is assumed to be in the middle of the EML.
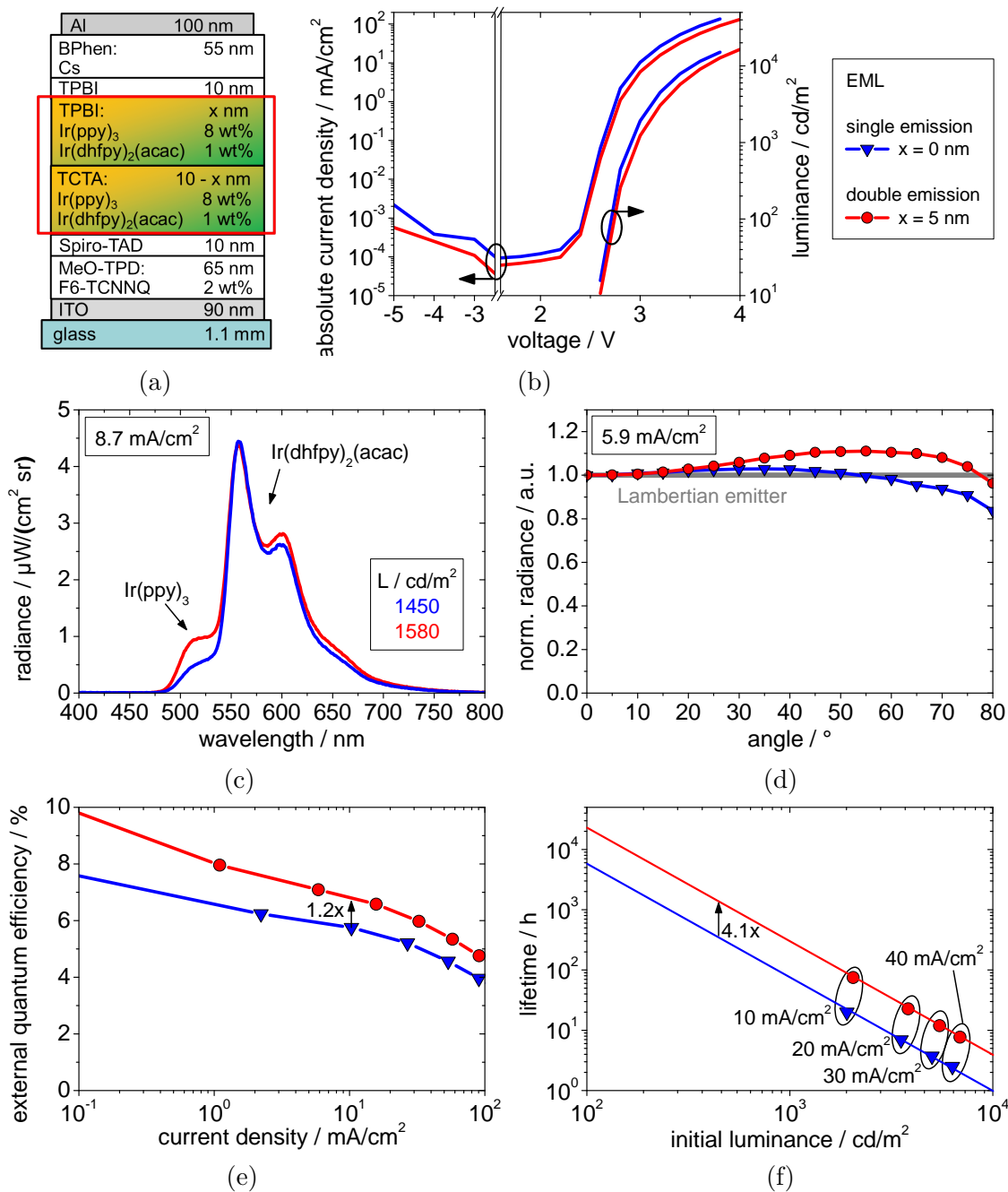
Figure 8.4: OLED layer structure (a) and performance (b-f) of the single and double emission layer PH unit. The double emission layer leads to an enhanced emission of the green emitter Ir(ppy)$_3$ (c) and thus increases efficiency by 1.2 at 10 mA/cm² (e). Furthermore, the lifetime is improved by a factor of 4.1 (f).

As known from OLEDs with DEML structure, the EQE and the lifetime are improved with respect to the SEML OLED. The enhancement factors are 1.2 and 4.1, respectively (Fig. 8.4 (e) and (f)). However, the roll-off for the DEML OLED is still very strong. The reason here might be that the overall thickness of the EML is only 10 nm, i.e. that the triplets are restricted to a small volume. Increasing the EML thickness could help to increase the EQE further and to improve the roll-off, but this has not been carried out within this work.

Variation of the hole transport layer

Since the charge carrier balance plays an important role in OLEDs, a variation of the HBL material has been performed. For the DEML OLED the following HBLs are applied: TPBI, BPhen, and BAlq2. Since these materials differ in HOMO and LUMO energy, a different charge injection onto the matrix material TPBI and therefore a change in charge balance is expected.

The layer architecture, the proposed energy level diagram, and the performance of the OLEDs under investigation are given in Fig. 8.5. The application of BPhen or BAlq2 leads to a shift of the IVL-curves of 0.2 V towards lower voltages. Since the LUMO energies of BPhen (-2.9 eV) and TPBI (-2.8 eV) are almost the same, more similar IVL characteristics would have been expected for these two materials than with BAlq2, which has a significantly lower LUMO energy of -3.2 eV. Therefore, it is very likely that in case of TPBI, the injection of electrons via the HBL is a direct injection onto the matrix material, while for BPhen and BAlq2, electrons are injected to the phosphorescent dopants. Hence, it is assumed that the LUMO energy of TPBI, $Ir(ppy)_3$, and $Ir(dhfpy)_2(acac)$ are not the same, but that the LUMO energy of at least one of the dopants is lower than -2.8 eV.

Interestingly, in this experiment, only the $Ir(dhfpy)_2(acac)$ emission changes for different blocker materials while the $Ir(ppy)_3$ emission remains constant (Fig. 8.5 (d)). This leads to the conclusion that a certain amount of charges can directly recombine on the $Ir(dhfpy)_2(acac)$ molecules, while the $Ir(ppy)_3$ emission results only from an energy transfer from the matrix. This is in good agreement with the fact that for BPhen and BAlq2 electrons are injected onto the dopant rather than onto the matrix.

The viewing angle characteristics exhibit small differences for the different blocker materials (Fig. 8.5 (e)). This change is a result of the different spectral emission, but also indicates a possible shift of the recombination zone. At low current densities (<1 mA/cm²), the OLED comprising BAlq2 as HBL exhibits the highest EQE (Fig. 8.5 (f)). However, due to the distinct roll-off, the EQE becomes comparable to the other two OLEDs at high current density (~100 mA/cm²). Since the incorporation of $Ir(dhfpy)_2(acac)$ leads to a worse roll-off[102], it is clear that the BAlq2 based OLED which shows highest $Ir(dhfpy)_2(acac)$ emission has also the strongest roll-off. Here, different TPA rates might be responsible for the different roll-off characteristics.

(a)

(b)

(c)

(d)

(e)

(f)
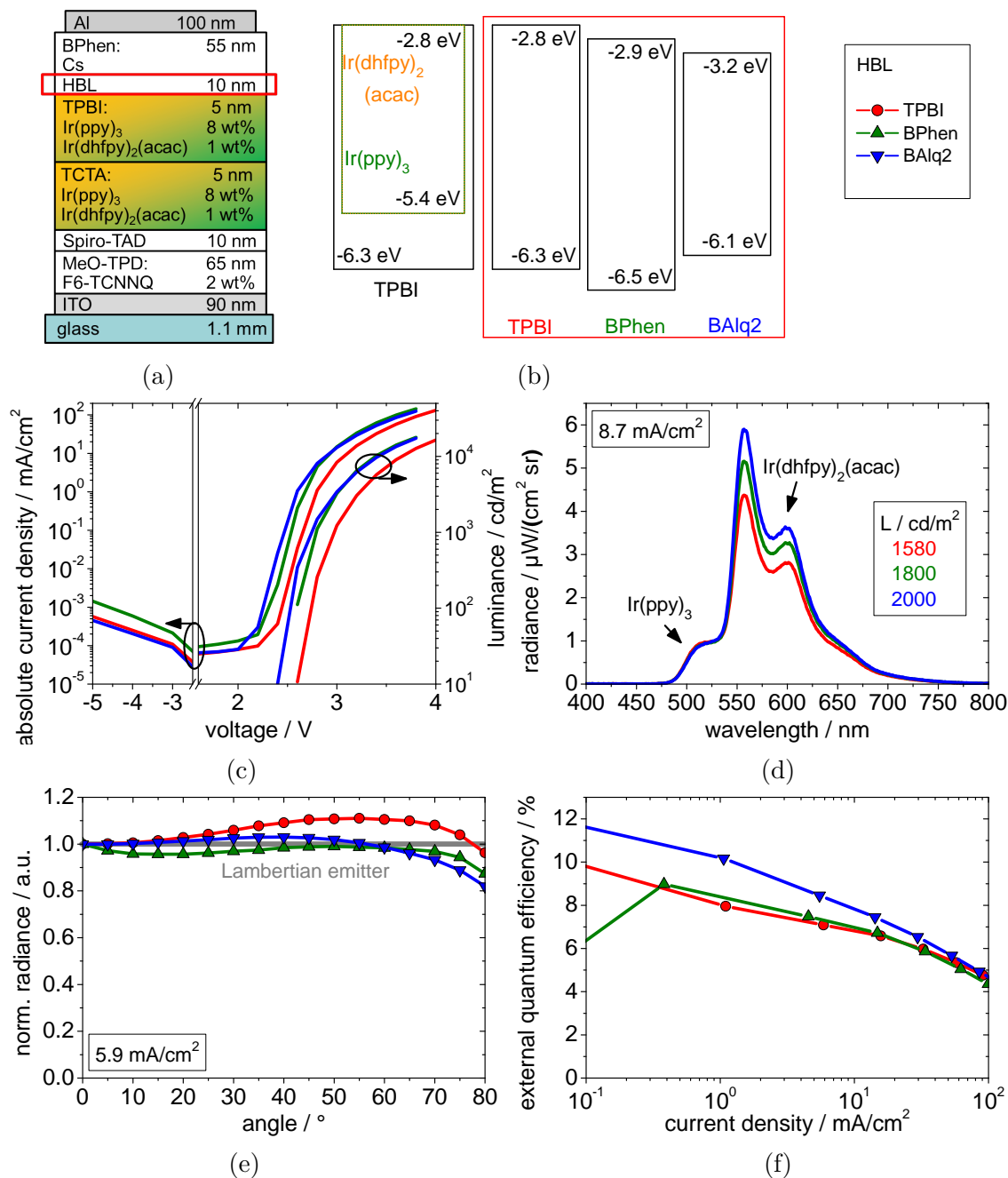
Figure 8.5: OLED layer structure (a), proposed energy diagram (b) and performance (c-f) of the DEML OLED with varying HBL. The OLED comprising TPBI shows a distinct voltage shift (c). Using BAlq2 as HBL leads to the highest efficiency, but exhibits a strong roll-off at the same time (f).

In summary, the influence of the HBL on the overall performance of the PH unit is quite small. Several mechanisms can be seen as reason for these differences, like the injection of electrons onto the dopant, the change in charge balance, or the shift of

the recombination zone. Rosenow suggested that the charge balance is not preserved when applying the single unit to the tandem OLED.[102] Thus, an HTL variation within the tandem OLED can be seen as meaningful and the corresponding results will be presented in Sec. 8.5.

8.4   Charge Generation Layer in Tandem OLEDs

The CGL is very important in the tandem OLED, since it generates additional charge carriers. When stacking two OLEDs on top of each other, the CGL is formed by the pn-junction of the ETL of the first and the HTL of the second unit. By incorporation of a 0.5 nm thick Al interlayer, the IV-characteristics and the efficiencies of the tandem OLED can be significantly improved.[102]

As alternative to Al, 0.5 nm of Ag is incorporated in the CGL in this experiment. Both metals have the same work function (-4.3 eV). However, it is known that Al shows a self doping effect when evaporated on BPhen:Cs due to penetration.[236] Optical changes are not expected, since 0.5 nm of metal layer form clusters rather than a closed layer and absorption at these clusters should play a minor role. Also SPP losses should be negligible because the EMLs are more than 85 nm away from the CGL. Figure 8.6 shows the layer stack and the performance of the OLEDs under investigation. For comparison the results of Rosenow, who used exactly the same materials and layer thicknesses, are plotted. Regarding the IVL-characteristics (Fig. 8.6 (b)), the OLED with the Ag interlayer shows slightly steeper curves. As expected, the OLED with Al interlayer is comparable to that of Rosenow.

The spectral emission for the Ag and the Al OLED is slightly different in particular for the green emitter Ir(ppy)$_3$ (Fig. 8.6 (c)). It is assumed that these changes occur from different charge balance factors caused by different penetration behavior and/or morphologies of Ag and Al clusters. Nevertheless, a strong deviation of the emission spectra in comparison to the device of Rosenow is observed, especially in the red, but also in the green and blue wavelength regime. Therefore, the efficiencies (Fig. 8.6 (e) and (f)) are not as high as those achieved by Rosenow. Because the same measurement equipment has been used for all OLEDs, the reason is most likely a processing error due to the large number of layers and the complicated structure. Since there has been a time frame of more than one year between the processing of the devices of Rosenow and those in this thesis, many parameters have changed, like material batches and tooling factors.[23] This reproducibility problem might also be caused by a contamination of chamber.

To overcome these issues, the thickness of the transport layers has been varied to adjust the spectral emission (Appendix A.4).

---

[23]The materials in Lesker tool are changed daily, since the processing of different OLED and OSC stacks is required.

(a)

(b)

(c)

(d)

(e)

(f)
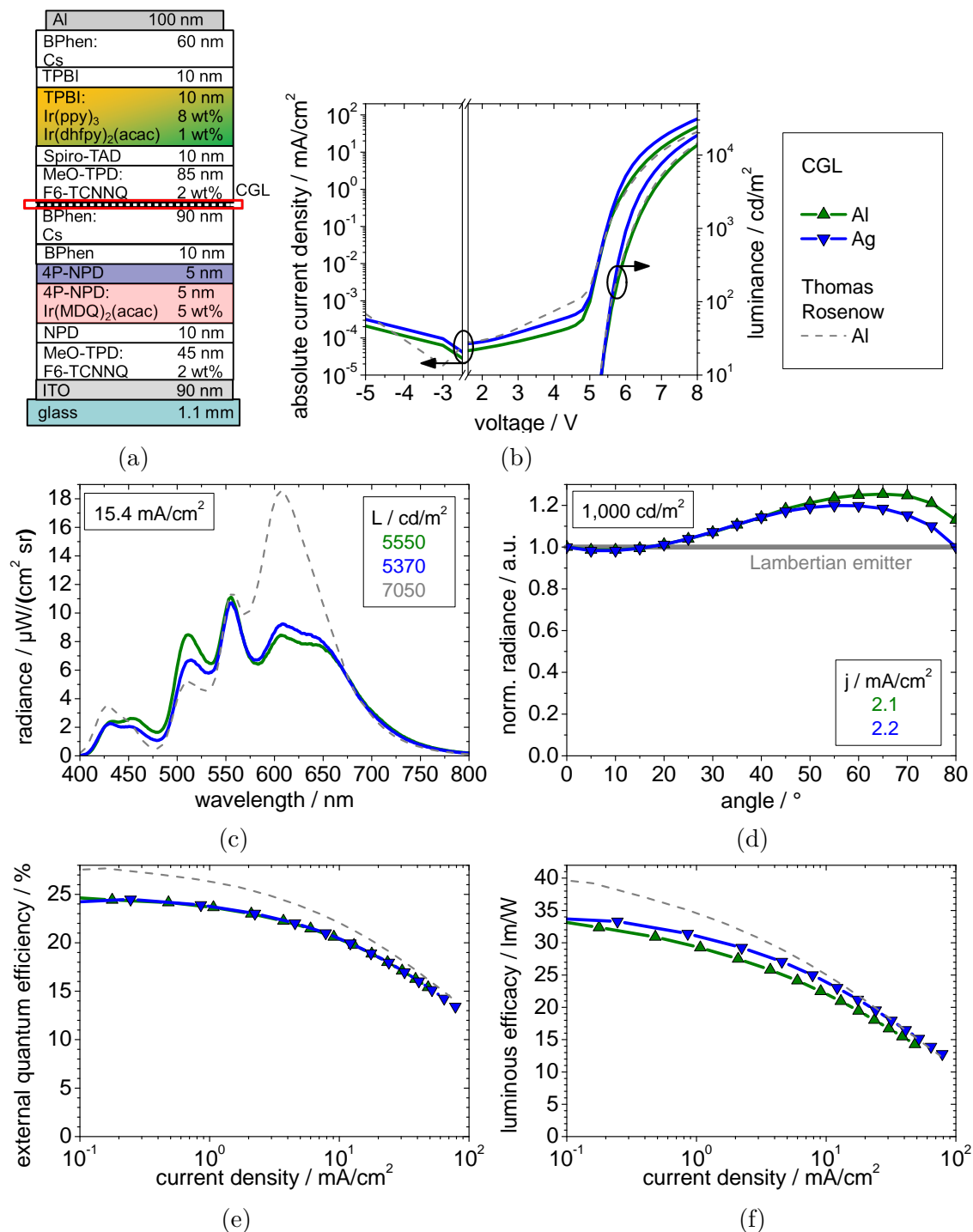
Figure 8.6: OLED layer structure (a) and performance (b-f) of the tandem OLED with varying CGL. Using Ag as CGL leads to a slightly better performance than Al. The results of Rosenow who used the same layer architecture is given in gray lines. Comparing the spectral radiance (c), especially in the red wavelength regime the emission is reduced which leads to lower efficiencies (e,f) than achieved by Rosenow.

The angular dependent emission characteristics are not significantly changing with the CGL material (Fig. 8.6 (d)). The small variations at viewing angles $> 45°$ are caused by the different spectral emission. Interestingly, the EQE is exactly the same for both interlayers (Fig. 8.6 (e)). Apparently any changes in outcoupling efficiency caused by shifts of the recombination zone are compensated by the charge carrier balance, since the effective radiative efficiency is expected to be constant for different CGLs. Due to the steeper IV-characteristics, the OLED with the Ag interlayer exhibits a slightly higher luminous efficiency (Fig. 8.6 (f)). Therefore, Ag is used as CGL instead of Al in further experiments.

8.5   Tandem OLED with Double Emission Layer

In the previous sections, the improvement of PH OLED using a DEML and the improvement of tandem unit using Ag as CGL has been demonstrated. Obviously, the combination of both systems should enhance the efficiency of a tandem OLED. Considering that the HBL of the PH unit is a crucial parameter, the HBL is varied and the results are presented in Fig. 8.7. As discussed in Sec. 8.4, the thickness of transport layers needed to be optimized. To adjust the optical cavity, the HTL thicknesses were reduced from 45 to 35 nm for the TH unit and from 85 to 75 nm for the PH unit (cf. Appendix A.4). Furthermore, a comparison to the results of Rosenow is given.

Like in the case of the single PH OLED (Sec. 8.3), TPBI as HBL leads to a slightly increased voltage (Fig. 8.7 (a) inset), which is attributed to the electron injection into the matrix TPBI, while for BPhen and BAlq2 the electron injection into $Ir(dhfpy)_2(acac)$ is present. However, compared to the work of Rosenow, the IVL-characteristics are significantly improved. Regarding the spectral emission, the TPBI OLED shows a better performance especially for the yellow and red emitter than the OLEDs with BPhen or BAlq2 (Fig. 8.7 (c)). This is in contrast to the results obtained for the single PH OLED, but confirms the fact that the charge balance is different in a tandem than in a single unit OLED. Comparing the spectral emission of the TPBI OLED and the tandem OLED of Rosenow, the red and yellow emission is enhanced, while the green emission is reduced. The improvement in red and yellow can be attributed to the better outcoupling introduced by the change of the HTL thicknesses. However, the reason for reduced green emission remains unclear.

The enhanced emission for the TPBI OLED in comparison to the OLEDs with BPhen and BAlq2 leads to the best efficiency performance (Fig. 8.7 (e) and (f)), although the viewing angle characteristics are slightly different (Fig. 8.7 (d)). Here, the BPhen and BAlq2 OLED have a more pronounced super-Lambertian emission characteristic. At a luminance of 1,000 cd/m² an LE (EQE) of 33 lm/W (25%) with CIE color coordinates of (0.528/0.425) are achieved. However, in comparison to Rosenow, a significant improvement regarding LE has not been obtained.

(a)

(b)

(c)

(d)

(e)

(f)
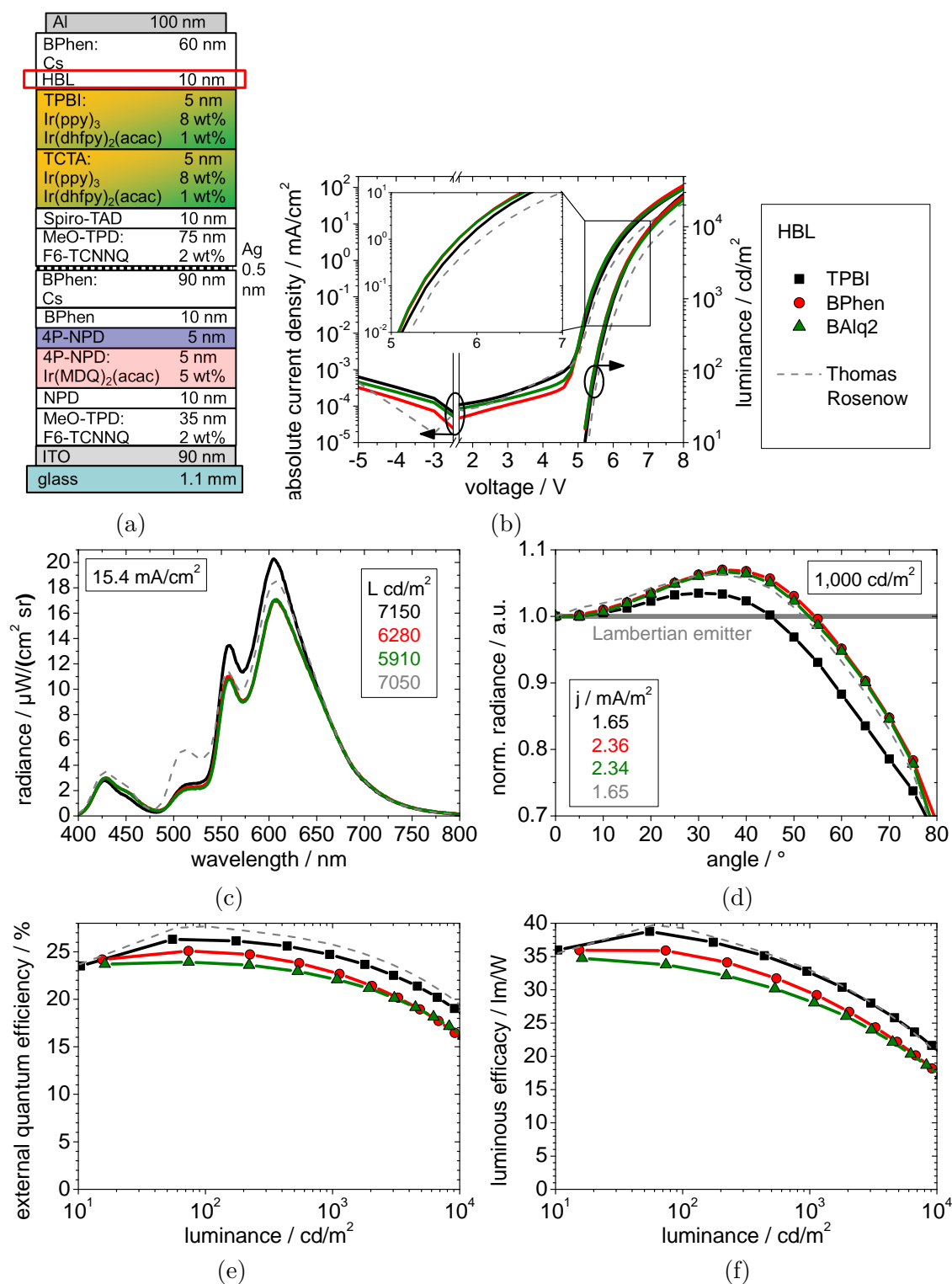
Figure 8.7: OLED layer structure (a) and performance (b-f) of the tandem OLED with DEML and varying HBL. Using TPBI as HBL leads to the highest efficiencies (e,f). A comparison to the results of Rosenow is given by gray lines. The OLED comprising TPBI as HBL reaches same efficiencies as the SEML tandem OLED of Rosenow.

A summary of the used OLED structure and important measurement parameters at 1,000 cd/m² in comparison to the device reported by Rosenow are given in Table 8.1. Although the driving voltage is reduced by 0.2 V, the efficiencies are not enhanced. Due to the reduced green emission (cf. Fig. 8.7 (c)), the CIE color coordinates are shifted from (0.505/0.422) to (0.528/0.425). Furthermore, the CRI significantly decreases from 78 to 62.

Table 8.1: Comparison of key parameters of the white tandem OLED with DEML to the work of Rosenow at 1,000 cd/m². The OLED stacks are given and differences are marked in red. The layer thicknesses in nm and doping concentrations in wt% are given in brackets.

	U V	j $\frac{mA}{cm^2}$	EQE %	LE lm/W	CIE	CRI
Rosenow	6.2 V	1.65	26	33	(0.505/0.422)	78
					(0.506/0.422) [450 cd/m²]	
					(0.491/0.415) [7,058 cd/m²]	

glass//ITO (90)//MeO-TPD:F6-TCNNQ (45, 2 %)//Spiro-TAD (10)//4P-NPD:Ir(MDQ)$_2$(acac) (5, 5 %)//
4P-NPD (5)//BPhen (10)//BPhen:Cs (90)//Al (0.5)//MeO-TPD:F6-TCNNQ (85, 5 %)//Spiro-TAD (10)//
TCTA:Ir(ppy)$_3$:Ir(dhfpy)$_2$(acac) (10, 8 %, 1 %)//TPBI (10)//BPhen:Cs (60)//Al (100)

	U V	j $\frac{mA}{cm^2}$	EQE %	LE lm/W	CIE	CRI
this work	6.0	1.65	25	33	(0.528/0.425)	62
					(0.527/0.425) [370 cd/m²]	
					(0.518/0.419) [7,153 cd/m²]	

glass//ITO (90)//MeO-TPD:F6-TCNNQ (35, 2 %)//Spiro-TAD (10)//4P-NPD:Ir(MDQ)$_2$(acac) (5, 5 %)//
4P-NPD (5)//BPhen (10)//BPhen:Cs (90)//Ag (0.5)//MeO-TPD:F6-TCNNQ (75, 5 %)//Spiro-TAD (10)//
TCTA:Ir(ppy)$_3$:Ir(dhfpy)$_2$(acac) (5, 8 %, 1 %)//TPBI:Ir(ppy)$_3$:Ir(dhfpy)$_2$(acac) (5, 8 %, 1 %) //
TPBI (10)//BPhen:Cs (60)//Al (100)

8.6   Conclusions and Outlook

In this chapter, the improvement of the single units and the white tandem OLED was investigated with the aim to increase LE and EQE. The existing OLED structure introduced by Thomas Rosenow had been used as starting point. For the red/blue TH OLED doping of the EML with a triplet manager NPD was carried out which leads to an enhanced charge and exciton transport on the dopant. Furthermore, a significant enhancement of the device lifetime (factor 3.5) was obtained, but no improvement regarding the device efficiency or roll-off. For the green/yellow PH OLED an EQE improvement factor of 1.2 was achieved using a double emission structure and it was found that for the double emission OLED BAlq2 as hole blocking layer exhibits the best performance.

For the tandem OLED, Al and Ag were tested as CGL material. Since Ag reduced the driving voltage while the spectral emission and angular dependence was almost maintained, the LE was slightly enhanced. By combining the new CGL interlayer material Ag with the double emission structure, a white tandem OLED with 33 lm/W (25% EQE, CIE (0.528/0.425)) at 1,000 cd/m² was obtained, which will be the used in further experiments (see Sec. 9.5).

Although the tandem OLED was step-wise improved, it did not exceed the efficiencies presented by Rosenow. The main reason for the different efficiencies compared to the work of Rosenow is presumably the change in material batches and differences caused by processing variations.

To improve the tandem OLED which has been already optimized by Rosenow is challenging if the same materials have to be used. Therefore, the research on emitters with a higher internal quantum yields is important. Furthermore, the application of outcoupling enhancement methods is seen to improve the efficiencies.

9   Silver Nanowire Electrodes

Alternative electrodes to ITO are essential for advanced applications of organic electronic devices. In this chapter, an electrode consisting of a network of silver nanowires embedded into a polymer matrix is investigated. Processing is described and important quality parameters of the new electrode are explained. White OLEDs comprising different buffer layers between the electrode and the organic layers are investigated in terms of efficiency and viewing angle characteristics. Furthermore, a light outcoupling study of the efficiency and color coordinates depending on the ETL thickness is performed. Finally, tandem white OLEDs on silver nanowire electrodes with state-of-the-art efficiencies are demonstrated.

9.1   Demand for Alternative Electrodes

For many years, ITO has been the material of choice not only as electrode material for OLEDs, but also for LCDs, plasma displays, or modern touch displays in mobile phones and tablets. The features of ITO are manifold: besides the two main advantages of high transparency in the visible wavelength regime ($> 85\%$) and high conductivity ($\sim 10^{-3}$ S/cm, sheet resistance ~20 Ω/sq), ITO layers have a low roughness of a few angstroms, can be etched very precisely, and are chemically resistant to moisture.[237, 238] From an application point of view, ITO is a beneficial electrode, since it is also opaque in the UV and thus protects the organic layers against UV light from the sun which might otherwise cause material degradation.

However, indium is a rare noble earth material. Due to the limited resources, it can be expected that the price for indium will increase in the next years. In 2011, the price for 1 kg indium has been 700 \$, which is almost comparable to silver (1,000 \$/kg). According to the US Mineral Resources Program, the remaining indium resources are estimated to about 11,000 tons. Assuming a refinery production of 550 tons/year, this means that in 20 years these resources will be exhausted.[239] Furthermore, ITO is brittle which makes it less suitable for applications of OLEDs on flexible substrates.

It has to be considered that in OLEDs an alternative electrode does not only influence electrical properties, but also the light outcoupling efficiency (cf. Sec. 4.5). A summary of efficiencies achieved for OLEDs on alternative electrodes is given in Table 9.1. Efficiencies of comparable ITO OLEDs are given, where available. However, the comparison has to be taken with care, as the alternative electrodes are mostly placed on a PET substrate, which itself exhibits a different outcoupling efficiency than ITO on glass.

In 2007, Fehse *et al.*[145] demonstrated an LE of 63.5 lm/W at 100 cd/m² for a green phosphorescent OLED using the highly conductive polymer PEDOT:PSS[24].

---

[24]poly-(4,3-ethylene dioxythiophene)

For green phosphorescent OLEDs, a high LE of 115 lm/W (40% EQE) at 1,000 cd/m² has been achieved by Wang *et al.*[240] using a $Ta_2O_5/Au/MoO_3$ electrode. The Ta_2O_5 acts as high index outcoupling layer, Au as conductive electrode, and MoO_3 as hole injection layer. The LE could even be enhanced to 180 lm/W (63% EQE) by attaching a glass half-sphere. Although this electrode design strongly enhances the outcoupling efficiency for green emission, it lowers at the same time the outcoupling efficiency for blue and red emission. This effect occurs mostly if a metal is used instead of ITO and complicates the design of white OLEDs.

Nevertheless, Mazzeo *et al.*[241] showed a white two-color OLED using an Ag/organic with emitters/Ag/organic/Ag structure. They achieved a LE of 15 lm/W (at 1,000 cd/m², CIE(0.41/0.43)) and CRI values above 80, which are extraordinarily high for a two-color white OLED. Usually, the viewing angle characteristics are as well strongly influenced in this strong optical cavities. Mazzeo and coworkers found a change of CIE coordinates with viewing angle from 0° to 60° of $\Delta(x/y)=(0.05/0.04)$ and a reduction of the CRI by more than 30.

Graphene might be another suitable alternative to ITO. In 2012, Han *et al.*[149] showed high efficiencies for a green phosphorescent OLED (max. LE of 102.7 lm/W). Furthermore, they were able to demonstrate a 5 x 5 cm² white OLED on a flexible PET substrate. Unfortunately, no LE or EQE values are given here. The graphene electrode used is doped with HNO_3 leading to a work function of -5.95 eV, improved hole injection, and a low sheet resistance of 30 Ω/sq.

First white polymer OLEDs with phosphorescent small-molecule emitter materials on silver nanowire (NW) electrodes were recently published by Li *et al.*[242]. Here, a maximum LE of 10.3 lm/W with CIE coordinates of (0.36/0.51) is obtained using a 3-color OLED.

In summary, ITO-free OLEDs have reached state-of-the art efficiencies only for monochrome devices so far. Recently, the research on white ITO-free OLEDs has started and comparable efficiencies to ITO-OLEDs were already achieved. However, highly efficient white OLEDs with state-of-the-art efficiencies have not been demonstrated up to now. Furthermore, there is a lack of investigations on angular emission properties, like the comparison to a Lambertian emitter, the CIE color change, and CRI deviations.

Table 9.1: Summary of green and white OLED performance for different electrode//substrate combinations. For green phosphorescent ITO-free OLEDs high efficiencies can be demonstrated. However, white ITO-free OLEDs with state-of-the-art efficiencies are not reported so far. Most electrodes show similar or superior performance when compared to a reference OLED with ITO electrode (gray values).

author	year	LE[1] lm/W	LE[2] lm/W	EQE[1] %	CE[1] cd/A	CE[2] cd/A	CIE[2], CRI[2]
GREEN PHOSPHORESCENT							
PEDOT:PSS//glass							
Fehse[145]	2007	63.5	18.7	—	62.0	—	—
		53.8	—	—	54.1	—	—
graphene//glass							
Sun[243]*	2010	0.38	—	—	0.75	—	—
Ta$_2$O$_5$/Au/MoO$_3$//PET							
Wang[240]	2011	160	115	40	—	—	—
		290[a]	180[a]	63[a]	—	—	—
		100	60	24	—	—	—
Ag NW//PET							
Li[147][b]	2011	5.7	12	—	30.6	—	—
		9.6	39	—	39.3	—	—
graphene-HNO$_3$//PET							
Han[149, 244]	2012	102.7	—	—	98.1	—	—
		85.6	—	—	81.8	—	—
WHITE 2-COLOR							
Ag//glass							
Mazzeo[241]	2010	—	15	—	—	11	(0.41/0.43), 29
		—	11	—	—	6.6	(0.39/0.43), 51
		—	12	—	—	7.4	(0.41/0.44), 86
		—	8	—	—	5.1	(0.29/0.33), 71
graphene-HNO$_3$//PET							
Han[149]	2012	—	—	—	16.3	—	(0.32/0.42)
		—	—	—	10.9	—	—
Ag NW//PET							
Li[242][b]	2012	6.0	—	12.3	20.3	—	(0.36/0.36)
		4.5	—	9.2	15	—	(0.35/0.33)
WHITE 3-COLOR							
Ag NW//PET							
Li[242][b]	2012	10.3	—	17.5	42.3	—	(0.36/0.51)
		8.0	—	12.7	30	—	(0.34/0.49)

[1] maximum value or at 100 cd/m²   [a] with half-sphere
[2] at 1,000 cd/m²   [b] polymer OLED
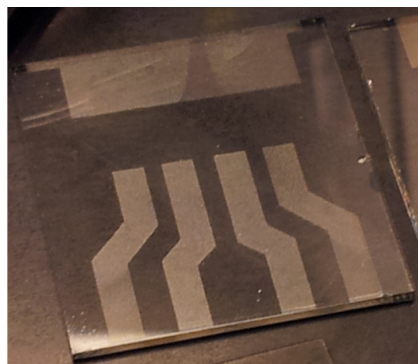* top-emitting   comparable ITO//glass OLED

9.2   Processing and Quality Characteristics

The fabrication and characterization of the Ag NW electrodes used in this work was done by Whitney Gaynor and Greyson Christoforo at Stanford University (USA).
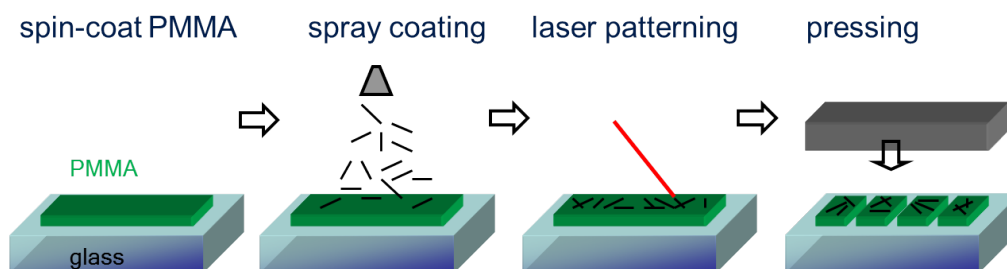
Fabrication

The processing steps for the NW electrodes are shown in Fig. 9.2. First, a 145 nm thick film of the polymer PMMA[25] is spin-coated onto the glass substrate. The NWs (Seashell Technology, Inc.), suspended in isopropanol, are then deposited via spray-coating, followed by patterning using an infrared laser. To ensure an easy fabrication and measurement of the OLEDs, the patterning layout is chosen to be the same as the common ITO structure at the IAPP (cf. Fig. 9.1). Finally, the NWs are embedded into the polymer using a heated flat-plate press. Further details about the equipment used and processing procedure can be found in Refs. [245–247].

Figure 9.1: Photograph of the NW electrodes on a glass substrate processed at Stanford University.

The samples were sealed under nitrogen atmosphere and sent to IAPP by mail, where they have been again stored under nitrogen environment. To remove water residuals, the NW electrodes have been heated out at 110°C for 30 min before OLED processing. No significant performance difference of the OLEDs was observed, when the substrates were heated in UHV or at normal pressure under nitrogen atmosphere.

Figure 9.2: Fabrication steps of the NW electrodes. After spin-coating PMMA on the glass substrate, the NWs are deposited via spray-coating and patterned by a laser. Embedding of the NW into PMMA is achieved using a heated flat-plate press.

---

[25]poly (methyl methacrylate)

Important Properties

The SEM image in Fig. 9.3 (a) shows the NWs after deposition on top of the PMMA film. It can be seen that the wires are dispersed into a random mesh. After pressing (Fig. 9.3 (b)), the NWs develop flat, fused junctions, and thus form a continuous network. This flat surface is expected to be beneficial for OLEDs, since leakage currents due to upstanding wires can be avoided.

(a)   (b)
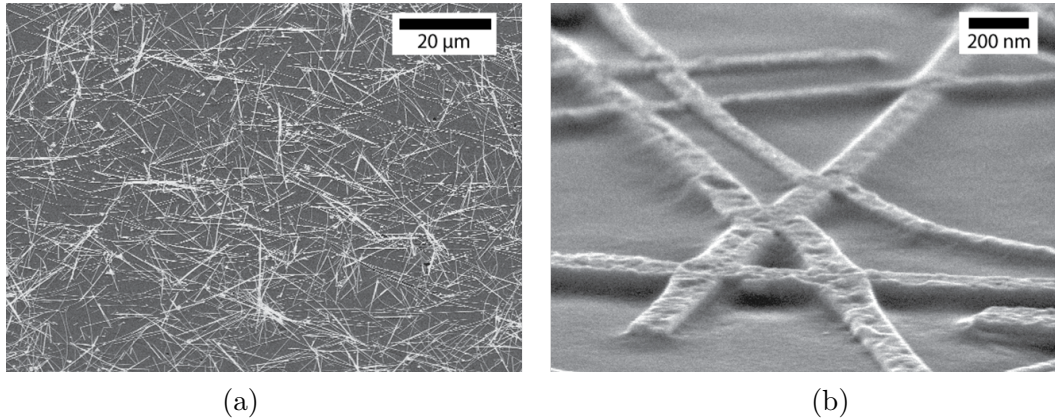
Figure 9.3: SEM images of the NWs after deposition on top of PMMA (a) and after pressing (b). The pressing leads to a connection of the single wires and forms a continuous, flat NW network. The images are provided by Whitney Gaynor.

The NW electrodes used in this work exhibit a sheet resistance of 12 Ω/sq, an average transmission of 92%[26], and an RMS roughness between 6 and 8 nm.

A figure of merit for large area applications is defined by the material's conductivity σ and the absorption coefficient α. For the samples used in this work, this ratio is $\alpha/\sigma = 1$ Ω^{-1} which is just enough to meet the criteria for large area application ($\alpha/\sigma \geq 1$ Ω^{-1}) stated by Rowell *et al.*[248].

The NW electrode has a diffuse appearance (cf. Fig. 9.1), meaning that this electrode features scattering properties. It is expected that the scattering positively influences the outcoupling efficiency and also the viewing angle characteristics in OLEDs. An average haze (= diffuse transmission/total transmission) of 6.8% is measured for the NW electrodes used in this work.

[26]This value is measured using a glass substrate as reference.

9.3   Influence of Organic Buffer Layers

In a first test, a hybrid white OLED stack comprising an interlayer to separate fluorescent and phosphorescent emission is used. This layer structure has been developed by Gregor Schwartz at the IAPP[249] and has been improved by Thomas Rosenow, who replaced the blue emitter Spiro-DPVBi [27] by the host:guest system MADN:TBPe.[102] The used OLED layer structure is shown in Fig. 9.5. This OLED stack has been chosen, because it exhibits the longest lifetime in comparison to other available white OLED structures.

  As one type of buffer layer, the polymer PEDOT:PSS is spin-coated[28] on top of the NW electrode. To avoid shorts, OLEDs are build with a thin and a thick HTL, so the HTL itself can act as well as a buffer layer.

Determination of HTL Thickness using Optical Simulation

To estimate the required thicknesses of the HTL, the field distributions at 0° of the OLEDs are calculated (Fig. 9.4) using ITO as electrode. It can be seen that for an HTL thickness of 50 nm (1st optical maximum) and 180 nm (2nd optical maximum), the emitters are placed in the respective field maximum of their peak emission wavelength (460 nm for blue, 500 nm for green, and 610 nm for red). In this manner, the ITO-OLEDs are optimized for light outcoupling into air. The simulation software does not allow to model a scattering layer such as the NW electrode. Therefore, the same HTL thicknesses are used for the NW-OLEDs like for the ITO-OLEDs in the following experiment.
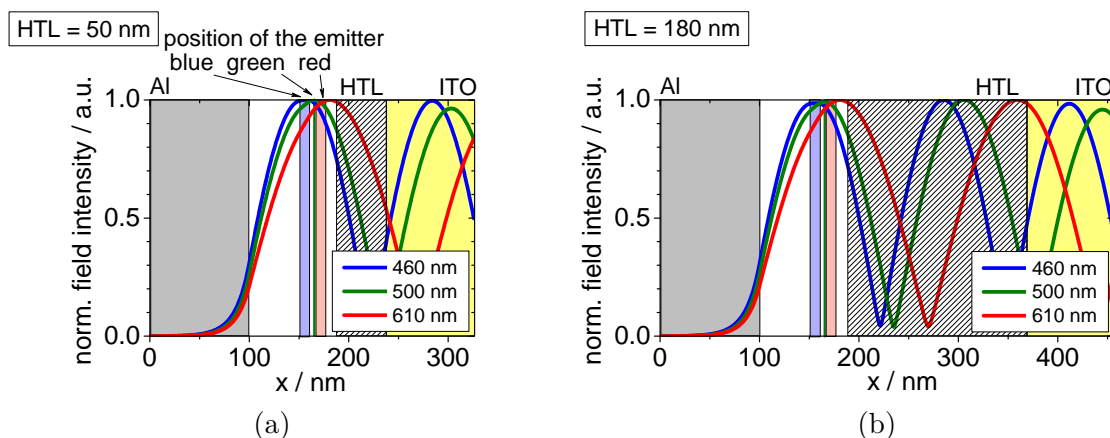
Figure 9.4: Simulated electromagnetic field distributions at 0° for the OLED stack shown in Fig. 9.5. An HTL thickness of 50 nm and 180 nm is found to place the emitters into their respective field maximum and will be used in the experiment.

---

[27]2,2',7,7'-tetrakis(2,2-diphenylvinyl) spiro-9,9'-bifluorene
[28]Spin-coating of PEDOT:PSS was carried out at Stanford University.

Experimental Results and Discussion

The performance characteristics of the NW-OLED and ITO-OLEDs are shown in Fig. 9.5. The NW-OLED without PEDOT:PSS and 50 nm HTL thickness was electrically short. This indicates that the organic layers cannot fully cover the NW network, but just fill the gaps between the wires. The IV characteristics (Fig. 9.5 (a)) show that for the ITO-OLEDs, the leakage currents are one to two orders of magnitude lower than for the NW-OLEDs (10^{-4} mA/cm² for ITO-OLEDs, 10^{-3}-10^{-2} mA/cm² for NW-OLEDs). Regarding only the NW-OLEDs, the device with the thickest buffer layers (with PEDOT:PSS and 180 nm HTL) shows, as expected, the lowest leakage current ($4 \cdot 10^{-3}$ mA/cm²). In forward direction, the NW-OLEDs show a voltage drop compared to the ITO-OLEDs, which is attributed to the less efficient hole injection caused either by the NWs or the PEDOT:PSS overcoat. For this reason the LV curve has a flatter shape for the NW-OLEDs at high voltages (> 3.5 V).

Interestingly, the second order NW-OLED with PEDOT:PSS shows a higher emission intensity at a wavelength of about 460 nm (Fig. 9.5 (c)). The angular dependent emission is close to the Lambertian emitter for all devices (Fig. 9.5 (d)). This is most pronounced in case of the second order PEDOT:PSS OLED.

While the PEDOT:PSS layer leads to a poorer performance in the first optical maximum, it induces similar efficiencies for the second order OLEDs (Fig. 9.5 (e) and (f)). However, highest efficiencies are reached with the first order ITO-OLED (16 lm/W, 8.1%, 18.1 cd/A, at 1,000 cd/m² with CIE color coordinates of (0.467/0.394) and CRI of 74), while the best NW-OLED (second order) exhibits 13 lm/W, 7.5%, and 14.4 cd/A at 1,000 cd/m² with (0.453/0.376) and a CRI of 76.
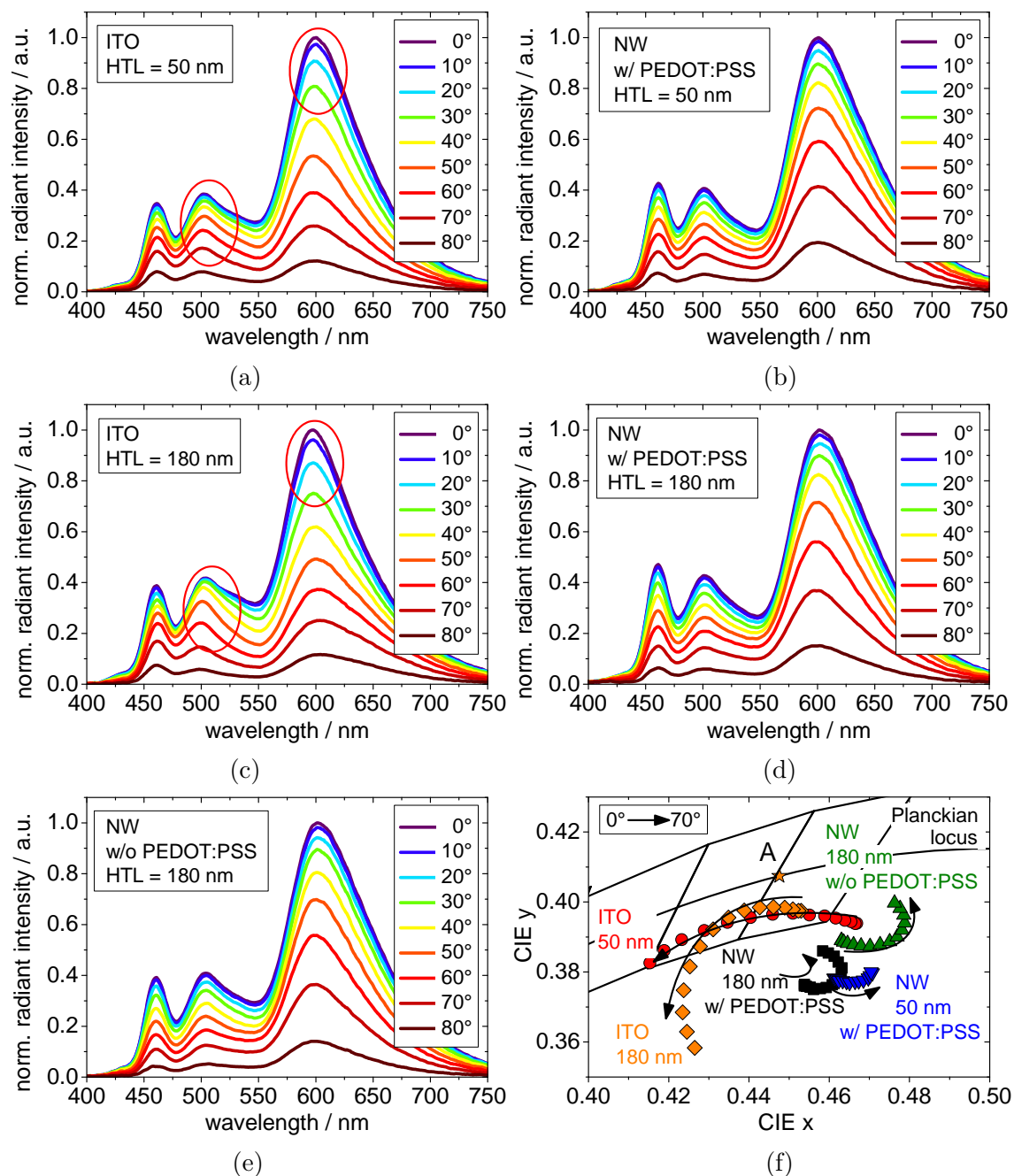
The angular dependent emission spectra of the first and second order OLEDs are shown in Fig. 9.6. Differences in the spectral emission can be particularly observed in the green and red wavelength regime (red marked). While for the ITO-OLEDs the radiant intensity of the green emission maximum is almost constant up to a viewing angle of 30°, the green emission peak decreases steadily for the NW-OLEDs. The red emission peak shows a much faster decrease in intensity in case of the ITO-OLED. These effects can be attributed to the light scattering properties of the NWs.

For the second order NW-OLEDs there is no significant difference in the angular dependent spectral emission for the samples with and without PEDOT:PSS (Fig. 9.6 (d) and (e)). It is noteworthy that the additional PEDOT:PSS layer does not influence the electrical or optical properties of the NW-OLEDs in a negative way.

Differences in the angular dependent emission spectra can be seen more clearly in the CIE color diagram (Fig. 9.6 (f)). Black arrows indicate the shift of the color coordinates from 0° to 70°. As expected, the ITO-OLEDs show a much larger shift of the color coordinates than the NW-OLEDs. Interestingly, the CIE coordinates for the ITO-OLEDs shift towards the blue, while those of the NW-OLEDs tend more towards the green or red spectral region. The reason for this effect is not yet fully understood.
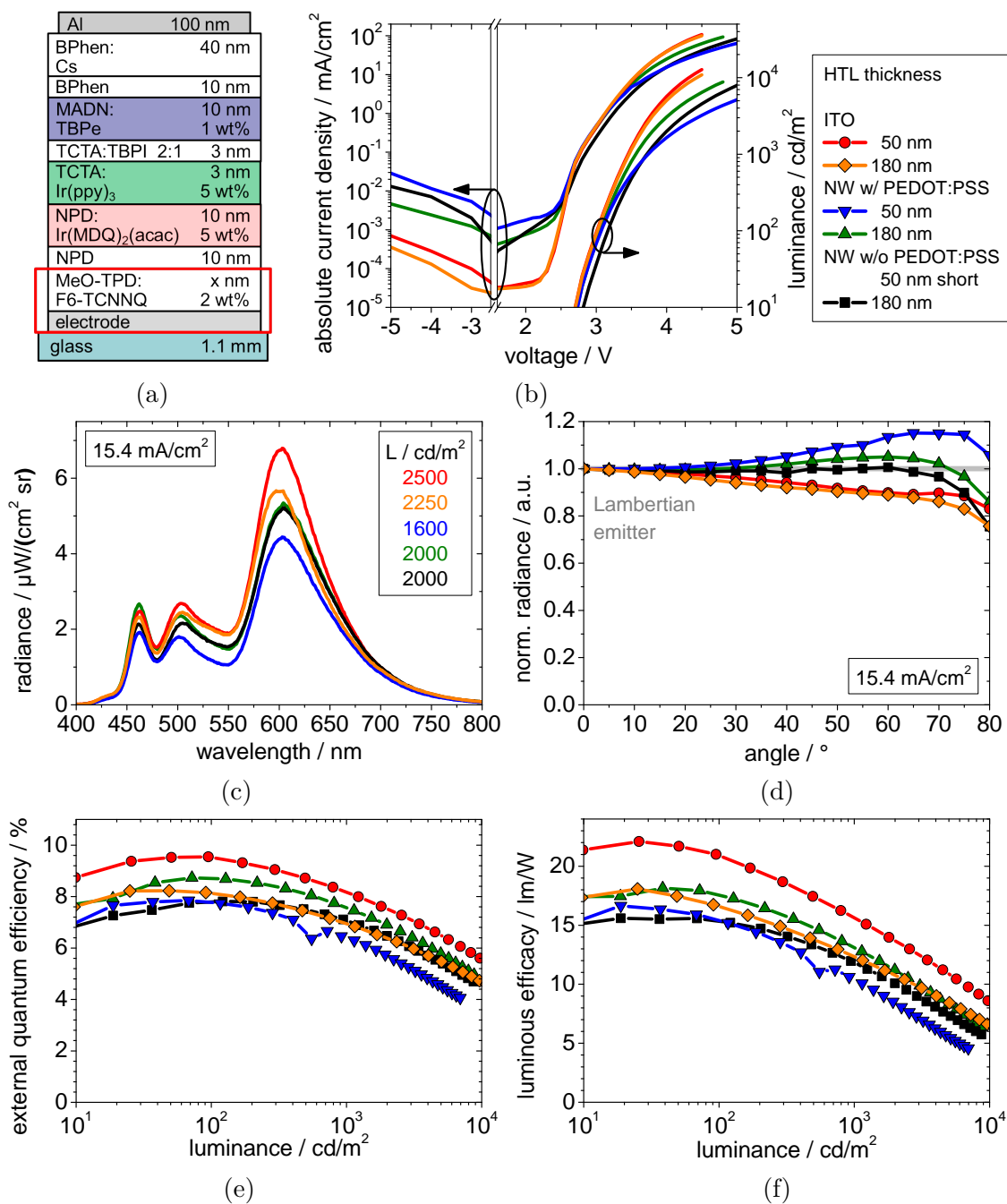
Figure 9.5: OLED layer structure (a) and performance (b-f) of the NW-OLEDs with and without PEDOT:PSS in comparison to ITO-OLEDs for different HTL thicknesses. While the PEDOT:PSS layer leads to a slightly poorer performance for OLEDs in the first optical maximum, it maintains comparable efficiencies for the second order OLEDs.

Figure 9.6: Angular dependent emission characteristics (a-e) and CIE color coordinates (f) of the ITO- and NW-OLEDs at a current density of 15.4 mA/cm². Differences in the spectral emission can be particularly observed in the green and red wavelength regime (red marked). The resulting color shift with viewing angle (black arrows in (f)) is reduced in case of the NW electrode, which can be attributed to their scattering properties.

The main observations and conclusion from this experiment are:

- Working OLEDs on NW electrodes are successfully fabricated.

- The organic buffer layers (either PEDOT:PSS and/or MeO-TPD:F6-TCNNQ) reduce the leakage current, because they cover inhomogeneities of the electrode which otherwise lead to local shorts in the OLED.

- The PEDOT:PSS buffer layer does not influence the optical performance of the NW-OLEDs significantly. Therefore, the PEDOT:PSS overcoat layer will be used as default in further experiments.

- The NW-OLEDs have slightly reduced efficiencies when compared to the ITO-OLEDs at the same HTL thickness, but exhibit superior viewing angle characteristics, especially with regard to the CIE color coordinates. Here, the scattering properties of nanowires are seen as reason for the reduced color shift with viewing angle.

- While the ITO-OLEDs could be optimized for high efficiencies using simulation software, it remains open if the NW-OLEDs are optically optimized. Therefore, an empirical study with varying transport layer thickness needs to be done which will be described in the next section.

## 9.4   Variation of the Electron Transport Layer Thickness

To study the light outcoupling properties and to optimize the OLEDs in terms of efficiency and white color coordinates, a variation of the ETL layer thickness is carried out. In this experiment, the same white hybrid OLED stack as described in the previous section is used (Fig. 9.7 (a)). The ETL thickness is varied from 40 to 265 nm in 15 nm steps for the reference ITO-OLEDs and from 40 to 250 nm in 30 nm steps for the NW-OLEDs. The HTL thickness is 180 nm as derived from the previous experiment (Sec. 9.3).

The IV curves of all OLEDs are shown in Fig. 9.7 (b). In agreement with the previous experiments, the leakage currents are more then one order of magnitude higher for the NW-OLEDs compared to the ITO-OLEDs. The expected reduction of the leakage current with increasing ETL thickness for the NW-OLEDs is not observed. In fact, the leakage currents are widely scattered, ranging from 10^{-2} to 10^{0} mA/cm² and no explicit trend can be deduced (inset in Fig. 9.7 (b)).

In forward direction all OLEDs have a similar IV characteristic. This is in contrast to the experiment described in the last section, where a voltage drop has been observed for the NW-OLEDs. One possible explanation is that the NWs and the PEDOT:PSS suffer a certain form of degradation while being shipped from Stanford to Dresden due to non-perfect sealing. In the first experiment (influence of organic buffer layers), the time frame between electrode fabrication and OLED processing has been three weeks. For the ETL variation a new batch of electrodes was sent and the OLED processing has taken place one week after electrode fabrication. This has been considered in further experiments and the time delay due to shipping has been minimized to less than a week.

As indicated with the superscript S, the efficiencies have been measured in the Ulbricht sphere at a luminance of 1,000 cd/m² with and without an attached half-sphere to investigate the outcoupling properties of the NW electrode (Fig. 9.7 (c) and (d)). The external quantum efficiency and the luminous efficacy show the typical maximum-minimum-maximum behavior as described in Sec. 4.5.

A similar trend can be observed when attaching a half-sphere. It is expected that the NW-OLEDs scatter waveguided modes into the substrate which would lead to a strong efficiency enhancement when attaching the half-sphere. Surprisingly, only small differences between NW-OLEDs and ITO-OLEDs are present here. This means that the NW-OLEDs exhibit similar outcoupling efficiencies like the ITO-OLEDs. The only significant difference between the NW-OLEDs and the ITO-OLEDs is that the second maximum occurs at thinner ETL thicknesses (~190 nm) than that of the ITO-OLEDs (~220 nm). This is important, because it means that a comparison of efficiencies at the same ETL thickness, especially in higher order OLEDs, has to be taken with care as they do not necessarily match the efficiency maximum.
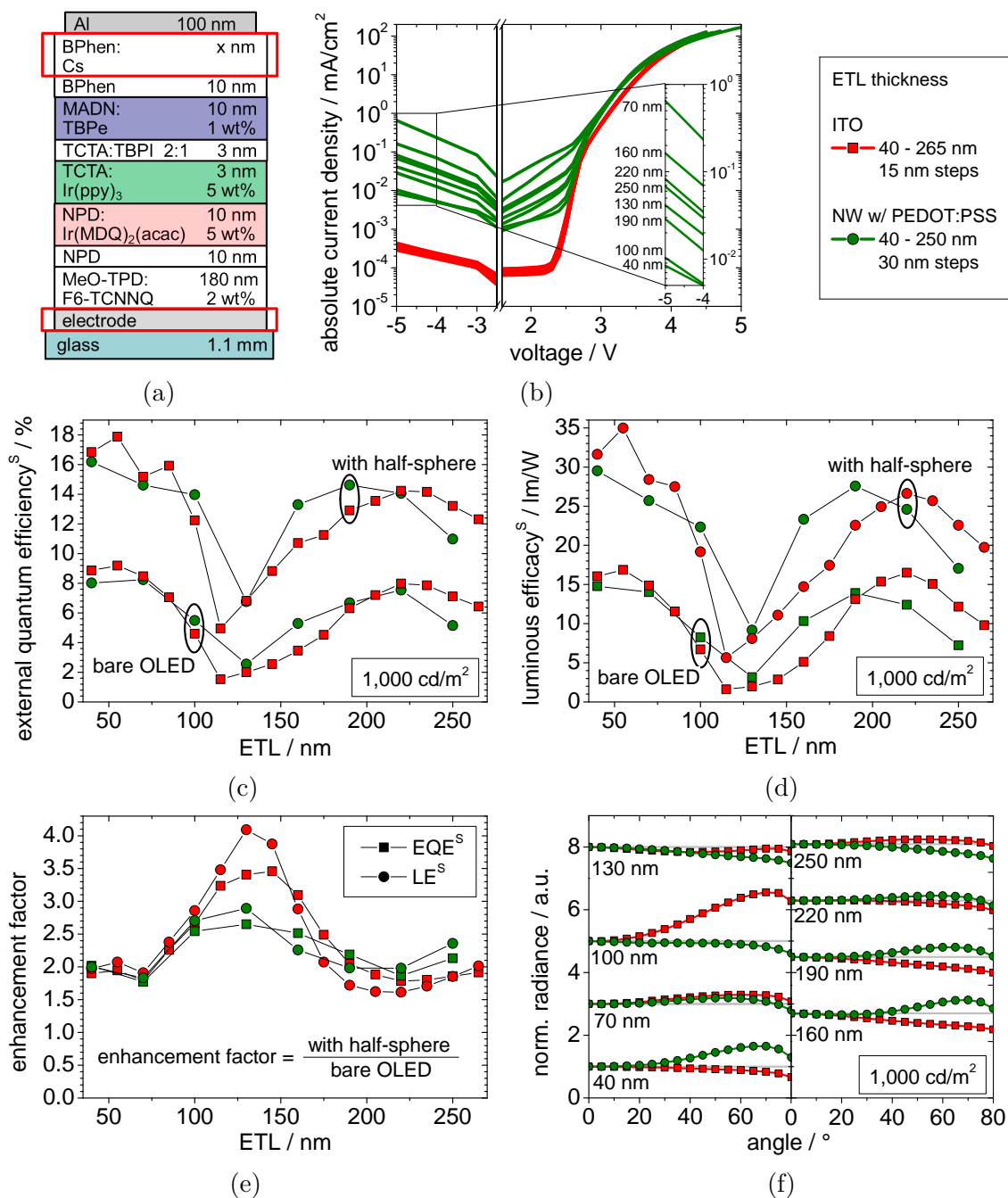
Figure 9.7: OLED layer structure (a) and performance (b-f) of ITO-OLEDs and NW-OLEDs with varying ETL thickness. The inset in the IV-diagram (b) shows that the leakage currents of the NW-OLEDs are widely scattered and no explicit trend regarding the ETL thickness is observed. As indicated by the superscript S, the efficiencies (c,d) are measured in the Ulbricht sphere at 1,000 cd/m² with and without a light outcoupling half-sphere. The enhancement factor (e) due to the half-sphere varies between 1.6 and 4 among OLEDs in the efficiency maximum and minimum. The radiance curves at 1,000 cd/m² (f), which are displaced for clarity, are characterized by the ETL thickness rather than by the electrode material.

In general, the ITO-OLEDs show slightly better efficiencies (about 15 % better). However, the NW-OLEDs and the ITO-OLEDs reach their highest efficiency in the first maximum at an ETL thickness of 40 and 55 nm, respectively. Here, the EQE$^{\text{S}}$ (LE$^{\text{S}}$) at 1,000 cd/m² is 8.0% (14.8 lm/W) for the NW-OLED and 9.2% (17.9 lm/W) for the ITO-OLED. To extract the substrate modes and to investigate if a stronger scattering of waveguided modes into the substrate is present when using NW electrodes, a glass half-sphere is attached to the OLEDs. As described in Sec. 4.5, with increasing ETL thickness the number of SPP modes is reduced while the number of waveguided modes increases. If the NW electrode scatters waveguided modes efficiently into the substrate, a steady increase of efficiency with increasing ETL thickness can be expected. However, the efficiencies (Fig. 9.7) provide a maximum-minimum-maximum behavior, which means that the NW electrode is not able to scatter waveguided modes efficiently.

Furthermore, the efficiency enhancement factor (Fig. 9.7 (e)) due to the half-sphere shows a similar trend for the NW- and the ITO-OLEDs. This means that the amount of substrate modes is more or less identical in the NW- and ITO-OLEDs at a constant ETL thickness. The efficiency enhancement factor is in the range of 1.6 to 2.2 if the OLEDs are in the efficiency maximum. It can be strongly increased up to a factor of 2.9 for NW-OLEDs and 4 for ITO-OLEDs, when the OLED is in the optical minimum (160 nm).

A strong dependence on the ETL thickness is observed when regarding the angular emission characteristics (at 1,000 cd/m², Fig. 9.7 (f)). For example, in the case of 40 nm or 250 nm ETL thickness, the ITO-OLED resembles a Lambertian emitter much more closely then the NW-OLED. The opposite trend can be seen for the OLEDs in the optical minimum at 100 nm. While the NW-OLED has almost perfect Lambertian emission, the corresponding ITO-OLEDs exhibits a strong super-Lambertian behavior. It can be seen that it is not a general rule that NW-OLEDs have a more Lambertian like emission characteristic. This property depends in fact on the design of the OLED cavity. Furthermore, the CIE color coordinates and the color shift for different viewing angles and varying ETL thickness are of interest and are shown in Fig. 9.8 at 1,000 cd/m². The color coordinates depend strongly on the ETL thickness. In general, the NW-OLEDs show smaller deviations of the color coordinates to the warm white point A and exhibit a smaller color shift with increasing viewing angle than the ITO-OLEDs.

The efficient ITO-OLED and NW-OLED in the first order cavity have white color coordinates. Furthermore, the ITO-OLED with 160 nm and the NW-OLED with 190 nm have CIE coordinates which are very close to the warm white color point A. However, these latter ETL thicknesses do not correlate to the ETL thicknesses for the OLEDs which reached highest efficiencies (i.e. to 190 nm and 220 nm). This trade-off between high efficiency and warm white color coordinates shows again the challenges involved in the design of efficient white OLEDs.
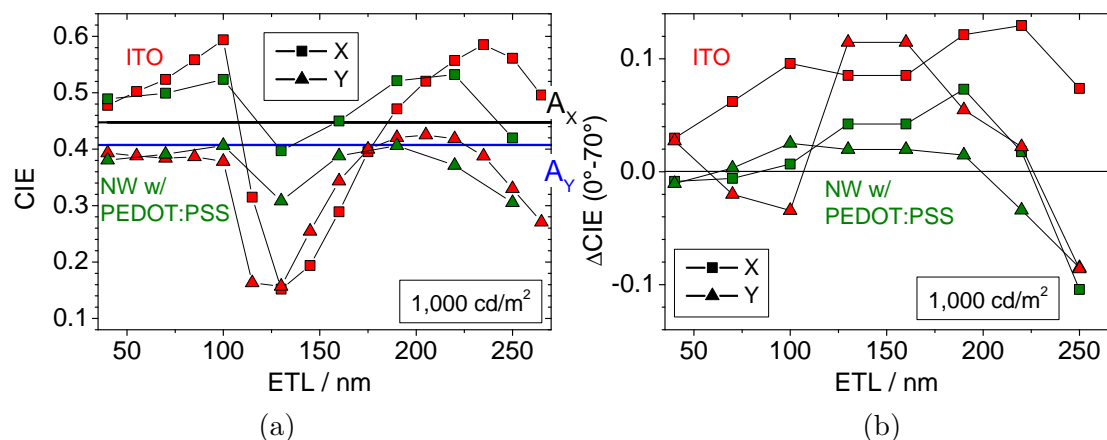
Figure 9.8: CIE color coordinates for 0° (a) and color shift with viewing angle ΔCIE (0°-70°) (b) for the ITO- and NW-OLEDs with varying ETL thickness at a luminance of 1,000 cd/m². The color coordinates and the color shift vary strongly with ETL thickness. In general, the NW-OLEDs show smaller deviations of the color coordinates to the warm white point A and exhibit a smaller color shift with viewing angle than the ITO-OLEDs.

With an EQE^S of 8-9% and LE^S of 15-17 lm/W at 1,000 cd/m², the OLEDs exhibit a good performance, but the demonstration of state-of-the-art efficiencies is still missing and will be investigated in the following section.

9.5   Highly Efficient OLEDs on Silver Nanowire Electrodes

The high efficiency tandem stack (cf. Sec. 8.5) is applied on the NW electrode. The performance of the tandem OLEDs on the NW electrodes is shown in Fig. 9.9. In this experiment, the intrinsic 4P-NPD layer thickness has been varied between 3 and 4 nm and the first HTL layer between 30 and 40 nm. The results are only shown for the devices which exhibited the highest LE^S, respectively. Interestingly, the optimal thicknesses for the NW- and the ITO-OLED are the same, namely a 4P-NPD thickness of 3 nm and an HTL thickness of 30 nm. The leakage current (Fig. 9.9 (b)) of the NW-OLED does not strongly differ from that of the ITO-OLED (~10^{-3} mA/cm²). Due to the thick organic layers (>320 nm), a low leakage current is expected. However, in previous experiments (Sec. 9.4) the organic layers had a total thickness of more than 400 nm and still showed significantly higher leakage currents than the ITO-OLEDs.

In previous experiments it has been found that the processing time between NW electrode and OLED plays an important role for the IV characteristics. Despite the fact that the processing of the OLEDs has taken place in less than one week after electrode fabrication, a voltage drop is observed in the IV curves of the NW-OLED in forward direction. Since a new batch of electrodes has been used for this experiments, the reason for the voltage drop is not fully understood and requires further investigation.

(a)

(b)

(c)

(d)

(e)

(f)
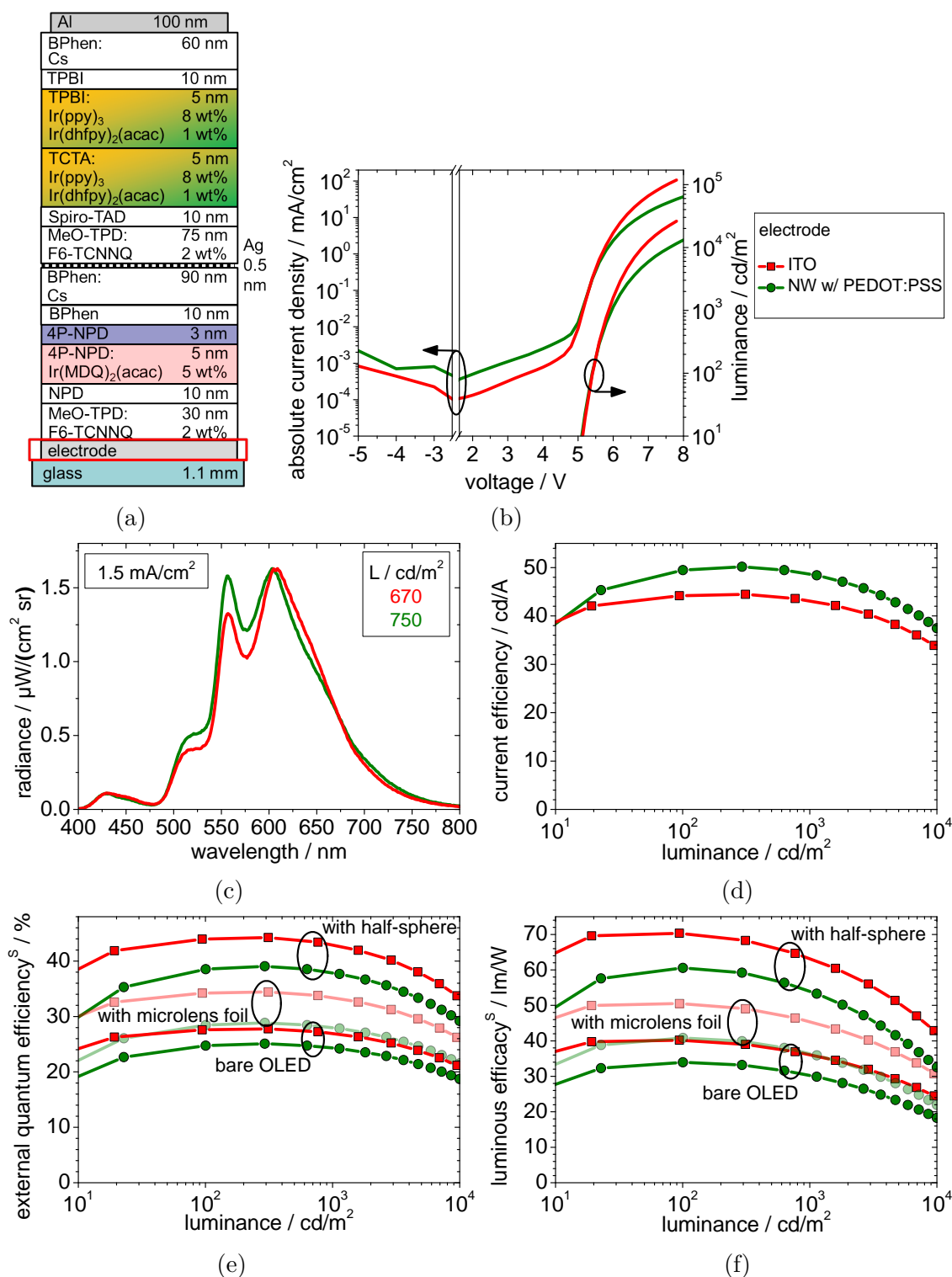
Figure 9.9: OLED layer structure (a) and performance (b-f) of the NW- and ITO-OLEDs based on a highly efficient white tandem structure. The device efficiencies of both OLEDs are comparable and can be similarly enhanced using different outcoupling techniques (d-f).

Therefore, a shorter time frame between the fabrication steps is necessary. However, due to electrode processing at Stanford University and the OLED processing at the IAPP, this has not been possible during this work.

Up to a luminance of 1,000 cd/m² the NW-OLED and the ITO-OLED exhibit nearly identical LV characteristic (Fig. 9.9 (b)). At higher luminance, the NW-OLED requires a higher voltage. The spectral emission of both devices at 0° at a low current density of 1.5 mA/cm² is similar, with a slightly higher contribution of green and yellow light for the NW-OLED (Fig. 9.9 (c)). This spectral difference consequently leads to a higher current efficiency for the NW-OLED (Fig. 9.9 (d)). At 1,000 cd/m², the CE of the NW-OLED is 49 cd/A and 43 cd/A for the ITO-OLED.

From an application point of view, the color stability with applied current density is important. At high current densities, the spectral distribution slightly changes and the CIE coordinates are shifted towards blue color coordinates. The color shift $\triangle$CIE from 1.5 mA/cm² to 15.4 mA/cm² (corresponding to a luminance of about 700 cd/m² and 6,000 cd/m², respectively) is (0.004/0.007) for the NW-OLED and (0.005/0.010) for the ITO-OLED. The small shift towards blue color coordinates can be explained by the fact that the phosphorescent emitters underlie stronger annihilation rates than the blue fluorescent emitter, due to the longer lifetime of the triplet state. Hence, at high current densities the emission of the phosphorescent emitters is reduced more than that of the blue fluorescent emitter.

At 1,000 cd/m², the EQE^S (LE^S) increases from 26.8% (35.8 lm/W) to 42.8% (63.0 lm/W) for the ITO-OLED and from 24.3% (30.3 lm/W) to 37.9% (53.9 lm/W) for the NW-OLED when attaching a half-sphere (Fig. 9.9 (e) and (f)). Despite the slightly better efficiencies of the ITO-OLED, the two devices are comparable, and the NW-OLED reaches remarkably high efficiencies compared to other studies (cf. Table 9.1), with a similar enhancement like the ITO-OLED when using an outcoupling half-sphere. Attaching a flat microlens foil, which is more suitable for practical applications than the half-sphere, the EQE^S (LE^S) is as high as 33.4% (45.4 lm/W) for the ITO-OLED and 28.0% (36.3 lm/W) for the NW-OLED.

Figure 9.10 shows the angular dependent emission characteristics of the OLEDs under investigation. Comparing the spectral emission intensity (Fig. 9.10 (a) and (b)) for the ITO- and NW-OLED, the NW-OLED shows a constant decrease in emission of the peaks from each of the four emitters, resulting in a consistent white color. In contrast, a clear change in spectral shape with increasing viewing angle is observed for the ITO-OLED. In particular, the red peak (610 nm) shows an initial increase that is not present in the NW device.
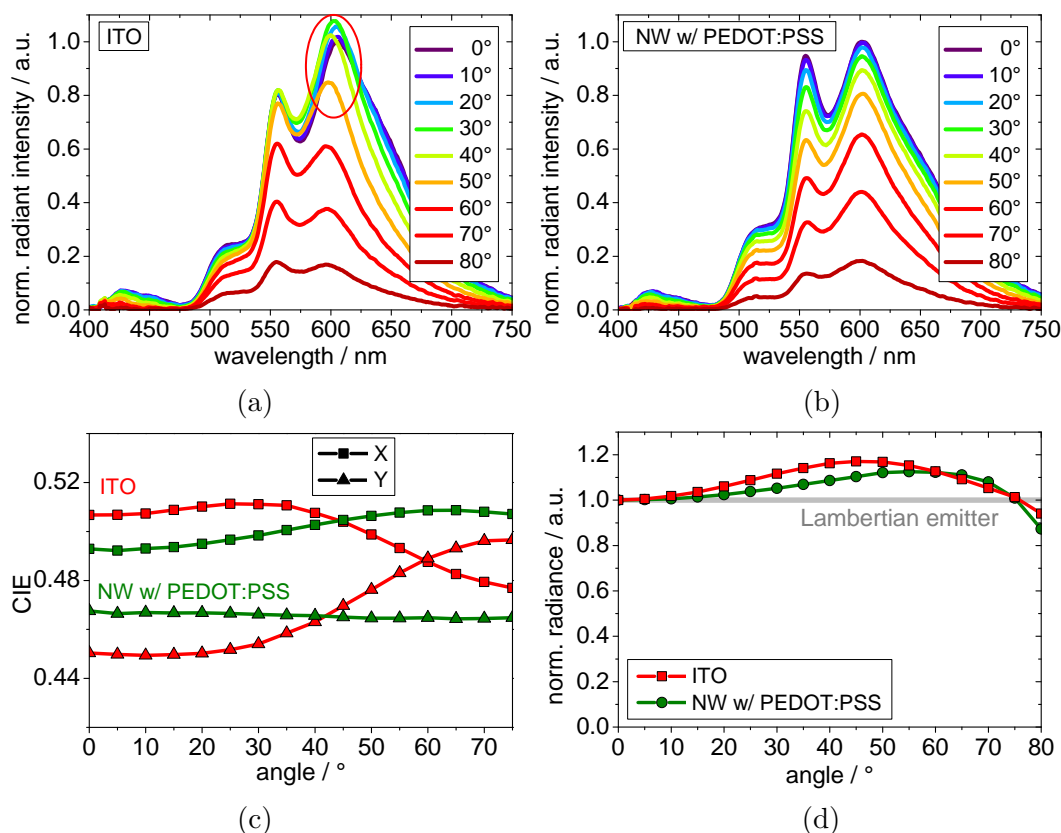
Figure 9.10: Viewing angle characteristics (a-d) of the highly efficient white tandem OLEDs at a luminance of 1,000 cd/m². The NW-OLED exhibits superior color stability (c) with increasing viewing angle compared to the ITO-OLED and shows a Lambertian like emission characteristic (d).

The resulting integrated emission is closer to the Lambertian ideal for the NW-OLED than for the ITO-OLED (Fig. 9.10 (d)). Additionally, CIE color coordinates (Fig. 9.10 (c)), CRI, and CCT are far more stable with viewing angle for the NW-OLED than for the ITO-OLED. The changes of CIE, CRI, and CCT from 0° to 75° are (0.030/0.047), 17, and 640 K for the ITO-OLED, and (0.014/0.003), 4, and 170 K for the NW-OLED, respectively. This superior angular dependence of the NW-OLEDs is attributed to the scattering properties of the electrodes. It is expected that electrodes with a higher haze factor improve the viewing angle characteristics even further. A larger haze factor might be obtained by increasing the NW density. However, the additional absorption will lower the absolute transmission of the electrode which will result in a lower efficiency of the OLED. Table 9.2 summarizes the most important performance properties of the highly efficient OLEDs and can be regarded as benchmark for further experiments.

Table 9.2: Summary of highly efficient white tandem NW- and ITO-OLED properties at a luminance of 1,000 cd/m². For the first time, white ITO-free OLEDs with state-of-the-art efficiencies and superior viewing angle characteristics are demonstrated.

|	U_{on} V	U V	j $\frac{mA}{cm^2}$	CIE	CRI	CCT K	CE cd/A	EQE^S %	LE^S lm/W
NW-OLED	5.0	6.0	2.3	$(0.493/0.468)^1$	69^1	2680^1	49	24.3	30.3
				$(0.507/0.465)^2$	65^2	2510^2		28.0^a	36.3^a
								30.3^b	53.9^b
ITO-OLED	5.0	5.9	2.6	$(0.507/0.449)^1$	73^1	2420^1	43	26.8	35.8
				$(0.477/0.496)^2$	56^2	3060^2		33.4^a	45.4^a
								42.8^b	63.0^b

[1] at 0°   [a] with microlens foil
[2] at 75°   [b] with half-sphere

Degradation and OLED Lifetime

From an application point of view, it is important that the NW electrode does not have a negative influence on the device lifetime. Residual water, solvents, or oxygen from the electrode processing may cause chemical reaction with the organic materials/emitter, which would result in a faster luminance drop and lower lifetime of the NW-OLED (extrinsic degradation). Therefore, a lifetime measurement of the highly efficient tandem white OLEDs has been performed. In general, ITO based OLEDs do not show extrinsic degradation due to the sophisticated encapsulation, but intrinsic degradation mostly caused by chemical reactions of the emitter molecules with one of the blocking layers.[113, 191, 192] Since a heating step of the NW electrodes is applied before OLED processing and the encapsulated OLEDs include a getter material, extrinsic degradation is not expected for the NW-OLEDs.

The dependence of the luminance on the operating time is shown in Fig. 9.11 (a) for the NW- and the ITO-OLED at a constant current density of 2 mA/cm² and 3 mA/cm², respectively. At 2 mA/cm², the NW-OLEDs exhibits a similar exponential luminance drop up to 200 h like the ITO-OLED. This confirms that the degradation is only caused by intrinsic degradation of the emitters. As expected, the CIE color coordinates shift strongly with time (Fig. 9.11 (b)), since the different emitters degrade at different rates. Within the first hours, the color coordinates shift from white to yellow/green. This is a result of the fact that the degradation of the blue emitter 4P-NPD and hence the TH unit is much faster than that of the yellow and green phosphorescent emitters $Ir(dhfpy)_2(acac)$ and $Ir(ppy)_3$.

However, a color shift with time is undesired and a lifetime of about 200 h is much too low for lighting applications. The understanding of degradation processes and the development of new stable emitters is important to overcome these problems in the future.
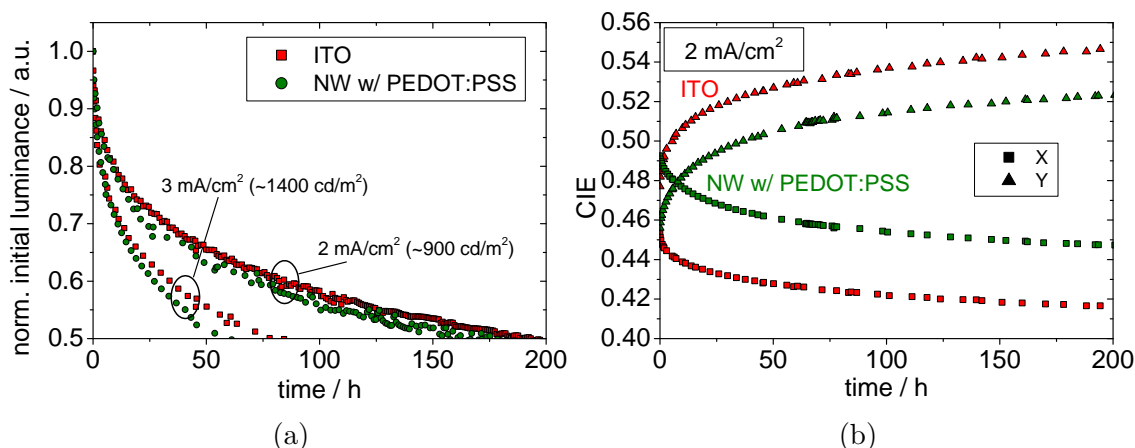
Figure 9.11: Lifetime properties of the highly efficient white tandem NW- and ITO-OLED. The drop of the initial luminance with time (a) is comparable for both devices, which means that the NW electrode does not lead to extrinsic degradation processes. The shift from white to yellow/green color coordinates is very strong during the first hours of operation (b). The reason is the fast degradation of the blue emitter 4P-NPD and the TH unit in comparison to the yellow and green phosphorescent emitters.

Local shorts and electrode delamination result in the formation of dark spots on an OLED pixel, which is undesired. To investigate the presence of dark spots, microscopic images of the NW- and ITO-OLED after 400 h of operation time (aged at 2 mA/cm²) are shown Fig. 9.12. In the off state, the active area of the ITO-OLED appears homogeneous in comparison to the NW-OLED, where the active area has a diffuse appearance. This results from the scattering properties of the NW electrodes and can be also observed for unaged devices. In the on state, there are no dark spots on any of the OLEDs. In comparison to the ITO-OLED, the NW-OLED shows a slightly enhanced inhomogeneous emission on microscopic length scales. However, on a macroscopic scale the emission of the NW-OLED is homogeneous as demonstrated in the photograph in Fig. 9.13.
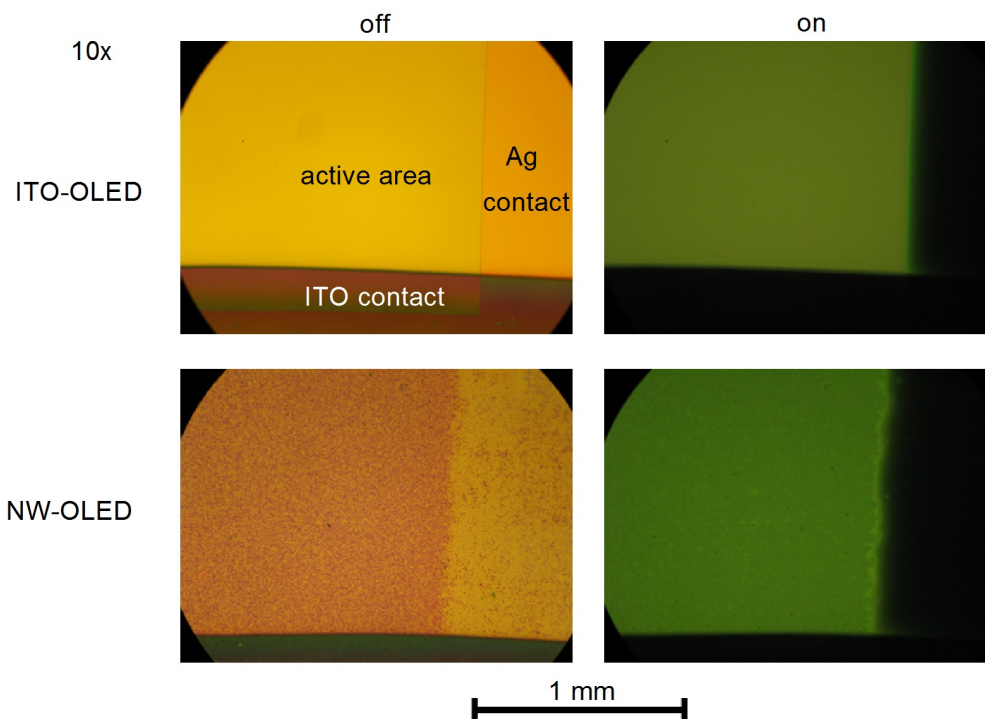
Figure 9.12: Microscope images of the NW- and ITO-OLED after 400 h of operation in the on and off state using 10 fold magnification. The scattering properties of the NW leads to an inhomogeneous appearance in the off state. In the on state, neither of the two OLEDs shows dark spots.

9.6   Summary and Outlook

In this chapter, white OLEDs on flattened Ag NW electrodes were investigated and compared to reference OLEDs on standard ITO electrodes. It was found that the NW-OLEDs exhibit a similar device performance in terms of IVL, spectral emission, EQE, LE, CIE, CRI, and lifetime. Highly efficient white tandem OLEDs with state-of-the-art efficiencies (30.3 lm/W, 24.3%, (0.493/0.468) at 1,000 cd/m²) were demonstrated for the first time for ITO-free OLEDs.

It was found that the achievement of a Lambertian emission characteristic depends on the cavity design and is not necessarily enforced by the scattering of the NWs. However, the NW-OLEDs showed superior qualities with respect to the color change with viewing angle. In general, the CIE color coordinates were more stable with increasing viewing angle for the NW-OLEDs. This color stability is attributed to the scattering properties of the NW electrode which showed an average haze of 6.8%.

By performing a variation of the ETL thickness, the influence of the NW electrode on the efficiency was studied to optimize the OLED structure. The NW-OLEDs followed the same trends as the reference ITO-OLEDs. Therefore, it was concluded that the NW electrode does not significantly influence the outcoupling efficiency and

is further not able to efficiently scatter waveguided modes. However, an additional scattering of the waveguided modes would be necessary to increase the outcoupling efficiency. The use of matrix materials and overcoats for the NWs with a higher refractive index than PMMA (n = 1.5 at λ = 578 nm)[250] or PEDOT:PSS (n $\approx$ 1.4 − 1.6)[145] would allow the coupling of more waveguided modes into the electrode. However, when using new materials it has to be ensured that the processing steps can still be applied and that the beneficial electrode properties like high conductivity, high transmission, and low roughness are maintained.

For future work and to make full use of the advantages of the NW electrode, a flexible PET substrate should be used. Furthermore, the processing time between the electrodes and the OLEDs should be shortened to avoid degradation effects.

Figure 9.13: Photograph of four operating white tandem OLEDs on NW electrodes. The picture has been taken by Caroline Murawski.

10 Concluding Remarks

10.1 Summary of Main Results

In this thesis, different approaches for the efficiency enhancement in white OLEDs were studied. Special focus was put on diffusion and transfer processes of singlet and triplet excitons. The generation of white light was achieved by employing the triplet harvesting concept[16, 17].

Using the blue fluorescent emitter 4P-NPD, which was found to have an isotropic orientation of the transition dipoles, triplet harvesting by the yellow phosphorescent emitter Ir(dhfpy)$_2$(acac) and by the red phosphorescent emitter Ir(MDQ)$_2$(acac) were demonstrated, respectively. For Ir(dhfpy)$_2$(acac), the EQE at low current density was more than doubled compared to the OLED without the phosphorescent emitter and for Ir(MDQ)$_2$(acac) the EQE even showed a three fold enhancement. Since TH from 4P-NPD by the green emitter Ir(ppy)$_3$ had not been possible due to the lower triplet energy of 4P-NPD, quantum chemical calculations were carried out with the aim to rise the triplet energy of 4P-NPD by small changes of the molecular structure. Two new emitters, 8M-4P-NPD and 8M-4P-FPD, were developed which indeed showed an increased triplet energy in comparison to 4P-NPD. For the first time, TH OLEDs were realized where TH took place from a blue bulk emitter to a green phosphorescent emitter. Also, three-color white TH OLEDs could be demonstrated where TH by the green emitter Ir(ppy)$_2$(acac) and Ir(MDQ)$_2$(acac) occurred simultaneously.

However, both new emitters showed significant disadvantages compared to 4P-NPD, which impeded the design of highly efficient white OLEDs. Most problematic in these OLEDs was the high energy barrier of > 1 eV between the EML and the HBL caused by the high LUMO energy of 8M-4P-NPD and 8M-4P-FPD. As a result, the electron injection into the EML was significantly reduced, leading to an impaired charge balance and a favored generation of exciplexes which subsequently lowered the effective radiative efficiency. In addition, OLEDs comprising 8M-4P-FPD showed very fast degradation complicating the angular dependent emission measurement.

Time- and spectrally-resolved measurements by a streak camera turned out to be a helpful tool to prove TH in OLEDs. Delayed emission of the phosphorescent emitter caused by triplet diffusion was found to be characteristic for TH OLEDs, while prompt emission could be assigned to singlet transfer and direct charge recombination on the phosphorescent emitter.

Additionally to triplet harvesting, singlet transfer was identified as a second transfer mechanism in the TH OLEDs under investigation. Using a distance variation between the singlet generation zone and a singlet sensor, this effect was used to study the singlet diffusion length in 4P-NPD in a simple and accurate manner. Applying Ir(ppy)$_3$ as sensor material, the singlet diffusion length for a range of current densities was obtained. Here, an analytical model based on the boundary conditions of ideal

blocking and quenching of singlets was applied. It was found that the expansion of the generation zone as well as the amount of direct recombination processes were crucial parameters when calculating the diffusion length. By these means, a singlet diffusion length of $L_{\mathrm{elec.}} = 4.6$ nm was obtained for 4P-NPD at a low current density of 0.15 mA/cm² , which was reduced to 4.0 nm at 154.08 mA/cm². Furthermore, this method provided an estimate of the emission profile in the EML, which is otherwise hardly accessible in small-molecule OLEDs.

To study the influence of the interaction of singlets with polarons and triplets on the diffusion length, photoluminescence experiments of pure 4P-NPD layers were carried out, changing the position of a thin $Ir(ppy)_3$ quenching layer inside a 4P-NPD film. The PL emission could be simulated assuming a Gaussian shaped diffusion profile. A diffusion length of $L_{\mathrm{opt.}} = 7$ nm was found. It is believed that the longer diffusion length obtained by optical excitation in comparison to electrical excitation results from the fact that singlet diffusion is not disturbed by polarons or triplets as it is within the OLED structure.

Another approach to overcome the problem of triplet harvesting by a green emitter is the stacking of two OLEDs on top of each other using a charge generation layer in between.[102, 158] Here, a green/yellow PH OLED using the emitters $Ir(ppy)_3$ and $Ir(dhfpy)_2(acac)$ doped into the matrix materials TCTA and TPBI was put on top of a red/blue TH OLED which included the emitters $Ir(MDQ)_2(acac)$ and 4P-NPD. Before studying the tandem OLED, both single OLEDs had been investigated separately: For the red/blue TH OLED, doping of the EML with the triplet manager material NPD was carried out, which led to an enhanced charge and exciton transport on NPD. Furthermore, a significant enhancement of the device lifetime (factor 3.5) was obtained, but no improvement in device efficiency or roll-off. For the green/yellow PH OLED, an EQE improvement factor of 1.2 was achieved using a double emission structure. Finally, a highly efficient white tandem OLED with an LE of 33 lm/W, an EQE of 25%, CIE coordinates of (0.528/0.425), and a CRI of 62 at a luminance of 1,000 cd/m² was obtained.

Furthermore, an alternative electrode based on flattened silver nanowires was investigated. It was found that the NW-OLEDs exhibited a similar device performance in terms of IVL, spectral emission, EQE, LE, CIE, CRI, and lifetime. The NW-OLEDs showed superior qualities with respect to the color change with viewing angle. In general, the CIE color coordinates were more stable with increasing viewing angle for the NW-OLEDs than for the reference ITO-OLEDs. This color stability was attributed to the scattering properties of the NW electrode. However, the NW electrode could not provide significant scattering of waveguided modes. Using the optimized tandem OLED structure described previously, highly efficient white tandem OLEDs with state-of-the-art efficiencies (30.3 lm/W LE, 24.3% EQE, CIE(0.493/0.468), and a CRI of 69 at 1,000 cd/m²) were demonstrated for the first time for ITO-free OLEDs.

10.2   Outlook: White TH OLEDs

As shown in this thesis, the design of highly efficient white TH OLEDs where blue emission occurs from a bulk emitter requires the consideration of many parameters: The most important ingredient is a fluorescent blue emitter, having suitable HOMO and LUMO energies (-5.3 $\pm$ 0.2 eV and -2.3 $\pm$ 0.2 eV, respectively) to ensure efficient electron and hole injection from the blocker materials. Furthermore, the emission spectrum should provide deep blue color coordinates to achieve a high CRI when used in a white OLED. Therefore, the singlet energy has to be in the range between 2.5 and 3.1 eV. The radiative efficiency/photoluminescence quantum yield needs to be adequate (PL-QY $\geq$ 40%). To ensure TH by a green emitter, the triplet energy needs to be sufficiently high ($\geq$ 2.4 eV). An increase in triplet energy can be obtained by maintaining the singlet energy and decreasing the singlet-triplet splitting.

For the development of a new blue emitter, it has to be considered that a low singlet-triplet splitting requires a small overlap of the HOMO and LUMO wave function, while a high PL-QY requires exactly the opposite. The tradeoff between high PL-QY and small singlet-triplet splitting impedes the design of highly efficient white TH OLEDs. In this thesis, the emitter 8M-4P-NPD showed a good PL-QY of 42% and a singlet-triplet splitting of 0.7 eV. Recently, Lee *et al.*[121] developed a blue fluorescent emitter with a very small HOMO-LUMO overlap resulting in singlet-triplet splitting of only 0.06 eV, while providing a remarkable PL-QY of 62%. The high PL-QY is achieved via thermally activated delayed fluorescence, i.e. triplets are converted into singlets via reverse intersystem crossing. Accounting only the fluorescence PL-QY, i.e. without TADF contribution, a value of 16% is obtained. In comparison to 8M-4P-NPD, the singlet-triplet splitting is reduced by a factor of 10, while the PL-QY is reduced by about a factor of 3. This means that for blue emitters, there is still room for decreasing the singlet-triplet splitting to the required range of 0.1 to 0.7 eV while maintaining a reasonable PL-QY. For TH, however, emitters which benefit from TADF are less suitable since triplets need to be transferred to the phosphorescent emitter, which means that they would not be able to efficiently contribute to the TADF process.

As discussed previously, the high LUMO energy of 8M-4P-NPD impedes electron injection and leads to a low EQE. Here, doping of 8M-4P-NPD into a suitable matrix material where exciton generation occurs on the matrix and singlets are transferred to 8M-4P-NPD via Förster transfer could help to improve the EQE. However, the advantage of 8M-4P-NPD as a bulk emitter would be lost, and the approach would then not be different to the work of Sun *et al.*[17] and Kondakova *et al.*[21].

For the design of white TH OLEDs, singlet transfer needs to be taken into account. To harvest triplets efficiently, the phosphorescent emitter needs to be as close to the exciton generation zone as possible, since the triplet density decreases exponentially with the distance. However, at small distances, singlet transfer can take place. It is

worth noting that singlets which are transferred to the phosphorescent emitter will still end up in the radiative triplet state. Therefore, these singlets are not really lost and the internal efficiency of the OLED is not decreased. However, additional singlet transfer lowers the amount of blue emission in white TH OLEDs, which is usually undesired. For the emitters 4P-NPD and 8M-4P-NPD, the critical distance below which significant singlet transfer is observed is 7 nm. To prevent singlet transfer, the diffusion of singlets towards the phosphorescent emitter needs to be avoided. This might be achieved by inserting a singlet blocking layer between the generation zone and the TH zone. However, it has to be ensured that this layer is at the same time electrically inert and does not hinder the triplet transfer.

For lighting applications, the efficacy, color shift with applied power, viewing angle characteristics, color coordinates, and CRI are important quality criteria which need to be considered. In the following, the theoretical achievable luminous efficacy (at a luminance of 1,000 cd/m²) of a white TH OLED is estimated based on the performance of two white TH OLEDs using 4P-NPD as blue emitter. The first OLED is the two-color single unit OLED using 4P-NPD and Ir(dhfpy)$_2$(acac) as emitters (cf. Chapter 6). The second OLED is the four-color tandem OLED described in Refs. [19, 20] and Chapter 8. For both OLEDs, the outcoupling efficiency η_{out} and the internal quantum efficiency η_{IQE} is calculated[29]. The results are summarized in Tab. 10.1. The experimentally achieved luminous efficacy at 1,000 cd/m² measured in an integrating sphere is also shown.

Table 10.1: Estimation of maximum luminous efficacy for white TH OLEDs at 1,000 cd/m² based on real performances. The maximum possible internal quantum efficiency η_{IQE} is 100% for the 2-color single unit OLED and 200% for the 4-color tandem OLED, respectively. The maximum possible outcoupling efficiency η_{out} is 100%.

	2-color, single unit Chapter 6	4-color, tandem Refs. [19, 20]
η_{out} [%]	23.2	20.0
η_{IQE} [%]	48.8	130
CIE	(0.46/0.45)	(0.51/0.42)
CRI	38	78
meas. LE$^{\mathrm{S}}$ [lm/W] at 1,000 cd/m²	32.6	33.0
theo. LE [lm/W] assuming max. η_{IQE}	67	51
theo. LE [lm/W] assuming max. η_{IQE} and η_{out}	289	255

[29]The calculations were done by Mauro Furno using the optical simulation software OLEDPower.

Assuming that the internal quantum efficiency can be increased to its maximum (100% for the single unit OLED and 200% for the tandem OLED) and that the LE increases proportionally to the EQE ($= \eta_{\text{out}} \cdot \eta_{\text{IQE}}$), luminous efficacies in the range of 50 to 60 lm/W are possible. The LE can be even further increased to values above 250 lm/W, if outcoupling losses can be reduced to a minimum.

The LE depends on the driving voltage U and current I ($\text{LE} \sim (UI)^{-1}$). Especially a higher η_{out} would result in a lower voltage and current necessary to achieve 1,000 cd/m^2, thus increasing the LE even more. It needs to be considered that both OLEDs do not match the warm white color point A (0.447/0.407), but are slightly shifted towards the reddish or greenish region in the CIE diagram. A shift of the color coordinates towards A requires basically the reduction of red/green emission, which usually goes side by side with a decreased LE.

The improvement of η_{IQE} is primarily seen in the development of new efficient emitter materials, whereas a significant improvement of η_{out} requires outcoupling techniques for waveguided and/or SPP modes. This, in conjunction with optical and electrical simulations, is essential for further device understanding and efficiency/efficacy enhancement.

Despite the fact that many outcoupling techniques are already known and have been applied to OLEDs (micro-lenses[142], index matching[14], gratings[152], scattering particles[151], etc.), an approach which does not harm the electrical efficiency, which can be used for white OLEDs, is cheap, and easy in fabrication is not known up to now. Furthermore, the research of annihilation processes to improve roll-off characteristics and the investigation of the dipole orientation of emitter molecules are important for the development of efficient white OLEDs.[23, 84]

Finally, the design of highly efficient OLEDs can to some extent be compared to a jigsaw puzzle, where a lot of small pieces have to be put together in the right way, to obtain a full picture. A large part of this puzzle is already known, with room for considerable improvement if electrical, excitonic, and optical losses can be overcome.
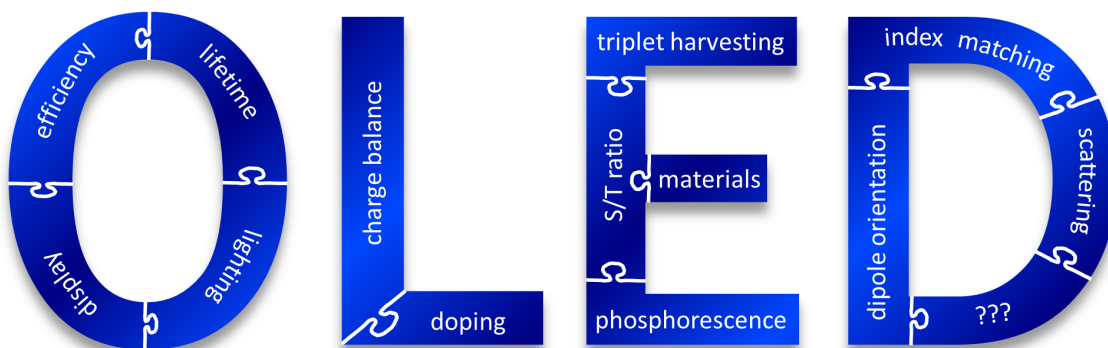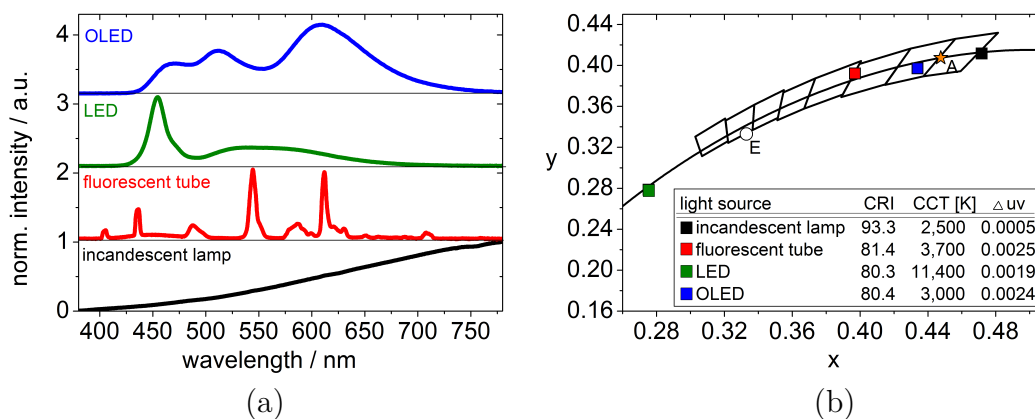
A   Appendix

A.1   White Light Sources

A measurement of the spectral distribution of different light sources has been performed using an Ocean Optics USB4000 fiber optics spectrometer. The results are shown in Fig. A.1. All lamps are commercially available. The incandescent lamp (100 W) has a continuously increasing spectrum in contrast to the fluorescent lamp(L58 W25, Osram), which shows several distinct peaks. For the LED (bike light), the Down-Conversion principle can be seen nicely, since there is a narrow blue peak resulting from the blue LED (at 460 nm) and a broad yellow component from the phosphor. The OLED (ORBEOS CDW-031, Osram) has three broad peaks which can be attributed to different organic emitters. All light sources have CIE color coordinates close to the Planckian curve and achieve good or very good CRI values (Fig. A.1 (b)). All light sources appear white, however, only the incandescent lamp, the fluorescent tube, and the OLED meet the Energy Star requirements.

light source	CRI	CCT [K]	△uv
■ incandescent lamp	93.3	2,500	0.0005
■ fluorescent tube	81.4	3,700	0.0025
■ LED	80.3	11,400	0.0019
■ OLED	80.4	3,000	0.0024

(a)   (b)

Figure A.1: Measured spectral emission of commercially available light sources (a) and calculated CIE color coordinates (b). The spectra are normalized and displaced for clarity. The table summarizes the color rendering index, the color correlated temperature, and the Euclidean distance (Δuv) to the Planck curve.

A.2   Energies and molecular orbitals of benzene

In Tab. A.1, different energy values for HOMO and LUMO, as well as the singlet energy level of benzene are compared to experimental data. All calculations are performed by Regina Luschtinetz at the *Institut für Physikalische Chemie und Elektrochemie*, TU Dresden. For the HOMO energy, the HF based calculations (-9.17 eV) show a very good agreement with the experiment (-9.15 eV). However, the predicted LUMO energies (HF: 2.31 eV, DFT: -1.40 eV, HF+DFT: -0.39 eV) strongly underestimate the experimentally found value (-3.51 eV). Interestingly, the band gap ΔE calculated by DFT (5.30 eV) fits well with the experiment (5.64 eV), while the other two methods overestimate ΔE by $>50\%$ (HF) and $>15\%$ (HF+DFT). Regarding the singlet energy level, the experimental data (4.46 eV) is about 20% to 40% below the theoretical data (HF: 5.97 eV, DFT: 5.30 eV, HF+DFT: 6.60 eV). For the band gap and the singlet energy level the DFT method is most appropriate.

This example demonstrates that even for a simple molecular structure like benzene, the comparison of energy eigenvalues to experimental data has to be taken with care.

Table A.1: Comparison of HOMO energy E_{HOMO}, LUMO energy E_{LUMO}, $\Delta E = |E_{\mathrm{HOMO}} - E_{\mathrm{LUMO}}|$, and singlet energy level S_1 of benzene using different theoretical methods. Experimental values are deduced as $E_{\mathrm{HOMO}} = $ ionization potential, and $E_{\mathrm{LUMO}} = $ ionization potential + optical band gap.

method	E_{HOMO} [eV]	E_{LUMO} [eV]	$\triangle E$ [eV]	S_1 [eV]
Hartree-Fock based	-9.17	2.31	11.48	5.97
DFT based	-6.70	-1.40	5.30	5.30
Hybrid functional of HF and DFT	-6.99	-0.39	6.60	5.39
Experiment	-9.15[251]	-3.51[54]	5.64	4.46[252]

The electron wave functions obtained by DFT calculations are displayed in Fig. A.2 for HOMO, LUMO and the σ orbitals. The different colors account for the different signs of the wave function (blue $= -$, red $= +$). While the σ orbital is localized at the core and has no knots, the π orbitals (HOMO and LUMO) form a delocalized electron cloud. The same shape of orbitals can be obtained by using HF calculations (not shown here).
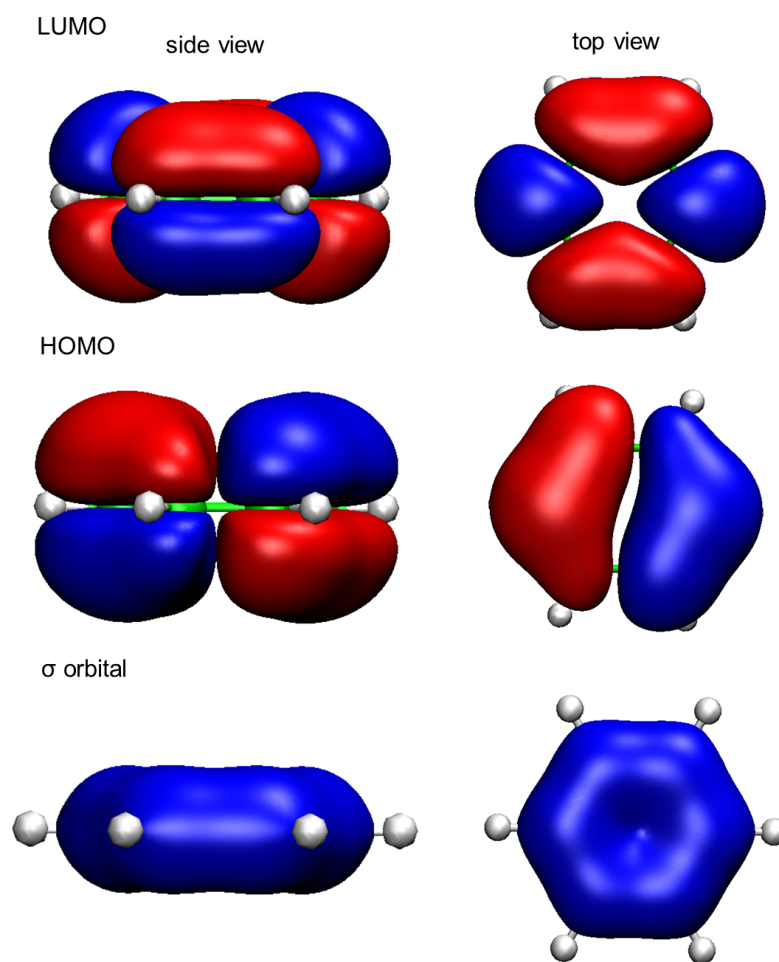
Figure A.2: Side and top view of the molecular orbitals of benzene calculated with DFT. While the π orbitals form a delocalized electron cloud, the σ electrons stay closely to the core. The different colors red and blue account for the sign of the electron wave function.

A.3 Twist of phenyl rings in 4P-NPD

In Sec. 6.2.1, an asymmetric shape of the calculated LUMO of 8M-4P-NPD with
respect to the molecular structure was found. To investigate this issue, additional
SCC-DFTB calculations of the second highest occupied molecular orbital (HOMO-1)
and the second lowest unoccupied molecular orbital are carried out for 4P-NPD having
different rotation angles between the phenyl rings. Figure A.3 (a) shows the molecular
orbitals and the energy values of 4P-NPD assuming that the four phenyl rings are
fixed to a planar position. The four molecular orbitals (HOMO, HOMO-1, LUMO,
LUMO+1) exhibit a symmetry according to the molecular structure, respectively.
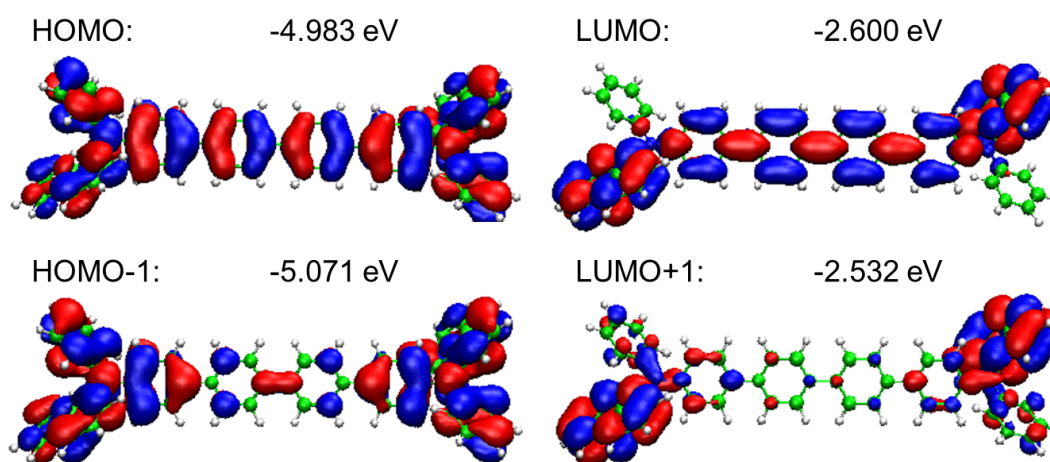
(a) 4P-NPD with planar phenyl rings
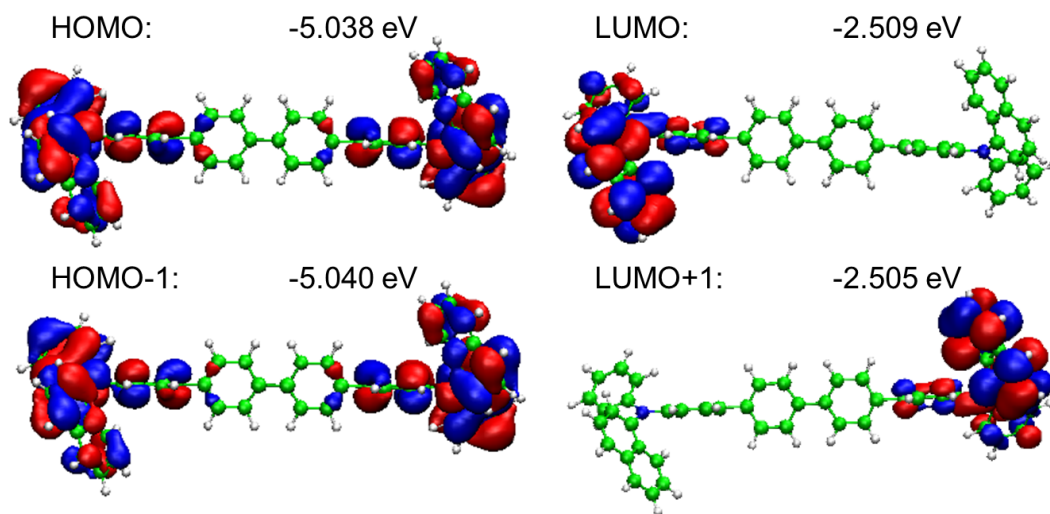
(b) 4P-NPD with planar inner phenyl rings and 90° twisted outer phenyl rings

Figure A.3: Molecular orbitals, HOMO, HOMO-1, LUMO, and LUMO+1 energy
values of 4P-NPD assuming planar structure of the four phenyl rings (a) and a 90°
twist of the outer phenyl rings (b). Calculations are done using SCC-DFTB.

The molecular structure of 8M-4P-NPD and 8M-4P-FPD is based on 4P-NPD having a twist of the outer phenyl rings by about 90°. The influence of this twist on the molecular orbitals and energy eigenvalues on 4P-NPD is shown in Fig. A.3 (b). While HOMO and HOMO-1 are localized on both naphthalene side groups, thus exhibiting a symmetric behavior, the LUMO is only localized on one of the naphthalene group. Interestingly, the LUMO+1 is found on the other naphthalene group having an almost identical energy (LUMO = -2.509 eV, LUMO+1 = -2.505 eV). This maintains the symmetry of the molecular orbital for the molecules under investigation.

Indeed, the energies of the HOMO-1 and the LUMO+1 in Fig. A.3 (b) approach those of the HOMO and LUMO, respectively. The steric hindrance of the CH_3 groups causes the rotation of the outer phenyl rings, which leads to the orbital splitting. As a result, the π-electrons cannot be distributed over the four phenyl rings as in case of the planar configuration (cf. Fig. A.3 (a)).

Since it is expected that 8M-4P-NPD and 8M-4P-FPD have split HOMO and LUMO orbitals, considerations resulting from the HOMO-LUMO overlap of these molecules should include the contribution of HOMO-1 and LUMO+1.

## A.4   Influence of HTL thickness in tandem OLEDs

In Section 8.4 it has been observed that the emission of the red emitter in the tandem OLED is too low compared to previous studies. To enhance the outcoupling in the red spectral region, the HTL thickness of the PH and TH unit has been varied. First the HTL of the PH unit is changed from 75 nm to 90 nm in 5 nm steps and the results are shown in Fig. A.4. For 75 nm, the red peak is significantly enhanced (Fig. A.4 (c)), while the emission of the other three emitters remains unchanged. Due to the overlapping IV-curves (Fig. A.4 (b)), the luminous efficacy is highest for the OLED with 75 nm HTL thickness (Fig. A.4 (d)).
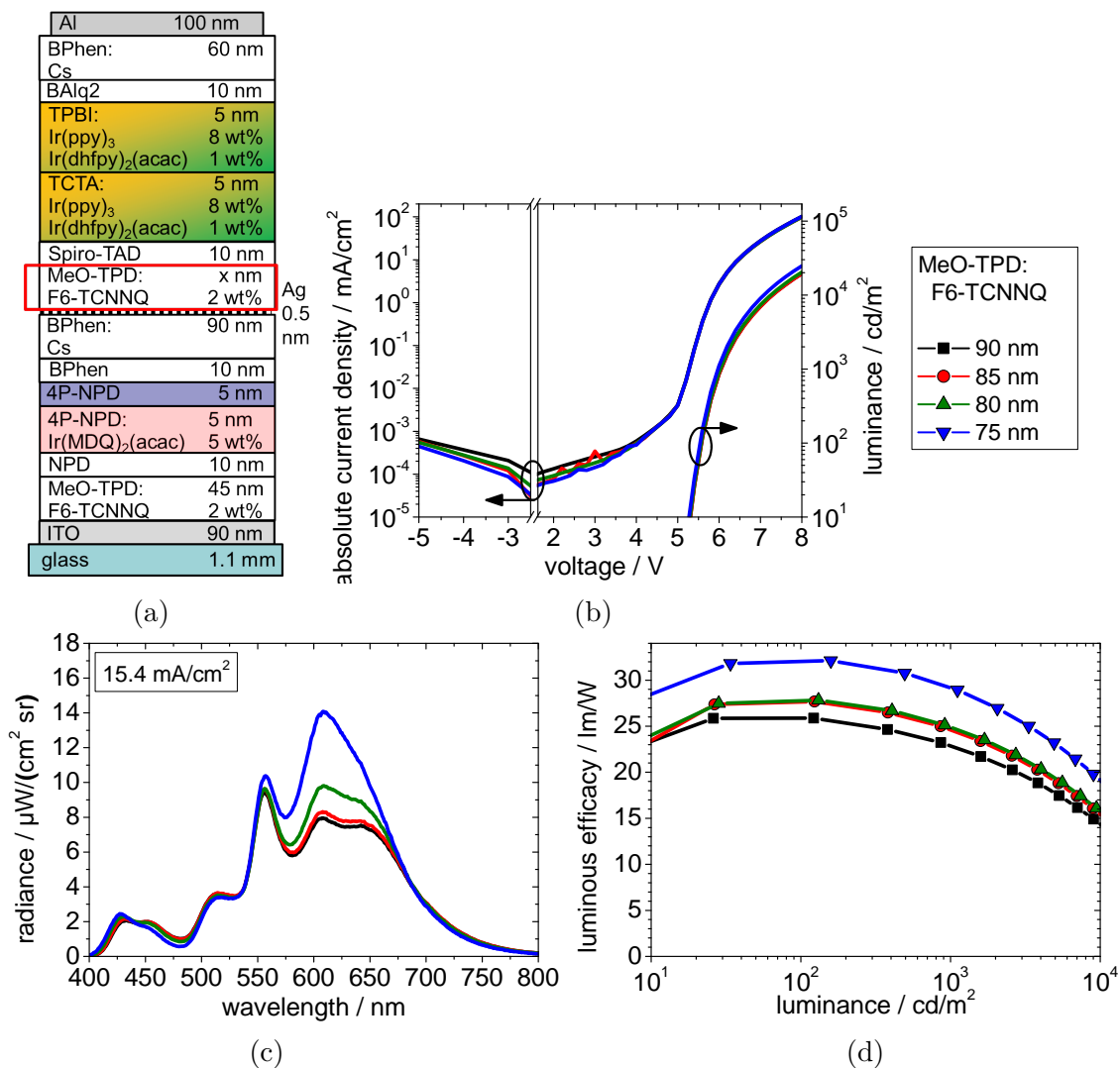
Figure A.4: OLED layer structure (a) and performance (b-d) of the tandem OLED with varying HTL thickness of the PH unit. A thickness of 75 nm is optimal in terms of spectral emission and luminous efficacy (c,d).

In a second step, the HTL thickness of the PH unit is kept to 75 nm and the HTL thickness of the TH unit is varied from 35 nm to 50 nm ((Fig. A.5). Again the red emission peak is enhanced for a reduced HTL thickness. At 35 nm, the yellow emission peak also increases, while the emission of the green and the blue emitter is constant for all layer thicknesses. As a result of the constant IV-curves, the performance of the LE is best for the sample with 35 nm.

In summary, it is possible to enhance the outcoupling in particular in the red spectral region by decreasing the HTL thicknesses in the tandem OLED. This further increases the LE. Based on these results, the HTL thickness is changed to 35 nm for the TH unit and to 75 nm for the PH unit, respectively.
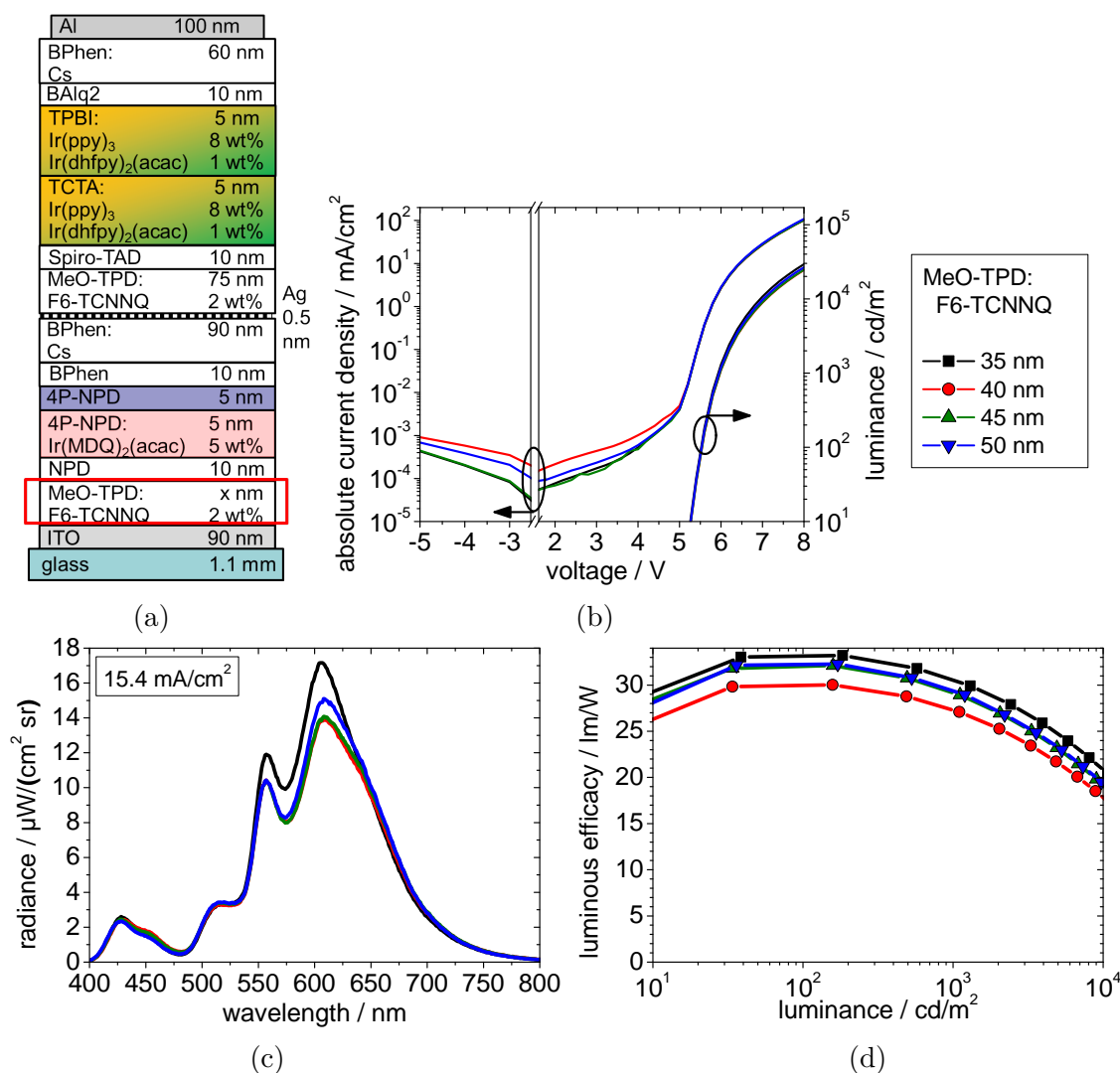
Figure A.5: OLED layer structure (a) and performance (b-d) of the tandem OLED with varying HTL thickness of the TH unit. A thickness of 35 nm is optimal in terms of spectral emission and luminous efficacy (c,d).

References

[1] http://www.mitsubishielectric.com/news/2012/0626.html/ (05.11.2012).

[2] C. W. Tang and S. A. VanSlyke. "Organic electroluminescent diodes". *Applied Physics Letters* **51**, 913 (1987).

[3] http://www.oled info.com/tags/market_reports (16.11.2012).

[4] http://www.itechnews.net/2009/04/19/philips-lumiblade-oled   lighting/ (16.11.2012).

[5] http://www.pro-physik.de/details/physiknews/1117541/Superflach_und _transparent.html (16.11.2012).

[6] http://www.holstcentre.com/NewsPress/PressList/Agfa_ITOfree_OLED.aspx (16.11.2012).

[7] J. Blochwitz, M. Pfeiffer, T. Fritz, and K. Leo. "Low voltage organic light emitting diodes featuring doped phthalocyanine as hole transport material". *Applied Physics Letters* **73**, 729 (1998).

[8] M. Pfeiffer, T. Fritz, J. Blochwitz, A. Nollau, B. Plönnigs, A. Beyer, and K. Leo. "Controlled Doping of Molecular Organic Layers: Physics and Device Prospects". *Advances in Solid State Physics* **39**, 77 (1999).

[9] J. Blochwitz. "Organic light-emitting diodes with doped charge transport layers". TU Dresden (Dissertation) (2001).

[10] J. Huang, M. Pfeiffer, A. Werner, J. Blochwitz, K. Leo, and S. Liu. "Low-voltage organic electroluminescent devices using pin structures". *Applied Physics Letters* **80**, 139 (2002).

[11] M. Pfeiffer, K. Leo, X. Zhou, J. S. Huang, M. Hofmann, A. Werner, and J. Blochwitz-Nimoth. "Doped organic semiconductors: Physics and application in light emitting diodes". *Organic Electronics* **4**, 89 (2003).

[12] C. Adachi, M. A. Baldo, M. E. Thompson, and S. R. Forrest. "Nearly 100 % internal phosphorescence efficiency in an organic light-emitting device". *Journal of Applied Physics* **90**, 5048 (2001).

[13] M. Furno, R. Meerheim, S. Hofmann, B. Lüssem, and K. Leo. "Efficiency and rate of spontaneous emission in organic electroluminescent devices". *Physical Review B* **85**, 115205 (2012).

[14] S. Reineke, F. Lindner, G. Schwartz, N. Seidler, K. Walzer, B. Lüssem, and K. Leo. "White organic light-emitting diodes with fluorescent tube efficiency.". *Nature* **459**, 234 (2009).

[15] L. Xiao, Z. Chen, B. Qu, J. Luo, S. Kong, Q. Gong, and J. Kido. "Recent Progresses on Materials for Electrophosphorescent Organic Light-Emitting Devices". *Advanced Materials* **23**, 926 (2011).

[16] G. Schwartz, K. Walzer, M. Pfeiffer, and K. Leo. "High-efficiency white organic-light-emitting diodes combining fluorescent and phosphorescent emitter systems". *Proceedings of SPIE* **6192**, 61920Q (2006).

[17] Y. Sun, N. C. Giebink, H.i Kanno, B. Ma, M. E. Thompson, and S. R. Forrest. "Management of singlet and triplet excitons for efficient white organic light-emitting devices". *Nature* **440**, 908 (2006).

[18] G. Schwartz, M. Pfeiffer, S. Reineke, K. Walzer, and K. Leo. "Harvesting Triplet Excitons from Fluorescent Blue Emitters in White Organic Light-Emitting Diodes". *Advanced Materials* **19**, 3672 (2007).

[19] T. C. Rosenow, M. Furno, S. Reineke, S. Olthof, B. Lüssem, and K. Leo. "Highly efficient white organic light-emitting diodes based on fluorescent blue emitters". *Journal of Applied Physics* **108**, 113113 (2010).

[20] M. Furno, T. C. Rosenow, M. C. Gather, B. Lüssem, and K. Leo. "Analysis of the external and internal quantum efficiency of multi-emitter, white organic light emitting diodes". *Applied Physics Letters* **101**, 143304 (2012).

[21] M. E. Kondakova, J. C. Deaton, T. D. Pawlik, D. J. Giesen, D. Y. Kondakov, R. H. Young, T. L. Royster, D. L. Comfort, and J. D. Shore. "Highly efficient fluorescent-phosphorescent triplet-harvesting hybrid organic light-emitting diodes". *Journal of Applied Physics* **107**, 014515 (2010).

[22] K. Saxena, V. K. Jain, and D. S. Mehta. "A review on the light extraction techniques in organic electroluminescent devices". *Optical Materials* **32**, 221 (2009).

[23] W. Brütting, J. Frischeisen, T. D. Schmidt, B. J. Scholz, and C. Mayr. "Device efficiency of organic light-emitting diodes: Progress by improved light outcoupling". *Physica Status Solidi A* (2012).

[24] A. Kumar and C. Zhou. "The race to replace tin-doped indium oxide: which material will win?". *ACS nano* **4**, 11 (2010).

[25] G. S. Smith. "An Introduction to Classical Electromagnetic Radiation". Cambridge University Press (Cambridge) (1997).

[26] J. H. Lambert. "Lamberts Photometrie". Wilhelm Engelmann Verlag (Leipzig) (1892).

[27] G. Schröder and H. Treiber. "Technische Optik". Vogel (Würzburg), 1st edition (2007).

[28] D. D. Chiras. "Human Biology". Jones & Bartlett Learning (Sudbury), 7th edition (2011).

[29] "Commission Internationale de l'Eclairage proceedings". Cambridge University Press (Cambridge) (1931).

[30] CIBSE Lighting Guide. "Interior Lighting Design Standards". (2002).

[31] J. P. Freyssinier, N. Narendran, and J. D. Bullough. "Luminance Requirements for Lighted Signage". *International Conference on Solid State Lighting, Proceedings of SPIE* **6337** (2006).

[32] http://spie.org/samples/PM184.pdf. "Introduction to Radiometry" (05.07.2012).

[33] T. Smith and J. Guild. "The C.I.E. colorimetric standards and their use". *Transaction of the Optical Society* **33** (1931).

[34] W. D. Wright. "A re-determination of the trichromatic coefficients of the spectral colours". *Transactions of the Optical Society* **30**, 141 (1929).

[35] P. Flesch. "Light And Light Sources - High-intensity Discharge Lamps". Springer (Heidelberg) (2006).

[36] T. Tsujimura. "Oled Display Fundamentals and Applications". John Wiley & Sons (Hoboken, New Jersey), 1st edition (2012).

[37] "Technical Report - Method of Measuring and Specifying Colour Rendering Properties of Light Sourcesl". Commission Internationale de l'Eclairage (Wien) (1995).

[38] US Enviromental Protection Agency and US Department of Energy. "ENERGY STAR Program Requirements for Solid State Lighting Luminaires Eligibility Criteria - Version 1.1".

[39] D. S. Ginley and D. Cahen. "Fundamentals of Materials for Energy and Environmental Sustainability". Cambridge University Press (New York) (2011).

[40] A. Jolly. "Managing Climate Risk - a practical guide for business". Thorogood Series. Thorogood (London) (2008).

[41] R. Pode and B. Diouf. "Solar Lighting". Green Energy and Technology. Springer (London), 1st edition (2011).

[42] Commission Internationale de l'Eclairage. "Activity report". *Devision 1: Vision and Colour* **TC 1-69**, 21 (2008).

[43] W. Davis and Y. Ohno. "Color quality scale". *Optical Engineering* **49**, 033602 (2010).

[44] B. Y. M. Wood. "When white light isn't white". , http://www.mikewoodconsulting.com/index.htm (28.06.2012).

[45] D. L. MacAdam. "Specification of small chromaticity differences". *Journal of the Optical Society of America* **33**, 18 (1943).

[46] S. Reineke. "Controlling Excitons - Concepts for Phosphorscent Organic LEDs at High Brightness". TU Dresden (Dissertation) (2009).

[47] Y.-S. Tyan. "Organic light-emitting-diode lighting overview". *Journal of Photonics for Energy* **1**, 011009 (2011).

[48] European Union. "Amtsblatt der Europäischen Union". *Verordnung (EG)* **244** (2009).

[49] H. G. Grimmeiss and J. W. Allen. "Light emitting diodes - How it started". *Journal of Non-Crystalline Solids* **352**, 871 (2006).

[50] http://www.leds.edn.com/blog/leds-blog/cree-claims-rd-record-white-led 254-lmwattg (18.07.2012).

[51] http://www.osram.de/osram_de/produkte/led-technologie/oled lichtgestaltung/orbeos/index.jsp (12.12.2012).

[52] http://www.konicaminolta.com/oled/products/index.html (05.07.2012).

[53] http://www.nostraforma.com/benwirth-cluster-pendelleuchte-led-oled-schwarz-clp-3l6-3-x-led-modul-6-x-oled-modul-p 13965.html?campaign=shopping (05.07.2012).

[54] W. Demtröder. "Experimentalphysik 3 - Atome, Moleküle und Festkörper". Springer (Berlin), 1st edition (1996).

[55] H. Haken and H. C. Wolf. "Atom- und Quantenphysik". Springer (Berlin), 8th edition (2004).

[56] M. Schwörer and H. C. Wolf. "Organic Molecular Solids". WILEY-VCH (Weinheim), 1st edition (2007).

[57] W. Brütting. "Physics of organic semiconductors". WILEY-VCH (Weinheim), 1st edition (2005).

[58] E. Keinan and I. Schechter. "Chemistry for the 21st century". WILEY-VCH (Weinheim), 1st edition (2001).

[59] C. P. Williams. "Explorations in Quantum Computing". Springer (London), 2nd edition (2011).

[60] M. Mueller. "Fundamentals of Quantum Chemistry - Molecular Spectroscopy and Modern Electronic Structure Computations". Kluver Academic/Plenum Publisher (New York), 1st edition (2001).

[61] P. Deak, T. Frauenheim, and M. R. Pederson. "Computer Simulation of Materials at Atomic Level". WILEY-VCH (Berlin), 1st edition (2000).

[62] V. Magnasco. "Elementary Methods of Molecular Quantum Mechanics". Elsevier (Amsterdam), 1st edition (2007).

[63] A. V. Kavokin, J. J. Baumberg, G. Malpuech, and F. P. Laussy. "Microcavities". Oxford University Press (New York), 1st edition (2007).

[64] P. W. Atkins and R. S. Friedman. "Molecular Quantum Mechanics". Oxford University Press (New York), 3rd edition (1997).

[65] A. Köhler and H. Bässler. "Triplet states in organic semiconductors". *Materials Science and Engineering R* **66**, 71 (2009).

[66] H. Haken and H. C. Wolf. "Molekülphysik und Quantenchemie". Springer (Berlin), 3th edition (1998).

[67] S. Schols. "Device Architecture and Materials for Organic Light-Emitting Devices". Springer(Dordrecht), 1st edition (2011).

[68] F. W. D. Rost. "Quantitative fluorescence microscopy". Cambridge University Press (Cambridge), 1st edition (1991).

[69] M. Pope and C. E. Swenberg. "Electronic processes in organic crystals and polymers". Oxford University Press (New York), 2nd edition (1999).

[70] H. Yersin. "Highly Efficient OLEDs with Phosphorescent Materials". WILEY-VCH (Weinheim), 1st edition (2008).

[71] N. J. Turro, V. Ramamurthy, and J. C. Scaiano. "Principles of Molecular Photochemistry - An Introduction". University Science Books (USA), 1st edition (2009).

[72] T. Förster. "Zwischenmolekulare Energiewanderung und Fluoreszenz". *Annalen der Physik* **6**, 55 (1948).

[73] D. L. Dexter. "A Theory of Sensitized Luminescence in Solids". *The Journal of Chemical Physics* **21**, 836 (1953).

[74] C. W. Tang, S. A. VanSlyke, and C. H. Chen. "Electroluminescence of doped organic thin films". *Journal of Applied Physics* **65**, 3610 (1989).

[75] H. Choukri, A. Fischer, S. Forget, S. Chenais, M.-C. Castex, D. Ades, A. Siove, and B. Geffroy. "White organic light-emitting diodes with fine chromaticity tuning via ultrathin layer position shifting". *Applied Physics Letters* **89**, 183513 (2006).

[76] O. Mikhnenko, R. Ruiter, P. Blom, and M. Loi. "Direct Measurement of the Triplet Exciton Diffusion Length in Organic Semiconductors". *Physical Review Letters* **108**, 137401 (2012).

[77] U. Würfel, M. Thorwart, and E. Weber. "Quantum Efficiency in Complex Systems, Part II: From Molecular Aggregates to Organic Solar Cells". Elsevier (USA), 1st edition (2011).

[78] A. Albini, R. Fausto, J. S. S. de Melo, A. Maldotti, F. Puntoriero, C. Clementi, and G. Favaro. "Photochemistry". The Royal Society of Chemistry (Cambridge), 3rd edition (2011).

[79] D. L. Pavia, G. M. Lampman, G. S. Kriz, and R. G. Engel. "A Microscale Approach to Organic Laboratory Techniques". Brooks/Cole (Belmont), 5th edition (2007).

[80] C. Szymanski. "Investigation of Photophysical and Photochemical Processes in Conjugated Polymer Nanoparticles by Single Particle and Ensemble Spectroscopy". ProQuest (Weinheim), 1st edition (2009).

[81] M. A. Baldo, C. Adachi, and S. R. Forrest. "Transient analysis of organic electrophosphorescence. II. Transient analysis of triplet-triplet annihilation". *Physical Review B* **62**, 10967 (2000).

[82] S. Reineke, G. Schwartz, K. Walzer, and K. Leo. "Direct observation of host-guest triplet-triplet annihilation in phosphorescent solid mixed films". *Physica Status Solidi-Rapid Research Letters* **3**, 67 (2009).

[83] S. Reineke, K. Walzer, and K. Leo. "Triplet-exciton quenching in organic phosphorescent light-emitting diodes with Ir-based emitters". *Physical Review B* **75**, 125328 (2007).

[84] N. C. Giebink and S. R. Forrest. "Quantum efficiency roll-off at high brightness in fluorescent and phosphorescent organic light emitting diodes". *Physical Review B* **77**, 235215 (2008).

[85] S.-J. Su, E. Gonmori, H. Sasabe, and J. Kido. "Highly Efficient Organic Blue- and White-Light-Emitting Devices Having a Carrier- and Exciton-Confining Structure for Reduced Efficiency Roll-Off". *Advanced Materials* **20**, 4189 (2008).

[86] W. Ji, L. Zhang, and W. Xie. "Improving efficiency roll-off in phosphorescent OLEDs by modifying the exciton lifetime". *Optics Letters* **37**, 2019 (2012).

[87] R. G. Kepler. "Charge Carrier Production and Mobility in Anthracene Crystals". *Physical Review* **119**, 1226 (1960).

[88] M. C. J. M. Vissenberg and M. Matters. "Theory of the field-effect mobility in amorphous organic transistors". *Phys. Rev. B* **57**, 12964 (1998).

[89] G. Horowitz, R. Hajlaoui, H. Bouchriha, R. Bourguiga, and M. Hajlaoui. "The Concept of "Threshold Voltage" in Organic Field-Effect Transistors". *Advanced Materials* **10**, 923 (1998).

[90] P. W. M. Blom, M. J. M. de Jong, and J. J. M. Vleggaar. "Electron and hole transport in poly(p-phenylene vinylene) devices". *Applied Physics Letters* **68**, 3308 (1996).

[91] N. Karl. "Charge carrier transport in organic semiconductors". *Synthetic Metals* **133**, 649 (2003).

[92] H. Bässler. "Charge Transport in Disordered Organic Photoconductors a Monte Carlo Simulation Study". *Physica Status Solidi (b)* **175**, 15 (1993).

[93] M. A. Lampert and P. Mark. "Current injection in solids". Electrical science series. Academic Press (California) (1970).

[94] A. Rose. "Space-Charge-Limited Currents in Solids". *Physical Review* **97**, 1538 (1955).

[95] P. W. M. Blom, C. Tanase, D. M. de Leeuw, and R. Coehoorn. "Thickness scaling of the space-charge-limited current in poly(p-phenylene vinylene)". *Applied Physics Letters* **86**, 092105 (2005).

[96] P. N. Murgatroyd. "Dimensional considerations for space-charge conduction in solids". *Journal of Physics D: Applied Physics* **3**, 1488 (1970).

[97] M. Pope, H. P. Kallmann, and P. Magnante. "Electroluminescence in Organic Crystals". *The Journal of Chemical Physics* **38**, 2042 (1963).

[98] W. Helfrich and W. G. Schneider. "Recombination Radiation in Anthracene Crystals". *Physical Review Letters* **14**, 229 (1965).

[99] H. Shirakawa, E. J. Louis, A. G. MacDiarmid, C. K. Chiang, and A. J. Heeger. "Synthesis of Electrically Conducting Organic Polymers: Halogen Derivatives of Polyacetylene (CH)x". *Journal of Chemical Society, Chemical Communications* **474**, 578 (1977).

[100] C. K. Chiang, C. R. Fincher Jr., Y. W. Park, A. J. Heeger, H. Shirakawa, E. J. Louis, S. C. Gau, and A. G. MacDiarmid. "Electrical Conductivity in Doped Polyacetylene". *Physical Review Letters* **39**, 1098 (1977).

[101] M. Maitrot, G. Guillaud, B. Boudjema, J. J. Andre, and J. Simon. "Molecular material-based junctions: Formation of a Schottky contact with metallophthalocyanine thin films doped by the cosublimation method". *Journal of Applied Physics* **60**, 2396 (1986).

[102] T. C. Rosenow. "White Organic Light Emitting Diodes". TU Dresden (Dissertation) (2010).

[103] J. Kido and T. Matsumoto. "Bright organic electroluminescent devices having a metal-doped electron-injecting layer". *Applied Physics Letters* **73**, 2866 (1998).

[104] A. Yamamori, C. Adachi, T. Koyama, and Y. Taniguchi. "Doped organic light emitting diodes having a 650-nm-thick hole transport layer". *Applied Physics Letters* **72**, 2147 (1998).

[105] R. Meerheim, S. Olthof, M. Hermenau, S. Scholz, A. Petrich, N. Tessler, O. Solomeshch, B. Lüssem, M. Riede, and K. Leo. "Investigation of C 60F36 as low-volatility p-dopant in organic optoelectronic devices". *Journal of Applied Physics* **109**, 103102 (2011).

[106] S. Olthof, R. Meerheim, M. Schober, and K. Leo. "Energy level alignment at the interfaces in a multilayer organic light-emitting diode structure". *Physical Review B* **79**, 245308 (2009).

[107] J. M. Bharathan and Y. Yang. "Polymer/metal interfaces and the performance of polymer light-emitting diodes". *Journal of Applied Physics* **84**, 3207 (1998).

[108] D. Gebeyehu, K. Walzer, G. He, M. Pfeiffer, K. Leo, J. Brandt, A. Gerhard, P. Stössel, and H. Vestweber. "Highly efficient deep-blue organic light-emitting diodes with doped transport layers". *Synthetic Metals* **148**, 205 (2005).

[109] T. Matsushima and C. Adachi. "Extremely low voltage organic light-emitting diodes with p-doped alpha-sexithiophene hole transport and n-doped

phenyldipyrenylphosphine oxide electron transport layers". *Applied Physics Letters* **89**, 253506 (2006).

[110] M. A. Baldo, D. F. O'Brien, Y. You, A. Shoustikov, S. Sibley, M. E. Thomson, and S. R. Forrest. "Highly efficient phosphorescent emission from organic electroluminescent devices". *Nature* **395**, 151 (1998).

[111] M. A. Baldo, M. E. Thompson, and S. R. Forrest. "Phosphorescent materials for application to organic light emitting devices". *Pure and Applied Chemistry* **71**, 2095 (1999).

[112] G. He, M. Pfeiffer, K. Leo, M. Hofmann, J. Birnstock, R. Pudzich, and J. Salbeck. "High-efficiency and low-voltage p-i-n electrophosphorescent organic light-emitting diodes with double-emission layers". *Applied Physics Letters* **85**, 3911 (2004).

[113] R. Meerheim, K. Walzer, M. Pfeiffer, and K. Leo. "Ultrastable and efficient red organic light emitting diodes with doped transport layers". *Applied Physics Letters* **89**, 061111 (2006).

[114] P. Wellmann, M. Hofmann, O. Zeika, A. Werner, J. Birnstock, R. Meerheim, G. He, K. Walzer, M. Pfeiffer, and K. Leo. "High-efficiency p-i-n organic light-emitting diodes with long lifetime". *Journal of the SID* **13/5**, 393 (2005).

[115] G. Schwartz, S. Reineke, T. C. Rosenow, K. Walzer, and K. Leo. "Triplet Harvesting in Hybrid White Organic Light-Emitting Diodes". *Advanced Functional Materials* **19**, 1319 (2009).

[116] J. Ye, C.-J. Zheng, X.-M. Ou, X.-H. Zhang, M.-K. Fung, and C.-S. Lee. "Management of Singlet and Triplet Excitons in a Single Emission Layer: A Simple Approach for a High-Efficiency Fluorescence/Phosphorescence Hybrid White Organic Light-Emitting Device". *Advanced Materials* **24**, 3410 (2012).

[117] N. C. Giebink, Y. Sun, and S.R. Forrest. "Transient analysis of triplet exciton dynamics in amorphous organic semiconductor thin films". *Organic Electronics* **7**, 375 (2006).

[118] J. Wünsche, S. Reineke, B. Lüssem, and K. Leo. "Measurement of triplet exciton diffusion in organic light-emitting diodes". *Physical Review B* **81**, 245201 (2010).

[119] B. Milian-Medina and J. Gierschner. "Computational design of low singlet-triplet gap all-organic molecules for OLED application". *Organic Electronics* **13**, 985 (2012).

[120] A. Endo, K. Sato, K. Yoshimura, T. Kai, A. Kawada, H. Miyazaki, and C. Adachi. "Efficient up-conversion of triplet excitons into a singlet state and its application for organic light emitting diodes". *Applied Physics Letters* **98** (8), 083302 (2011).

[121] S. Y. Lee, T. Yasuda, H. Nomura, and C. Adachi. "High-efficiency organic light-emitting diodes utilizing thermally activated delayed fluorescence from triazine-based donor-acceptor hybrid molecules". *Applied Physics Letters* **101**, 093306 (2012).

[122] L. H. Smith, J. A. E. Wasey, I. D. W. Samuel, and W. L. Barnes. "Light Out-Coupling Efficiencies of Organic Light-Emitting Diode Structures and the Effect of Photoluminescence Quantum Yield". *Advanced Functional Materials* **15**, 1839 (2005).

[123] T. Tsutsui, E. Aminaka, C. P. Lin, and D.-U. Kim. "Extended molecular design concept of molecular materials for electroluminescence: sublimed-dye films, molecularly doped polymers and polymers with chromophores". *Philosophical Transactions of the Royal Society of London. Series A: Mathematical, Physical and Engineering Sciences* **355**, 801 (1997).

[124] N. C. Greenham, R. H. Friend, and D. D. C. Bradley. "Angular Dependence of the Emission from a Conjugated Polymer Light-Emitting Diode: Implications for Efficiency Calculations". *Advanced Materials* **6**, 491 (1994).

[125] M.-H. Lu and J. C. Sturm. "Optimization of external coupling and light emission in organic light-emitting devices: modeling and experiment". *Journal of Applied Physics* **91**, 595 (2002).

[126] X.-W. Chen, W. C. H. Choy, S. He, and P. C. Chui. "Comprehensive analysis and optimal design of top-emitting organic light-emitting devices". *Journal of Applied Physics* **101**, 113107 (2007).

[127] S. Nowy, B.C. Krummacher, J. Frischeisen, N.A. Reinke, and W. Brütting. "Light extraction and optical loss mechanisms in organic light-emitting diodes: Influence of the emitter quantum efficiency". *Journal of Applied Physics* **104**, 123109 (2008).

[128] B. C. Krummacher, S. Nowy, J. Frischeisen, M. Klein, and W. Brütting. "Efficiency analysis of organic light-emitting diodes based on optical simulation". *Organic Electronics* **10**, 478 (2009).

[129] M. C. Gather, M. Flämmich, N. Danz, D. Michaelis, and K. Meerholz. "Measuring the profile of the emission zone in polymeric organic light-emitting diodes". *Applied Physics Letters* **94**, 263301 (2009).

[130] S. L. M. van Mensfoort, M. Carvelli, M. Megens, D. Wehenkel, M. Bartyzel, H. Greiner, R. A. J. Janssen, and R. Coehoorn. "Measuring the light emission profile in organic light-emitting diodes with nanometre spatial resolution". *Nature Photonics* **4**, 329 (2010).

[131] R. Meerheim, M. Furno, S. Hofmann, B. Lüssem, and K. Leo. "Quantification of energy loss mechanisms in organic light-emitting diodes". *Applied Physics Letters* **97**, 253305 (2010).

[132] D. S. Setz, T. D. Schmidt, M.l Flämmich, S. Nowy, J. Frischeisen, B. C. Krummacher, T. Dobbertin, K. Heuser, D. Michaelis, N. Danz, W. Brütting, and A. Winnacker. "Comprehensive efficiency analysis of organic light-emitting devices". *Journal of Photonics for Energy* **1**, 011006 (2011).

[133] M. Flämmich, M. C. Gather, N. Danz, D. Michaelis, A. H. Bräuer, K. Meerholz, and A. Tünnermann. "Orientation of emissive dipoles in OLEDs: Quantitative in situ analysis". *Organic Electronics* **11**, 1039 (2010).

[134] M. Flämmich, J. Frischeisen, D. S. Setz, D. Michaelis, B. C. Krummacher, T. D. Schmidt, W. Brütting, and N. Danz. "Oriented phosphorescent emitters boost OLED efficiency". *Organic Electronics* **12**, 1663 (2011).

[135] M. Flämmich, D. Michaelis, and N. Danz. "Accessing OLED emitter properties by radiation pattern analyses". *Organic Electronics* **12**, 83 (2011).

[136] J. Frischeisen, D. Yokoyama, C. Adachi, and W. Brütting. "Determination of molecular dipole orientation in doped fluorescent organic thin films by photoluminescence measurements". *Applied Physics Letters* **96**, 073302 (2010).

[137] J. Frischeisen, D. Yokoyama, A. Endo, C. Adachi, and W. Brütting. "Increased light outcoupling efficiency in dye-doped small molecule organic light-emitting diodes with horizontally oriented emitters". *Organic Electronics* **12**, 817 (2011).

[138] T. D. Schmidt, D. S. Setz, M. Flämmich, J. Frischeisen, D. Michaelis, B. C. Krummacher, N. Danz, and W. Brütting. "Evidence for non-isotropic emitter orientation in a red phosphorescent organic light-emitting diode and its implications for determining the emitter's radiative quantum efficiency". *Applied Physics Letters* **99**, 163302 (2011).

[139] D. Yokoyama. "Molecular orientation in small-molecule organic light-emitting diodes". *Journal of Materials Chemistry* **21**, 19187 (2011).

[140] P. Liehm. "Untersuchungen zur internen Quanteneffizienz in organischen Leuchtdioden". TU Dresden (Diploma thesis) (2012).

[141] S. Mladenovski, K. Neyts, D. Pavicic, A. Werner, and C. Rothe. "Exceptionally efficient organic light emitting devices using high refractive index substrates.". *Optics Express* **17**, 7562 (2009).

[142] S. Möller and S. R. Forrest. "Improved light out-coupling in organic light emitting diodes employing ordered microlens arrays". *Journal of Applied Physics* **91**, 3324 (2002).

[143] M.-K. Wei and I-L. Su. "Method to evaluate the enhancement of luminance efficiency in planar OLED light emitting devices for microlens array.". *Optics Express* **12**, 5777 (2004).

[144] H. Mu, W. Li, R. Jones, A. Steckl, and D. Klotzkin. "A comparative study of electrode effects on the electrical and luminescent characteristics of Alq3/TPD OLED: Improvements due to conductive polymer (PEDOT) anode". *Journal of Luminescence* **126**, 225 (2007).

[145] K. Fehse, K. Walzer, K. Leo, W. Lövenich, and A. Elschner. "Highly Conductive Polymer Anodes as Replacements for Inorganic Materials in High-Efficiency Organic Light-Emitting Diodes". *Advanced Materials* **19**, 441 (2007).

[146] Z. Yu, Q. Zhang, L. Li, Q. Chen, X. Niu, J. Liu, and Q. Pei. "Highly Flexible Silver Nanowire Electrodes for Shape-Memory Polymer Light-Emitting Diodes". *Advanced Materials* **23**, 664 (2011).

[147] L. Li, Z. Yu, W. Hu, C.-H. Chang, Q. Chen, and Q. Pei. "Efficient Flexible Phosphorescent Polymer Light-Emitting Diodes Based on Silver Nanowire-Polymer Composite Electrode". *Advanced Materials* **23**, 5563 (2011).

[148] S.-Y. Hsu, M.-C. Lee, K.-L. Lee, and P.-K. Wei. "Extraction enhancement in organic light emitting devices by using metallic nanowire arrays". *Applied Physics Letters* **92**, 013303 (2008).

[149] T.-H. Han, Y. Lee, M.-R. Choi, S.-H. Woo, S.-H. Bae, B. H. Hong, J.-H. Ahn, and T.-W. Lee. "Extremely Efficient Flexible Organic Light-Emitting Diodes with Modified Graphene Anode". *Nature Photonics* **6**, 105 (2012).

[150] B. Riedel, Y. Shen, J. Hauss, M. Aichholz, X. Tang, U. Lemmer, and M. Gerken. "Tailored Highly Transparent Composite Hole-Injection Layer Consisting of Pedot:PSS and SiO2 Nanoparticles for Efficient Polymer Light-Emitting Diodes". *Advanced Materials* **23**, 740 (2011).

[151] C.-H. Chang, K.-Y. Chang, Y.-J. Lo, S.-J. Chang, and H.-H. Chang. "Four-fold power efficiency improvement in organic light-emitting devices using an embedded nanocomposite scattering layer". *Organic Electronics* **13**, 1073 (2012).

[152] J. Frischeisen, Q. Niu, A. Abdellah, J. B. Kinzel, R. Gehlhaar, G. Scarpa, C. Adachi, P. Lugli, and W. Brütting. "Light extraction from surface plasmons and waveguide modes in an organic light-emitting layer by nanoimprinted gratings.". *Optics Express* **19**, 7 (2011).

[153] J. Hauss, T. Bocksrocker, B. Riedel, U. Geyer, U. Lemmer, and M. Gerken. "Metallic Bragg-gratings for light management in organic light-emitting devices". *Applied Physics Letters* **99**, 103303 (2011).

[154] M. C. Gather, A. Köhnen, and K. Meerholz. "White Organic Light-Emitting Diodes". *Advanced Materials* **23**, 233 (2011).

[155] K. T. Kamtekar, A. P. Monkman, and M. R. Bryce. "Recent Advances in White Organic Light-Emitting Materials and Devices (WOLEDs).". *Advanced Materials* **22**, 572 (2010).

[156] H. J. Bolink, F. De Angelis, E. Baranoff, C. Klein, S. Fantacci, E. Coronado, M. Sessolo, K. Kalyanasundaram, M. Grätzel, and M. K. Nazeeruddin. "White-light phosphorescence emission from a single molecule: application to OLED". *Chemical Communications* , 4672 (2009).

[157] Y. B. Yuan, S. Li, Z. Wang, H. T. Xu, and X. Zhou. "White organic light-emitting diodes combining vacuum deposited blue electrophosphorescent devices with red surface color conversion layers". *Optics Express* **17**, 1577 (2009).

[158] L. S. Liao, K. P. Klubek, and C. W. Tang. "High-efficiency tandem organic light-emitting diodes". *Applied Physics Letters* **84**, 167 (2004).

[159] Y. Sun and S. R. Forrest. "Enhanced light out-coupling of organic light-emitting devices using embedded low-index grids". *Nature Photonics* **2**, 483 (2008).

[160] B. W. D'Andrade, R. J. Holmes, and S.R. Forrest. "Efficient Organic Electrophosphorescent White-Light-Emitting Device with a Triple Doped Emissive Layer". *Advanced Materials* **16**, 624 (2004).

[161] Y. Sun and S. R. Forrest. "Multiple exciton generation regions in phosphorescent white organic light emitting devices". *Organic Electronics* **9**, 994 (2008).

[162] H. Sasabe, J.-I. Takamatsu, T. Motoyama, S. Watanabe, G. Wagenblast, N. Langer, O. Molt, E. Fuchs, C. Lennartz, and J. Kido. "High-Efficiency Blue and White Organic Light-Emitting Devices Incorporating a Blue Iridium Carbene Complex". *Advanced Materials* **22**, 5003 (2010).

[163] G. Schwartz, S. Reineke, K. Walzer, and K. Leo. "Reduced efficiency roll-off in high-efficiency hybrid white organic light-emitting diodes". *Applied Physics Letters* **92** (5), 053311 (2008).

[164] The sublimation has been done by Annette Petrich, Tina Träger, and Sylke Furkert at IAPP.

[165] V. Coropceanu, N. E. Gruhn, S. Barlow, C. Lambert, J. C. Durivage, T. G. Bill, G. Nöll, S. R. Marder, and J.-L. Bredas. "Electronic Couplings in Organic Mixed-Valence Compounds: the Contribution of Photoelectron Spectroscopy". *Journal of the American Chemical Society* **126**, 2727 (2004).

[166] P. K. Koech, A. B. Padmaperuma, L. Wang, J. S. Swensen, E. Polikarpov, J. T. Darsell, J. E. Rainbolt, and D. J. Gaspar. "Synthesis and Application of 1,3,4,5,7,8-Hexafluorotetracyanonaphthoquinodimethane (F6-TNAP): A Conductivity Dopant for Organic Light-Emitting Devices". *Chemistry of Materials* **22**, 3926 (2010).

[167] S. Olthof. "Photoelectron Spectroscopy on Doped Organic Semiconductors and Related Interfaces". TU Dresden (Dissertation) (2010).

[168] P. van Gemmern, V. van Elsbergen, S. P. Grabowski, H. Boerner, H.-P. Löbl, H. Becker, H. Kalisch, M. Heuken, and R. H. Jansen. "Influence of carrier conductivity and injection on efficiency and chromaticity in small-molecule white organic light-emitting diodes based on 4,4'-bis(2,2'-diphenylvinyl)-1,1'-spirobiphenyl and rubrene". *Journal of Applied Physics* **100**, 123707 (2006).

[169] M. Ikai, S. Tokito, Y. Sakamoto, T. Suzuki, and Y. Taga. "Highly efficient phosphorescence from organic light-emitting devices with an exciton-block layer". *Applied Physics Letters* **79**, 156 (2001).

[170] M. Aonuma, T. Oyamada, H. Sasabe, T. Miki, and C. Adachi. "Material design of hole transport materials capable of thick-film formation in organic light emitting diodes". *Applied Physics Letters* **90**, 183503 (2007).

[171] V. I. Adamovich, S. R. Cordero, P. I. Djurovich, A. Tamayo, M. E. Thompson, B. W. D'Andrade, and S. R. Forrest. "New charge-carrier blocking materials for high efficiency OLEDs". *Organic Electronics* **4**, 77 (2003).

[172] T.-Y. Chu, Y.-S. Wu, J.-F. Chen, and C. H. Chen. "Characterization of electronic structure of aluminum (III) bis(2-methyl-8-quninolinato)-4-phenylphenolate (BAlq) for phosphorescent organic light emitting devices". *Chemical Physics Letters* **404**, 121 (2005).

[173] P. Kundu, K. R. Justin Thomas, J. T. Lin, Y.-T. Tao, and C.-H. Chien. "High-Tg Carbazole Derivatives as Blue-Emitting Hole-Transporting Materials for Electroluminescent Devices". *Advanced Functional Materials* **13**, 445 (2003).

[174] S. O. Jeon, K. S. Yook, C. W. Joo, H. S. Son, S. E. Jang, and J. Y. Lee. "High efficiency red phosphorescent organic light-emitting diodes using a spirobenzofluorene type phosphine oxide as a host material". *Organic Electronics* **10**, 998 (2009).

[175] X. Ren, J. Li, R. J. Holmes, P. I. Djurovich, S. R. Forrest, and M. E. Thompson. "Ultrahigh Energy Gap Hosts in Deep Blue Organic Electrophosphorescent Devices". *Chemistry of Materials* **16**, 4743 (2004).

[176] S. Lamansky, P. Djurovich, D. Murphy, F. Abdel-Razzaq, H. E. Lee, C. Adachi, P. E. Burrows, S. R. Forrest, and M. E. Thompson. "Highly Phosphorescent Bis-Cyclometalated Iridium Complexes: Synthesis, Photophysical Characterization, and Use in Organic Light Emitting Diodes". *Journal of the American Chemical Society* **123**, 4304 (2001).

[177] J.-P. Duan, P.-P. Sun, and C.-H. Cheng. "New Iridium Complexes as Highly Efficient Orange-Red Emitters in Organic Light-Emitting Diodes". *Advanced Materials* **15**, 224 (2003).

[178] Y. Kawamura, J. Brooks, J. J. Brown, H. Sasabe, and C. Adachi. "Intermolecular Interaction and a Concentration-Quenching Mechanism of Phosphorescent Ir(III) Complexes in a Solid Film". *Physical Review Letters* **96**, 017404 (2006).

[179] The measurements have been performed at IAPP by Rene Michel and Caroline Weichsel using a Fluormax (SPEX) spectrophotometer.

[180] HOMO values are taken from the ionization potential determined by Selina Olthof at IAPP via UPS. LUMO values are calculated using the HOMO energy and the optical band gap.

[181] N. Seidler. "Entwicklung einer Architektur für effiziente blaue OLEDs". TU Dresden (Diploma thesis) (2008).

[182] K. S. Yook, S. O. Jeon, C. W. Joo, and J. Y. Lee. "Fabrication of high efficiency and color stable white organic light-emitting diodes by an alignment free mask patterning". *Organic Electronics* **10**, 384 (2009).

[183] W. A. Luhman and R. J. Holmes. "Enhanced exciton diffusion in an organic photovoltaic cell by energy transfer using a phosphorescent sensitizer". *Applied Physics Letters* **94**, 153304 (2009).

[184] C. Falkenberg. "Optimizing Organic Solor Cells - Transparent Electron Transport Materials for Improving the Device Performance". TU Dresden (Dissertation) (2011).

[185] The measurements have been performed at IAPP. Thickness and sheet resistance are obtained using a Veeco Dektak 150 profilometer and Lucas Labs 304 4-point probe measurement setup, respectively.

[186] The measurements have been performed at IAPP using a Perkin Elmer Lambda 900 spectrophotometer.

[187] P. Freitag. "White Top-Emitting OLEDs on Metal Substrates". TU Dresden (Dissertation) (2010).

[188] The OLEDs at the Lesker tools have been processed by Tobias Günther, Caroline Walde, and Andreas Wendel.

[189] S. Hofmann. "Untersuchung der Winkelabhängigkeit topemittierender organischer Leuchtdioden". TU Dresden (Diploma thesis) (2009).

[190] H. Aziz, Z. D. Popovic, N.-X. Hu, A.-M. Hor, and G. Xu. "Degradation Mechanism of Small Molecule-Based Organic Light-Emitting Devices". *Science* **283**, 1900 (1999).

[191] S. Scholz, R. Meerheim, B. Lüssem, and K. Leo. "Laser desorption/ionization time-of-flight mass spectrometry: A predictive tool for the lifetime of organic light emitting devices". *Applied Physics Letters* **94**, 043314 (2009).

[192] R. Seifert, S. Scholz, B. Lüssem, and K. Leo. "Comparison of ultraviolet- and charge-induced degradation phenomena in blue fluorescent organic light emitting diodes". *Applied Physics Letters* **97**, 013308 (2010).

[193] I. R. de Moraes, S. Scholz, B. Lüssem, and K. Leo. "Analysis of chemical degradation mechanism within sky blue phosphorescent organic light emitting diodes by laser-desorption/ionization time-of-flight mass spectrometry". *Organic Electronics* **12**, 341 (2011).

[194] R. Seifert. "Untersuchung zu Ursachen und Mechanismen der Degradation an blauen Singulett-Emittern". TU Dresden (Diploma thesis) (2009).

[195] The time and wavelength calibration were done by Jens Ludwig and Paul-Anton Will using defined light pulses and a different color filters, respectively.

[196] http://sales.hamamatsu.com/assets/pdf/hpspdf/Guidetostreak.pdf. "Guide to streak cameras".

[197] J. Ludwig. "Time Resolved Spectroscopy on thin films of Oligothiophene molecules". TU Dresden (Diploma thesis) (2011).

[198] H. Benisty, R. Stanley, and M. Mayer. "Method of source terms for dipole emission modification in modes of arbitrary planar structures". *Journal of the Optical Society of America A* **15**, 1192 (1998).

[199] The optical constants of the materials are either obtained by ellipsometry measurements at the Fraunhofer IPMS (Dresden) or by transmission and reflection measurements at the IAPP. The calculation of n&k values is done using an algorithm introduced by Fritz et al. [253].

[200] R. Meerheim, R. Nitsche, and K. Leo. "High-efficiency monochrome organic light emitting diodes employing enhanced microcavities". *Applied Physics Letters* **93**, 043310 (2008).

[201] M. Furno, R. Meerheim, M. Thomschke, S. Hofmann, B. Lüssem, and K. Leo. "Outcoupling efficiency in small-molecule OLEDs: from theory to experiment". *Proceedings of SPIE* **7617**, 761716 (2010).

[202] S. Hofmann, M. Thomschke, P. Freitag, M. Furno, B. Lüssem, and K. Leo. "Top-emitting organic light-emitting diodes: Influence of cavity design". *Applied Physics Letters* **97**, 253308 (2010).

[203] http://www.gaussian.com/ (24.08.2012).

[204] http://www.dftb plus.info/ (24.08.2012).

[205] http://www.dftb.org/ (24.08.2012).

[206] http://www.cmbi.ru.nl/molden/ (24.08.2012).

[207] http://www.ks.uiuc.edu/Research/vmd/ (24.08.2012).

[208] G. Schwartz. "Novel Concepts for High-Efficiency White Organic Light-Emitting Diodes". TU Dresden (Dissertation) (2007).

[209] C.-L. Ho, W. Y. Wong, Q. Wang, D. Ma, L. Wang, and Z. Lin. "A Multifunctional Iridium-Carbazolyl Orange Phosphor for High-Performance Two-Element WOLED Exploiting Exciton-Managed Fluorescence/Phosphorescence". *Advanced Functional Materials* **18**, 928 (2008).

[210] V. Jankus, C. Winscom, and A. P. Monkman. "Dynamics of triplet migration in films of N, N'-diphenyl-N, N'-bis(1-naphthyl)-1, 1'-biphenyl-4, 4"-diamine". *Journal of Physics: Condensed Matter* **22**, 185802 (2010).

[211] M. Cocchi, D. Virgili, G. Giro, V. Fattori, P. Di Marco, J. Kalinowski, and Y. Shirota. "Efficient exciplex emitting organic electroluminescent devices". *Applied Physics Letters* **80**, 2401 (2002).

[212] K.i Goushi and C. Adachi. "Efficient organic light-emitting diodes through up-conversion from triplet to singlet excited states of exciplexes". *Applied Physics Letters* **101**, 023306 (2012).

[213] S. Reineke, T. C. Rosenow, B. Lüssem, and K. Leo. "Improved high-brightness efficiency of phosphorescent organic LEDs comprising emitter molecules with small permanent dipole moments.". *Advanced Materials* **22**, 3189 (2010).

[214] T. C. Wong, J. Kovac, C. S. Lee, L. S. Hung, and S. T. Lee. "Transient electroluminescence measurements on electron-mobility of N-arylbenzimidazoles". *Chemical Physics Letters* **334**, 61 (2001).

[215] A. K. Ghosh and T. Feng. "Merocynanine organic solar cells". *Journal of Applied Physics* **49**, 5982 (1978).

[216] R. Signerski and G. Jarosz. "Diffusion length of singlet excitons in copper phthalocyanine films". *Photonics Letters of Poland* **3**, 107 (2011).

[217] D. Kurrle and J. Pflaum. "Exciton diffusion length in the organic semiconductor diindenoperylene". *Applied Physics Letters* **92**, 133306 (2008).

[218] S. Banerjee, A. P. Parhi, S. S. K. Iyer, and S. Kumar. "Method of determining the exciton diffusion length using optical interference effect in Schottky diode". *Applied Physics Letters* **94**, 223303 (2009).

[219] N. Matsusue, S. Ikame, Y. Suzuki, and H. Naito. "Charge-carrier transport and triplet exciton diffusion in a blue electrophosphorescent emitting layer". *Journal of Applied Physics* **97**, 123512 (2005).

[220] S. Cook, H. Liyuan, A. Furube, and R. Katoh. "Singlet Annihilation in Films of Regioregular Poly (3-hexylthiophene): Estimates for Singlet Diffusion Lengths and the Correlation between Singlet Annihilation Rates and Spectral Relaxation". *The Journal of Physical Chemistry C* **114**, 10962 (2010).

[221] D. E. Markov, E. Amsterdam, P. W. M. Blom, A. B. Sieval, and J. C. Hummelen. "Accurate measurement of the exciton diffusion length in a conjugated polymer using a heterostructure with a side-chain cross-linked fullerene layer". *The Journal of Physical Chemistry A* **109**, 5266 (2005).

[222] S. Cook, A. Furube, R. Katoh, and L. Han. "Estimate of singlet diffusion lengths in PCBM films by time-resolved emission studies". *Chemical Physics Letters* **478**, 33 (2009).

[223] A. J. Lewis, A. Ruseckas, O. P. M. Gaudin, G. R. Webster, P. L. Burn, and I. D. W. Samuel. "Singlet exciton diffusion in MEH-PPV films studied by exciton-exciton annihilation". *Organic Electronics* **7**, 452 (2006).

[224] H. Gommans, S. Schols, A. Kadashchuk, and P. Heremans. "Exciton Diffusion Length and Lifetime in Subphthalocyanine Films". *Journal of Physical Chemistry C* **113**, 2974 (2009).

[225] A. Holzhey, C. Uhrich, E. Brier, E. Reinhold, P. Bäuerle, K. Leo, and M. Hoffmann. "Exciton diffusion and energy transfer in organic solar cells based on dicyanovinyl-terthiophene". *Journal of Applied Physics* **104**, 064510 (2008).

[226] J. Kalinowski, V. Fattori, and P. Di Marco. "Surface reactions of singlet excitons in solid films of 8-hydroxyquinoline aluminium (Alq 3)". *Chemical Physics* **266**, 85 (2001).

[227] R. Schüppel, T. Dienel, K. Leo, and M. Hoffmann. "Time-resolved luminescence quenching in thin films of perylene-tetracarboxylic-dianhydride". *Journal of Luminescence* **110**, 309 (2004).

[228] R. R. Lunt, N. C. Giebink, A. A. Belak, J. B. Benziger, and S. R. Forrest. "Exciton diffusion lengths of organic semiconductor thin films measured by spectrally resolved photoluminescence quenching". *Journal of Applied Physics* **105**, 053711 (2009).

[229] S. R. Scully and M. D. McGehee. "Effects of optical interference and energy transfer on exciton diffusion length measurements in organic semiconductors". *Journal of Applied Physics* **100**, 034907 (2006).

[230] B. A. Gregg, J. Sprague, and M. W. Peterson. "Long-Range Singlet Energy Transfer in Perylene Bis(phenethylimide) Films". *The Journal of Physical Chemistry B* **101**, 5362 (1997).

[231] M. Lebental, H. Choukri, S. Chenais, S. Forget, A. Siove, B. Geffroy, and E. Tutis. "Diffusion of triplet excitons in an operational organic light-emitting diode". *Physical Review B* **79**, 165318 (2009).

[232] B. W. D'Andrade, M. E. Thompson, and S. R. Forrest. "Controlling Exciton Diffusion in Multilayer White Phosphorescent Organic Light Emitting Devices". *Advanced Materials* **14**, 147 (2002).

[233] Y. C. Zhou, L. L. Ma, J. Zhou, X. M. Ding, and X. Y. Hou. "Effect of a sensing layer on triplet exciton diffusion in organic films". *Physical Review B* **75**, 132202 (2007).

[234] J. Wünsche. "Investigation of triplet-exciton diffusion in organic semiconductors". TU Dresden (Diploma thesis) (2009).

[235] Y. Zhang, M. Slootsky, and S. R. Forrest. "Enhanced efficiency in high-brightness fluorescent organic light emitting diodes through triplet management". *Applied Physics Letters* **99**, 223303 (2011).

[236] S. Scholz, Q. Huang, M. Thomschke, S. Olthof, P. Sebastian, K. Walzer, K. Leo, S. Oswald, C. Corten, and D. Kuckling. "Self-doping and partial oxidation of metal-on-organic interfaces for organic semiconductor devices studied by chemical analysis techniques". *Journal of Applied Physics* **104**, 104502 (2008).

[237] P. M. S. Monk, R. J. Mortimer, and D. R. Rosseinsky. "Electrochromism". VCH (Weinheim), 1st edition (1995).

[238] C.G. Zoski. "Handbook of Electrochemistry". Elsevier (Amsterdam), 1st edition (2007).

[239] http://minerals.usgs.gov/. "U.S. Geological Survey, Mineral Commodity Summaries" (02.05.2012).

[240] Z. B. Wang, M. G. Helander, J. Qiu, D. P. Puzzo, M. T. Greiner, Z. M. Hudson, S. Wang, Z. W. Liu, and Z. H. Lu. "Unlocking the full potential of organic light-emitting diodes on flexible plastic". *Nature Photonics* **5**, 753 (2011).

[241] M. Mazzeo, F. della Sala, F. Mariano, G. Melcarne, S. D' Agostino, Y. Duan, R. Cingolani, and G. Gigli. "Shaping White Light Through Electroluminescent Fully Organic Coupled Microcavities". *Advanced Materials* **22**, 4696 (2010).

[242] L. Li, Z. Yu, C. Chang, W. Hu, X. Niu, Q. Chen, and Q. Pei. "Efficient White Polymer Light-Emitting Diodes Employing a Silver Nanowire-Polymer Composite". *Physical Chemistry Chemical Physics* , accepted (2012).

[243] T. Sun, Z. L. Wang, Z. J. Shi, G. Z. Ran, W. J. Xu, Z. Y. Wang, Y. Z. Li, L. Dai, and G. G. Qin. "Multilayered graphene used as anode of organic light emitting devices". *Applied Physics Letters* **96**, 133301 (2010).

[244] T.-H. Han, Y. Lee, M.-R. Choi, S.-H. Woo, S.-H. Bae, B. H. Hong, J.-H. Ahn, and T.-W. Lee. "Supplementary Information_Extremely Efficient Flexible Organic Light-Emitting Diodes with Modified Graphene Anode". *Nature Photonics* **6**, 105 (2012).

[245] W. Gaynor, J.-Y. Lee, and P. Peumans. "Fully solution-processed inverted polymer solar cells with laminated nanowire electrodes". *ACS NANO* **4**, 30 (2010).

[246] W. Gaynor, G. F. Burkhard, M. D. McGehee, and P. Peumans. "Smooth Nanowire/Polymer Composite Transparent Electrodes". *Advanced Materials* **23**, 2905 (2011).

[247] W. Gaynor, S. Hofmann, M. G. Christoforo, C. Sachse, S. Mehra, A. Salleo, M.D. McGehee, M. C. Gather, B. Lüssem, L. Müller-Meskamp, P. Peumans, and K. Leo. "Color in the Corners: ITO-Free White OLEDs with Angular Color Stability". *in preparation* (2012).

[248] M. W. Rowell and M. D. McGehee. "Transparent electrode requirements for thin film solar cell modules". *Energy & Environmental Science* **4**, 131 (2011).

[249] G. Schwartz, K. Fehse, M. Pfeiffer, K. Walzer, and K. Leo. "Highly efficient white organic light emitting diodes comprising an interlayer to separate fluorescent and phosphorescent regions". *Applied Physics Letters* **89**, 083509 (2006).

[250] P. Michel, J. Dugas, J. M. Cariou, and L. Martin. "Thermal variations of refractive index of PMMA, polystyrene, and poly (4-methyl-1 -pentene)". *Journal of Macromolecular Science, Part B* **25** (1986).

[251] P. Mulvey. " Hydrocarbons". *Enviromental Earth & Sciences - TECHNICAL PAPER* **2**.

[252] E. K. C. Lee, M. W. Schmidt, R. G. Shortridge Jr., and G. A. Haninger Jr. "Fluorescence Quenching by Singlet Energy Transfer. I. From Benzene and Toluene to pi-Bonded Molecules". *Journal of Physical Chemistry* **73**, 1805 (1969).

[253] T. Fritz, J. Hahn, and H. Böttcher. "Determination of the optical constants of evaporated dye layers". *Thin Solid Films* **170**, 249 (1989).

Acknowledgments

First, I would like to say that I'm thankful for every experience I could make at the IAPP. The motivation, assistance, and backup of so many people was essential to successfully finish this work. Especially, I would like to thank:

Versicherung

Hiermit versichere ich, dass ich die vorliegende Arbeit ohne unzulässige Hilfe Dritter und ohne Benutzung anderer als der angegebenen Hilfsmittel angefertigt habe; die aus fremden Quellen direkt oder indirekt übernommenen Gedanken sind als solche kenntlich gemacht. Die Arbeit wurde bisher weder im Inland noch im Ausland in gleicher oder ähnlicher Form einer anderen Prüfungsbehörde vorgelegt.

Diese Arbeit wurde am Institut für Angewandte Photophysik der Technischen Universität Dresden unter der wissenschaftlichen Betreuung von Prof. Dr. Karl Leo angefertigt.

Ich erkenne die Promotionsordnung der Fakultät Mathematik und Naturwissenschaften der Technischen Universität Dresden vom 23. Februar 2011 an.

Dresden, den

(Simone Hofmann)